2016

Pyroglutamylated amyloid beta peptides enhance non-fibrillogenic aggregation of the unmodified peptide

Gregory Goldblatt
University of Central Florida

PYROGLUTAMYLATED AMYLOID BETA PEPTIDES ENHANCE NON-FIBRILLOGENIC AGGREGATION OF THE UNMODIFIED PEPTIDE

by

GREGORY L. GOLDBLATT
B.S. University of Central Florida, 2012
M.S. University of Central Florida, 2015

A dissertation submitted in partial fulfillment of the requirements
for the degree of Doctor of Philosophy
in the Burnett School of Biomedical Sciences
in the College of Medicine
at the University of Central Florida
Orlando, Florida

Spring Term
2016

Major Professor: Suren A. Tatulian

ABSTRACT

Alzheimer's disease (AD) is accompanied by abnormal extracellular deposition of amyloid β (Aβ) peptide. This has led to the amyloid cascade hypothesis, causatively relating Aβ with AD. While Aβ deposits assume a fibrillar cross-β structure, prefibrillar oligomers of Aβ have been identified as the main cytotoxic agents in AD. Pyroglutamylated amyloid beta (AβpE) peptides are N-terminally truncated and pyroglutamylated (at Glu3 or Glu11) Aβ molecules that display enhanced cytotoxicity and represent up to 50% of total Aβ in AD brains. AβpE significantly enhances the toxicity of unmodified Aβ by an unknown mechanism. Although *in situ* Aβ populations are heterogeneous, the majority of studies have been conducted on single Aβ species.

Here, we examined the structural and morphological changes that occur in mixed Aβ/AβpE samples. Circular dichroism and transmission electron microscopy data indicate that $A\beta_{pE3\text{-}42}$ forms β-sheet structure and undergoes delayed fibrillogenesis compared to unmodified $A\beta_{1\text{-}42}$. Further, $A\beta_{pE3\text{-}42}$ decelerates β-sheet formation in mixed $A\beta_{1\text{-}42}/A\beta_{pE3\text{-}42}$ samples. FTIR measurements, using ^{13}C-labeled $A\beta_{1\text{-}42}$ and unlabeled $A\beta_{pE3\text{-}42}$, indicate that $A\beta_{pE3\text{-}42}$ inhibits cross-β-sheet formation by $A\beta_{1\text{-}42}$, which explains the retardation of fibrillogenesis. FTIR on peptides ^{13}C-labeled at specific segments provided site specific structural information. Based on these data, the monomeric Aβ structure has been modeled as a β-hairpin stabilized by intramolecular H-bonding with an

N-terminal α-helix. These hairpins likely form higher order aggregates through ionic and hydrophobic interactions between the C-terminus of one hairpin and the N-terminus of another. Utilizing a novel technique, hydration from gas phase, we examined the α-helix to β-sheet transitions of these peptides. When combined, $A\beta_{pE3-42}$ and $A\beta_{1-42}$ mutually inhibit intermolecular β-sheet formation, instead promoting formation of $A\beta_{pE3-42}/A\beta_{1-42}$ hetero-oligomers of intramolecular H-bonding.

These hetero-oligomers displayed enhanced toxicity to PC12 cells compared to individual peptides and induced greater calcium release from lipid vesicles than unmodified Aβ. These results indicate that Aβ and AβpE mutually inhibit fibrillogenesis and stabilize hetero-oligomers of enhanced cytotoxicity, possibly through a membrane permeabilization mechanism. Collectively, our findings lead to a new concept that Aβ/AβpE hetero-oligomers, not just Aβ or AβpE oligomers, are the main cytotoxic species in AD.

This work is dedicated to my parents for everything they have done to help me get to where I am today

ACKNOWLEDGMENTS

I would like to first and foremost acknowledge my mentor Dr. Suren A Tatulian. Your expertise and guidance have been instrumental in my education. In three short years I learned more than I could have dreamed. Through you I learned how to approach problems differently and be more objective of my own work. Thank you for making me into the scientist I am today.

To the other members of my committee, Dr. Ken Teter Dr. Bo Chen and Dr. Stephen King, I thank you for your membership on my committee; your input on this project was invaluable. You forced me to broaden my thinking making sure I did not get become too focused on things and lose sight of the bigger picture.

I would also like to graciously thank Dr. Ken Teter for the support without which I would not have been able to finish this project.

I would like to thank Dr. Bo Chen, Jaekyun Jeon and the rest of the Chen lab for your collaboration in collecting the TEM data for my project.

I would like to thank my former and current coworkers in the Tatulian lab especially Jason Matos, Jeremy Gornto, and Nabin Kandel.

TABLE OF CONTENTS

LIST OF FIGURES

LIST OF TABLES

LIST OF ACCRONYMS AND ABBREVIATIONS

Adenosine tri phosphate (ATP)

Alzheimer's disease (AD)

Amyloid beta (Aβ)

Amyloid beta 1-40 ($A\beta_{1-40}$)

Amyloid beta 1-42 ($A\beta_{1-42}$)

Amyloid precursor protein (APP)

APP intracellular domain (AICD)

Apolipoprotein E (ApoE)

Blood brain barrier (BBB)

Calcium induced calcium release (CICR)

Cellular prion protein (PrP^{c})

Cerebral amyloid angiopathy (CAA)

Circular dichroism (CD)

Cyclin dependent kinase 5 (Cdk5)

Down syndrome (DS)

Dynamin related protein 1 (drp1)

Endoplasmic reticulum (ER)

Eukaryotic elongation factor 2 (eEF2)

Familial Alzheimer's disease (FAD)

Fourier transform infrared spectroscopy (FTIR)

Glutaminyl cyclase (QC)

Glyceraldehyde 3-phosphate dehydrogenase (GAPDH)

Guanosine tri phosphate (GTP)

Hexafluoro Isopropanol (HFIP)

Inducible nitric oxide synthase (iNOS)

Long-term potentiation (LTP)

Low density lipoprotein receptor-related protein 1 (LRP1)

Metabotropic glutamate receptor 5 (MGluR5)

Neurofibrillary tangles (NFTs)

Neuronal nitric oxide synthase (nNOS)

N-methyl D-aspartate receptor (NMDAR)

Nitric oxide (NO)

Nitric oxide synthase (NOS)

Nuclear magnetic resonance (NMR)

Presenilin 1 (PSEN1)

Presenilin 2 (PSEN2)

Pyroglutamylated amyloid beta (pE-Aβ)

Pyroglutamylated amyloid beta 3-42 ($A\beta_{pE3-42}$)

Reactive nitridative species (RNS)

Reactive oxidative species (ROS)

Ryanodie receptor 3 (RyR3)

S-nitrosylation (SNO)

Solid-State Nuclear Magnetic Resonance (ssNMR)

Sporadic Alzheimer's disease (SAD)

Very low density lipoprotein receptor (VLDLR)

1-palmitoyl-2-oleoyl-sn-glycero-3-phosphocholine (POPC)

1-palmitoyl-2-oleoyl-sn-glycero-3-phosphoglycerol (POPG)

CHAPTER ONE: INTRODUCTION

Alzheimer's disease (AD) is a neurodegenerative disease affecting more than 35 million people worldwide. The primary symptom of AD is progressive loss of memory and other cognitive faculties leading to death within 3-9 years of diagnoses (1). AD is the most common form of dementia representing over 50% of cases examined at autopsy or clinical series (1). AD primarily affects the elderly. The odds of being diagnosed with AD double every 5 years after the age of 65, and the odds of receiving a positive diagnosis after the age of 85 is 1:3 (2). Due to an aging population, the number of cases of AD in the United States is rising rapidly. By 2050 there will be an estimated 13 million cases representing a yearly economic cost of $1 trillion (3).

Effective treatments for AD are lacking and the success rate of AD drugs in clinical trials falls below 1% (4). There is significant loss of neuronal synapses in AD correlating closely with cognitive symptoms and predating neuronal death (5). Familial Alzheimer disease (FAD) is caused by genetic mutation with symptoms generally appearing in the early 40s. Sporadic Alzheimer disease (SAD), which makes up the majority of AD cases, usually manifests after the age of 65. FAD and SAD are indistinguishable from one another histologically. The two main hallmarks of AD are beta amyloid plaques and neurofibrillary tangles (NFTs). Plaques are extracellular protein aggregates composed of the Aβ peptide; NFTs are intracellular aggregates consisting largely of hyper-phosphorylated tau. Aβ peptides are small, hydrophobic peptides of no known physiological function, while tau normally associates with microtubules.

The amyloid cascade hypothesis states that AD is a consequence of the buildup of Aβ peptides, through either increased production or decreased clearance (6). Evidence points to soluble aggregates of Aβ as the cytotoxic species in AD (7, 8).

Amyloid Beta Peptide

Aβ peptides are formed by cleavage of the amyloid precursor protein (APP) a transmembrane glycoprotein. The N-terminus of the APP is in extracellular space, while the C-terminus terminates within the cytosol. The exact function of the APP is unknown, but it is believed to play a role in cell growth and proliferation, as well as influencing synaptogenesis (9). In the non-amyloidogenic pathway, the APP is cleaved by α-secretase in the middle of the amyloid beta transmembrane segment creating the C83 fragment. The C83 fragment is then cleaved by γ-secretase forming the APP Intracellular Domain (AICD) and a truncated Aβ fragment known as p3 (9-11). The AICD enters the cytosol and is believed to play a role in nuclear signaling while the p3 seems pathologically irrelevant. Interaction between β-secretase and the APP can lead to amyloidogenic cleavage at D^{672} freeing the N-terminus of the Aβ and creating the C99 fragment (12). The C99 fragment is then cleaved by γ-secretase freeing the Aβ peptide and forming the AICD (8, 10). This cleavage most frequently occurs at V^{40} forming the $A\beta_{1–40}$ fragment, but cleavage also occurs at nearby A^{42} and G^{38} positions on the C99 forming the $A\beta_{1–42}$ and $A\beta_{1-38}$ respectively (12-14). The Aβ peptide leaves the membrane and enters the extracellular space

following cleavage (10, 11, 14). Most mutations associated with FAD are associated with Aβ production and involve the APP or its processing (15-19). There are many different species of Aβ peptide and in situ Aβ populations are heterogeneous (13, 20). Although the most common Aβ found in the brain is the $A\beta_{1-40}$ the $A\beta_{1-42}$ is most often associated with AD (13, 21). Additionally, pyroglutamylated Aβ is a major species in the AD brain and has been found to make up to 50% of the soluble Aβ load (13, 20, 22). Amyloid beta builds up intracellularly as well, through production at either the endoplasmic reticulum (ER) or vesicles, as well as re uptake of oligomers (23-26). The intracellular buildup of Aβ often precedes extracellular increases in Aβ concentration and onset of synaptic dysfunction (24, 25).

Current Issues in AD

No current treatments exist that delay the progression of AD. Currently, five drugs are FDA approved for the treatment of AD, the cholinesterase inhibitors: Tacrine, Donepezil, Revastigmine, and Galantamine; and the N-methyl-D-aspartate (NMDA) receptor antagonist Memantine. There have been no new AD drugs approved since 2003 (4). Between 2002 and 2012, only one of the 230 compounds assessed for the treatment of AD passed phase 3 clinical trials and was approved for treatment(4). This failure rate of 99.6% is the highest of any therapeutic area (27, 28). High profile AD drug failures include the anti Aβ monoclonal antibody drugs bapineuzumab and solanezumab. As well as the Aβ reducing drugs Phenserine, which reduces APP expression (29),

and Flurizan, which reduces $A\beta_{1-42}$ levels, likely through a mechanism involving γ-secretase (30, 31). Data has not been released as to whether these drugs failed to have an effect on Aβ load, or whether they decreased Aβ load, but there was no corresponding decrease in cognitive decline. The failure of these drugs to translate from animal models into humans calls into question the accuracy of existing AD models and necessitates re-evaluation of the amyloid cascade hypothesis.

Shortcomings of the Amyloid Cascade Hypothesis

In the decades since the amyloid cascade hypothesis was first postulated, many new discoveries have been made. (32-35). Recent findings have shifted focus from insoluble fibrils to soluble oligomers of Aβ as the main cytotoxic entity in AD. Soluble oligomers of Aβ have been shown to inhibit long-term potentiation (LPT), and the population of soluble oligomers is an accurate predictor of synaptic decline (7, 8, 23, 36-39). Additionally, plaque levels do not correlate with disease state and are found in the brains of cognitively normal patients (40, 41). In fact, cognitive impairment in AD correlates better with tangle burden than plaque levels (42). Additionally, studies have found Aβ neurotoxicity to be tau dependent, both in vivo and in vitro casting doubt on the completeness of the amyloid cascade hypothesis (43-45). Studies have shown oligomers to be significantly more cytotoxic than fibrils (46, 47). Some of these oligomers may be intermediates of fibrillogenesis, however others are formed via distinct pathways (48, 49). Neurotoxic oligomers appear to propagate via a prion-like mechanism, with pyroglutamylated

amyloid beta (AβpE) in particular having a profound effect on toxicity even at low molar ratios (44, 50, 51). Dot blot experiments have shown that hybrid $A\beta_{pE3-42}$:$A\beta_{1-42}$ oligomers and similar sized oligomers formed by $A\beta_{1-42}$ alone are distinct structurally with hybrid oligomers having significantly enhanced toxicity (44). Surprisingly, Aβ monomers appear neuroprotective, against both oxidative stress as well as the absence of insulin (52, 53). $A\beta_{1-40}$ has demonstrated a protective effect by inhibition of $A\beta_{1-42}$ aggregation (52). These findings necessitate the altering of the amyloid cascade hypothesis, shifting focus from large fibrillar aggregates to small soluble oligomers of Aβ. An illustration of this refined amyloid cascade where oligomers formed as intermediates during fibrillogenesis or via other aggregation pathways lead to AD is shown in Figure 1. Little is known about the Aβ peptide following cleavage from the membrane and prior to formation of proto-fibrils.

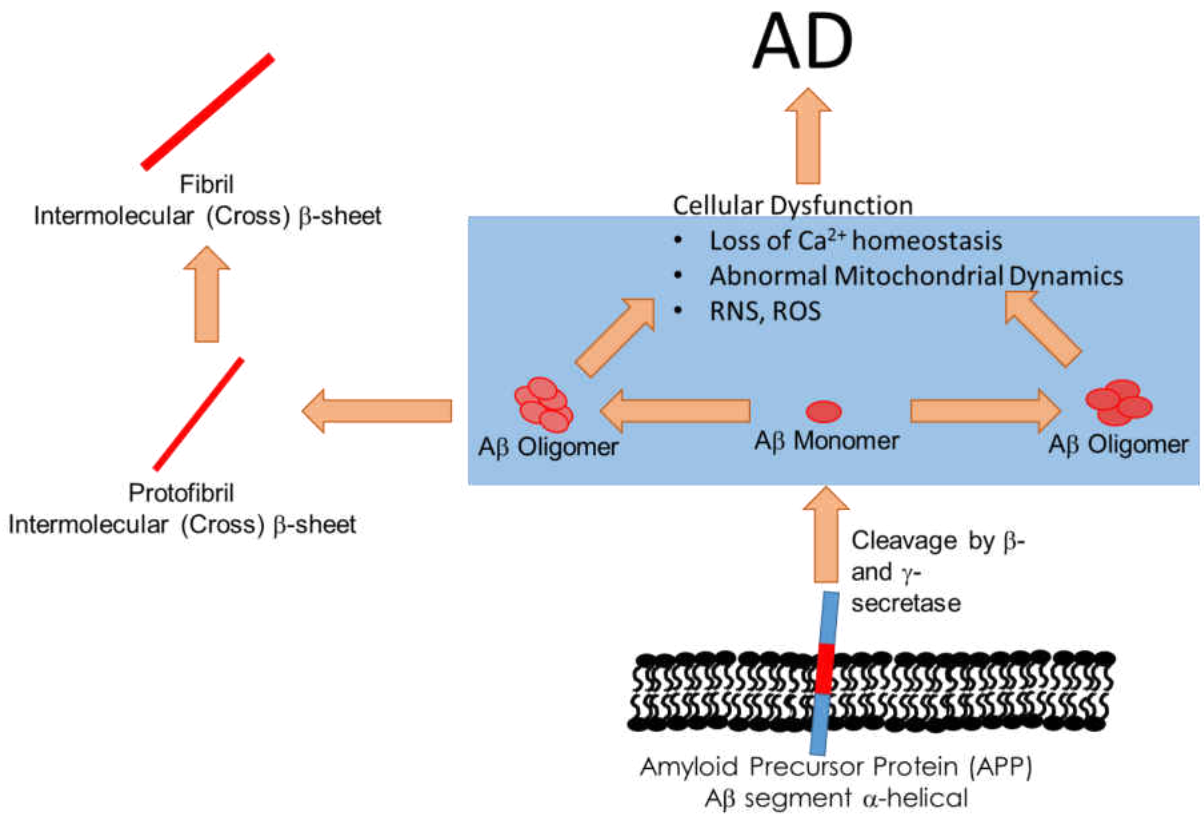

Figure 1. Potential pathway for the pathogenesis of AD via Aβ oligomers. Little is known about the aspects of this pathway contained within the blue box.

Pyroglutamylated Amyloid Beta

The N-truncated, N-modified pyroglutamylated Aβ (AβpE) is a major Aβ species in the AD brain and can make up as much as 50% of total soluble Aβ load (13, 20, 22, 54). Pyroglutamylation occurs when glutamic acid is at the N-terminus of the peptide, most often due to upstream aminopeptidase degradation. The N-terminal glutamic acid is then cyclized in a

dehydration reaction carried out via glutaminyl cyclase (QC) (55). Pyroglutamylated Aβ are believed to be highly involved in the pathogenesis of AD (20, 44, 54, 56). Aβ population changes over time with the fraction of AβpE increasing with disease progression (20, 57). In addition, QC expression is found in the peripheral blood of AD patients (58). The most common AβpE is the $A\beta_{pE3\text{-}42}$ fragment, however $A\beta_{pE11\text{-}42}$, $A\beta_{pE3\text{-}40}$, and $A\beta_{pE11\text{-}40}$ have all been observed in AD brains (20, 59, 60).

Over expression of QC in mice was found to cause behavioral deficits while knockout or inhibition of QC had a rescue effect (55, 61). Loss of calcium homeostasis, an early event in AD, has been shown to increase QC expression leading to an increased in AβpE production (62). Studies indicate that AβpE has altered aggregation, forming greater numbers and longer lived oligomers compared to unmodified Aβ (63, 64). Pyroglutamylated Aβ and hybrid $A\beta_{1\text{-}42}/A\beta_{pE3\text{-}42}$ oligomers display increased toxicity when compared to unmodified Aβ (44, 56). Additional studies found AβpE to be more resistant to astrocyte degradation and have increased cytotoxicity to cultured neurons compared to both $A\beta_{1\text{-}42}$ and $A\beta_{1\text{-}40}$ (22). A correlation between AβpE and adjacent deposits of hyper-phosphorylated tau has been found in AD brains, providing evidence of a link between AβpE and tau phosphorylation (56). This is strong evidence towards the involvement of AβpE in AD.

Gaps in Knowledge of Aβ Oligomers

Although they are believed to be the cytotoxic species in Aβ, structural data on Aβ oligomers is lacking. Previous structural studies have often used non-physiological conditions calling into question the disease relevance of their results (65, 66). Additionally, most structural studies have taken place on a single species of Aβ, and not a heterogeneous population as is found *in situ*. More detailed structural understandings of Aβ oligomers and early aggregates are necessary to better understand the role of these oligomers in the pathogenesis of AD. Of particular interest are the changes that occur in mixed samples of AβpE and Aβ. This work aimed to characterize structural and morphological changes exerted on Aβ by AβpE. We found that AβpE and Aβ mutually inhibit fibrillogenesis by inhibiting intermolecular β-sheet formation of one another. Instead, in combination they form hetero-oligomers composed of β-hairpins which aggregate through ionic or hydrophobic bonds of a C-terminus of one hairpin and the N-terminus of another. These hetero-oligomers had increased cytotoxicity to PC12 cells. This study highlights the importance of Aβ: AβpE hetero-oligomers in the pathogenesis of AD. These hetero-oligomers may represent a promising target in the search for promising new ways to effectively treat AD.

CHAPTER TWO: LITERATURE SEARCH

Before moving forward with this project, it was necessary to re-evaluate the amyloid cascade hypothesis to ensure the pertinence of Aβ peptides in AD. Research was conducted on the genetics of AD, as well as the role tau plays in AD. This data supports Aβ peptides as the initiator of AD pathology. In addition, current literature was searched on the structure and aggregation of Aβ, especially oligomeric Aβ. Finally, as this project related Aβ to the neuronal death associated with AD, it is necessary to examine current literature on possible mechanisms of neurotoxicity in AD.

Genetics of AD

Since the discovery of the first genetic link in AD, multiple genes have been implicated in AD, with many mutations found to be fully penetrant. The most prevalent FAD mutations occur on the APP, PSEN1, and PSEN2, all genes associated with production of Aβ (67, 68). One of the first genes associated with AD was the APP on chromosome 21. Many different mutations have been identified on the APP most of them leading to FAD (15, 16, 69, 70). Some APP mutations are neuroprotective, and hypothesized mechanisms of protection include: the lowering of Aβ load, inhibition of the APP transforming growth factor β2 (TGFβ2) cell mediated death pathway, or through the alteration of aggregation kinetics (15, 71).

Conversely, APP mutations implicated in FAD have been linked to: higher Aβ production, increased levels of tau, and increases in the $A\beta_{1-42}/A\beta_{1-40}$ ratio (16, 70). The majority of FAD mutations are linked to presenilin protein mutations (17). Mutations have been found for both PSEN1 located on chromosome 14 and PSEN2 located on chromosome 1 (17, 18, 72). PSEN 1 and 2 along with the accessory proteins nicastrin, APH-1, and PEN2 form the γ-secretase, which is responsible for the final cleavage of Aβ from the membrane. The prevailing proposed mechanism of PSEN mutations causing FAD is through partial loss in function of γ-secretase activity, leading to only partial processing of $A\beta_{1-42}$ and increasing the $A\beta_{1-42}/A\beta_{1-40}$ ratio in the brain (19, 68, 73).

The previously discussed genes have been linked to FAD, which represents <1% of AD cases (74). The vast majority of AD cases are SAD, with the strongest known risk factor being Apolipoprotein E allele (ApoE). ApoE has multiple isoforms with the E2 being neuroprotective and E4 being a risk factor for AD (74). ApoE aids in the degradation of amyloid beta within microglial cells, and the ability of astrocytes to clear diffuse Aβ deposits (75-77). Previous studies have also demonstrated retardation of blood brain barrier (BBB) clearance of amyloid-ApoE aggregates compared to free Aβ via redirection of clearance from the LRP1 to the VLDLR, which internalizes Aβ-ApoE complexes more slowly (75). This clearance delay is isoform dependent with the E4 allele clearing more slowly than E3 and E2. This clearance slowdown may contribute to buildup of amyloid structures on blood vessels and explain the increased risk of cerebral amyloid angiopathy (CAA) associated with the E4 allele of ApoE (75).

Trisomy 21 and AD

Due to the location of the APP gene on chromosome 21, there is a strong correlation between AD and trisomy 21 or Down syndrome (DS). Two-thirds of full trisomy 21 translocation patients develop dementia by the age of 60 (78). Interestingly, this association is only present if the APP gene is present on the extra chromosome, granting a third copy of the gene (79, 80). Patients without a third copy of APP will have DS without the increased risk of developing AD, normally associated with it. Furthermore, translocation of a small fragment of chromosome 21 causing duplicate APP copies on a single chromosome cause FAD but not DS (69, 81). The relationship between an extra copy of APP and AD is strong evidence in support of Aβ as the causative agent in AD.

The Role of Tau in AD

One of the hallmarks of AD is the presence of intracellular aggregates composed of highly phosphorylated tau. Tau is a protein involved in the stabilization of microtubules (5). Tau has multiple phosphorylation sites, and increased phosphorylation levels has an inhibitory effect on microtubule binding leading to a corresponding increase of soluble tau (82, 83)Phosphorylated tau has been shown to closely interact with F-actin causing bundling and aggregation of F-actin forming actin rich rods (84). F-actin is present at the dendritic synapse making tau mediated F-actin aggregation a possible mechanism of synaptic loss in AD (85). The presence of NFTs is

linked to a reduction in expression of synaptic vesicle transport proteins. Levels of soluble tau correlate with AD implicating soluble tau as the neurotoxic form of tau (83, 86, 87). Aβ has been shown to cause dendritic spine loss in the absence of tau; however, neuronal death was tau dependent (88).

Excitotoxicity has been implicated as a mechanism of neuronal death involved in AD (89, 90). Knockout of tau has been shown to attenuate hyper-excitability in mouse models overexpressing Aβ (91). Strong evidence suggests that tau and Aβ act in concert in AD to cause synaptic loss and neuronal death (43, 45, 86, 92, 93). However, in the front cortex of AD patients, Aβ levels were found to be increased prior to the onset of significant tau pathology (94). Additionally, reduction in soluble Aβ levels has been linked to a decrease in tau accumulation. Increased levels of Aβ peptides have also been linked to the phosphorylation of tau (82, 93, 95, 96). Aβ dimers isolated from AD brains induce phosphorylation of tau causing neuritic degeneration (97).This evidence suggests that although a strong link between tau and AD exists, tau phosphorylation and aggregation is likely a downstream effect of Aβ buildup. This supports the case that although tau is intimately linked to AD, buildup of Aβ peptide is likely the initiating factor in AD pathogenesis.

Aβ Structural Studies

Consistent with the majority of transmembrane proteins, the amyloid beta segment of the APP is α-helical prior to cleavage and exit from the lipid membrane. Supporting this is data from NMR studies on a segment of the APP containing the Aβ sequence embedded in micelles which show the Aβ sequence to form an α-helix with a disordered C-terminus (98, 99). Structural changes and aggregation commences once the hydrophobic Aβ peptides enter an aqueous environment.

Amyloid Beta Fibrils

Both solid-state nuclear magnetic resonance (ssNMR) and X-ray diffraction have shown mature amyloid fibrils to possess a cross β-structure; meaning the β-sheet plane and backbone hydrogen bonds connecting β-strands are parallel to the main fibril axis while the β-strands run perpendicular to the fibrillar axis (100, 101). Recently, studies have shown the presence of steric zippers in amyloid fibrils (102, 103). Steric-zippers are formed by the C-terminus of pairs of cross β-sheets with interdigitating side chains (102, 103). TEM studies have shown mature fibrils to contain one or more protofilaments and to display two-fold symmetry with the fibril cross section superimposing with itself after 180 degree rotation (104-106).

Studies indicate that amyloid fibrils, formed by both the $A\beta_{1-40}$ and $A\beta_{1-42,}$ are composed of in-register parallel β-sheets (107-109). However, fibrils formed by the Iowa mutant Aβ peptide can have either parallel or antiparallel architecture (110). Aβ fibrils and oligomers are polymorphic

with their internal structure often changing in an environment dependent manner, highlighting the importance of utilizing relevant experimental conditions (108). Fibrils seeded by brain extracts of AD patients had different structures, indicating that different seeds can induce formation of distinct fibrils and that fibril structure is not necessarily consistent between patients (107). Aβ samples often show intra-sample polymorphism; meaning that measurements such as NMR and CD demonstrate the average and/or most prevalent of the multiple different structures within a sample (108). The polymorphic nature of Aβ aggregates complicates the reproducibility of Aβ structural data.

Oligomeric Amyloid Beta

The toxicity of Aβ oligomers is linked to both oligomer size and structure. Dodecamers of Aβ isolated from the brains of Tg2576 mice disrupted the memory of young rats (111). While Aβ dimers isolated from the cerebral cortex of AD brains inhibited LPT in rat hippocampal slices and impaired memory when injected into rats (112), Aβ dimers, trimers, and tetramers were found to inhibit LTP in mouse hippocampal neurons at physiological concentrations, with trimers having the greatest effect (38).Ion mobility, coupled with mass spectroscopy experiments, found that $A\beta_{1-40}$ monomers form dimers, which then dimerize, and then likely undergo fibrillogenesis while $A\beta_{1-42}$ tetramers went on to form hexamers, and then dodecamers (113).

It is commonly believed that the toxic species of Aβ are oligomers of mixed α-helix/β-sheet content formed during the transition from α-helical monomer to cross β-sheet fibril (114-116).The transient nature of these aggregates makes their study difficult, therefore structural data on oligomeric Aβ is lacking. Studies that have been conducted on the oligomeric Aβ have found presence of both parallel and antiparallel β-sheet, along with mixed α/β structures (117-122). One group demonstrated that inhibiting the formation of antiparallel β-sheet led to a corresponding decline in toxicity (119). Many studies have used non-physiological conditions in order to stabilize these oligomers, calling into question the physiological relevance of their findings (49, 66, 115, 116, 123).

Aβ Aggregation

Protein fibrillization is implicated in multiple human diseases including AD, Parkinson's disease, and Huntington's disease. Fibrillization takes place in three stages: a lag phase during which prefibrillar intermediates are formed, a growth phase of rapid fibril growth and elongation, and finally growth plateaus once fibrillogenesis reaches equilibrium (124, 125). Aβ fibrillization takes place via nucleated growth with the C-terminus being critical in the seeding of fibrillization (126-129). The rate of fibrillogenesis is dependent on both pH and temperature (130, 131). Studies have indicated that formation of a turn at residues ~23-28 is critical to Aβ fibrillization and toxicity. This sequence is home to multiple mutations that lead to FAD, indicating the importance of this

turn to the disease state (132). Structural studies indicate that this turn is part of a β-hairpin structure formed as an intermediate during aggregation (114, 133). Previous studies have found $A\beta_{pE3–42}$ to aggregate faster than, and have a higher β-sheet propensity than $A\beta_{1–42}$., likely due to increased hydrophobicity (125, 134). Conversely, other studies have found that $A\beta_{pE3-42}$ aggregates slower and has lower β-sheet propensity (135). Additionally, it was found that $A\beta_{pE3-42}$ increased the lag phase of $A\beta_{1-42}$ and delayed β-sheet formation (135). Further studies are needed to clarify fibrillization kinetics of $A\beta_{1-42}$ and $A\beta_{pE3-42}$ as well as the effect $A\beta_{pE3-42}$ has on $A\beta_{1-42}$ fibrillogenesis.

Cell Death in AD

There have been many proposed mechanisms of Aβ mediated cytotoxicity. Many different mechanisms have been demonstrated in vitro, but more study is needed to ascertain their relationship to the disease in vivo. These mechanisms include the alteration of mitochondrial dynamics, loss of calcium homeostasis, and trans-nitrosylation of proteins due to increased RNS production.

Alteration of Mitochondrial Dynamics

Mitochondrial dynamics, or their constant fission and fusion, is used to dilute mitochondrial DNA damage and maintain a healthy mitochondria population (136). Alterations in mitochondrial dynamics has been implicated as a mechanism of both synaptic degradation and neuronal death in AD. Neurons are highly energy dependent due to the large energy exertion required to maintain synapses, as well as the re-uptake and release of neurotransmitters. Aged mitochondria display reduced activity of complex I and IV in the respiration chain (137). Mitochondrial DNA mutations accumulate over time due to oxidative species formed during respiration (138). Fractionated mitochondria and broken cristae have been found in AD brains, indicating a loss of mitochondrial dynamics homeostasis (139). Fragmented mitochondria produce less ATP production and more reactive oxidative species (ROS) (136). Oxidative damage has been described in lipid membranes and proteins in AD brains, providing evidence for the role altered mitochondrial dynamics play in the disease (139, 140). Increases in mitochondrial derived ROS have been linked to upregulation of APP increasing Aβ levels in a positive feedback mechanism (141). Increased ROS production is also an early signal of apoptosis (142). Fusion of mitochondria is carried out via a complex of mitofusins 1 and 2 and optic atrophy 1 (136, 143). Mitochondrial fission is carried out via dynamin-related protein 1 (drp1), which is targeted to the mitochondrial outer membrane via: mitochondrial fission factor mitochondrial fission protein 1 and, mitochondrial elongation factor 1 (136). Up-regulation of mitochondrial fission in AD is believed to be due to increased activity or localization of drp1 due to post-translational modification, although the exact mechanism is controversial. Some groups have theorized that this occurs

through increased GTPase activity of Drp1 via nitrosylation (144, 145). Other groups argue that the altered dynamics is due to increased targeting of drp1 to mitochondria due to phosphorylation of drp1 (146). Additionally, enhanced levels of glycogen synthase kinase 3β (GSK3β) have been found in AD patients (96). GSK3β has been linked to phosphorylation of drp1 upregulating its activity, as well as an increase in Cdk5 activity and tau expression (95, 147).

Loss of Calcium Homeostasis

Loss of intracellular calcium homeostasis is also implicated in AD neuronal death. Calcium is a vital intracellular signaling molecular responsible for regulating many signal cascades. Loss of calcium homeostasis has been linked to cellular apoptosis (148). Studies have shown Aβ peptides to cause deregulation of calcium homeostasis, providing evidence for it being a mechanism of cellular death in AD (149-155).

There have been many proposed pathways that Aβ affect calcium regulation. Aβ peptides have been linked to the upregulation of ryanodine receptors, specifically Ryanodine Receptor 3 (RyR3) (153-155). These receptors release calcium from the endoplasmic reticulum (ER) in response to increases in intracellular calcium termed calcium induced calcium release (CICR). Increased levels of tau and Aβ are linked to increased glutamate levels through increased expression and inhibition of re-uptake and transport (156-159). Glutamate can activate both RyR3 and NMDAR increasing intracellular calcium. Soluble Aβ oligomers were found to have high

affinity for PrP^c. These complexes were found to interact with a complex of mGluR5 and Fyn, causing increased NMDAR activity and thus calcium influx (160). It was also found that these Aβ-PrP^c-mGluR5 complexes mediate dendritic spine loss through eEF2 phosphorylation. Additionally, Aβ peptides have been shown to inhibit the activity of mGlu7 an NMDAR regulator further increasing NMDAR activation and subsequence calcium influx. Increases in intracellular Ca^{2+} concentrations mediates signaling changes via multiple mechanisms. In response to increased calcium the calcium dependent protease calpain cleaves the Cyclin dependent kinase 5 (Cdk5) activators p35 to p25 or p39 to p29, causing aberrant increased Cdk5 activity (161, 162). This increased Cdk5 activity has been demonstrated to lead to an increase in Aβ production as well as production and hyper-phosphorylation of tau (95, 161, 162).

Amyloid Pore Formation

Another mechanism of loss of calcium homeostasis in AD is the formation of calcium permeable channels composed of Aβ in the organelles and plasma membranes of neurons (121, 149, 163-167). These pores have been observed in AD brains and in vitro assays have demonstrated an influx of calcium through Aβ pores at physiological peptide concentrations, lending credence to this theory (163, 164, 167). Evidence shows that Aβ behaves similarly to gramicidin, an antimicrobial agent which has mostly β-sheet structure and forms pores in plasma membranes (168). Additionally, the Aβ oligomer conformation specific antibody A11 binds

selectively to the bacterial pore forming protein αHL as well as human perforin, indicating shared homology and possibly similar mechanisms of pore formation (169). A close link was found for both $A\beta_{1-42}$ and $A\beta_{1-40}$ between pore formation and cytotoxicity (121). Structural studies indicate that these pores may consist of β-barrel like structures composed of monomers of Aβ in either parallel or antiparallel β-sheet (170, 171). Other MD simulations on short Aβ peptides predict octameric pores composed of mostly α-helical structure (172).

Nitrosylation of Proteins in AD

Excess levels of nitric oxide (NO) leading to increased S-nitrosylation (SNO) of proteins has been linked to AD (173). NO is produced by nitric oxide synthases (NOS) by the conversion of L-arginine to L-citrulline, it easily defuses through plasma membranes allowing it to signal neighboring cells. The two NOS relevant to AD are neuronal nitric oxide synthase (nNOS) and inducible nitric oxide synthase (iNOS). nNOS is found in neurons and is constitutively active, producing low levels of NO. iNOS is constitutively inactive, and when activated, produces high levels of NO. Excessive NMDAR activation in AD has been shown to lead to increased levels of ROS and NO through nNOS activation (174). Additionally, tangle-bearing neurons in the AD brain have been shown to have activated iNOS (175). SNO is a post-translational modification wherein a nitric oxide species undergoes a redox reaction with a thiol group on a cysteine (176). Increasing SNO of proteins has been linked to multiple neurodegenerative diseases, including AD and Parkinson's disease (144, 145, 161, 177, 178). High levels of SNO proteins has a pro apoptotic

affect (179). Transnitrosylation via S-nitrosylating proteins has been identified as a major mechanism in the proliferation of SNO proteins throughout cells. Numerous proteins have been identified as having the ability to transnitrosylate other proteins including GAPDH, Cdk5, and caspase 3 (176, 180). Cdk5 has been shown to be S-nitrosylated at amino acids 83 and 157 via interaction with iNOS (181). SNO-Cdk5 can act in several neurotoxic mechanisms, including Transnitrosylation of drp1, activation of the pro apoptotic protein ATM, and phosphorylation and loss of function of WAVE1 (180, 182, 183). SNO-Cdk5 has been shown to transnitrosylate Drp1, enhancing its GTPase activity leading to altered mitochondrial dynamics (144, 145, 180, 181). SNO-GAPDH has been found in AD brains; SNO-GAPDH binds Siah1 and translocates to the nucleus where it initiates apoptosis (178, 184, 185). There is also evidence that NO causes cyclin dependent kinase 1 (Cdk1) mediated phosphorylation of drp1 enhancing GTPase activity and mitochondrial fission (146).

The nature of AD, namely the long time scale and the difficulty of studying neurons both in vivo and in vitro, make pin-pointing of a single mechanism of neuronal death difficult. It is likely that some of the aforementioned mechanisms of cytotoxicity are downstream consequences of AD and not direct causes; however, it is reasonable to assume that there are multiple often interconnected neurotoxic pathways in AD. The lack of a single mechanism to target complicates drug development in AD. A stronger understanding of the relationship between Aβ structure and toxicity may pave the way the development of early diagnostic tests for AD or novel structure based AD drugs.

Methodology Literature Search

The polymorphic nature of the Aβ peptide required detailed review of existing literature. To ensure that consistent and reproducible results are obtained, it was necessary to use uniform, monomeric solutions of Aβ in each experiment. Fluorinated alcohols such as 1,1,1,3,3,3-hexafluoro-2-propanol (HFIP) are commonly used to induce α-helical structure and monomerization in Aβ peptides (186, 187). In this work, protein secondary structure was determined by CD, literature was therefore reviewed in order to interpret CD spectra (188).

Review of FTIR

Due to the importance of FTIR spectroscopy in this work a thorough review of current literature on FTIR was conducted. Infrared spectroscopy is also called vibrational spectroscopy; absorption of light is associated with various vibrational modes of chemical groups within a molecule. Polychromatic infrared radiation is passed through the sample, when the frequency of infrared radiation matches the vibrational frequency of chemical bonds present in the sample, absorbance occurs. The absorption frequency of FTIR spectra is displayed in wavenumbers where wavenumber $W=1/\lambda=\nu/c$; where λ is wavelength, ν is temporal frequency of vibration, and c is the speed of light. The vibrational frequency ν for a diatomic molecule can be approximated using equation 1; where the spring constant k is proportional to chemical bond strength.

$$V = \frac{1}{2\pi}\sqrt{k(\frac{1}{(m_1} + \frac{1}{m_2})} \quad (1)$$

There are many vibrational modes that can be observed in FTIR, but the two most relevant to biological study are the amide I and amide II. The amide I vibrational mode is located 1700-1600 cm^{-1} and is primarily generated by C=O stretching vibration. These vibrations are coupled through covalent bonding, H-bonding, and through space, these couplings shift vibrational frequency. Protein secondary structure geometry is highly conserved, making the C=O vibrational frequencies of various secondary structures also highly conserved. This allows accurate attribution of an FTIR absorbance band to a specific secondary structure. Research was conducted on the locations of these amide I secondary structure absorbance peaks in order to interpret experimental results (189-191). The peak wavenumber and extinction coefficient of various protein secondary structures can be found in chart 1. The amide II is located 1570-1540 cm^{-1} and is primarily composed of NH in-plane bending. The amide II can be utilized to measure the solvent accessibility of the protein. Amide hydrogen-deuterium exchange will take place with the addition of D_2O based buffer. The increased mass of deuterium causes a downshift in absorption and corresponding loss of absorbance 1570-1540 cm^{-1}. Proteins in more open or solvent accessible conformations will undergo more H-D exchange and thus lose amide II signal intensity more quickly than tightly packed proteins.

^{13}C Labeling of Proteins

The ^{13}C-labeling of specific amino acid stretches or entire proteins is a technique to investigate protein interaction and examine protein secondary structure in a site-specific manner. The amide I absorbance peaks of peptides ^{13}C-labeled is downshifted thus allowing dissection of the structure of labeled segments or proteins from unlabeled segments or proteins. This downshift was reviewed in order to accurately interpret experimental results (192). The downshifted absorbance of a ^{13}C labeled secondary structure can be accurately predicted as shown in equation 2 by taking the ratio of vibrational frequency of the $^{13}C=^{16}O$ bond over the $^{12}C=^{16}O$ and multiplying the result by the known absorbance of ^{12}C secondary structures shown in table 1 (Equation 2). For example, by taking the known ^{12}C parallel β-sheet absorbance at 1636-1630 cm^{-1} and multiplying it by the calculated factor of 0.978, we can predict the absorbance of a ^{13}C parallel β-sheet to be 1600-1594 cm^{-1}.

$$\sqrt{\frac{\frac{1}{13}+\frac{1}{16}}{\frac{1}{12}+\frac{1}{16}}} = \sim 0.978 \qquad (2)$$

Table 1. Characteristic amide I wavenumber relative extinction coefficients, and integrated absorbance extinction coefficients (B) of various protein secondary structures in D_2O, integrated extinction coefficient come from (193).

Secondary Structure	Absorbance D_2O (cm^{-1})	Relative Integrated Extinction Coefficient	B ($M^{-1}cm^{-2}$)
α-helix	1655-1638	1	5.1×10^7
Parallel β-sheet (Intramolecular)	1636-1630	1.37	7.0×10^7
Anti-Parallel β-sheet	1636-1630 (Strong)	1.37	7.0×10^7
	1680-1670 (Weak)	Multiply large component by 1.07	(7% of Strong Component)
Intermolecular (cross-β) β-sheet	1625-1613	1.37	7.0×10^7
β-turns	1675-1640	1.08	5.5×10^7
Unordered Structure	1648-1640	0.88	4.5×10^7

CHAPTER THREE: METHODOLOGY

In this project, we examined $A\beta_{1-42}$, $A\beta_{pE3-42}$, and combined samples at both equimolar and 9:1 ($A\beta_{1-42}$:$A\beta_{pE3-42}$) ratios. These molar ratios were utilized because AβpE has been observed in AD brains at up to 50% of total soluble Aβ load but is commonly present at a lower ratio (13, 20, 22). However, it has also been demonstrated to have a profound affect even at low molar ratios (44, 194). The secondary structures of early oligomers and intermediate structures were determined utilizing FTIR and CD. Peptides were first dissolved at concentrations of either 200 or 50 μM in HFIP to break up pre-formed aggregates. Monomer formation of the peptides was confirmed by the formation of α-helix in HFIP (187). The removal of HFIP was conducted by streaming N_2 gas over the samples until dried then vacuum desiccating samples for 15 minutes.

Bulk aqueous buffer was then added to the dried samples. Two different buffers were used one at near-physiological ionic concentration and one with low ionic content. The near-physiological buffer was 50 mM phosphate buffer + 50 mM NaCl pH 7.2 (pD 6.8 for FTIR samples in D_2O buffer) and the buffer of low ionic content was 10 mM phosphate pH 7.2 (pD 6.8 for FTIR samples in D_2O buffer). Buffer was added to produce a final peptide concentration of 50 μM. The $A\beta_{pE3-42}$ is missing 3 N-terminal charges compared to the unmodified Aβ. It is likely these charges form ionic bonds stabilizing the peptides, increasing ionic pressure will weaken these bonds and can cause changes in structure distribution. Examining structural changes of the peptides in both conditions provides information on the structure formed by the N-terminus of the peptide.

Cytotoxicity Assays

Cytotoxicity assays were conducted with collaboration with Dr. Lucia Cilenti in the laboratory of Dr. Kenneth Teter. To assay the cytotoxicity of Aβ aggregates, PC12 cells were grown in RPMI 1640 media, supplemented 10% fetal bovine serum, 50-units/ml penicillin and 50 μg/ml streptomycin. For MTS viability assays cells were seeded in 96-well plates in triplicate/samples at a density of 10,000 cells/well in 100 μL complete medium for 18 hours. Following this, 100 μL of fresh medium containing Aβ samples aggregated for 2, 4 and 24 hours by stirring at 37 °C in PBS, was added to cells followed by incubation at 37 °C for 28 and 50 hours. Cell viability was determined by MTS assay, a cell proliferation assay, to monitor methanethiosulfonate tetrazolium reduction as an estimate of cell viability, according to the manufacturer's instructions (Promega). In the assay, 20μl of MTS tetrazolium substrate solution was added to the wells at 28 and 50 hours followed by further incubation at 37 °C for 3 hours, Cell viability in each well was assayed by reading the absorbance at 590 nm in a BioTek microplate reader Synergy 2. Percentage of cell viability was calculated by subtracting the average of the triplicate samples at 490nm absorbance from medium control (no cells/background) from all other absorbance values.

Membrane Calcium Release

The ability of Aβ aggregates to induce the release of calcium from lipid vesicles was assayed using Quin-2. 40 μM Quin-2 in the presence of 100 nm unilamellar vesicles of POPC/POPG/cholesterol (6:3:1) loaded with 30 mM $CaCl_2$ in aqueous buffer pH 7.2. The total lipid concentration was 0.5 mM and peptides were added for a final ratio 1:100 peptide:lipid. Peptides were added after 2 and 24 hours of aggregation at 37 ^{o}C in PBS. Control was conducted by addition of PBS followed by complete release of all entrapped Ca^{2+} via addition of 0.05% Triton X-100 which disrupted vesicles.

FTIR

All FTIR measurements were taken on a Vector-22 FTIR spectrometer (Bruker Optics, Billerica, MA, USA) equipped with a liquid N_2 cooled Hg-Cd-Te detector with a 2 cm^{-1} resolution. All buffers were made utilizing D_2O, and not H_2O, to avoid artifacts caused by absorption of H_2O in the amide I region. Transmission spectra collected for all samples were taken by co-adding either 500 or 1000 consecutive scans. Peptides dissolved in HFIP were first deposited on the CaF_2 FTIR window, and then desiccated for 15 minutes to remove HFIP. Transmission spectra were then taken and absorption was calculated using a reference transmission spectra. After the collection of a dried sample, buffer was added along with a second CaF_2 window. Separating CaF_2 windows was a 50 μm Teflon spacer. Transmission spectra were then taken consecutively and

absorbance was calculated using a buffer reference. Data for both uniformly and segmentally ^{13}C labelled peptides was obtained similarly along with data for mixed samples. Samples of atmospheric vapor was collected separately and used to clean up spectra as necessary. Spectra were smoothed using a 13-point Savitzky-Golay linear least squares algorithm and then baselined. Absorbance spectra were prepared using OPUS spectroscopy software.

Curve-Fitting of FTIR Spectra

Curve-fitting of FTIR spectra was performed using GRAMS IO spectroscopy software. The locations of amide I components were based on negative peaks in the second derivative. Curve-fitting was considered acceptable when peak wavenumbers of components were in agreement with the second derivatives, the sum of all components reasonably fit the experimental spectra, and the peak component widths were within reasonable limits i.e. width at half height of less than 40 wavenumbers (190). The relative fraction F_i of either α-helix (α), β-sheet (β), β-turn (t), and other structures, were calculated based on the area of fit peaks using equation 3 where B refers to the average integrated extinction coefficient of the described structures as previously described (195).

$$F_{i=}\frac{a_i}{B_i(\frac{a_a}{B_a}+\frac{a_\beta}{B_\beta}+\frac{a_t}{B_t}+\frac{a_{other}}{B_{other}})} \quad (3)$$

Hydration FTIR

To facilitate examination of early peptide intermediates and structural transformations peptide transition was delayed by hydrating from gas phase, using D_2O vapor and not aqueous buffer. This was done using two separate mechanisms. In the first, dried peptides both individually and in combination, were hydrated via exposure to ambient humidity. For the second a custom apparatus was designed to hydrate peptides inside the FTIR spectrometer via the pumping in of D_2O laden N_2 gas (Figure 1). In this setup two separate hoses of N_2 gas was bubbled through two flasks of D_2O and then piped into the spectrometer. Peptides were prepared from 50 μM stocks in HFIP as described earlier. To examine the effect of co-incubation peptides were dried on either the same side or opposite sides of the CaF_2 windows to allow comparison between interacting and non-interacting peptides (Figure 1A).

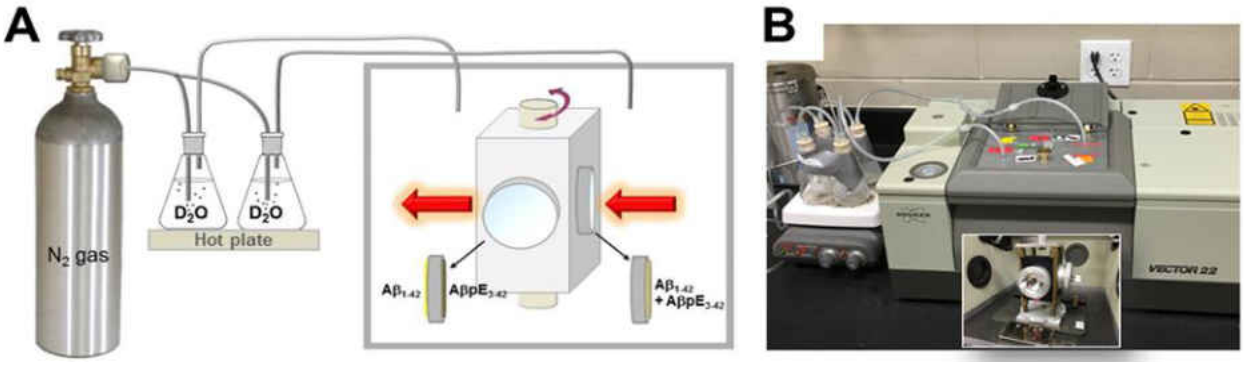

Figure 2. A) Schematic depiction of the experimental set-up. Nitrogen gas is pumped through simmering D_2O into the sample compartment. Only two of four flasks with D_2O are shown for simplicity. Two sample holders are mounted vertically, at 90 degrees, one with two peptides at opposite sides of a CaF2 window and one with both peptides blended at one side. Consecutive FTIR spectra of the two samples are measured while the sample holder frame is turned back and forth by 90 degrees. Red arrows represent the infrared light. B) Photograph of the FTIR spectrometer during an actual experiment. The inset (middle bottom) provides a glimpse into the sample compartment.

Circular Dichroism

CD measurements of Aβ in HFIP were taken in either a 0.5 mm cylindrical cuvette or a 4x4 mm rectangular quartz cuvette. Measurements were conducted on a Jasco J-810 spectropolarimeter (Tokyo, Japan). For measurements in aqueous buffer HFIP was removed with N_2 gas followed by desiccation for 30 minutes, prior to the addition of buffer. After the addition of 50 mM phosphate + 50 mM NaCl pH 7.2 aqueous buffer samples were incubated at 37ºC while stirring and a final protein concentration of 50 μM. CD measurements were taken between 330-180 nm. After collection spectra were smoothed in Spectra Manager software using 9 point Savitzky-Golay linear least squares algorithm.

TEM

TEM measurements were performed with the assistance of the lab of Dr. Bo Chen (University of Central Florida, Orlando, FL, USA). Peptides were dissolved in HFIP, dried, and buffer was added as previously described. Samples were then stirred at 37ºC for 24 hours. For measurements 5 mL of sample was placed on graphene coated grids. After five minutes excess buffer was removed. Samples were then washed twice with diH_2O and negatively stained with 3% uranyl acetate. Samples were measured on a JEOL TEM-1011 (Tokyo, Japan) at 80kV. Samples were examined at 2,4,12, and 24 hours to examine aggregation and morphology.

CHAPTER FOUR: RESULTS

Pyroglutamylated Amyloid-β Peptide Reverses Cross β-Sheets by a Prion-Like Mechanism

Circular Dichroism of Aβ Proteins

We first sought to clear up disagreement in the literature about the β-sheet propensity of AβpE compared to the unmodified peptide. Some groups reported AβpE to have a lower β-sheet propensity than the unmodified peptide while others have proposed the opposite. To clear up this contradiction we examined the structural changes of AβpE and unmodified Aβ throughout aggregation using CD.

To prepare monomeric samples Aβ was first dissolved in HFIP to break up pre-formed aggregates. HFIP disrupts β-sheet formation and promotes formation of α-helical structure (187). CD spectra of peptides dissolved in HFIP at 50 μM show a minima at 203 with a shoulder at 220 nm (Figure 3A). This is indicative of α-helix and disordered structures. This is in agreement with previous data of Aβ proteins in HFIP and implies a monomeric solution. Spectra taken after the removal of HFIP indicate that the peptides are α-helical shown by two minima located at 208-209 nm and 221-224 nm (Figure 3B). Interestingly, the $A\beta_{pE3-42}$ has a significantly reduced $\theta_{208}/\theta_{222}$ ratio, indicating a more flexible or disordered α-helix (196).

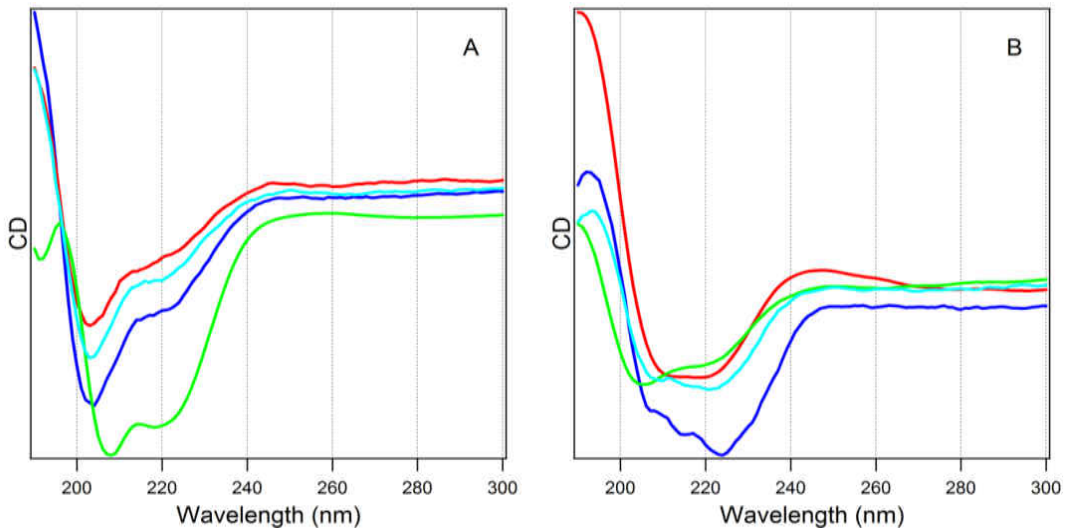

Figure 3. (A) CD spectra of $A\beta_{1-42}$ (red), $A\beta_{pE3-42}$ (blue) their 9:1 (teal) and, equimolar (green) ratios in HFIP at a peptide concentration of 50 μM. (B) CD spectra of the same peptides following HFIP removal via N_2 drying and vacuum desiccation.

Following desiccation aqueous buffer was added to the sample for a final peptide concentration of 50 μM and samples were constantly stirred at 37°C. In physiological buffer conditions $A\beta_{1-42}$ rapidly forms β-sheet as shown by the broad minima at 216-219 nm present 10 minutes after the addition of buffer (Figure 4A). After 16 hours this minima had red shifted to 220 nm possibly indicating decreased accessibility of the solvent due to tight packing during aggregation, such as in fibrillogenesis. Alternatively, $A\beta_{pE3-42}$ spectra at 10 minutes has a wide minima from 208-230 nm likely indicating presence of α-helical, β-sheet, and turn structures (Figure 4B). After 2 hours this minima has shrunk to 212-223 nm indicating the presence of a combination of both α-helical and β-sheet structures. After 24 hours of aggregation a single minima at 219 nm is present indicating a majority β-sheet structure. This demonstrates that $A\beta_{1-42}$

readily forms β-sheets while $A\beta_{pE3-42}$ has a higher propensity to retain α-helical structure and delayed formation of β-sheet.

The 9:1 ($A\beta_{1-42}$:$A\beta_{pE3-42}$) combination after 10 minutes of aggregation contains a wide minima at 217 nm consistent with the presence of mostly β-sheet (Figure 4C). Throughout aggregation this peak grows in intensity, after 24 hours a single minima at 219 nm is present indicating the likely presence of fibrils. For the first hour the equimolar combination contains mixed α-helix/β-sheet content indicated by the wide minima 210-216 at ten minutes and two minima at 212 and 222 nm after one hour (188). At 2 hours of aggregation onward a minima located at 217 nm indicates presence of mostly β-sheet structure. The equimolar combination after one hour resembles the $A\beta_{pE3-42}$ in that it retains α-helical structure and resists converting fully to β-sheet structure (Figure 4D).

This data indicates that AβpE has a lower β-sheet propensity than unmodified Aβ. Data from combined samples indicates that $A\beta_{pE3-42}$ alters $A\beta_{1-42}$ structural transition. Alone, $A\beta_{1-42}$ rapidly forms fully β-sheet aggregates, while forming mixed α-helix/β-sheet aggregates in equimolar combination with $A\beta_{pE3-42}$.

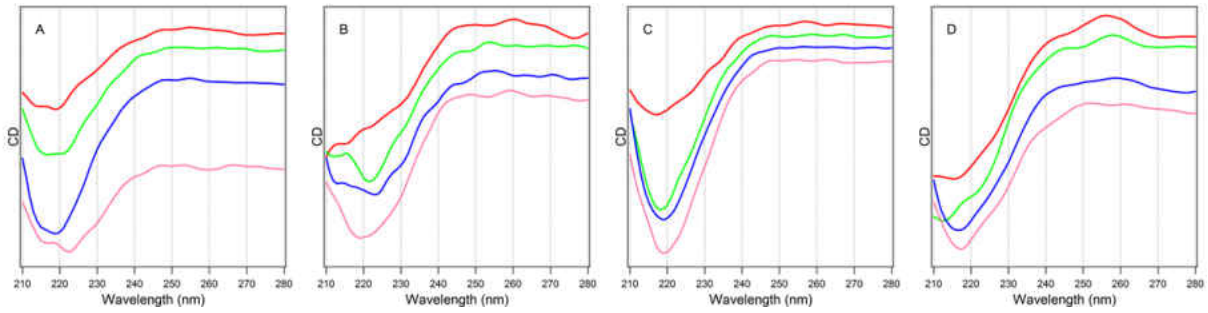

Figure 4. CD spectra of $A\beta_{1-42}$ (A), $A\beta_{pE3-42}$ (B), their 9:1 ($A\beta_{1-42}/A\beta_{pE3-42}$) (C) and, equimolar (D) ratios in 50 mM phosphate 50 mM NaCl buffer pH 7.2 Spectra are shown 10 minutes (red), 1 hour (green), 2 hours (blue) and, 24 hours (pink) after addition of buffer. Final peptide concentration was 50 μM and aggregation took place at 37^0C with constant stirring. For $A\beta_{1-42}$ the spectra in pink corresponds to 17h as subsequent time points gave weak signal due to evaporation of the sample. Spectra were cut at 210 nm due to weak signal from Cl and peptide absorbance.

TEM of Aβ Fibrils

Secondary structure is linked to fibrillogenesis and fibril morphology (134). The structural differences between the two peptides therefore indicate a strong possibility of altered fibrillogenesis. There are currently disagreements in the literature about the fibrillization kinetics of AβpE in comparison to the unmodified peptides. To clear this up, fibril formation and morphology was examined via TEM. Samples were examined at 2,4,12, and 24 hours of aggregation in 50 mM phosphate + 50 mM NaCl buffer pH 7.2. To determine the effect of peptide interaction peptides were examined separately as well as in equimolar and 9:1 ($A\beta_{1-42}$:$A\beta_{pE3-42}$) mixed samples.

The largest differences between samples was observed after 2 hours of incubation. The $A\beta_{pE3-42}$ sample is dominated by irregularly shaped prefibrillar aggregates with dimensions

between 30-100 nm (Figure 5b). The $A\beta_{1-42}$ sample at 2 hours consists mostly of fibrils with a smaller number of pre fibrillar aggregates (Figure 5a). The rapid formation of pre-fibrillar aggregates by $A\beta_{pE3-42}$ may be due to its increased hydrophobicity. Both the 9:1 (Figure 5c) and 1:1 (Figure 5d) samples resemble the $A\beta_{pE3-42}$ sample with a large number of pre-fibrillar aggregates compared to mature fibrils. At 4 hours fibrils were present in all samples along with significant amounts of prefibrillar aggregates (Figure 5e-h). At 12 (Figure 5i-l) and 24 (Figure 5m-p) hours fibrillogenesis continued and more mature fibrils were found in all samples along with decreased levels of prefibrillar aggregates.

This data demonstrates that the unmodified Aβ undergoes more rapid fibrillogenesis than AβpE. This data agrees with CD data showing that $A\beta_{1-42}$ rapidly forms β-sheet indicative of fibril formation while $A\beta_{pE3-42}$ and the 1:1 combination retain a prominent α-helical component. The increased levels of prefibrillar aggregates compared to fibrils at two hours in mixed samples demonstrates that $A\beta_{pE3-42}$ has a profound effect on fibrillogenesis particularly in the early stages of aggregation (135). The lack of fibrils in the 9:1 sample is evidence of the strong effect $A\beta_{pE3-42}$ can exert even at low molar ratios. Interestingly, in the 9:1 sample there was no delay in β-sheet formation coinciding with the delay in fibrillogenesis. This indicates that the delay in fibrillogenesis found in mixed samples may not simply be due to inhibition of β-sheet formation.

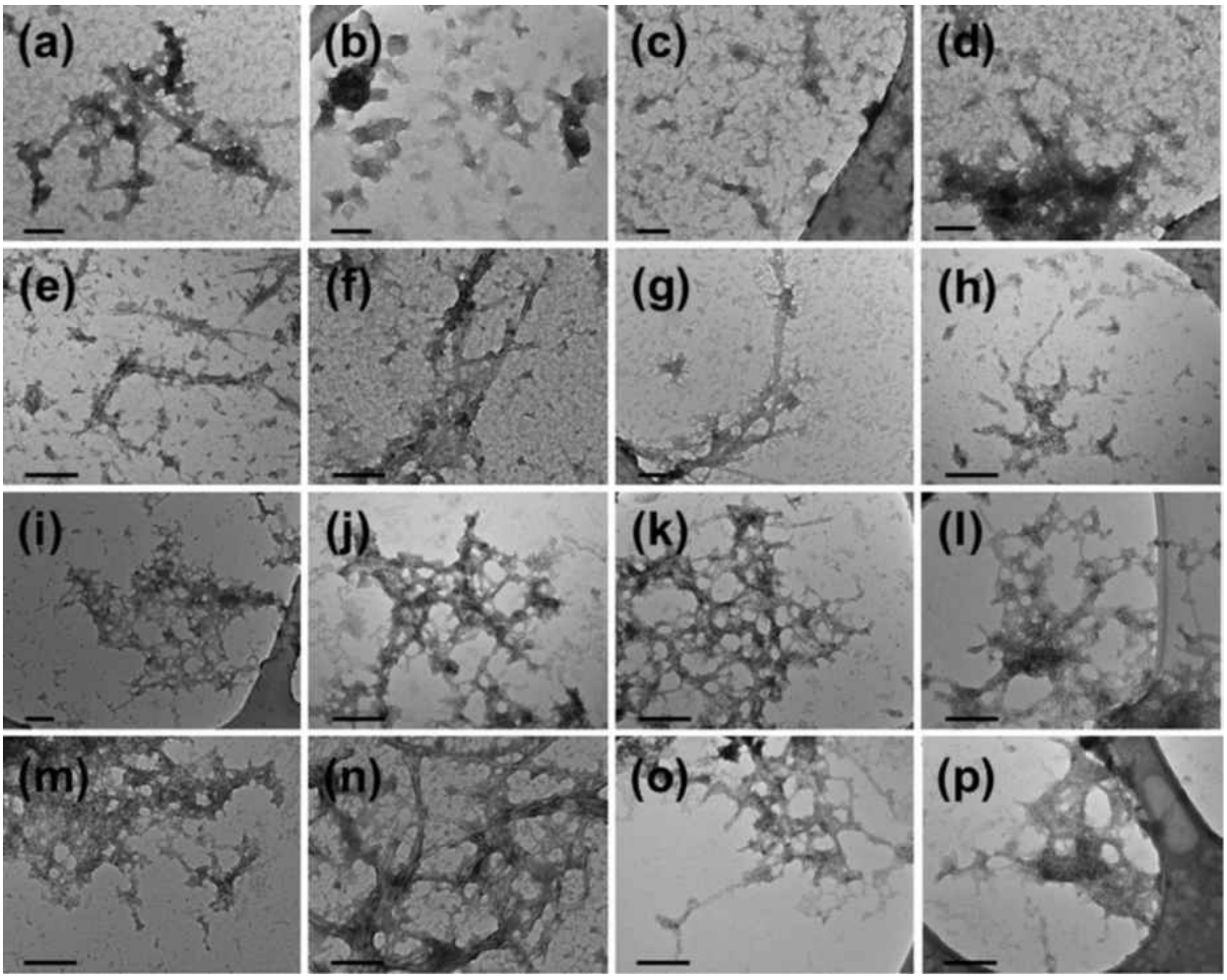

Figure 5. TEM images of $A\beta_{1-42}$ (a, e, i, m), $A\beta_{pE3-42}$ (b, f, j, n), $A\beta_{pE3-42}/A\beta_{1-42}$ = 1:9 (c, g, k, o), and $A\beta_{pE3-42}/A\beta_{1-42}$ = 1:1 (d, h, l, p) incubated in aqueous buffer of 50 mM NaCl + 50 mM Na,K-phosphate (pH 7.2) for 2 h (a−d), 4 h (e−h), 12 h (i−l), and 24 h (m−p) at 37 °C with constant stirring. The horizontal bar in each panel equals 100 nm.

FTIR of Amyloid Beta Peptides

We next sought to examine the structure of these peptides in greater detail utilizing FTIR. FTIR gives greater structural resolution than CD allowing, for instance, the determination of whether the protein is forming intramolecular or intermolecular β-sheet. Formation of

intramolecular β-sheet and not intermolecular β-sheet, as found in fibrils, may explain the delay of fibrillogenesis despite rapid β-sheet conversion of the 9:1 sample. Utilizing uniformly ^{13}C-labeled $A\beta_{1-42}$ allowing the assignment of structural components to individual peptides in mixed samples. This allowed the probing of structural changes in both peptides caused by interaction with one another.

Peptides were first examined individually by depositing 40 μL of a 200 μM solution of Aβ in HFIP to the CaF_2 FTIR window. HFIP was then removed via vacuum desiccation for 15 minutes and FTIR measurements were taken of the proteins in a dried state. The $^{13}CA\beta_{1-42}$ spectra contains a major peak at 1588 cm^{-1} indicating the presence of intermolecular β-sheet structure (Figure 6). It also contains a broad component likely corresponding to β-turns (~1660 cm^{-1}) and an insignificant α-helical component (1617 cm^{-1}). The $A\beta_{pE3-42}$ is forming intramolecular β-sheet that is possibly anti-parallel as indicated by the peak at 1634 cm^{-1} and small shelf present at 1695 cm^{-1}(189) (Figure 6). The presence of structures other than α-helix in the dry samples indicates that the peptides can undergo structural transitions in the absence of aqueous buffer due to atmospheric humidity.

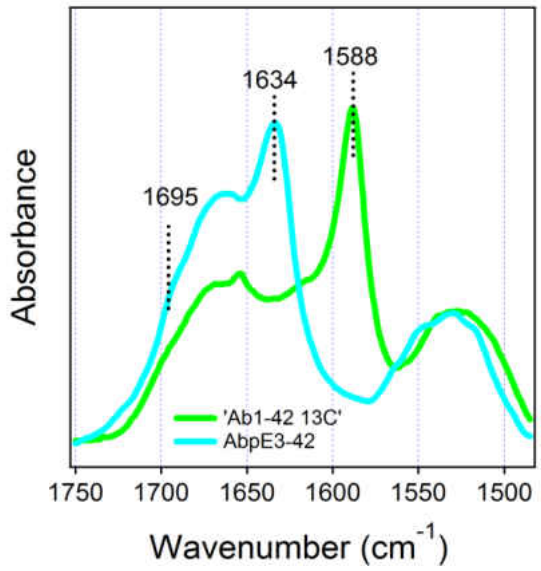

Figure 6. FTIR spectra of $A\beta_{pE3-42}$ (Light Blue) and uniformly ^{13}Clabeled $A\beta_{1-42}$ (Green) dried from a 200 μM HFIP solution on a CaF_2 Window. The amide I area of spectra was normalized.

The observation that atmospheric humidity was sufficient to induce structural changes gave us the idea to examine the effect of $A\beta_{pE3-42}$ on the early stages of $A\beta_{1-42}$ aggregation utilizing atmospheric humidity. Using humidity we examined early transitions of both equimolar and 9:1 molar combination samples. Samples in HFIP were added to FTIR windows and HFIP was removed by desiccation as described earlier. Samples were then exposed to atmospheric humidity for either 10 or 20 minutes and FTIR spectra was taken. Individual peptides were also measured after 15 minutes of atmospheric humidification and their weighted sum was compared to combined samples. The absorption of atmospheric humidity is demonstrated by a corresponding increase in absorbance in the H_2O band located 3450-3150 cm^{-1} (Figure 7A). In the 9:1 molar ratio, as the sample is hydrated the structure transitions from α-helix (1617 cm^{-1}) to β-sheet (1592 cm^{-1}) evidenced by an increased 1592/1617 ratio in the 20 minute sample when compared to the 10

minute sample (Figure 7B). The broad peak ~1655 cm^{-1} likely corresponds to $A\beta_{1-42}$ turn structure as well as $A\beta_{pE3-42}$ turn and α-helical structures. The lower absorbance by the weighted sum of individual peptides at 1617 cm^{-1} indicates less α-helical content in the $A\beta_{1-42}$ in the absence of $A\beta_{pE3-42}$. This is evidence that $A\beta_{pE3-42}$ restricts α-helix to β-sheet transition of the $A\beta_{1-42}$. The differences in the equimolar samples are even more pronounced. The weighted sum at 15 minutes contains prominent peaks at 1588 and 1634 cm^{-1} likely corresponding to intermolecular β-sheet of the $A\beta_{1-42}$ and intramolecular β-sheet of the $A\beta_{pE3-42}$ respectively (Figure 7C). The broad shelf ~1660 cm^{-1} is likely composed of $A\beta_{1-42}$ turns as well as $A\beta_{pE3-42}$ α-helix and turn structures. Experimental spectra at 10 minutes show a decrease in α-helix-to-β-sheet transition of $A\beta_{pE3-42}$ evidenced by a decrease in 1634/1658 ratio when compared to the weighted sum. The $A\beta_{1-42}$ α-helix-to-β-sheet transition is also inhibited at 10 minutes as demonstrated by an increase in peak height at 1617 cm-1 and a decrease in the corresponding β-sheet height present at 1595 cm^{-1} in the experimental and 1588 cm^{-1} in weighted sum spectra's respectively. The peak at 1595 cm^{-1} likely corresponds to intra- not intermolecular β-sheet structure. At 20 minutes the differences are even more pronounced. The major peak at 1658 cm^{-1} indicates that $A\beta_{pE3-42}$ is mostly α-helical. Minor shelves located at 1617 and 1595 cm^{-1} correspond to $A\beta_{1-42}$ α-helix and intramolecular β-sheet respectively. The similar intensities at 1617 cm^{-1} for both 10 and 20 minutes indicate a lack of transition from α-helix of the $A\beta_{1-42}$.

This data indicates that at 10% of total peptide $A\beta_{pE3-42}$ delays formation of cross-β structure of $A\beta_{1-42}$. At 50% the effect is even more pronounced with $A\beta_{pe3-42}$ inhibiting

intermolecular β-sheet formation of $A\beta_{1-42}$ in favor of intramolecular at 10 minutes, and inhibiting any β-sheet formation at 20 minutes. Additionally, the $A\beta_{pE3-42}$ forms more α-helix than β-sheet when in combination with $A\beta_{1-42}$, this indicates that $A\beta_{1-42}$ inhibits $A\beta_{pE3-42}$ α-to-β conversion.

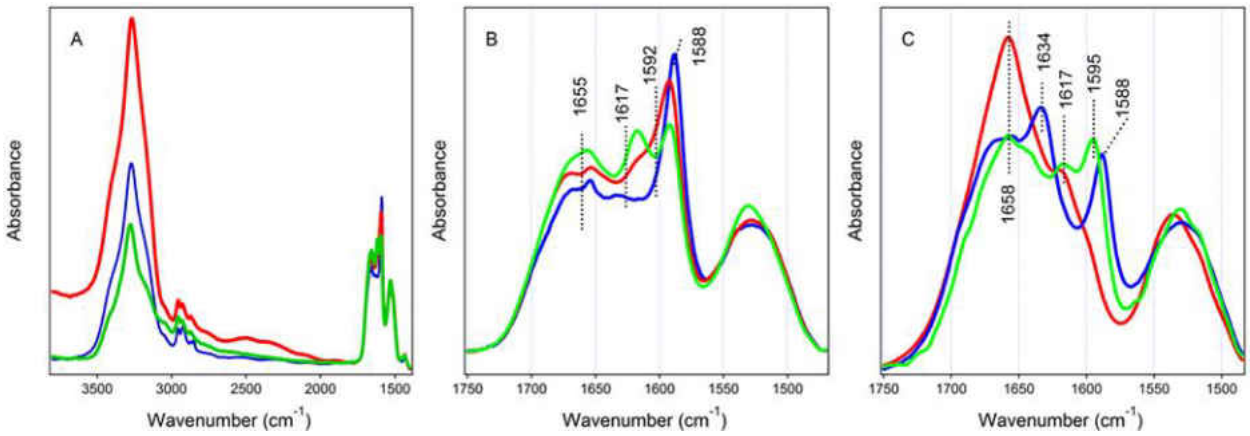

Figure 7. FTIR spectra of $A_{\beta pE3-42}$ and uniformly $^{13}CA\beta_{1-42}$ at 1:9 molar ratio (A and B) and 1:1 molar ratio (C). Green and Red lines are experimental spectra of a sample prepared in HFIP, followed by solvent removal by desiccation and exposure to atmosphere for 10 and 20 min, respectively. The Blue is the weighted sum of the spectra of each peptide measured individually, exposed to the atmosphere for 15 min. Construction of the weighted sum spectra is described under Figure 4. Panel B is a zoom-in into the amide I/II region of spectra shown in panel A.

We next examined structural differences between the peptides in aqueous buffer, 10 mM phosphate pD 6.8 buffer was added to samples following measurement of the dried peptides and spectra were taken every ten minutes. After the addition of buffer both peptides formed predominantly intermolecular β-sheet structure evidenced by a major peak at 1628 cm^{-1} for the $A\beta_{pE3-42}$ (Figure 8B)and 1585 cm^{-1} for the $^{13}CA\beta_{1-42}$ (Figure 8A). Additionally, the $A\beta_{pE3-42}$ had significant turn and α-helical components as evidenced by the secondary peak ~1673 cm^{-1}. The small peak at 1673 cm^{-1} in the $^{13}CA\beta_{1-42}$ sample is likely due to trifluoroacetic acid (TFA) which is commonly found in synthesized peptides.

Examination of the Amide II components of spectra gives additional insight into protein structure. Use of a D_2O based buffer causes hydrogen-deuterium (H-D) exchange and a corresponding loss of amide II intensity around 1540 cm^{-1}(190, 197). Examination of the Amide II of both peptides for two hours shows a loss of amide II intensity for the $A\beta_{pE3-42}$ and no loss of intensity for $A\beta_{1-42}$ (Figure 8). The lack of a drop in Amide II intensity indicates that the amide hydrogens are being shielded from the buffer via formation of a more compact tertiary structure and/or a less flexible secondary structure, as is found in mature fibrils.

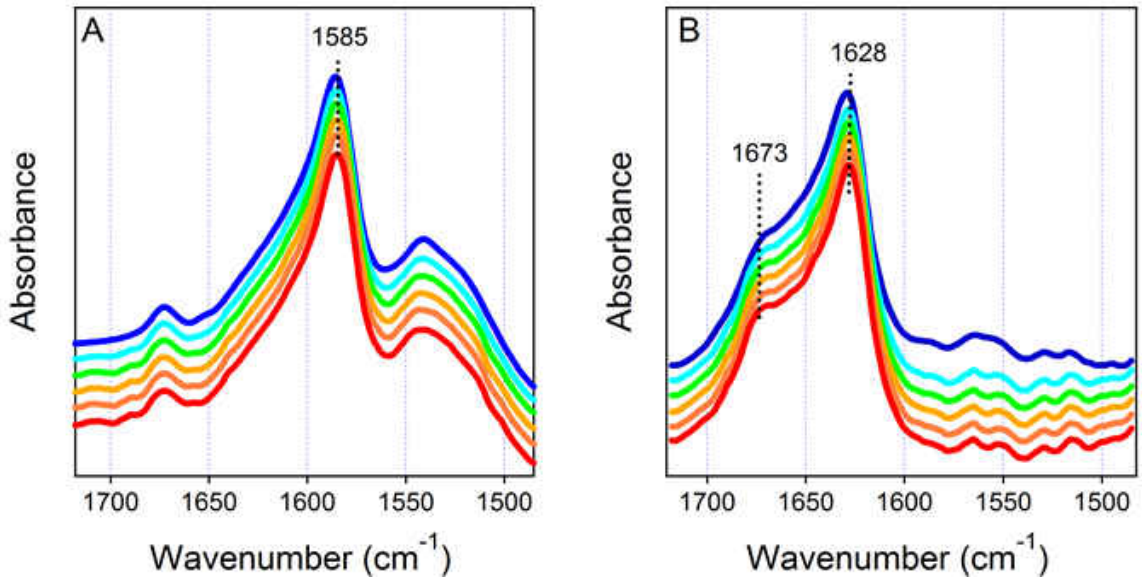

Figure 8. FTIR spectra of $A\beta_{1-42}$ (A) and $A\beta_{pE3-42}$ (B) in 10 mM Na,K-phosphate in D2O, pD 7.2. Change from Blue to Red corresponds to time of exposure of the peptides to the buffer for 10, 30, 50, 70, 90, and 120 min.

Next, we examined spectra of mixed $^{13}CA\beta_{1-42}$ and $A\beta_{pE3-42}$ samples to determine structural effects of co-incubation. After 2 hours of incubation in 10 mM phosphate pD 6.8 experimental spectra were compared to the weighted sum of individual spectra. When compared to the weighted

sums of individual spectra the $A\beta_{1-42}$ β-sheet peak (1585 cm^{-1}) is upshifted by 3 and 10 cm^{-1} in the 9:1 (Figure 9A) and 1:1 samples (Figure 9B) respectively. The latter shift to 1595 cm^{-1} implies formation of intra- not inter-molecular β-sheet. The $A\beta_{pE3-42}$ β-sheet peak (1626-1628 cm-1) was downshifted compared to individual peptides by 4 cm^{-1} in the equimolar combination. These shifts are likely due to ^{13}C:^{12}C coupling and imply strong interactions between the two peptides. It is thus clear that $A\beta_{1-42}$ and $A\beta_{pE3-42}$ form hybrid oligomers composed mostly of β-sheets. Curiously, in the 9:1 sample $A\beta_{pE3-42}$ is upshifted 10 cm^{-1} from 1626 to 1636 cm^{-1} (Figure 4A). This peak can most likely be attributed to intramolecular not intermolecular β-sheet which is characteristic of mature fibrils. This implies that when incubated with $A\beta_{1-42}$ at low molar ratio $A\beta_{pE3-42}$ fibrillogenesis may be inhibited.

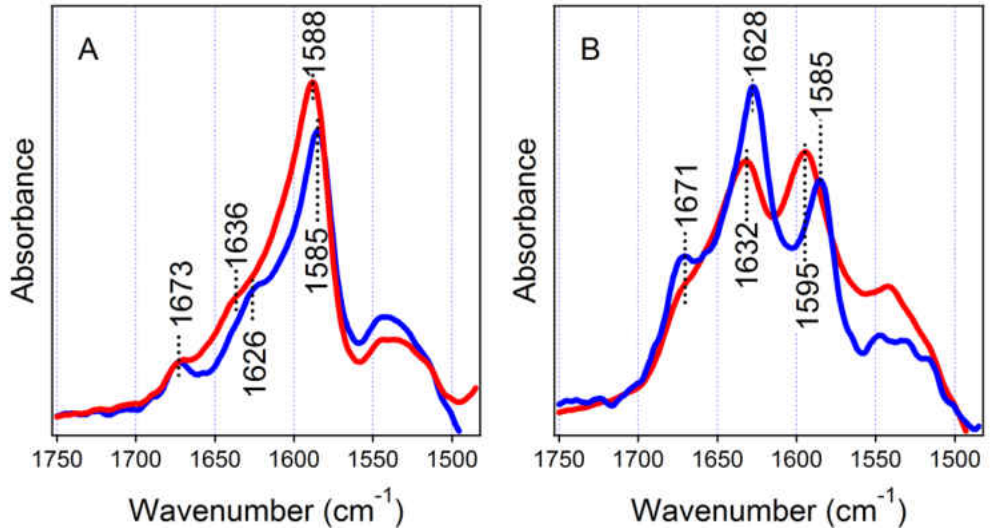

Figure 9. FTIR spectra of $A\beta_{pE3-42}$ and $^{13}CA\beta_{1-42}$ combined at 1:9 (A) and 1:1 (B) molar ratios, incubated in a D_2O-based phosphate buffer (pD 7.2) for 2 h, at a total peptide concentration of 100 μM. Red and Blue lines are the experimental spectra obtained on the two peptides combined in one sample and the weighted sums of individual spectra, respectively. The weighted sums were obtained as A = Σf iAi, where fi is the molar fraction and Ai is the absorbance spectrum of each individual peptide measured separately.

This project gave insight into the structural transitions of $A\beta_{1-42}$ and $A\beta_{pE3-42}$ as well as the structure of early oligomers. It was found that $A\beta_{1-42}$ has a greater β-sheet forming propensity than $A\beta_{pE3-42}$. Additionally, in hybrid samples $A\beta_{pE3-42}$ delays or even reverses formation of cross β-sheet by $A\beta_{1-42}$. The effect of AβpE on fibrillogenesis was demonstrated via TEM data showing mature fibrils in the $A\beta_{1-42}$ samples while the $A\beta_{pE3-42}$ sample contains mostly prefibrillar aggregates. The hybrid samples resemble the $A\beta_{pE3-42}$ indicating a strong effect on fibrillogenesis. FTIR data indicates that AβpE inhibits formation of $A\beta_{1-42}$ intermolecular β-sheet which makes up fibrils. This inhibition of β-sheet formation and thus fibrillization of $A\beta_{1-42}$ by $A\beta_{pE3-42}$ is interesting and a possible mechanism of increased toxicity. Delay or inhibition of fibrillization likely leads to a corresponding increase in the population of soluble oligomers or drive the formation of off-pathway aggregates of increased toxicity. However, the lack of α-helical structure in FTIR of dried peptides indicates structural transitions had occurred before buffer addition, calling these results into question. In addition the peptides were examined in buffer with significantly less ionic content that in physiological conditions. Moving forward with this project, we sought to examine the early oligomer structure of AβpE and unmodified Aβ as well as address these two concerns.

Isotope-Edited FTIR Reveals Distinct Structural Features of Unmodified and Pyroglutamylated Amyloid-β Peptides During oligomerization

Next, we sought to characterize the structure of oligomers formed by $A\beta_{1-42}$ and $A\beta_{pE3-42}$ as well as hybrid oligomers (198). In mixed samples it was observed that $A\beta_{pE3-42}$ inhibits cross β-sheet formation and fibrillogenesis of $A\beta_{1-42}$. Aβ oligomers are heavily implicated in AD but little is known of their structures, so we wished to better characterize the structure of the oligomers formed by these peptides. Here we utilized peptides ^{13}C- and ^{15}N-labeled at specific stretches, these labels allow site specific determination of secondary structure as well as provide tertiary and quaternary structural information. Labeled proteins were examined in both 10 mM phosphate buffer pD 6.8 as well as in near-physiological 50 mM phosphate + 50 mM NaCl buffer pD 6.8. These data provide structural constraints for the modeling of early monomers and oligomers of Aβ. Using these constraints, we propose a possible structure for monomeric Aβ as well as likely mechanisms of early oligomerization.

Isotope Labeling of Peptides

In order to gain site-specific secondary structural information we utilized peptides that had been ^{13}C and ^{15}N labelled at specific locations. Peptides were generated with labels in two locations, $K^{16}L^{17}V^{18}$ and $V^{36}G^{37}G^{38}V^{39}$. Solution NMR studies of the Aβ containing APP segment reconstituted in micelles show an α-helix starting at $K^{16}L^{17}V^{18}$ and a bend involving $V^{36}G^{37}G^{38}V^{39}$ near the C-terminus. After cleavage of Aβ from the membrane this α-helical structure undergoes

structural transitions eventually forming the cross β-sheet structure found in fibrils. The ^{13}C labelling of these segments causes a downshift in the amide I spectra allowing site-specific secondary structural information. In addition by examining the carbon coupling of these labelled segments we are able to gain quaternary structural information. If two labelled segments are in close proximity as is found in the in-register parallel β-sheet characteristic of fibrils they will undergo ^{13}C:^{13}C coupling and a further downshift of absorbance will occur. If the labelled segments are not in close proximity to one another they will instead undergo ^{13}C:^{12}C coupling and a slight upshift of their associated absorbance peak will occur.

FTIR of Dried Proteins

Prior to the addition of buffer, measurements were taken of the peptides dried from HFIP. Peptides in HFIP were first deposited on the CaF_2 window and then HFIP was removed via desiccation. It was previously observed that atmospheric humidity is sufficient to induce structural changes. In order to obtain reliable data, HFIP is used break up pre-formed aggregates and monomerize Aβ. Previously, in CD of proteins dried from HFIP we observed α-helical structures. We sought to capture this α-helical structure in FTIR to ensure consistent Aβ populations prior to the addition of bulk aqueous buffer. To ensure this, we lowered the protein concentration to 50 μM in HFIP, as high concentrations have been shown to induce aggregation (199). When peptides were dried from HFIP, using the lower concentration and keeping care not to keep samples in the

humid lab air for long, both $A\beta_{pE3-42}$ and $A\beta_{1-42}$ as well as their equimolar combination form mostly α-helical structure, evidenced by the absorption peak at 1658-1662 cm^{-1} (Figure 10A). This absorbance is higher than is found in more stable α-helices (1647-1657 cm^{-1}) and suggests that the α-helix formed by Aβ peptides is more flexible. This more flexible α-helix agrees with previous data of the $A\beta_{1-42}$ segment of the APP (98, 99). To accurately place and quantify the additional peak generated by the labeled residues the second derivative of dried spectra was calculated (Figure 10B). Peak fitting was then performed to quantify the additional peaks (Table 2) (Appendix A). For $K^{16}L^{17}V^{18}$ labeled peptides an additional peak at 1624-1628 cm^{-1} is found corresponding to the labelled segment. This area is consistent with α-helix composed of 1-4 ^{13}C labeled residues (190). The reason for the less-than-expected downshift is i-i+4 H-bonding with unlabeled peptides. In peptides labeled at $V^{36}G^{37}G^{38}V^{39}$ the dried spectra contains an additional peak at 1596-1602 cm^{-1}. This peak is located at a lower wavenumber and is lower intensity than would be expected from a ^{13}C α-helix comprising 4/42 or 4/40 suggesting that the C-terminus of the protein is disordered and the peptides are acting as isolated oscillators (Table 2) (190). This data indicates that in a dry state the peptides adopt a flexible α-helical structure involving $K^{16}L^{17}V^{18}$ while the $V^{36}G^{37}G^{38}V^{39}$ sequence close to the C-terminus is unordered. This agrees with previous observations of Aβ containing segments of the APP reconstituted in micelles as well as MD simulations (98, 99, 200). This demonstrates that these dried peptides resemble Aβ prior to membrane release into an aqueous environment, making them a biologically relevant starting material for the study of Aβ structural changes and aggregation.

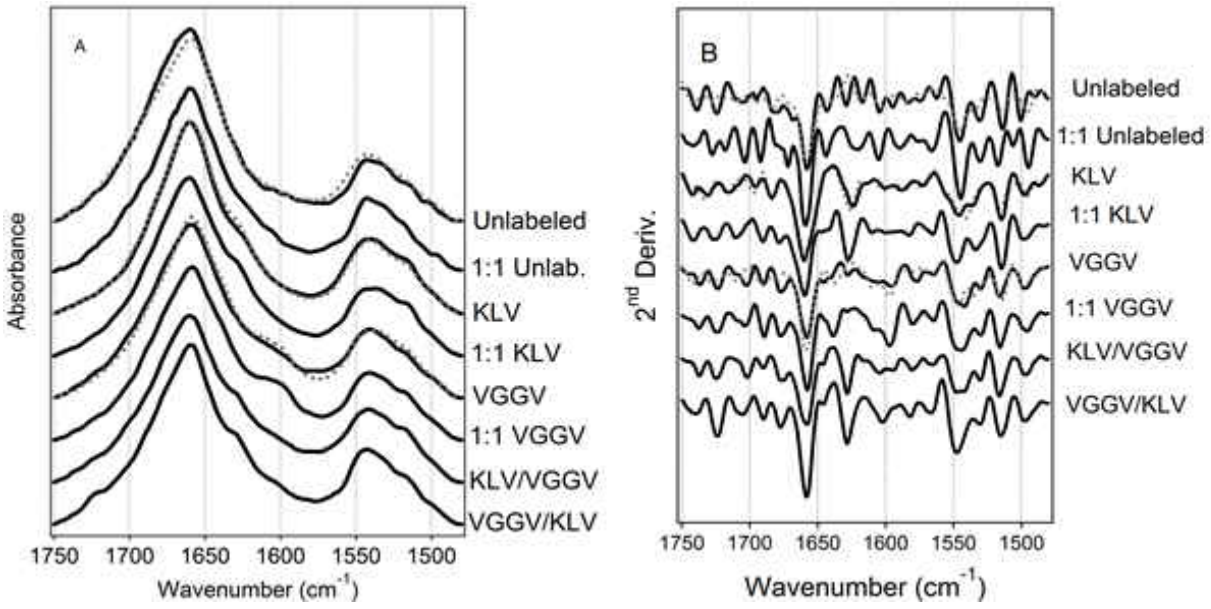

Figure 10. (A) FTIR spectra of dry peptides in the amide I regions. Spectra for unlabeled and isotopically labeled $A\beta_{1-42}$ and $A\beta_{pE3-42}$ peptides and their 1:1 combinations are presented. Gray dotted lines correspond to $A\beta_{pE3-42}$, and solid black lines correspond either to Ab_{1-42} or to combined samples, as indicated. KLV or VGGV imply the peptides have been labeled at $K^{16}L^{17}V^{18}$ or $V^{36}G^{37}G^{38}V^{39}$, respectively. In KLV/VGGV or VGGV/KLV samples, the first stretch applies to $A\beta_{1-42}$ and the second to $A\beta_{pE3-42}$. (B) Second derivatives of the corresponding FTIR spectra.

Table 2. Relative amide I content of the ^{13}C labeled peaks in peptides dried from HFIP. In the columns with two different labels the first one corresponds to $A\beta_{1-42}$ and the second to $A\beta_{pE3-42}$.

	$A\beta_{1-42}$	$A\beta_{pE3-42}$	1 to 1	KLV/VGGV	VGGV/KLV	Total
KLV	12.3%	15.5%	13.3%	13.0%	12.6%	13.3±1.3%
VGGV	8.2%	12.4%	8.9%	2.2%	7.4%	7.8±3.7%

FTIR of Unlabeled Peptides

After measurement of dried peptides aqueous buffer was added and measurements were taken consecutively (1000 scans takes ~10 minutes). After 10 minutes in 10 mM Phosphate buffer pD 6.8 the peptides and their equimolar combination form type 1 β-turn and intramolecular β-sheet as evidenced by the major peaks at 1673 and 1635-1630 cm^{-1} respectively (Figure 11D) (190). Consistent with previous observations, the peptides retain some α-helical structure evidenced by absorption ~1660 cm^{-1}. Peptides in near-physiological buffer conditions have similar absorption peaks and shape indicating formation of type 1 β-turn, α-helix, and intramolecular β-sheet (Figure 11A). After 2 hours the location of the β-sheet was downshifted 2-5 cm^{-1} likely due to H-D exchange. This indicates that the peptides are in a loose conformation allowing solvent access to the majority of peptides residues (Figure 11C). The β-sheet absorbs 1633-1628 cm^{-1} indicating the presence of intramolecular β-sheet as intermolecular β-sheets absorb at a lower wavenumber 1613-1625 cm^{-1}. In near physiological conditions $A\beta_{pE3-42}$ contains more α-helix and less β-sheet compared to $A\beta_{1-42}$ indicated by a higher ratio 1660/1630-35 cm^{-1}(Figure 11A-C). In low ionic buffer conditions the opposite is true with $A\beta_{1-42}$ containing more α-helix and less β-sheet than $A\beta_{pE3-42}$ (Figure 11D-F). These differences are evident when examining $A\beta_{1-42}$ –$A\beta_{pE3-42}$ difference spectra. In physiological ionic conditions a negative peak at 1660 cm^{-1} and a positive peak at 1620 cm^{-1} indicate more α-helix and less β-sheet in the $A\beta_{pE3-42}$ sample compared to the $A\beta_{1-42}$ (Figure 12A). The opposite is seen in low salt buffer with a large negative peak at 1620 cm^{-1} and a positive peak at 1660 indicating less α-helix and more β-sheet in the $A\beta_{pE3-42}$ (Figure 12C).

Taking the difference spectra of the 1:1 and the weighted sums of the individual peptides show differences caused by peptide interactions. If there were no changes due to peptide interaction this line would be flat. In physiological ionic conditions difference spectra has positive components at 1670 and 1653 cm^{-1} and a negative component at 1625 cm^{-1}, indicating peptide interaction enhances formation of β-turn and α-helix and inhibits β-sheet formation (Figure 12B). In low salt a positive component at 1673 cm^{-1} and a negative one at 1625 cm^{-1} are present (Figure 12D). This indicates that peptide interaction causes formation of more β-turn and less β-sheet structure. In near-physiological conditions the 1:1 sample more closely resembles the $A\beta_{pE3-42}$ forming more α-helix and less β-sheet; this agrees with previous data that $A\beta_{pE3-42}$ strongly influences the structure of hybrid samples. In low salt conditions the 1:1 more closely resembles the $A\beta_{1-42}$ forming more β-turn and less β-sheet structure.

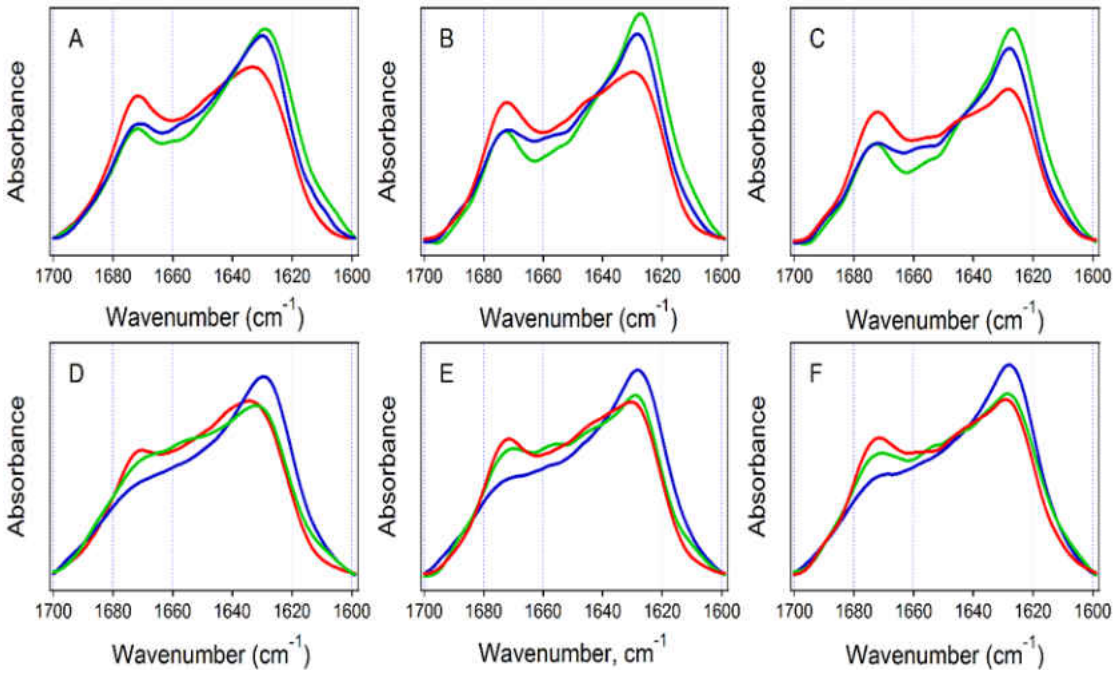

Figure 11. FTIR spectra of 50 mM $A\beta_{1-42}$ (Green) $A\beta_{pE3-42}$ (blue) and their equimolar combination (Red) in 50 mM phosphate + 50 mM NaCl pD 7.2 (ABC) and in 10 mM phosphate pD 6.8 (DEF) buffers. Time points shown are 10 minutes (A,D) 60 minutes (B,E) and 120 minutes (C,F). Total peptide concentration is 50 μM

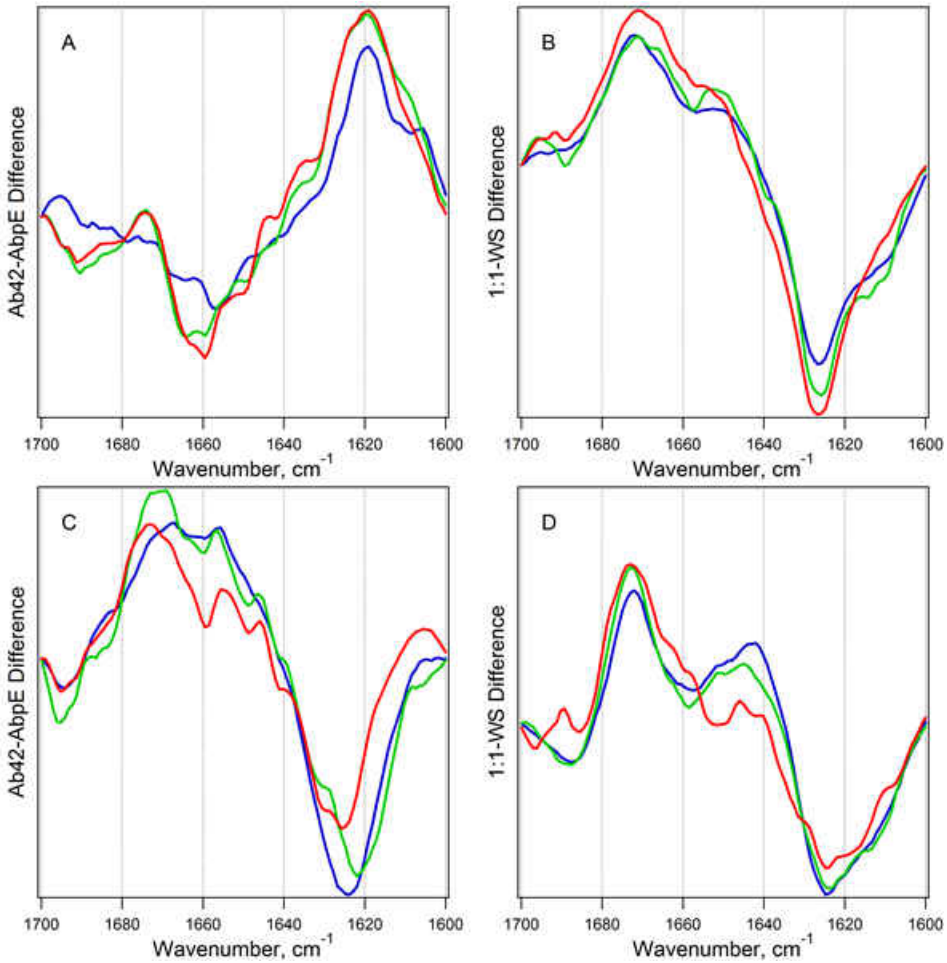

Figure 12. Difference FTIR spectra of $A\beta_{1-42}$ and $A\beta_{pE3-42}$ peptides and their equimolar combinations in 50 mM NaCl + 50 mM phosphate buffer (A, B) and 10 mM phosphate buffer (C, D), pD Spectra in A) and C) show the difference $A\beta_{1-42}$ - $A\beta_{pE3-42}$, and those in B) and D) show the difference between 1:1 combination and the normalized sum of the spectra of the two peptides. Blue, green, and red correspond to the peptide samples incubated in a D_2O-based buffer for 10, 60 and 120 min, respectively. Total peptide concentration is 50 μM.

In order to quantitate the relative fractions of secondary structure present peak fitting was performed with peaks being placed based on the second derivative of the spectra (Appendix B). While peak fitting it was noticed that in 50 mM phosphate + 50 mM NaCl pD 6.8 buffer the 1:1 α-helix was downshifted to ~1653 cm^{-1}. This downshift is likely due to helix stabilization. Peaks were assigned to secondary structures based on location of the absorbance peak. Data after 10, 60,

and 120 minutes of hydration was averaged (Table 3). In physiological buffer conditions $A\beta_{pE3-42}$ contains more α-helix and less β-sheet than $A\beta_{1-42}$ while the opposite is true in buffer of less ionic content. The 1:1 combination similarly resists α-helix-to-β-sheet conversion.

This is consistent with our previous observations that $A\beta_{pE3-42}$ is able to retard β-sheet formation in hybrid samples. The changing α-helical propensity based on ionic conditions is evidence that the α-helix is located in the N-terminus of the peptides. The α-helix of $A\beta_{1-42}$ can be stabilized by ionic interactions at the N-terminus such as D^1-K^{16}, E^3-K^{16}, D^1-R^5, R^5-E^{11}. Higher concentrations of ionic charges will weaken this ionic stabilization. The $A\beta_{pE3-42}$ is missing three N-terminal charges and thus does not form some of these stabilizing ionic interactions.

Table 3. Secondary structures of $A\beta_{1-42}$, $A\beta_{pE3-42}$, and their equimolar combination in 50 mM phosphate 50 mM NaCl pD 6.8 (light blue) and 10 mM phosphate pD 6.8 (unshaded) determined by curve fitting of amide 1 spectra. Numbers shown are averages taken after 10, 60, and 120 minutes in buffer. Other refers to all other peaks fit and is primarily composed of unordered structure.

	$A\beta_{1-42}$	$A\beta_{pE3-42}$	1 to 1
α-helix	11.0±2.4	18.7±3.2	22.9±3.6
	24.8±5.1	13.6±1.8	16.3±2.1
β-sheet	50.4±4.6	43.0±4.4	34.5±3.9
	38.7±4.8	48.9±3.6	34.2±3.2
β-turn	18.1±3.3	20.3±1.7	28.4±2.4
	24.0±2.7	19.8±1.3	27.7±3.6
other	20.5±3.9	18.0±2.2	14.2±1.3
	12.5±3.6	17.7±2.6	21.8±2.7

FTIR of Labeled Peptides

After dry measurement of the labeled peptides buffer was applied and consecutive measurements were taken as with the unlabeled peptides. After ten minutes in both buffers the spectra for the peptide resembles the unlabeled with major peaks ~1673 cm^{-1} and between 1637-1628 cm^{-1} corresponding to type 1 β-turn and intramolecular β-sheet respectively (Figure 12). Overlaying the $K^{16}L^{17}V^{18}$ and $V^{36}G^{37}G^{38}V^{39}$ spectra over the unlabeled spectra discussed

previously identifies an additional peak located ~1598-1604 cm^{-1}(Figure 13). This peak can be attributed to the ^{13}C labeled amino acids in the peptides.

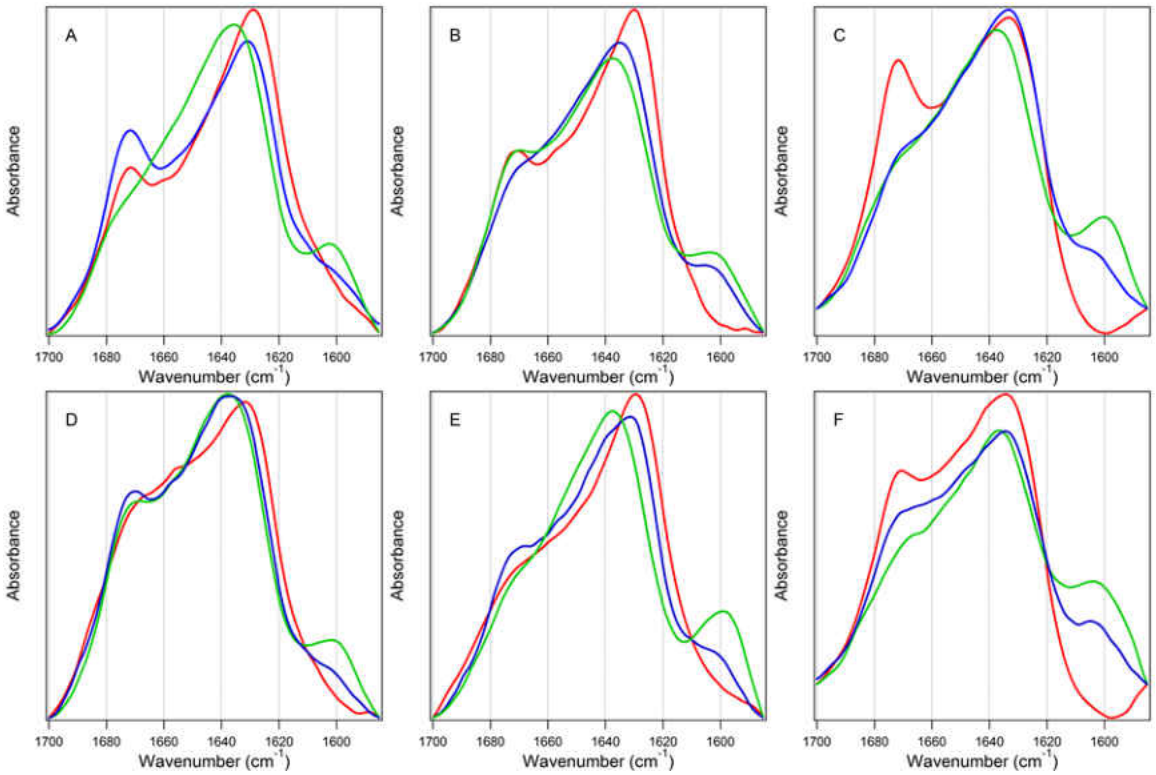

Figure 13. FTIR spectra of $A\beta_{1-42}$ (A,D), $A\beta_{pE3-42}$ (B,E) and, their 1:1 combination (C,F) after 10 minutes in 50 mM phosphate 50 mM NaCl pD 7.2 (A,B,C) and 10 mM phosphate pD 7.2 (D,E,F) buffers. Colors correspond to unlabeled peptide (Red) as well as proteins ^{13}C- and ^{15}N- labeled at $K^{16}L^{17}V^{18}$ (Blue) and $V^{36}G^{37}G^{38}V^{39}$ (green). Total peptide concentration is 50 μM.

When labeled at $K^{16}L^{17}V^{18}$ in 50 mM phosphate + 50 mM NaCl pD 6.8 buffer the $A\beta_{pE3-42}$ retains more α-helix than $A\beta_{1-42}$ as with the unlabeled peptides (Figure 14 A-C). The $A\beta_{1-42}$ instead forms more type 1 β-turn structure demonstrated by the larger absorbance at 1673 cm^{-1}.

Additionally, the β-sheet absorbance of the $A\beta_{1-42}$ is downshifted 3-5 wavenumbers in comparison to the $A\beta_{pE3-42}$ indicating faster formation of β-sheet compared to the $A\beta_{pE3-42}$. The 1:1 combination β-sheet peak absorbs ~1633cm^{-1} between $A\beta_{1-42}$ and $A\beta_{pE3-42}$. This agrees with our previous observations that $A\beta_{pE3-42}$ has lower β-sheet propensity than $A\beta_{1-42}$ and could retard β-sheet formation of the $A\beta_{1-42}$ in hybrid samples. When labeled at $V^{36}G^{37}G^{38}V^{39}$ the $A\beta_{pE3-42}$ contained more β-turn and less β-sheet structure than $A\beta_{1-42}$ indicated by peak heights at 1673 and ~1635 cm^{-1} respectively (Figure 14 D-F). As with the $K^{16}L^{17}V^{18}$ labeled proteins the β-sheet peak of $A\beta_{1-42}$ is at lower frequencies than $A\beta_{pE3-42}$ indicating faster β-sheet formation.

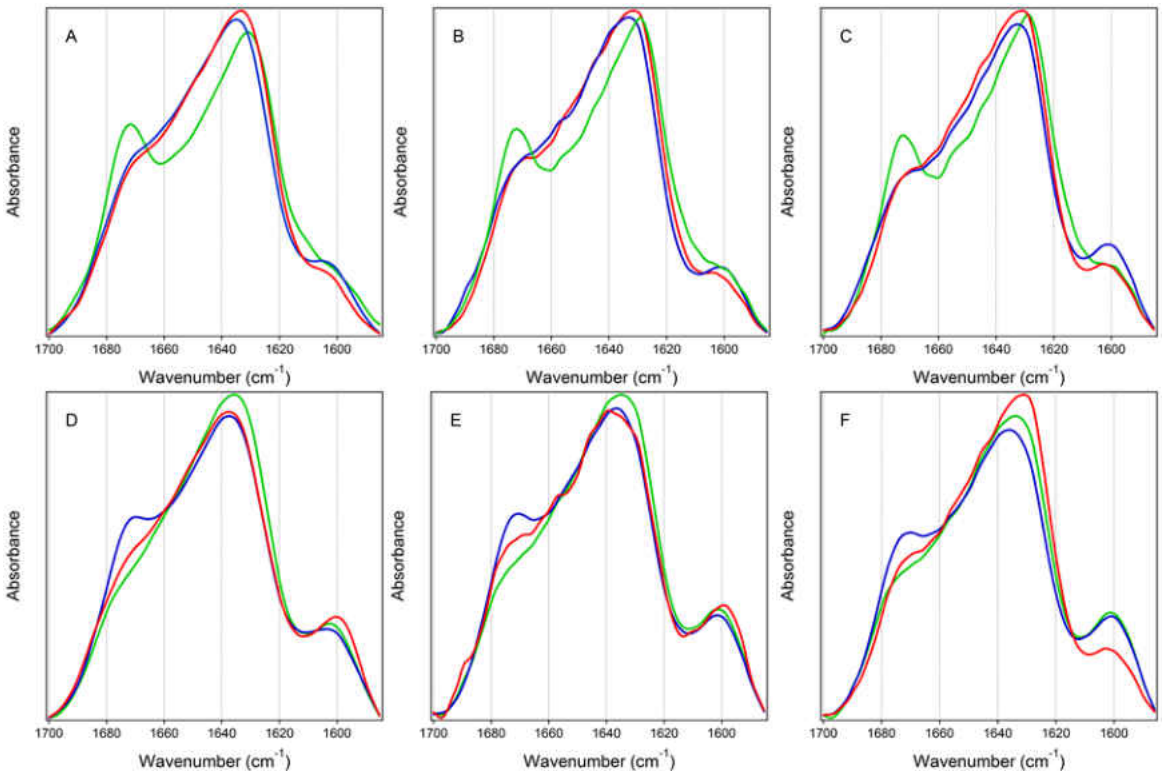

Figure 14. FTIR spectra of $A\beta_{1\text{-}42}$ (green), $A\beta_{pE3\text{-}42}$ (blue) and, their equimolar (red) combinations after 10 (A,D) 60 (B,E) and, 120 (C,F) minutes in 50 mM phosphate 50 mM NaCl pD 7.2 buffer. Peptides are ^{13}C- and ^{15}N-labeled at $K^{16}L^{17}V^{18}$ (A,B,C) and $V^{36}G^{37}G^{38}V^{39}$ (D,E,F). Total peptide concentration is 50 μM.

When 10 mM phosphate pD 6.8 buffer was added to the peptides the $A\beta_{1\text{-}42}$ formed a higher fraction of β-turn structure indicated by the peak at 1673cm^{-1} (Figure 15). Additionally, in the $K^{16}L^{17}V^{18}$ labeled peptides the β-sheet peak wavenumber of the $A\beta_{pE3\text{-}42}$ is shifted several wavenumbers lower than $A\beta_{1\text{-}42}$ indicating faster β-sheet formation by the $A\beta_{pE3\text{-}42}$ (Figure 15A-C). The 1:1 β-sheet is again located between the $A\beta_{1\text{-}42}$ and $A\beta_{pE3\text{-}42}$ β-sheet wavenumbers indicating that $A\beta_{1\text{-}42}$ retards β-sheet formation in the hybrid sample. This agrees with our previous data that $A\beta_{pE3\text{-}42}$ has a lower β-sheet propensity than the $A\beta_{1\text{-}42}$ and can delay β-sheet formation in hybrid samples in physiological buffer conditions while the opposite is true in buffer of low

ionic content

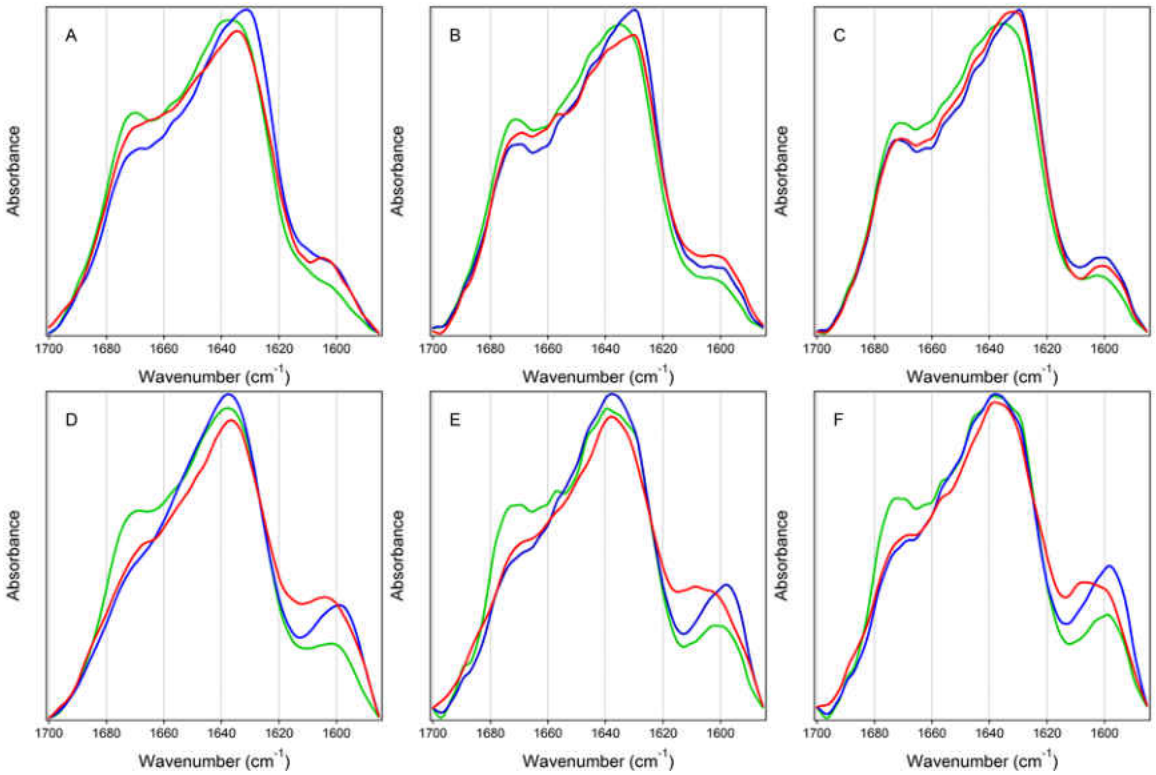

Figure 15. FTIR spectra of $A\beta_{1-42}$ (green), $A\beta_{pE3-42}$ (blue) and, their equimolar (red) combinations after 10 (A,D) 60 (B,E) and, 120 (C,F) minutes in 10 mM phosphate pD 7.2 buffer. Peptides are ^{13}C- and ^{15}N-labeled at $K^{16}L^{17}V^{18}$ (A,B,C) and $V^{36}G^{37}G^{38}V^{39}$ (D,E,F). Total peptide concentration is 50 μM.

To facilitate placement of the labeled peak the second derivative was calculated, examination of the second derivative show a peak that can be assigned to the labeled segment ~1603-1598 cm^{-1} (Figure 16). To further quantify this peak as well as to examine secondary structure distribution peak fitting was conducted for spectra taken 10, 60, and 120 minutes after buffer addition (Appendix C). Taking into account our observed intramolecular β-sheet peaks of 1637-1628 cm^{-1} we can predict ^{13}C-labeled β-sheets to absorb 1601-1592 cm^{-1} therefore we can reliably say that the labeled segment is forming intramolecular β-sheet. As discussed earlier, in

samples containing both ^{13}C- and^{12}C-labeled samples the ^{13}C-labeled residues can undergo vibrational coupling with either ^{13}C or ^{12}C-labeled residues depending on whichever is in close proximity. This coupling changes vibrational frequency with ^{13}C:^{13}C coupling causing a downshift and ^{13}C:^{12}C coupling causing an upshift in absorbance wavenumber. Taken with our previous calculation we can reasonably assign an absorbance 1603-1599 to ^{13}C-labeled β-sheets undergoing ^{13}C:^{12}C-coupling and the absorbance 1596-1592 to ^{13}C-labeled β-sheets undergoing ^{13}C:^{13}C-coupling. Therefore, based on the location of the labeled peak in the second derivative we can reasonably conclude that in these samples in any combination neither $K^{16}L^{17}V^{18}$ nor $V^{36}G^{37}G^{38}V^{39}$ segments are adjacent to themselves or one another.

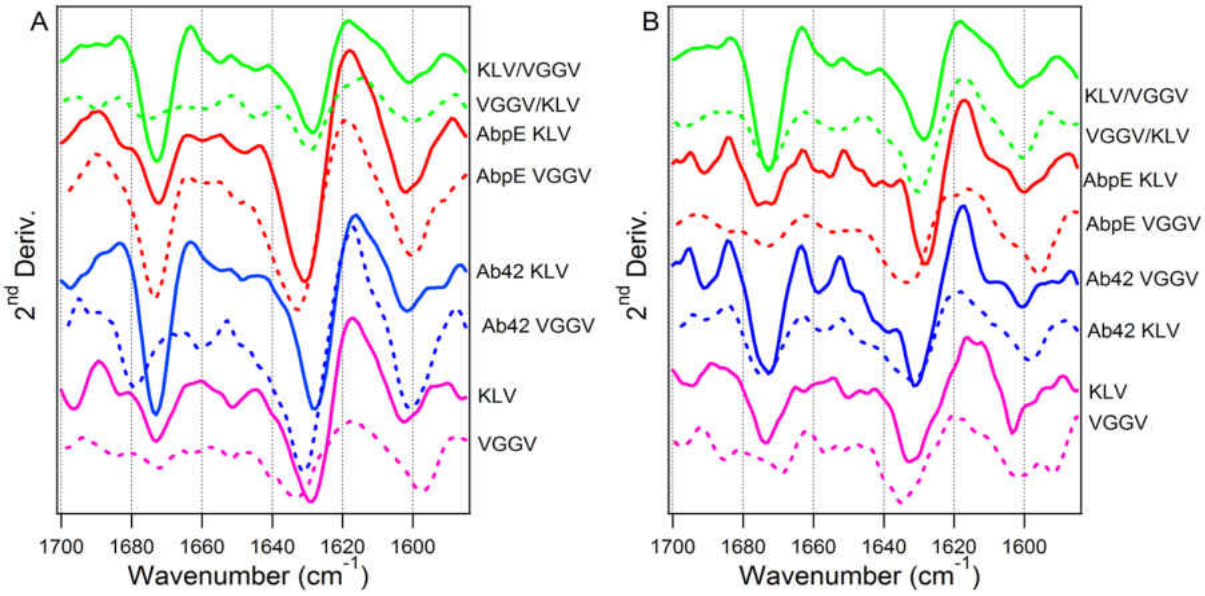

Figure 16. Second derivative of FTIR spectra taken 10 minutes after the addition of A) 50 mM phosphate + 50 mM NaCl pD 6.8 and B) 10 mM Phosphate buffer pD 6.8. For spectra labeled KLV/VGGV or VGGV/KLV the first corresponds to $A\beta_{1\text{-}42}$ and the second to $A\beta_{pE3\text{-}42}$.

Aβ Modeling

Although FTIR data generally does not give tertiary or quaternary structural information site-specific ^{13}C-labeling gave site-specific structural information. This information along with the other data collected here gives structural constraints useful in the modeling of early Aβ oligomers and oligomerization. First, in aqueous buffer both $A\beta_{1\text{-}42}$ and $A\beta_{pE3\text{-}42}$ forms a mixture of primarily intramolecular-β-sheet with lesser amounts of, α-helix, β-turn, and unordered structures. This α-helix can be placed at the N-terminus based on data collected in buffers with two different ionic contents indicating that $A\beta^{pE3\text{-}42}$ has a higher α-helix propensity than $A\beta_{1\text{-}42}$ in physiological conditions while the opposite is true in buffer with low ionic content. Second, the segments $K^{16}L^{17}V^{18}$ and $V^{36}G^{37}G^{38}V^{39}$ both form intramolecular β-sheet. Third these segments are undergoing ^{13}C:^{12}C coupling meaning they are not adjacent to one another. The final constraint is based on the small size of these peptides as well as the significant fraction of α-helix this makes formation of parallel intramolecular β-sheets impossible. Based on these constraints we propose that the monomeric Aβ is forming a β-hairpin with two β-strands connected by turn structure downstream of $K^{16}L^{17}V^{18}$ with an N-terminal α-helix (Figure 16). The turn segment is likely stabilized by a salt bridge between D^{23} and K^{28} as predicted in other studies (201).The presence of α-helix with majority β-sheet has been previously observed in Aβ oligomers which display more toxicity to cultured PC12 cells compared to mature fibrils which contain no α-helical component (115).

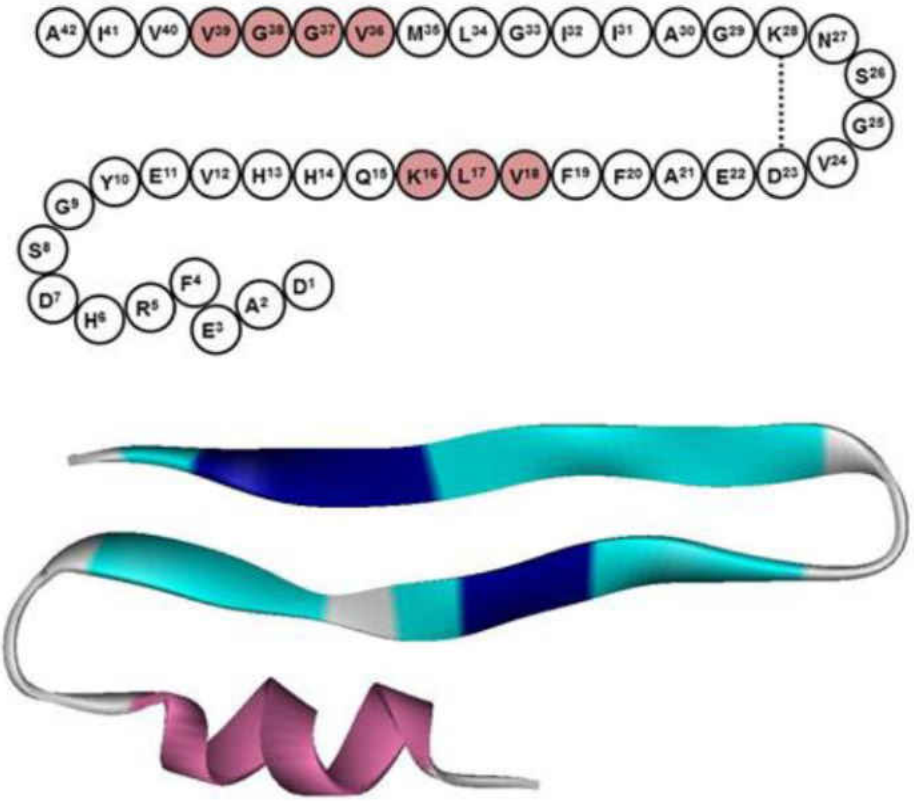

Figure 17. The amino acid sequence of $A\beta_{1-42}$ arranged in a structure involving a b-hairpin stabilized by D^{23}-K^{28} ionic bridge, and an N-terminal stretch that may assume a-helical conformation. The isotopically labeled amino acids are shaded. Underneath is a ribbon model for Ab monomer, composed of a β-hairpin and an N-terminal α-helix. The segments $K^{16}L^{17}V^{18}$ and $V^{36}G^{37}G^{38}V^{39}$ are both involved in the b-hairpin and are marked by dark blue colors.

These data also give us hints as to how these early monomers aggregate. The lack of ^{13}C:^{13}C coupling exclude the possibility of parallel in-register stacking with the aggregation axis perpendicular to hairpin plane as found in mature fibrils (Figure 17A). Stacking in an anti-parallel arrangement would also cause ^{13}C:^{13}C coupling and can thus be ruled out (Figure 17B). Next we examined oligomerization through interactions between the C-termini or N-termini of neighboring hairpins. The lack of intermolecular β-sheet signal indicates that this interaction is through non-H bonding possibly hydrophobic or ionic. Aggregation in this manner in either a parallel (Figure 17C) or antiparallel (Figure 17D) orientation would again lead to ^{13}C:^{13}C coupling and therefore

can be confidently ruled out. We then examined dimerization through non-H bonding between the C-termini of one hairpin strand with the N-terminus of a neighboring hairpin in either a parallel (Figure 17E) or antiparallel (Figure 17F) manner. In this arrangement there would not be any ^{13}C:^{13}C coupling matching our experimental observations and is thus not ruled out. This stacking could take place with the β-strands laterally or in a vertical manner reminiscent of steric zippers. This vertical stacking could take place alternatively between strands (Figure 17E) or alternating between entire hairpins (Figure 17F).

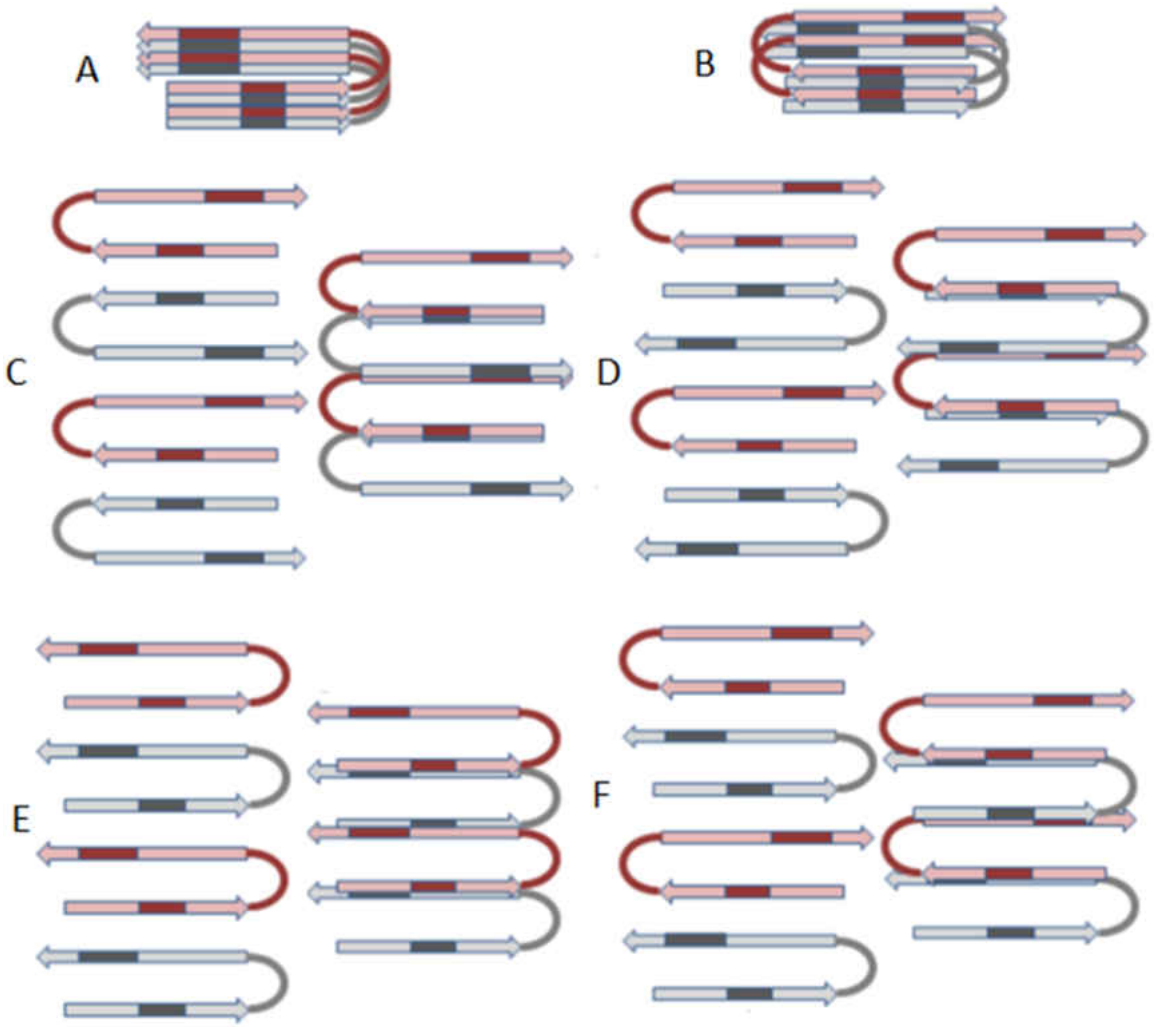

Figure 18. Schematic models for Aβ oligomerization through interactions between the core β- hairpin structures. Two arrows in each molecule represent two β-strands, connected by a loop or turn. The monomers are colored gray and pink, and the isotopically labeled segments are indicated by darker color. In all cases, the structures are stabilized by intramolecular H-bonding and intermolecular non-H-bonding contacts, *i.e.* ionic and/or hydrophobic interactions. The plane of the picture is parallel to the hairpin plane. In A,B the aggregation axis is perpendicular, and in C-F it is coplanar to the picture plane.

Here we conducted FTIR on peptides ^{13}C-labeled at specific segments in order to obtain site-specific structural information for $A\beta_{1\text{-}42}$, $A\beta_{pE3\text{-}42}$, and their equimolar combinations. Using this information as well as information obtained in two buffers with distinct ionic content allow us to propose a model for an early monomer composed of a β-hairpin with an N-terminal α-helix.

Additionally, we propose that these monomers aggregate through non-H-bonding interactions between the N-terminus of one hairpin and the C-terminus of another. These oligomers are structurally distinct form mature fibrils and are formed via a different mechanism of aggregation. The consistency of this data throughout repeated experiments, in spite of the polymorphic nature of these proteins, lends credibility to these results.

Mutual inhibition of fibrillogenesis by Aβ peptides

Next, we sought to characterize the transitions and intermediate structures during oligomer formation. The toxic Aβ species is thought to be created sometime during the transition from the α-helical monomer to the mature cross β-fibrils. However, it is unknown whether these oligomers are formed as intermediates during fibrillogenesis or are formed via alternative pathways. We sought to answer this question by examining the α-to-β transition of the peptides. To accomplish this we used a novel approach, hydration from gas phase, (see methods) based on our previous use of atmospheric humidity to induce structural changes in Aβ (Figure 6).

Individual Peptides

Prior to examining hybrid samples we first characterized the behavior of individual peptides. After desiccating the proteins onto the windows as described earlier, spectra of the dried peptide was collected. These spectra indicate that both $^{13}CA\beta_{1\text{-}42}$ and $A\beta_{pE3\text{-}42}$ are forming primarily α-helical structure shown by peaks at 1616 and 1657 cm^{-1} respectively (Figure 18). In the $^{13}CA\beta_{1\text{-}42}$ spectra a shelf present ~1590 indicates presence of a small amount of β-sheet and the peak ~1673 cm^{-1} likely corresponds to residual TFA from peptide synthesis.

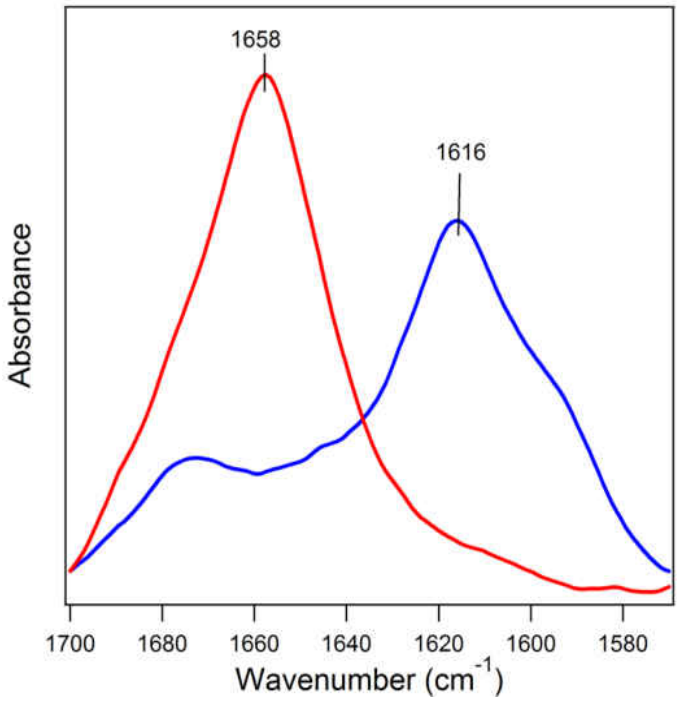

Figure 19. FTIR spectra of 50 μM $A\beta_{pE3-42}$ (red) and $^{13}CA\beta_{1-42}$ (blue) in HFIP added to FTIR windows followed by HFIP removal by vacuum desiccation.

Following measurement of dried peptides structural transitions were initiated by beginning the flow of D_2O laden N_2 gas into the sample chamber. The buildup of D_2O within the chamber is indicated by increasing intensity of spectral features generated by D_2O stretching ~2500 (Figure 20). This data indicated that D2O saturation level reached one third of maximum after 5 minutes and then slowly rose until maximum saturation is reached approximately 3 hours later. After the onset of D_2O hydration the peak associated with the $^{13}CA\beta_{1-42}$ α-helix rapidly diminished while a peak corresponding to β-sheet ~1590 cm^{-1} quickly grew indicating a rapid initial rate of α-helix-to-β-sheet transition (Figure 21A). The peak ~1673 cm^{-1} is unchanged throughout hydration and can be attributed to TFA. Hydration of the $A\beta_{pE3-42}$ caused a decrease in α-helix and a corresponding increase in β-sheet content indicated by growth of a peak at 1633 cm^{-1} (Figure 21B).

Over time, the reduction in α-helical intensity revealed an additional peak at 1673 cm^{-1} which we have previously attributed to type 1 β-turns. Additionally, the $A\beta_{1-42}$ retained an amide II absorbance while the $A\beta_{pE3-42}$ amide II was fully deuterated, as previously observed. This α-to-β transition is easily observed by looking at the second derivative of the initial spectra and one after five hours of gas phase hydration (Figure 21C,D). Examination of second derivatives reveal a component at 1613 cm^{-1} in $^{13}CA\beta_{1-42}$, this peak indicates retention of α-helical structure (Figure 21C). The downshift in wavenumber is likely due to amide dueteration throughout hydration. A small component ~1660 cm-1 in the AβpE likely corresponds to some residual α-helix as well (Figure 21D).

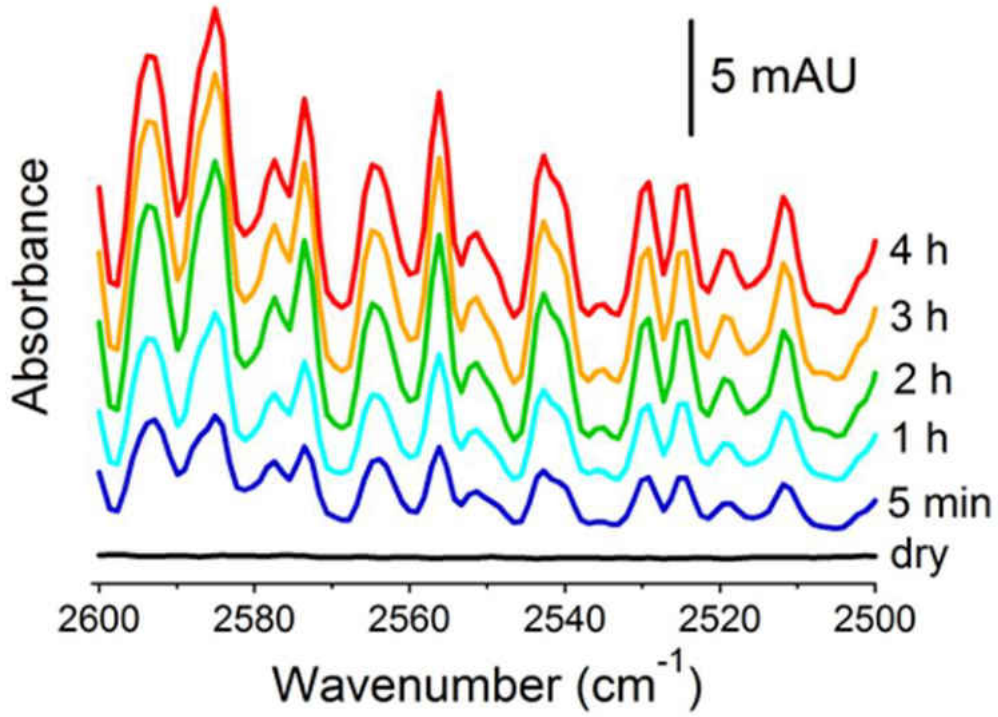

Figure 20. FTIR Spectra of $A\beta_{pE3-42}$ sample in D_2O absorbance region at various times of continuous injection of D_2O-saturated nitrogen. The intensity of D_2O asymmetric stretching vibrational-rotational mode increases as D_2O vapor is being pumped into the sample compartment of the FTIR instrument. The spectra have been stacked for clarity.

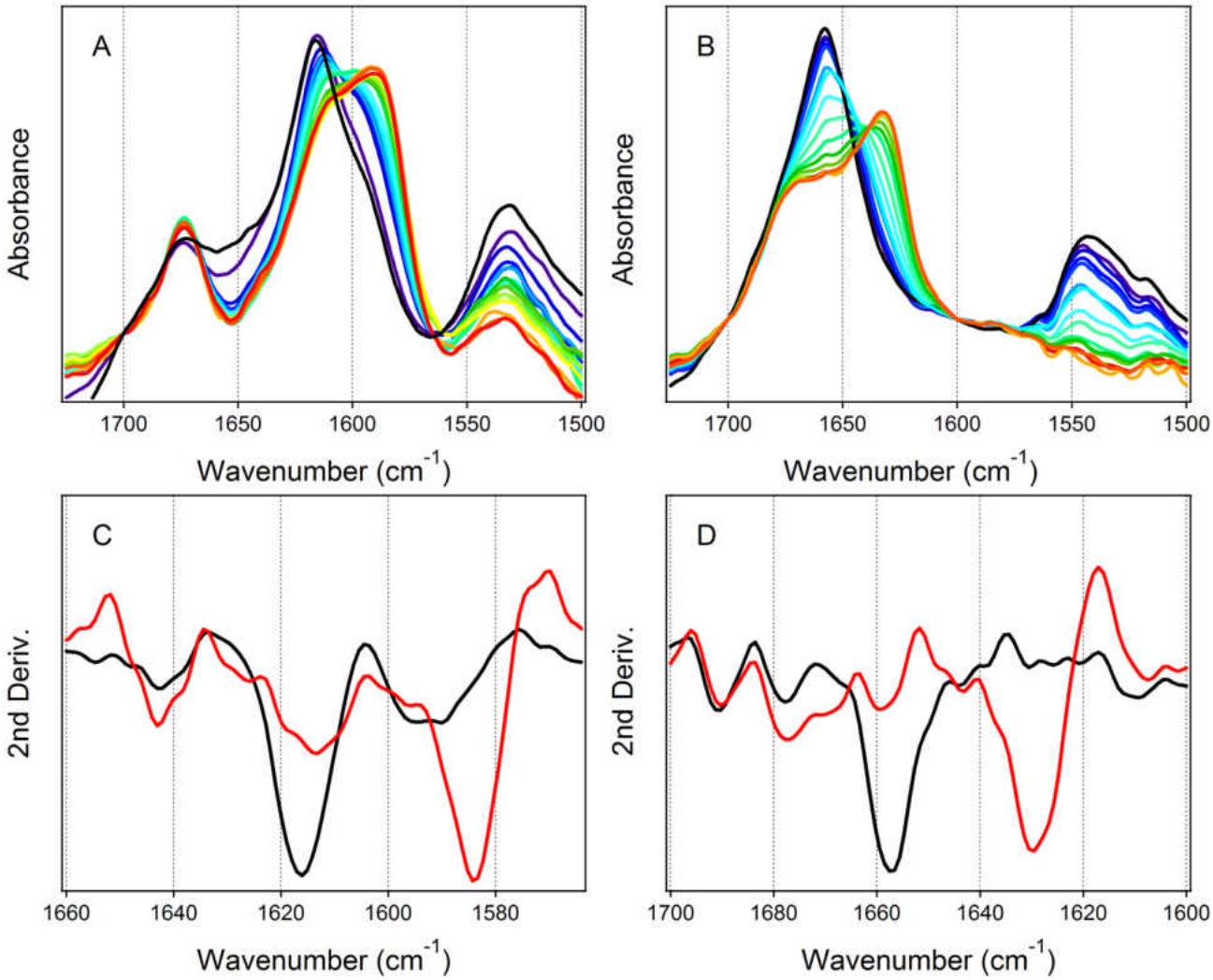

Figure 21. FTIR spectra of ^{13}C-A$\beta_{1\text{-}42}$ (A) and A$\beta_{pE3\text{-}42}$ (B) dried on a CaF_2 window (black lines) and upon injection of D_2O-saturated nitrogen for ~5 hours (blue to red). Amide I areas have been normalized. Time points of consecutive spectra can be determined from data of Fig. 21. The second derivatives of spectra corresponding to the dry and after five hours of vapor hydration for the A$\beta_{1\text{-}42}$ (C) and A$\beta_{pE3\text{-}42}$ (D).

Although both peptides transitioned from α-helix to β-sheet the kinetics of this transition were quite different. The A$\beta_{pE3\text{-}42}$ transition occurs much slower at first and then more rapidly later on. To examine the kinetics of this transition we plotted A_α/A_β as well as the height of the amide II peak versus time (Figure 22). In the A$\beta_{1\text{-}42}$ for the first hour, the A_{1590}/A_{1616} rapidly increased

while the amide II height rapidly diminished (Figure 22A). After an hour this trend continued but at a reduced rate. Conversely, the $A\beta_{pE3-42}$ transitions were sigmoidal in behavior. Little change occurred in the first hour, followed by rapid change in both amide II height and A_{1633}/A_{1658} (Figure 22B). The delayed β-sheet formation of the AβpE compared to the unmodified peptide agrees with our previous observations.

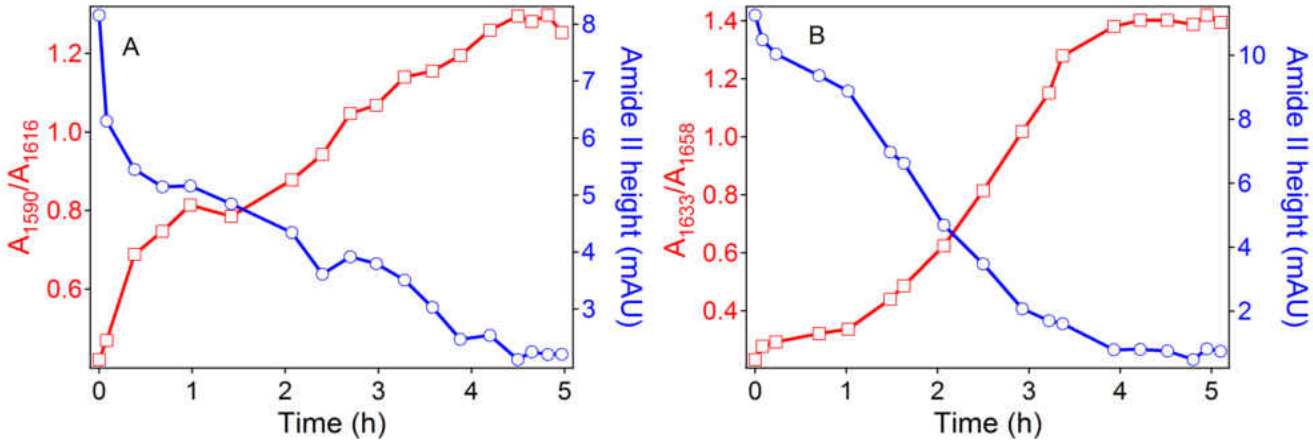

Figure 22. Dependence of β-structure formation (red) in ^{13}C-$A\beta_{1-42}$ (A) and $A\beta_{pE3-42}$ (B) and amide II intensities (blue) on time of pumping D_2O-saturated nitrogen into the sample compartment.

Combined Sample α-to-β Transition

Following measurement of the individual peptides we examined the structural effects of combination of the peptides. Two peptide ratios were used a 9:1 ($A\beta_{1-42}$:$A\beta_{pE3-42}$) ratio and an equimolar ratio, as we used in previous experiments. Two samples were prepared and examined sequentially while exposed to the same vapor environment, the first has both peptides dried together on one side of the CaF_2 FTIR window, in the other sample the two peptides are dried on opposite sides of the CaF_2 window so the signal from both peptides is present in the spectra but

peptide interaction is not occurring (See Methods). When dried at either ratio, both $A\beta_{1\text{-}42}$ and $A\beta_{pE3\text{-}42}$ form α-helix indicated by absorbance peaks at 1617-1619 and ~1658 cm^{-1} respectively (Figure 23 A,B). The α-helix location is unchanged between separated and combined samples implying a lack of ^{13}C:^{12}C coupling. Therefore, we can conclude that in the α-helical state the peptides are not interacting. Curiously in all samples the $^{13}CA\beta_{1\text{-}42}$ α-helix absorbs at a lower intensity than would be expected from peptide ratios.

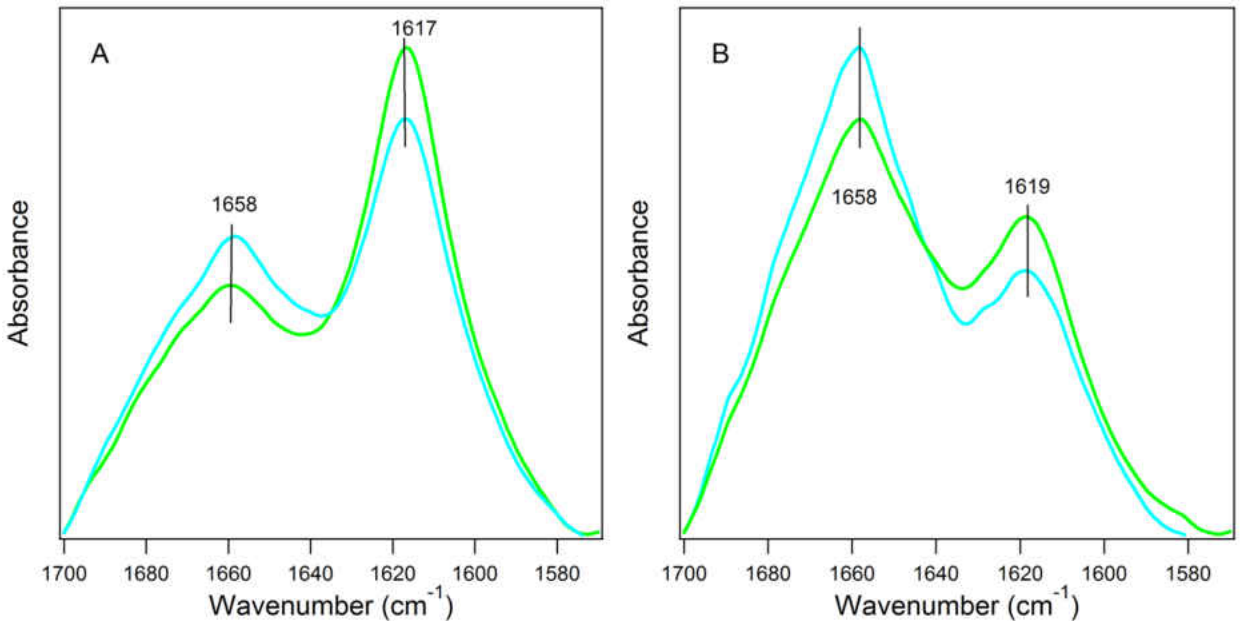

Figure 23. FTIR spectra of the dried peptides at a 9:1 (A) and 1:1 (B) ratios. The teal spectra corresponds to separated peptides while the green is the peptides in combination. Amide I areas have been normalized.

Both peptides when either separated or combined at a 9:1 ratio underwent α-to-β transition in response to D_2O vapor. After 5 hours of vapor hydration, the α-helical peaks have diminished and in their place β-sheet peaks corresponding to both peptides have formed, as well as a peak at 1673 cm^{-1} corresponding to TFA with some likely contribution from $A\beta_{pE3\text{-}42}$ β-turn (Figure 24A,B). In the separated sample the $A\beta_{pE3\text{-}42}$ β-sheet was located at 1625 cm^{-1} while in

combination it absorbed weaker and higher at 1639 cm^{-1}. These peaks could normally be assigned to inter- and intramolecular β-sheet respectively. However, the high molar ratio of $^{13}CA\beta_{1-42}$ means that this this upshift could also be caused by transition dipole coupling, thus further investigation is required. Examination of the second derivative of spectra taken after 5 hours of vapor hydration (Figure 24C,D), shows absorbance peaks at 1625 and 1639 cm^{-1} in both separate and combined samples. The presence of these peaks in both samples implies that both intra- and intermolecular β-sheets are formed in both samples but co-incubation with unmodified Aβ shifts structural propensity of AβpE from inter- to intramolecular β-sheet. In $^{13}CA\beta_{1-42}$ the β-sheet is located at 1585 and 1587 cm^{-1} in separate and combined samples respectively. These peaks indicate presence of intermolecular or cross β-sheet, the small upshift in the combined sample is likely due to ^{13}C:^{12}C coupling with unlabeled $A\beta_{pE3-42}$. The lack of a structural shift in the $^{13}CA_{\beta1-42}$ is expected, due to the high molar excess of $A\beta_{1-42}$ and the solid nature of the sample there is likely little interaction between most $A\beta_{1-42}$ peptides and $A\beta_{pE3-42}$.

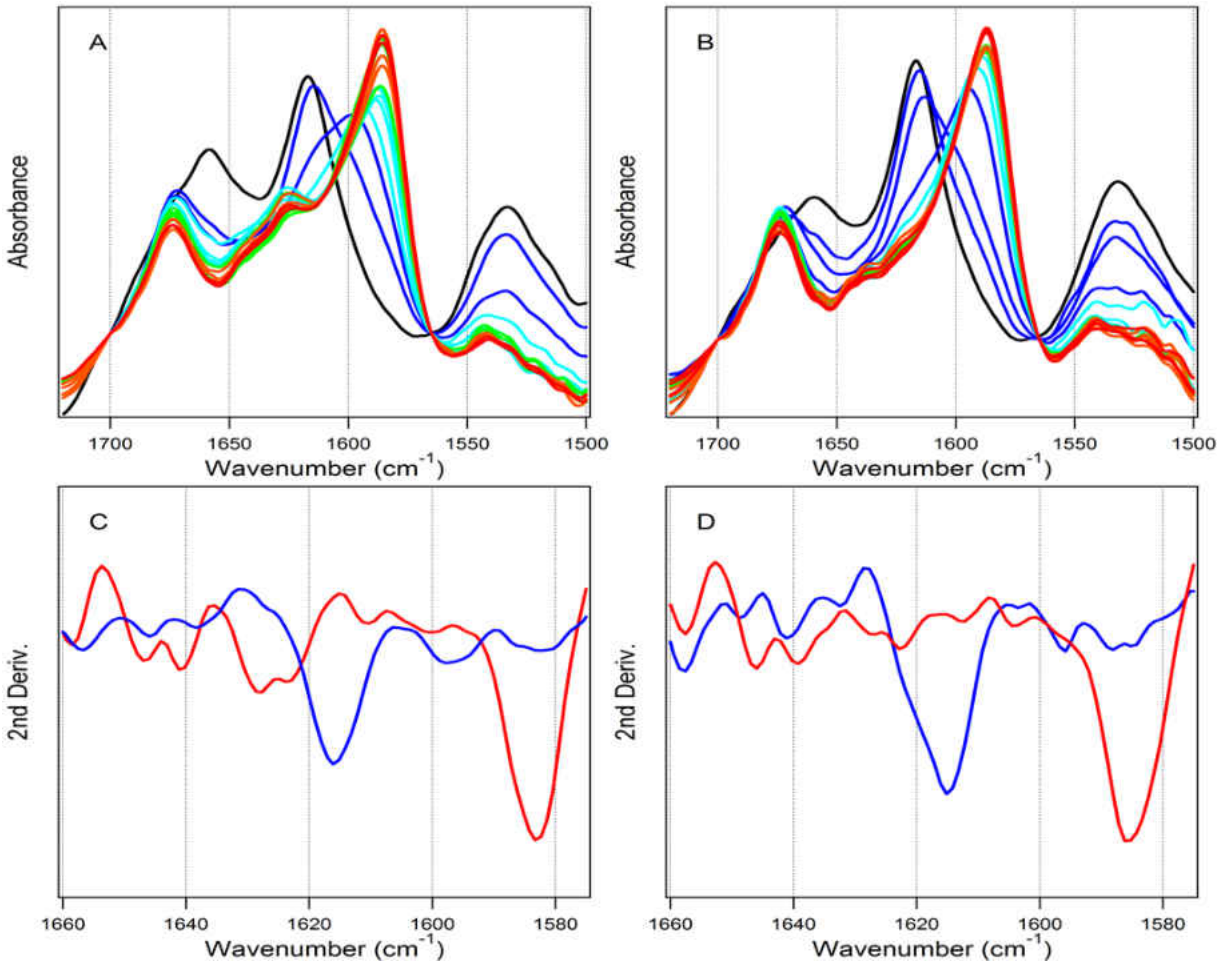

Figure 24. FTIR spectra of $A\beta_{pE3-42}$ and ^{13}C-$A\beta_{1-42}$ peptides at opposite sides of a CaF_2 window (A) or combined on the same side of a window (B) at a 9:1 mole ratio. Black lines are spectra of dry samples. Change in color from blue to red corresponds to injection of D_2O-saturated nitrogen for ~5 hours. Amide I areas have been normalized. Time intervals between consecutive spectra can be determined from data of Fig. 26. C,D) Second Derivative of FTIR spectra after 5 minutes (blue) and 5 hours (red) of hydration for both separate (C) and combined (D) peptides.

The equimolar samples also undergo α-to-β transition. Diminishing of the $A\beta_{pE3-42}$ α-helical peak throughout hydration again uncovers the peak located at 1673 cm^{-1} likely composed of both TFA from the $^{13}CA\beta_{1-42}$ and β-turn of the $A\beta_{pE3-42}$ (Figure 25A,B). Along with this peak are peaks corresponding to β-sheet of both peptides. After five hours of hydration from gas phase the β-sheet peak of $A\beta_{pE3-42}$ the major peak is located at 1628 when separate and 1638 cm^{-1} when combined.

When separate the $A\beta_{1-42}$ β-sheet peak is located at 1586 cm^{-1} while in combination it shifts to 1597 cm^{-1}. For both peptides the former can be attributed to intermolecular β-sheet while the latter can be attributed to intramolecular β-sheet. Examination of the second derivative of 5 hour spectra show peaks corresponding to intra- and inter β-sheets for both peptides (i.e. peaks at 1637, 1628, 1597, and 1586 cm^{-1}) indicating that the shifted peak comes from structural shifts and not simply ^{13}C:^{12}C coupling (Figure 25C,D). Additionally, these spectra contain peaks at 1656-1654 and 1617-1616 cm^{-1} these peaks likely represent residual α-helix of $A\beta_{pE3-42}$ and $A\beta_{1-42}$ respectively, indicating incomplete α-to-β transition. This data along with the data from the 9:1 ratio indicate that $A\beta_{pE3-42}$ forms more intra- than inter-molecular β-sheet in the presence of $A\beta_{1-42}$, while $A\beta_{1-42}$ similarly forms more intra- than inter-molecular β-sheet in the presence of $A\beta_{pE3-42}$. This relationship is demonstrated by overlaying the separated and combined samples spectra after 5 hours of D_2O hydration (Figure 26).

To quantify this shift we examined the ratio A_{intra}/A_{inter} after five hours which gives the ratio of intra to inter-β-sheet present in the sample, which will henceforth refer to as R_β. Taking $R_{\beta\ comb}/R_{\beta\ sep}$ allows quantification of the change in this ratio caused by peptide interaction (Table 5). The values for the 9:1 $^{13}CA\beta_{1-42}$ are not calculated as it did not form any significant fraction of intramolecular β-sheet. For both $A\beta_{1-42}$ and $A\beta_{pE3-42}$ $R_{\beta\ comb}/R_{\beta\ sep}$ is above 1 at both 9:1 and 1:1 ratios indicating shifts in β-sheet formation caused by peptide interaction. This is compelling evidence that the peptides act upon one another to mutually inhibit cross β-sheet formation. Curiously, the structural components are consistent with their molar ratios after hydration in both

9:1 and 1:1 samples. This means that the altered ratios observed in dry samples is caused by a lowered extinction coefficient for $^{13}CA\beta_{1\text{-}42}$ α-helical structure and not improper peptide ratios.

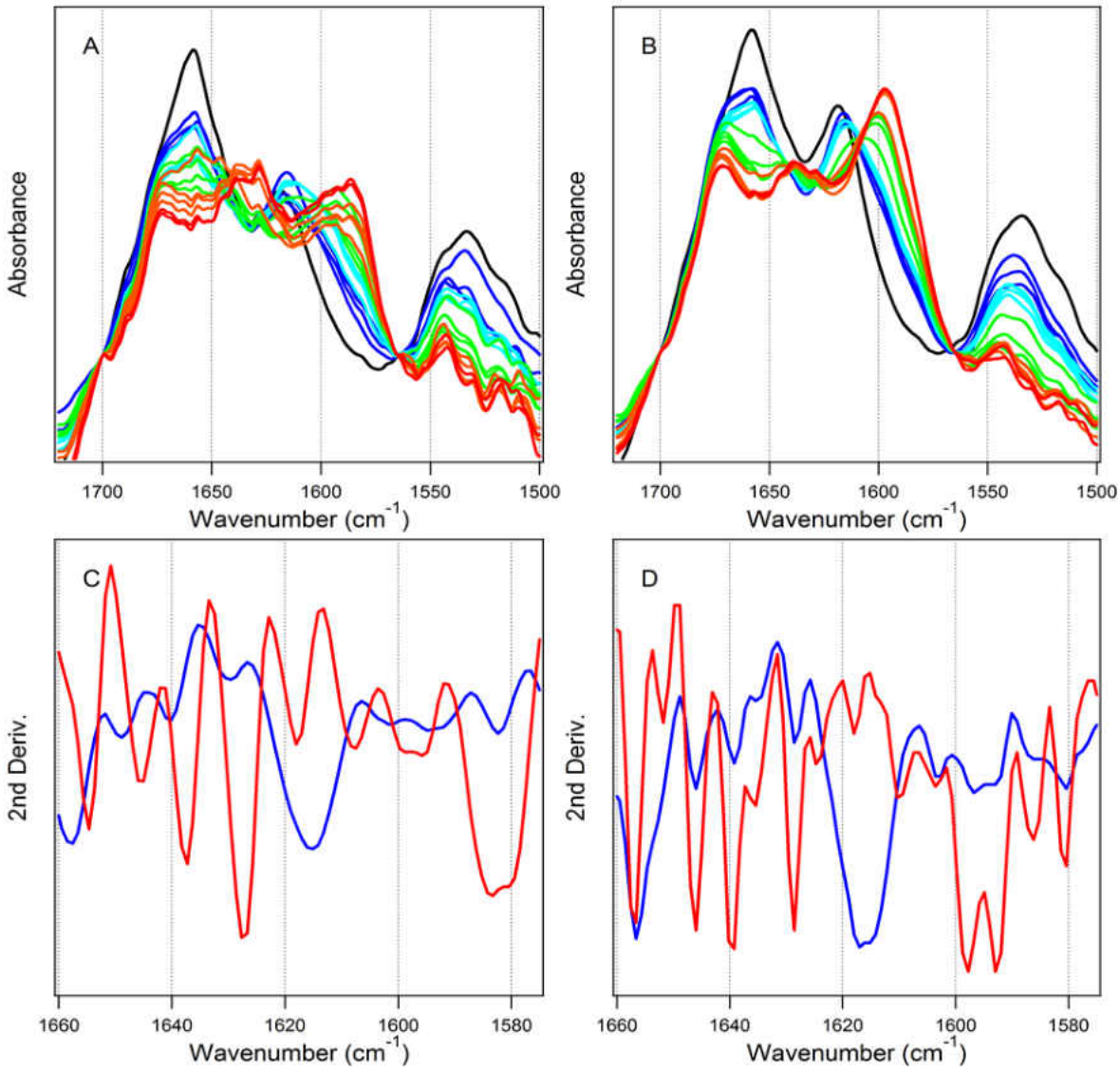

Figure 25. FTIR spectra of $A\beta_{pE3-42}$ and ^{13}C-$A\beta_{1-42}$ peptides at opposite sides of a CaF_2 window (A) or combined on the same side of a window (B) at a 1:1 mole ratio. Black lines are spectra of dry samples. Change in color from blue to red corresponds to injection of D_2O-saturated nitrogen for ~5 hours. Amide I areas have been normalized. Time intervals between consecutive spectra can be determined from data of Fig. 26. C,D) Second Derivative of FTIR spectra after 5 minutes (blue) and 5 hours (red) of hydration for both separate (C) and combined (D) peptides.

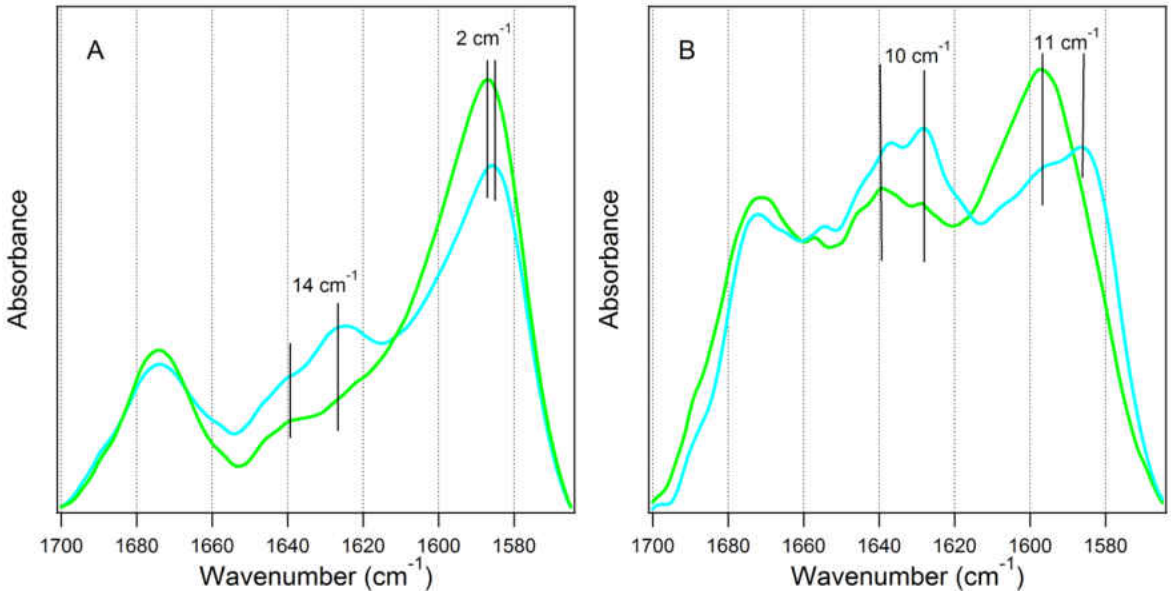

Figure 26. FTIR spectra for 9:1 (A) and 1:1 (B) molar ratios taken after 5 hours of continuous vapor hydration. The teal spectra corresponds to separated peptides while the green is the peptides in combination.

Table 4. Quantitative data describing α-helix to β-sheet transitions in $A\beta_{pE3-42}$ and ^{13}C-$A\beta_{1-42}$ peptides at opposite sides of a CaF_2 window or combined together at one side of a window at 1:9 or 1:1 molar ratios. Δν is the shift in wavenumbers from α-helix to β-sheet and ΔΔν is the difference between combined and separated samples. A_{intra} and A_{inter} correspond to the major b-sheet peaks as found experimentally and shown in the table.

	9:1 ($^{13}CA\beta_{1-42}$:$A\beta_{pE3-42}$)		1:1 ($^{13}CA\beta_{1-42}$:$A\beta_{pE3-42}$)	
	$A\beta_{pE3-42}$	$^{13}CA\beta_{1-42}$	$A\beta_{pE3-42}$	$^{13}CA\beta_{1-42}$
	α→β Transition			
Separate	1659→1625	1617→1585	1659→1628	1619→1586
Peak Shift Δν (cm^{-1})	34	32	30	33
R_{sep} (A_{intra}/A_{inter})	0.97	-	0.95	0.93
Combined	1659→1639	1617→1587	1658→1638	1619→1597
Peak Shift Δν	20	30	20	22
R_{comb} (A_{intra}/A_{inter})	1.08	-	1.05	1.41
ΔΔν	14	2	10	11
$R_{\beta\ comb}/R_{\beta\ sep}$	1.11	-	1.11	1.51

The kinetics of α→β transition was examined by taking the ratio of the absorbance intensity at the peaks associated with β-sheet in both separated and combined samples over the intensity of the α-helical peak, and tracking it against time of hydration (Figure 27). At a 9:1 ratio

there is very little shift in the β-sheet peak of the $^{13}CA\beta_{1-42}$ between the separated and combined samples as expected due to the low ratio of AβpE and solid nature of the samples. When the kinetics of β-sheet formation in both separated and combined samples is examined they closely resemble one another as well as the $A\beta_{1-42}$ individually, in that they undergo transition rapidly initially before then slowing but continuing to transition with time. The $A\beta_{pE3-42}$ initially underwent transition more slowly than the unmodified peptide, in agreement with previous observations. In both separate and combined samples the $A\beta_{pE3-42}$ forms more inter- than intra-molecular β-sheet. However, the difference between the two narrows in combined samples indicating a shift from inter- to intra-β-sheet formation (Black and white circles Figure 27 A,B). In the 1:1 samples the kinetics are similar with $A\beta_{1-42}$ transitioning rapidly at first and then slowing while $A\beta_{pE3-42}$ transition appeared to speed up with time (Figure 27 C,D). Examination of β-sheet formation in combination yields strong evidence that the peptides mutually inhibit intermolecular β-sheet formation in favor of intramolecular β-sheet formation. For both peptides, when separated intermolecular β-sheet formation is favored while the opposite is true in combined samples (White circles and squares are increased compared to colored in separate samples while the opposite is true in combination). Interestingly the effect of $A\beta_{pE3-42}$ on $A\beta_{1-42}$ appeared to be most pronounced after 3 hours, with the rate of intramolecular β-sheet formation increasing greatly compared to the formation of intermolecular β-sheet.

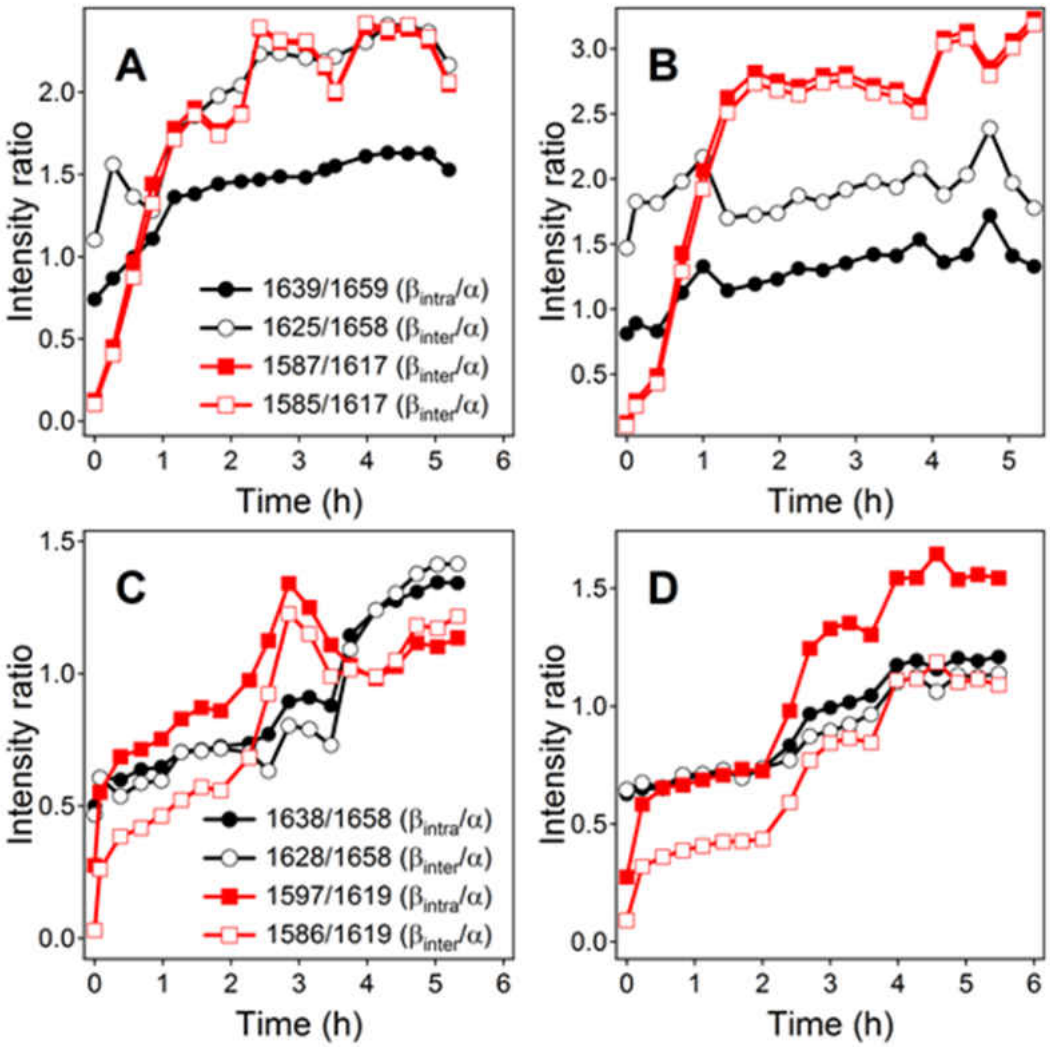

Figure 27. Changes in β-sheet/α-helix amide I intensity ratios with time of pumping D_2O-saturated nitrogen. A, B: $A\beta_{pE3-42}/^{13}C\text{-}A\beta_{1-42}$ = 1:9; C,D: $A\beta_{pE3-42}/^{13}C\text{-}A\beta_{1-42}$ = 1:1. A, C: peptides are physically separated, i.e. are at opposite sides of a CaF_2 window, B, D: peptides are combined at one side of a CaF_2 window. Symbols in A are identical to B, and symbols in C is identical to D. Black graphs describe transitions in $A\beta_{pE3-42}$, red graphs describe transitions in $^{13}C\text{-}A\beta_{1-42}$. $A\beta_{pE3-42}$ and $^{13}C\text{-}A\beta_{1-42}$

This data indicates that $A\beta_{pE3-42}$ and $A\beta_{1-42}$ mutually inhibit intermolecular β-sheet formation of one another, instead promoting formation of intramolecular β-sheet. This data agrees with previous observations of the $A\beta_{pE3-42}$ ability to inhibit cross β-sheet formation of the $A\beta_{1-42}$

(Figures 7,9). Kinetic data shows a decelerated rate of intermolecular β-sheet formation in mixed samples supporting this conjecture (Figure 27). Conceivably, this could be caused by intervention of non-identical peptide molecules into structures formed by the other peptide shifting the H-bonding from intermolecular to intramolecular. Peptides forming intermolecular β-sheets eventually go on to form mature fibrils while these intramolecular β-sheets likely resemble the β-hairpins we described earlier (Figure 16). The presence of residual α-helix agrees with earlier findings and supports this conclusion. It can therefore be concluded that $A\beta_{1\text{-}42}$ and $A\beta_{pE3\text{-}42}$ mutually inhibit formation of intermolecular β-sheet, instead promoting off-pathway formation of mixed α/β hairpins (Figure 28). This conclusion agrees with previous observations of delayed fibrillogenesis of mixed samples (Figure 5).

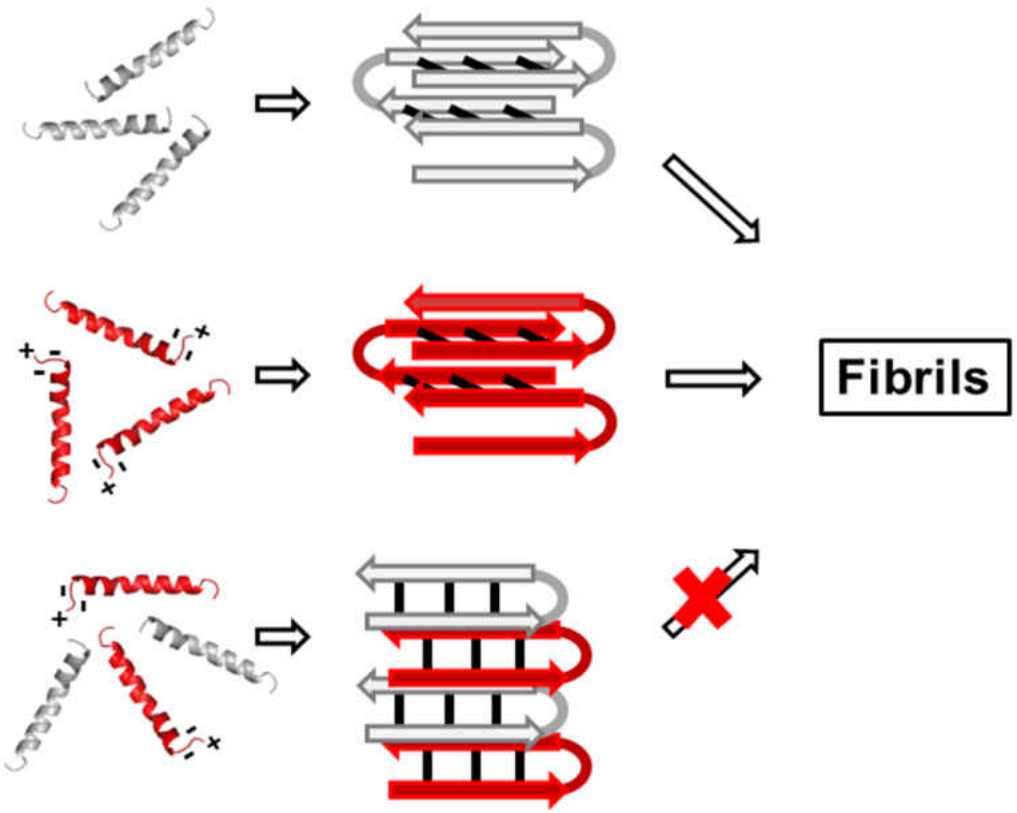

Figure 28. Scheme for aggregation of $A\beta_{pE3-42}$ (gray), $A\beta_{1-42}$ (red), and their combination, accompanied with an α-helix to β-sheet transition. At the N-terminus of $A\beta_{1-42}$ there are 3 additional charges, a positive charge of the N-terminal α-amino group and 2 negative charges of the side chains of Asp1 and Glu3. Helices are shown as spirals, β-strands as arrows, and H-bonds as black bars.

MTS Viability Assay

We next wished to examine the effect of these Aβ hetero-oligomers on Aβ aggregates through collaboration with Dr. Kenneth Teter and Dr. Lucia Cilenti. In this data the most toxic species is the equimolar combination of $A\beta_{pE3-42}$ and $A\beta_{1-42}$ at two hours of aggregation (Figure 29). This is the time period where the greatest population of hetero-oligomer is thought to exist. This data demonstrates the enhanced cytotoxic properties of these hetero-oligomers.

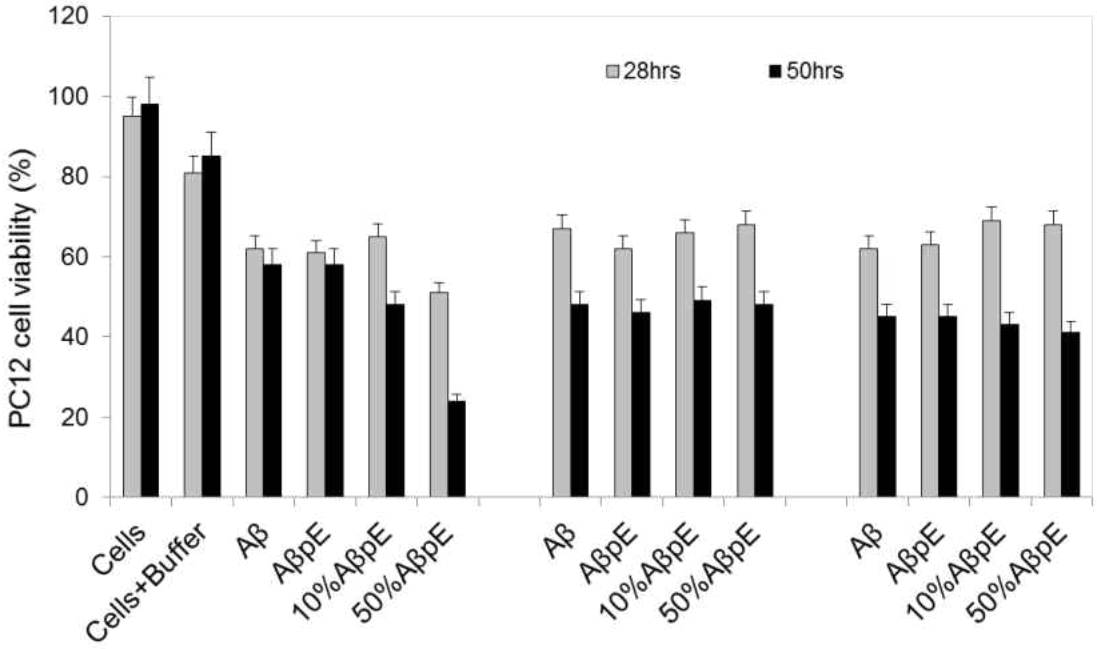

Figure 29. Change in cellular viability caused by Aβ aggregates as demonstrated by MTS assay. Studies were conducted in triplicate and normalized so that the control is equivalent to 100% viability. Aβ peptides were added to peptides at a final concentration of 10 μM for 28 or 50 hours. Ab peptides that had been aggregating in PBS at 37°C for 2 hours (First group) 4 hours (second group) and 24 hours (final group)

Aβ Mediated Membrane Calcium Leakage

The formation by Aβ of calcium permeable membrane pores is a hypothesized mechanism of Aβ mediated cytotoxicity in AD. To examine the effect of these oligomers, Aβ aggregates were added to a solution containing calcium bound in unilamellar lipid vesicles composed of 60% POPC 30% POPG and 10% cholesterol after 2 and 24 hours of aggregation. The release of calcium from vesicles was demonstrated via increase in fluorescence of Quin-2. Maximum fluorescence is demonstrated by popping all of the vesicles with triton-X. The results of this are striking, at two hours of aggregation $A\beta_{1-42}$ does not induce any greater calcium release than buffer control.

However, $A\beta_{pE3-42}$ as well as 9:1 and 1:1 combinations induce significant release of calcium (Figure 30A). At 24 hours of aggregation the combinations had a lesser effect than at two hours, consistent with pore formation by oligomers but not mature fibrils (Figure 30B). Curiously, the $A\beta_{pE3-42}$ actually had a greater effect on calcium release at 24 hours than 2 hours. Additionally, at 24 hours the 9:1 had a greater effect than the 1:1.

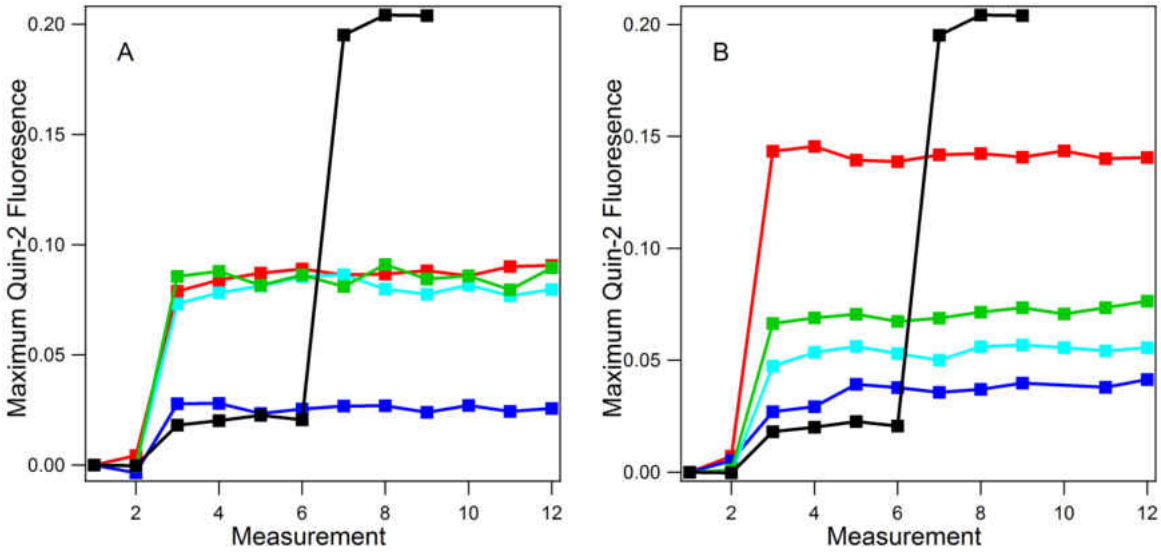

Figure 30. Vesicular calcium release as assayed by Quin-2. Aβ peptides were added to vesicles after 2 hours (A) and 24 hours (B) of aggregation via stirring at 37 °C. Data for release via $A\beta_{1-42}$ (blue), $A\beta_{pE3-42}$ (red), 9:1 (green) 1:1 (teal) and buffer control (black) are shown. Peptides were added following two measurements to establish a baseline, 0.5% Triton X-100 was added to the control after 6 measurements to disrupt vesicles and measure maximum fluorescence.

This data demonstrates that these hetero-oligomers do in-fact induce a significant drop in cellular viability compared to individual peptides. These hetero-oligomers also induced greater release of intra-vesicular calcium. The far greater effect of $A\beta_{pE3-42}$ at 24 hours as well as the greater effect of 9:1 than 1:1at 24 hours, is not consistent with toxicity data. To confirm these results follow up studies are being conducted. If confirmed, this data implies that formation of

calcium pores in lipid membranes may not be the primary Aβ-mediated pathway of cellular dysfunction in AD.

CHAPTER FIVE: CONCLUSIONS

Recent evidence has shifted focus from fibrillar to soluble oligomeric species of Aβ as the primary cytotoxic species in AD. Due to the difficulty of their study, namely their structural heterogeneity, dynamics, and polymorphic nature, little is known about the structure and formation of Aβ oligomers. Pyroglutamylated Aβ are major species of Aβ in the AD brain displaying increased toxicity. Studies have demonstrated the ability of $A\beta_{pE3-42}$ to increase the toxicity of unmodified Aβ in low molar ratio through structural changes however, little is known about the mechanism.

This project sought to investigate Aβ oligomer structure. In particular we aimed to examine the structural effect of AβpE on unmodified Aβ. Current evidence implicates these oligomers as the cytotoxic Aβ agent in AD (38, 46). Pyroglutamylated Aβ species make up a significant fraction of the soluble Aβ in AD brains. $A\beta_{pE3-42}$ has been demonstrated to cause significant changes to oligomers of $A\beta_{1-42}$ and $A\beta_{pE3-42}$, altering both their structure and toxicity, even when it is present in low molar ratio (44). We first sought to examine the effects of $A\beta_{pE3-42}$ on the structure and fibrillization kinetics of $A\beta_{1-42}$. Data collected via CD indicate that $A\beta_{pE3-42}$ delays β-sheet formation of the unmodified peptide in mixed samples. TEM images of the unmodified Aβ collected after two hours of aggregation contain mature fibrils while samples of AβpE and mixed samples contained greater numbers of globular aggregates. FTIR data indicates that AβpE inhibits cross β-sheet formation of the unmodified peptide, thus retarding fibrillogenesis. Inhibiting fibril

formation may increase the population of Aβ oligomers or promote formation of off-pathway aggregates of enhanced toxicity.

We next sought to characterize the early oligomers of AβpE and unmodified Aβ as well as the structural changes upon co-incubation. To further investigate the structure of Aβ oligomers we utilized peptides selectively ^{13}C-labeled at two specific segments $K^{16}L^{17}V^{18}$ and $V^{36}G^{37}G^{38}V^{39}$. These allow site specific determination of protein secondary structure. Data was collected of $A\beta_{1-42}$, $A\beta_{pE3-42}$, and, their equimolar combination labeled at two locations and in two buffers of different ionic content. This data indicates that early oligomers are composed of α-helix, intramolecular β-sheet, and β-turn structure, and that the labeled segments were forming β−sheets. Changes in α-helical content in different buffer conditions indicate that the a-helix is located at the N-terminus. Additionally, the carbon coupling of labeled residues indicates a lack of ^{13}C:^{13}C coupling giving both tertiary and quaternary structural insight. These data allow us to propose a possible structure for the monomeric Aβ namely a β-hairpin with an N-terminal α-helix and a β-turn occurring downstream of $K^{16}L^{17}V^{18}$. Data indicates that oligomerization likely occurs through non H-bonding interactions between neighboring β-hairpin strands.

After structural characterization of early peptides we sought greater detail on the early dynamics of oligomerization. In the plasma membrane as well as HFIP Aβ peptides are α-helical. In buffer they quickly form β-sheets and begin to aggregate. We have already observed that $A\beta_{pE3-42}$ inhibits this β-sheet formation of the $A\beta_{1-42}$ in aqueous buffer. To observe these changes we gradually hydrated the peptides using D_2O vapor. Upon exposure to vapor both peptides undergo

α-to-β transition but with different kinetics. $A\beta_{1-42}$ transitions rapidly in the first hour and continued to transition slowly afterwards, while $A\beta_{pE3-42}$ transitioned in a sigmoidal manner. When combined the peptides exerted a mutual effect upon one another to intermolecular β-sheet formation instead forming intramolecular β-sheets. Data from vesicle calcium release studies and MTS assays indicate that in combination the peptides have a more pronounced effect on cellular viability than the peptides individually and induce greater release of calcium than the unmodified peptide alone. Thus hybrid AβpE and unmodified samples exhibit enhanced cytotoxicity possibly due to increased formation of off pathway mixed α/β oligomers instead of the intermolecular β-sheet structures that make up mature fibrils. These hetero-oligomers induce greater calcium release from lipid membranes and exert a greater effect on cellular viability than the unmodified Aβ.

Previous studies on Aβ oligomers have found an antiparallel orientation while studies on mature fibrils show a parallel in-register orientation. In FTIR spectra antiparallel β-sheet is indicated by a major peak 1636-1630 cm^{-1} and a minor peak 1680-1670 cm^{-1}. Although several spectra appear to contain a peak corresponding to antiparallel β-sheet (Figures 6, 16A,B), the low intensity of this peak makes it impossible to differentiate from other structural components. In $A\beta_{pE3-42}$ this peak is located in a similar location to β-turn and TFA while in $^{13}CA\beta_{1-42}$ this peak (~1643-1633 cm^{-1}) corresponds with $A\beta_{pE3-42}$ β-sheet absorbance. Therefore, it is not possible to determine whether these oligomers are in a parallel or antiparallel orientation. Curve fitting of spectra indicate that α-helical and β-sheet fractions of peptides vary to a degree (Tables 3,4). This

indicates low barrier energy between these structures; and represents a possible source of Aβ polymorphism.

Significance

It is believed that the toxic Aβ species in AD is formed during the transition from the α-helical structure formed prior to lipid membrane exit to the intermolecular β-sheet structure found in mature fibrils. Here we characterized this transition as well as proposing a data-based model of early Aβ monomers as well as aggregation. Data indicate that $A\beta_{1\text{-}42}$ and $A\beta_{pE3\text{-}42}$ mutually inhibit cross-β-sheet formation of one another instead forming mixed α/β hairpins. Inhibition of cross β-sheet formation delayed fibrillogenesis and lead to an increase in the population of globular aggregates. Studies have found oligomers of mixed α/β content to display enhanced cytotoxicity (114-116). These hetero-oligomers had a greater effect on the viability of PC12 cells than either peptide alone indicating their potent effect. Additionally, vesicle calcium release assays demonstrate that this effect may in part be due to enhanced formation of calcium permeable pores in lipid membranes. This work highlights the importance of hetero-oligomers in the pathogenesis of AD. This data gives insight into oligomer structure and formation as discussed in figure 1 (Figure 31).

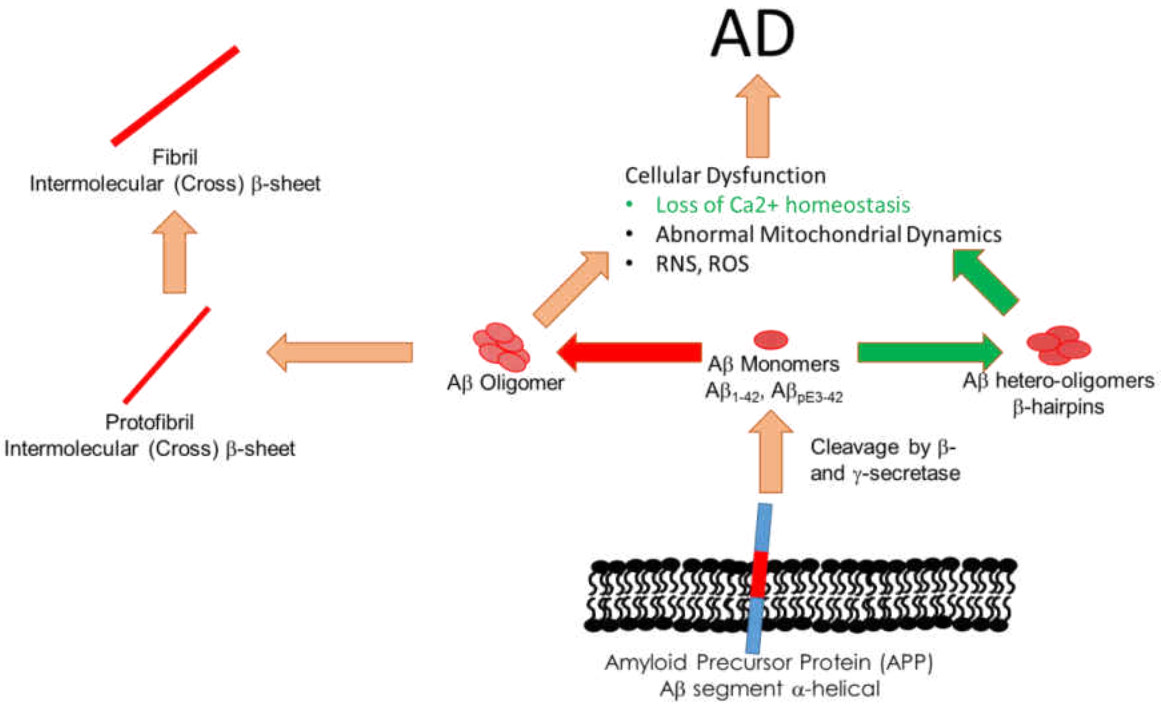

Figure 31. Update of Figure 1 using data collected during this work. Mixed populations of Ab1-42 and AbpE3-42 promote formation of hetero-oligomers via a non-fibrillogenic pathway. These oligomers display increased cytotoxicity to PC12 cells possibly through the formation of calcium permeable membrane pores leading to loss of Ca^{2+} homeostasis.

Future Studies

Targets for future study include $A\beta_{1\text{-}40}$ and its pyroglutamylated counterpart the $A\beta_{pE3\text{-}40}$. In vivo Aβ populations are heterogeneous but little is known about the behavior of mixed peptide populations. These species are prevalent in the AD brain and examination should be conducted on whether they have similar structural effects upon one another. If they possess the same mutual inhibitory relationship, it is strong evidence that this effect may occur with other pyroglutamylated

Aβ species. We also seek a method to stabilize oligomers for the time scales necessary for ssNMR analysis. Of particular interest is stabilization of oligomers formed in physiologically relevant conditions without using methods that may induce structural changes. High resolution structural data from ssNMR would represent strong supporting evidence for the β-hairpin model proposed here. Follow-up studies should also be conducted to investigate inconsistencies between vesicular calcium release and cellular viability studies.

APPENDIX A: PEAK FITTING OF DRY SPECTRA

Peak fitting of Dry FTIR spectra. The original spectra (blue), peak fit (dotted red), and baseline (black) are shown. Fit peaks corresponding to alpha helix (orange) and the labeled segment (pink) are also shown. Peaks shown in grey are considered other in area concentration and correspond primarily to unordered structure. Peaks corresponding to side chain interactions are dotted grey and are not included in area calculations.

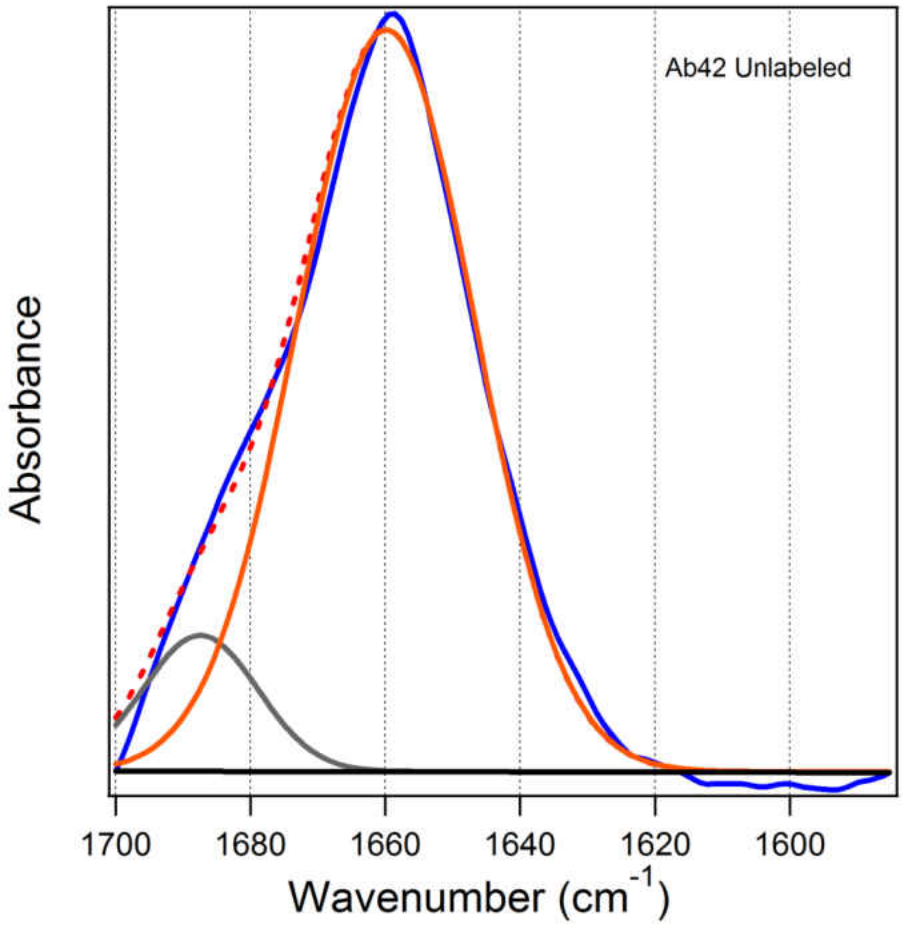

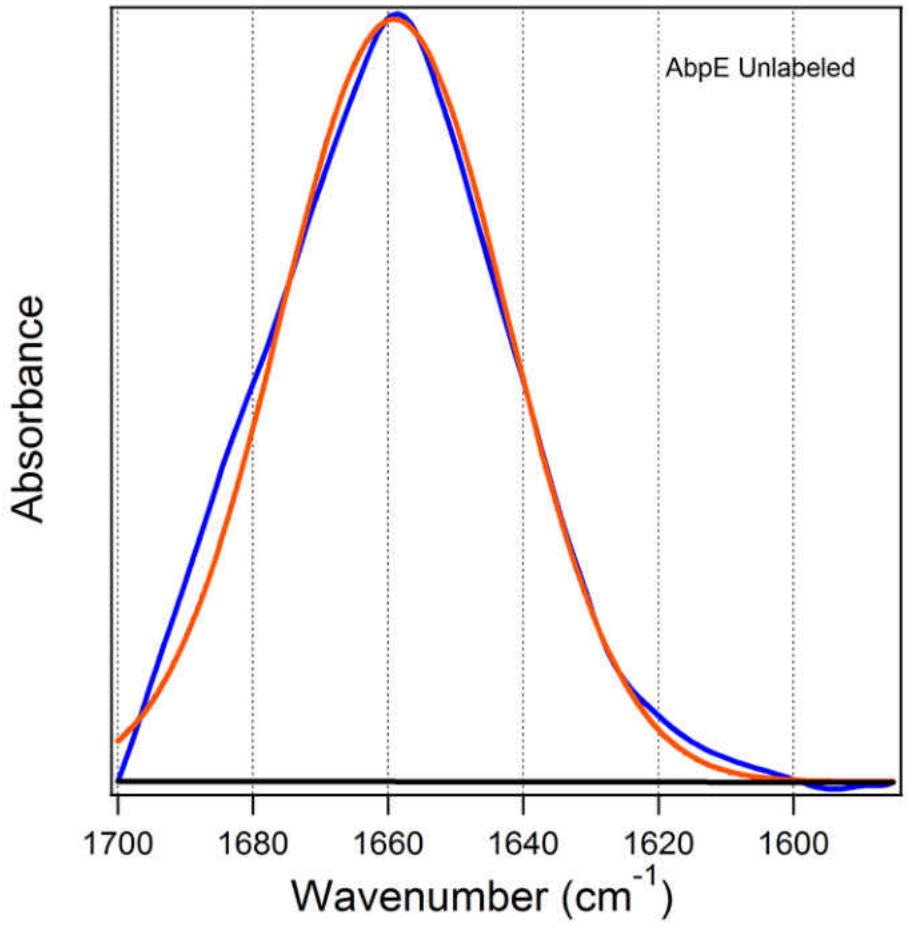
AbpE Unlabeled
Absorbance
1700
1680
1660
1640
1620
1600
Wavenumber (cm-1)

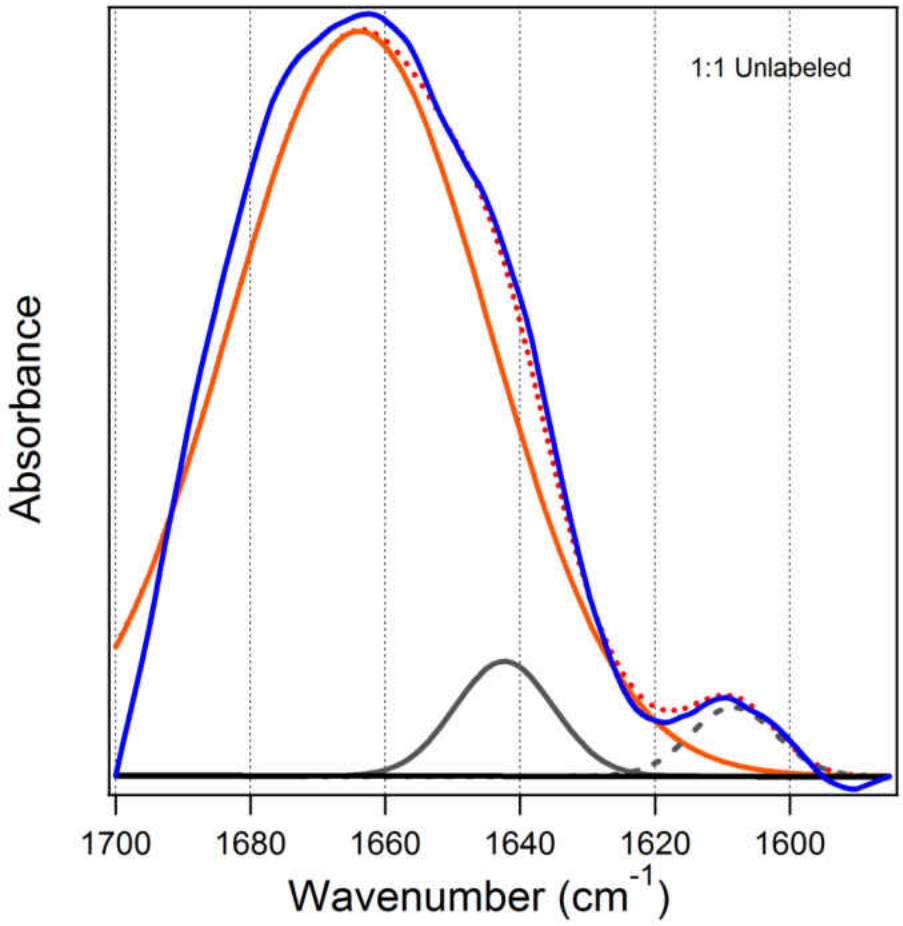
1:1 Unlabeled
Absorbance
1700
1680
1660
1640
1620
1600
Wavenumber (cm-1)

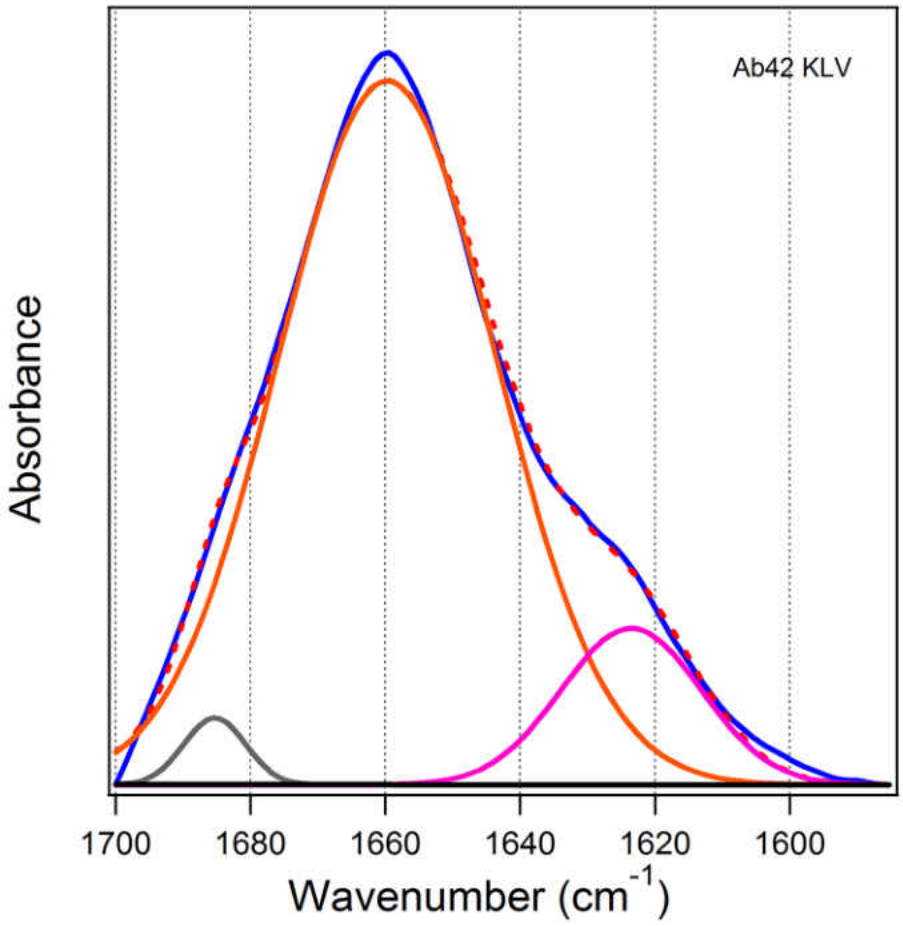
Ab42 KLV
Absorbance
1700
1680
1660
1640
1620
1600
Wavenumber (cm-1)

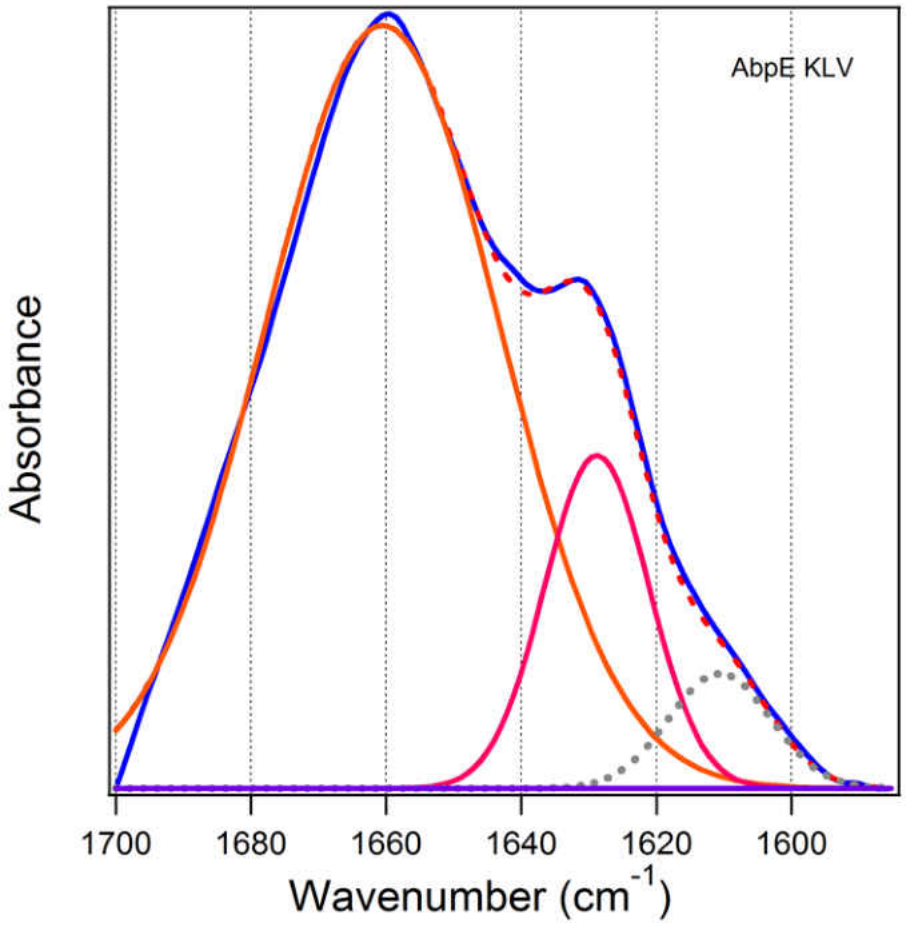
AbpE KLV
Absorbance
1700
1680
1660
1640
1620
1600
Wavenumber (cm-1)

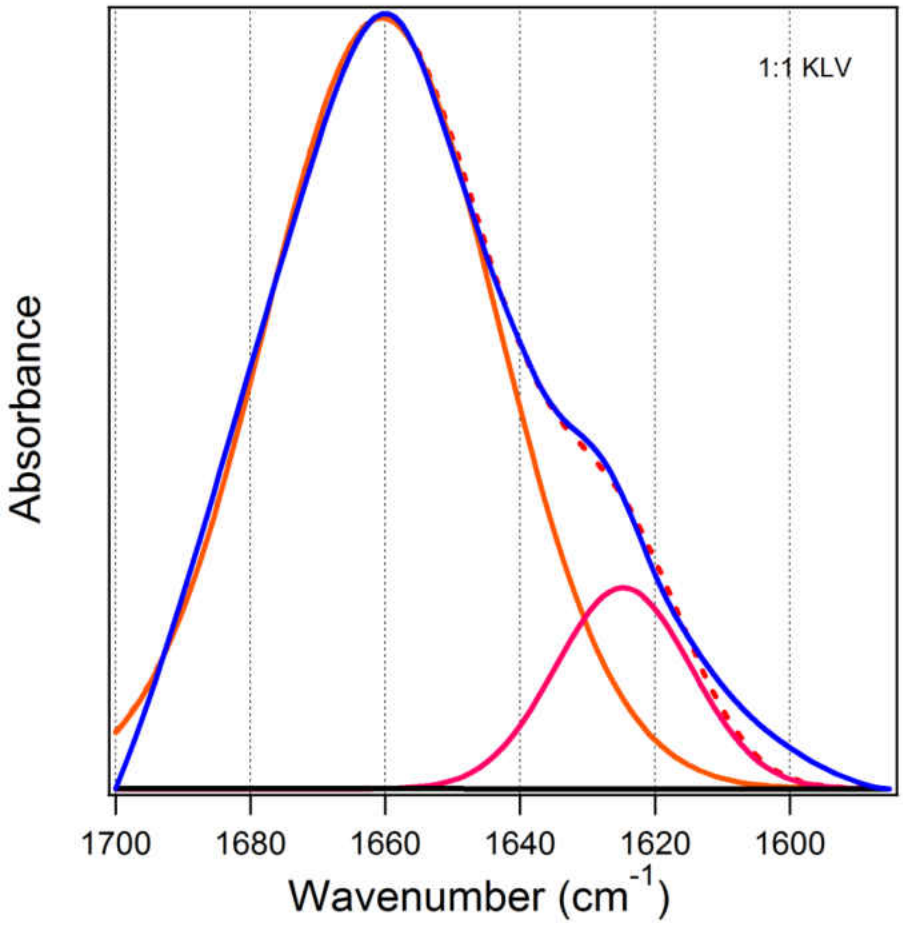
1:1 KLV
Absorbance
1700
1680
1660
1640
1620
1600
Wavenumber (cm-1)

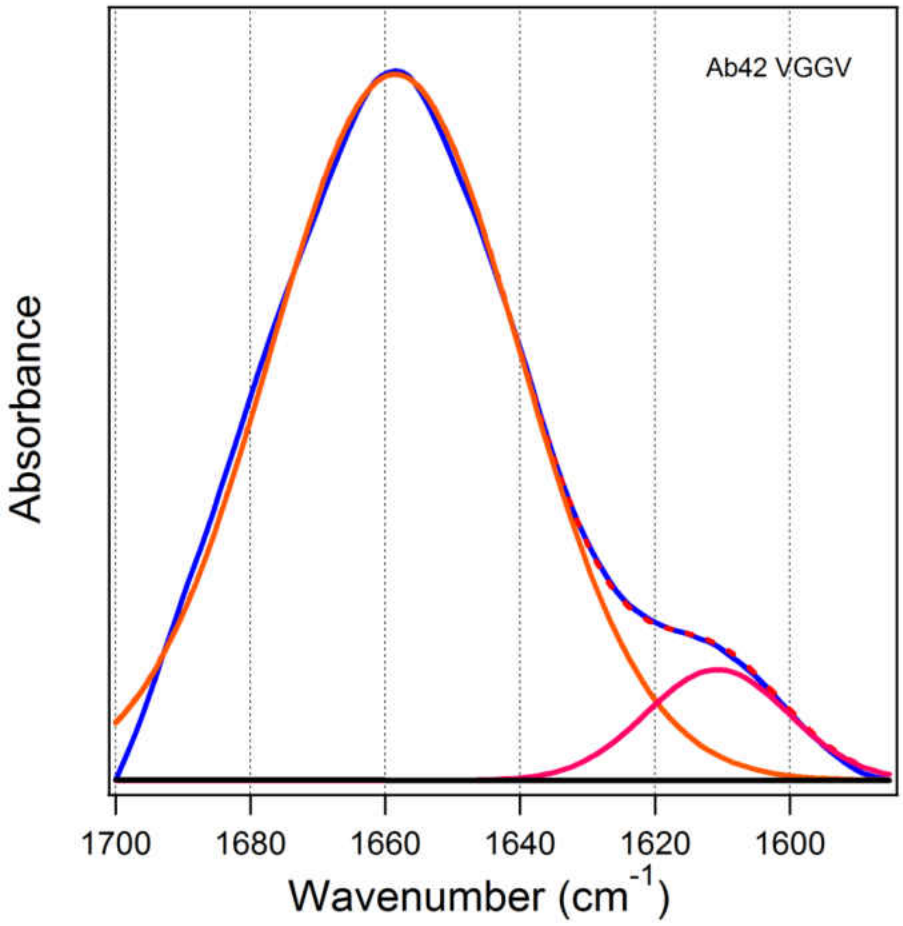
Ab42 VGGV
Absorbance
1700
1680
1660
1640
1620
1600
Wavenumber (cm-1)

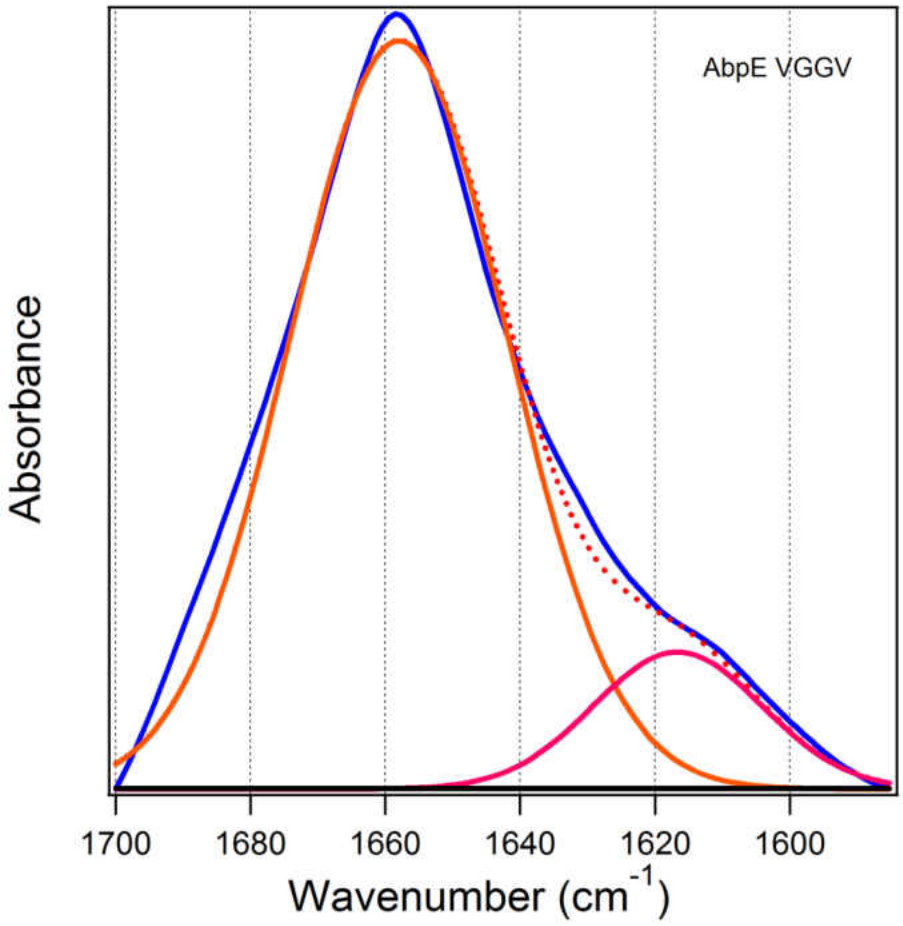
AbpE VGGV
Absorbance
1700
1680
1660
1640
1620
1600
Wavenumber (cm-1)

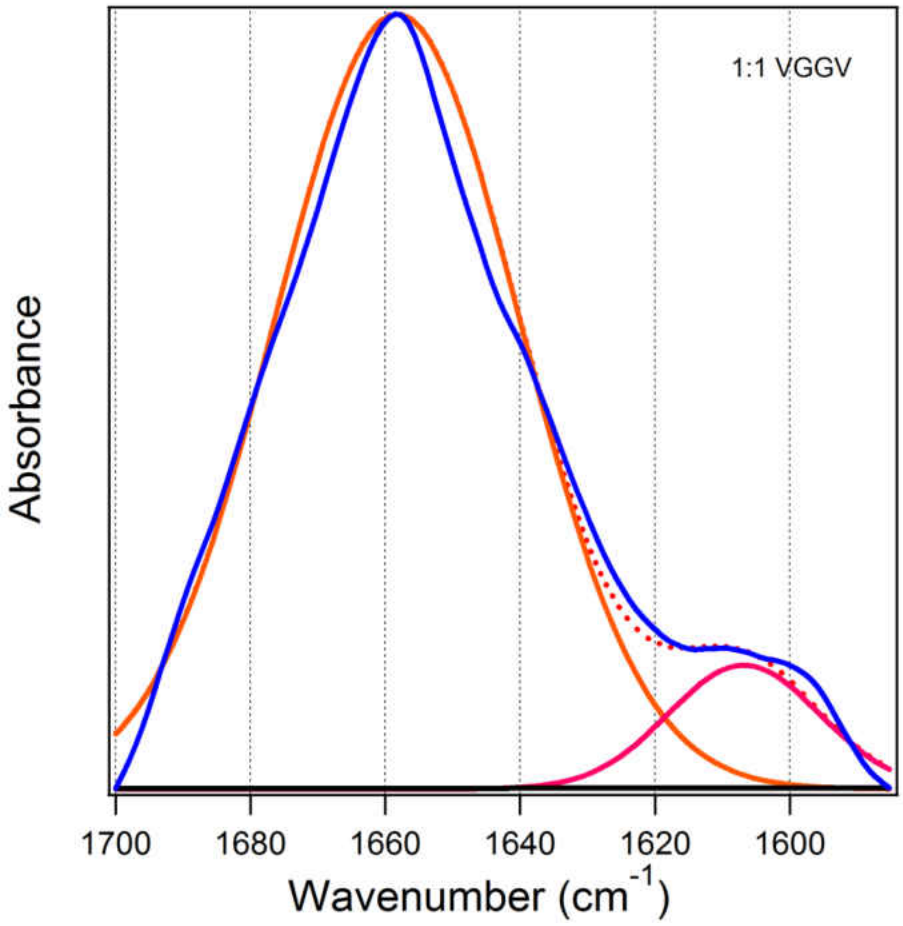
1:1 VGGV
Absorbance
1700
1680
1660
1640
1620
1600
Wavenumber (cm-1)

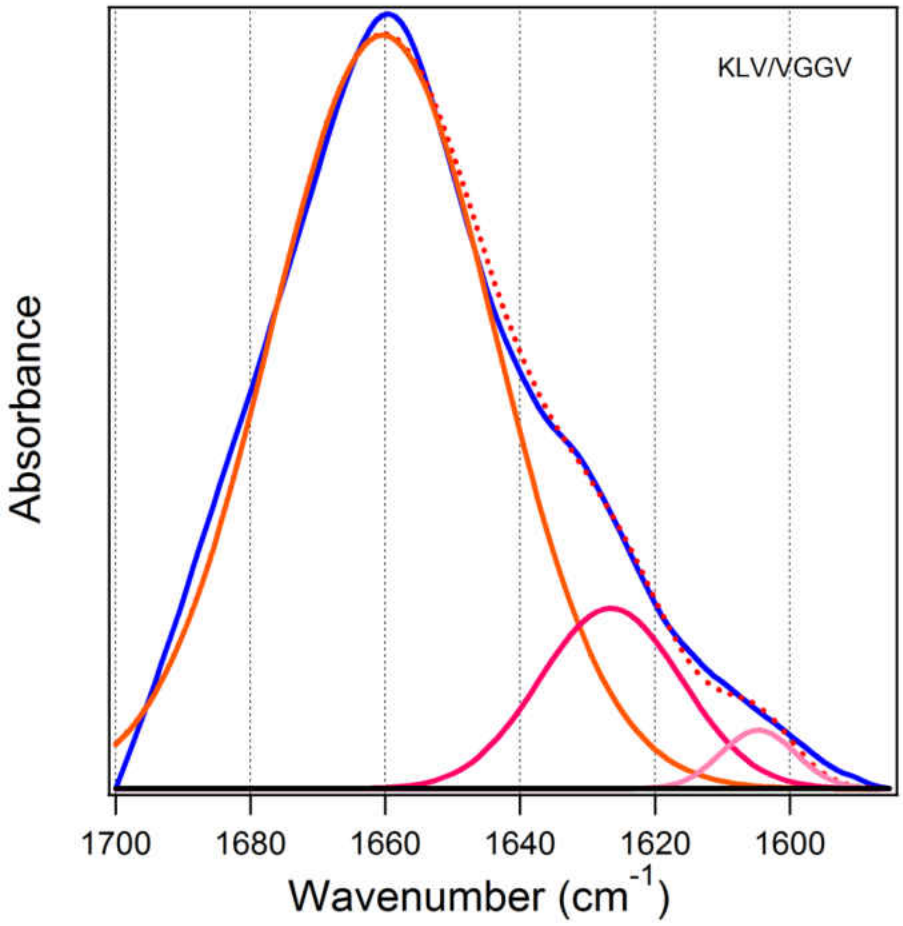
KLV/VGGV
Absorbance
1700
1680
1660
1640
1620
1600
Wavenumber (cm-1)

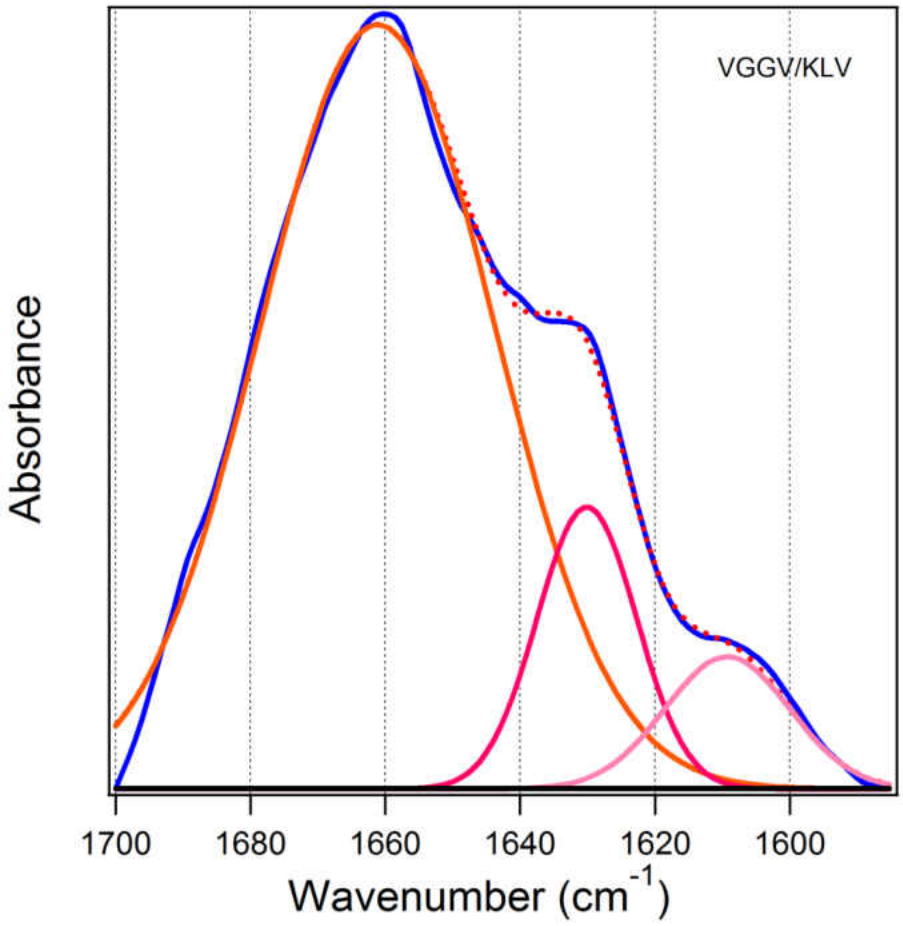
VGGV/KLV
Absorbance
1700
1680
1660
1640
1620
1600
Wavenumber (cm-1)

APPENDIX B: PEAK FITTING UNLABELED PEPTIDES

. Peak Fit Spectra of $A\beta_{1-42}$ $A\beta_{pE3-42}$ and their equimolar combination in 10 mM phosphate pD 6.8 buffer labeled here as low salt as well as 50 mM phsosphate 50 mM NaCl pD 6.8 labeled here as high salt for 10, 60, and 120 minutes. The experimental measurement is shown in Blue while the Red dotted line is the sum of all components, fit peaks correspond to turn (green), α-helix (orange), and β-sheet (purple) unattributed peaks are shown in grey and are primarily composed of unordered structure. Peaks corresponding to side chain interactions are shown in dotted grey and are not included in area calculations. The second derivative of the experimental spectra is shown in black underneath. Total peptide concentration is 50 μM.

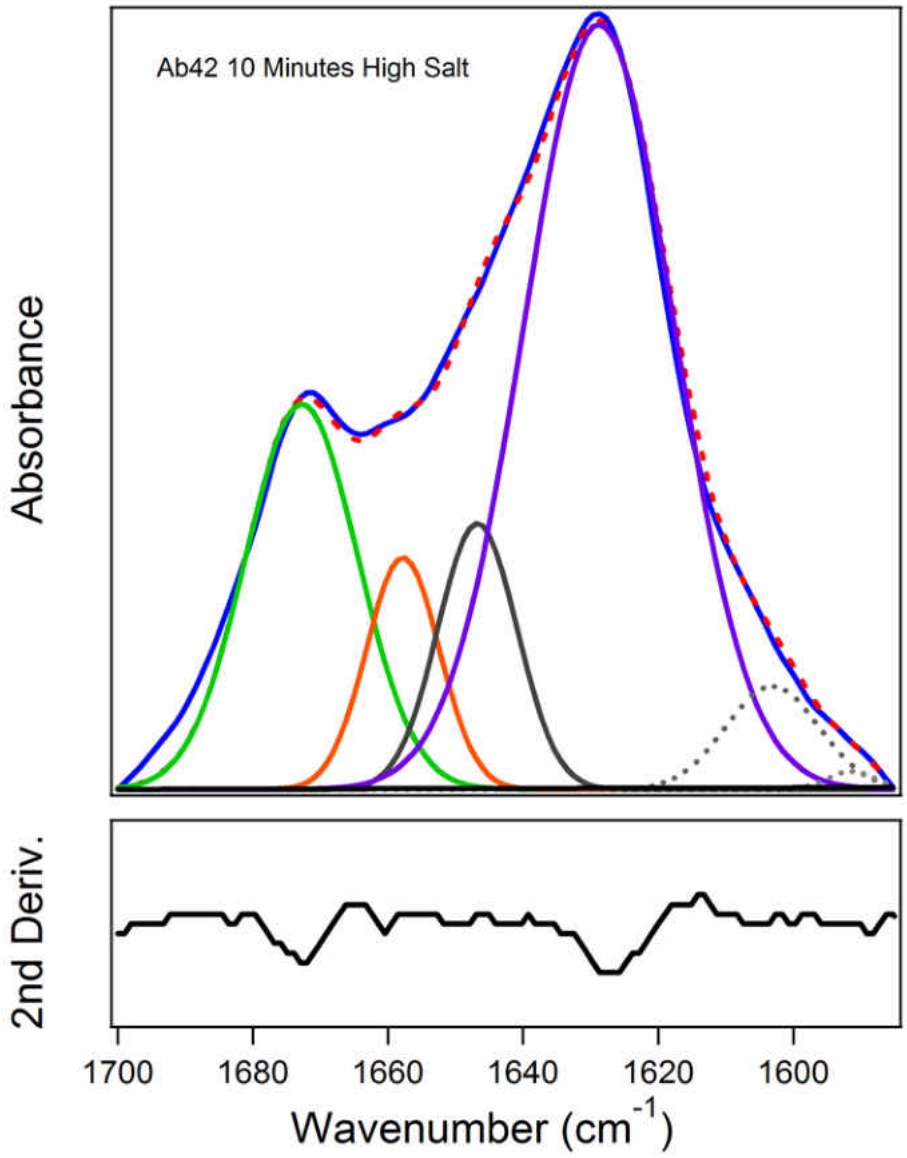
Ab42 10 Minutes High Salt
Absorbance
2nd Deriv.
1700
1680
1660
1640
1620
1600
Wavenumber (cm-1)

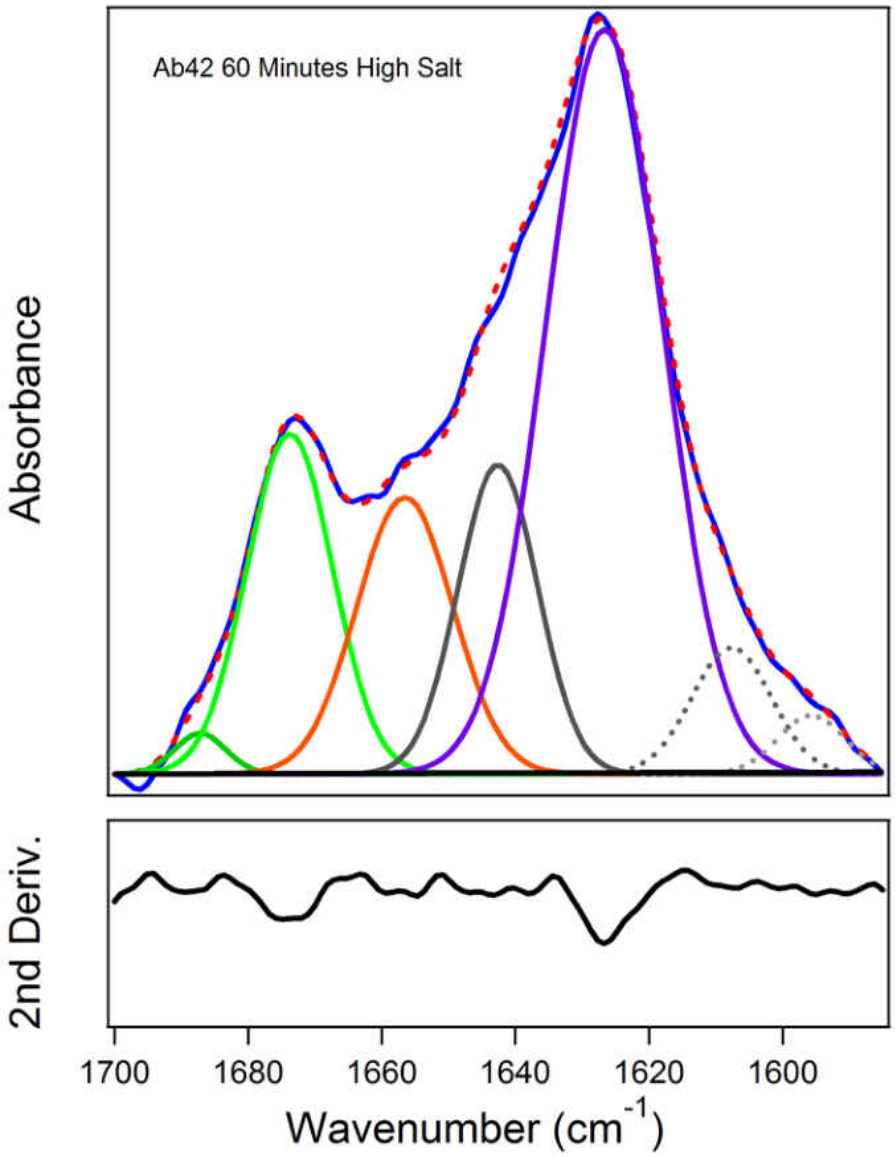
Ab42 60 Minutes High Salt
Absorbance
2nd Deriv.
1700
1680
1660
1640
1620
1600
Wavenumber (cm-1)

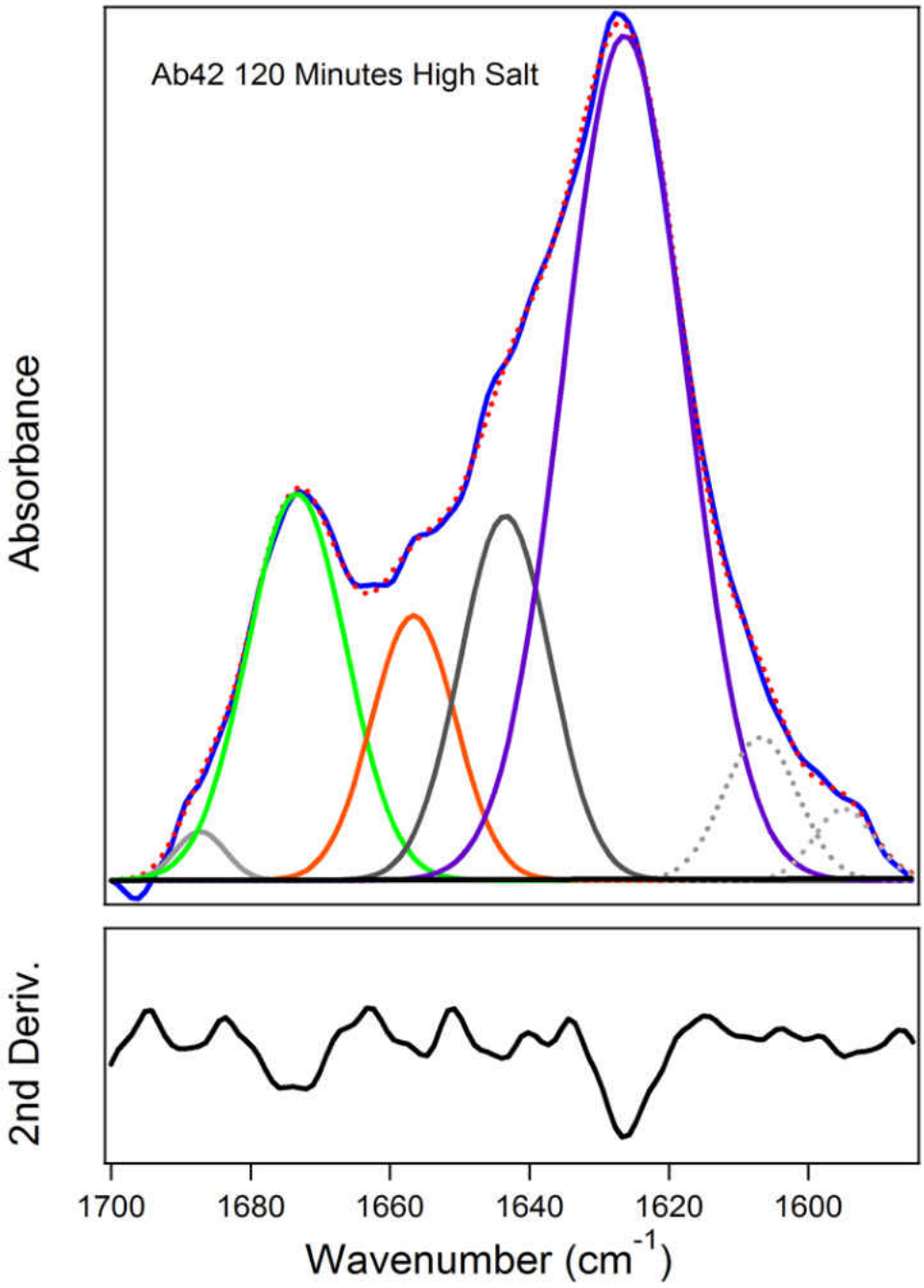
Ab42 120 Minutes High Salt
Absorbance
2nd Deriv.
1700
1680
1660
1640
1620
1600
Wavenumber (cm-1)

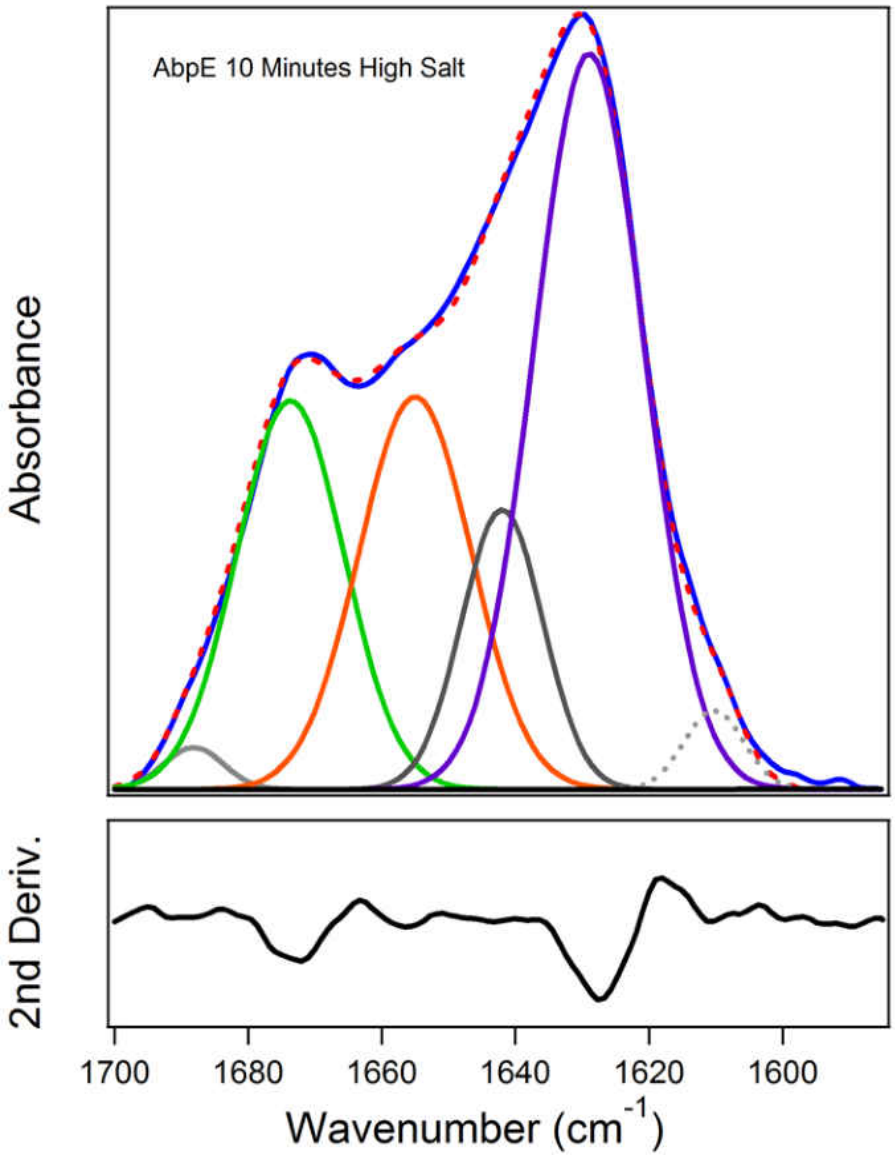
AbpE 10 Minutes High Salt
Absorbance
2nd Deriv.
1700
1680
1660
1640
1620
1600
Wavenumber (cm-1)

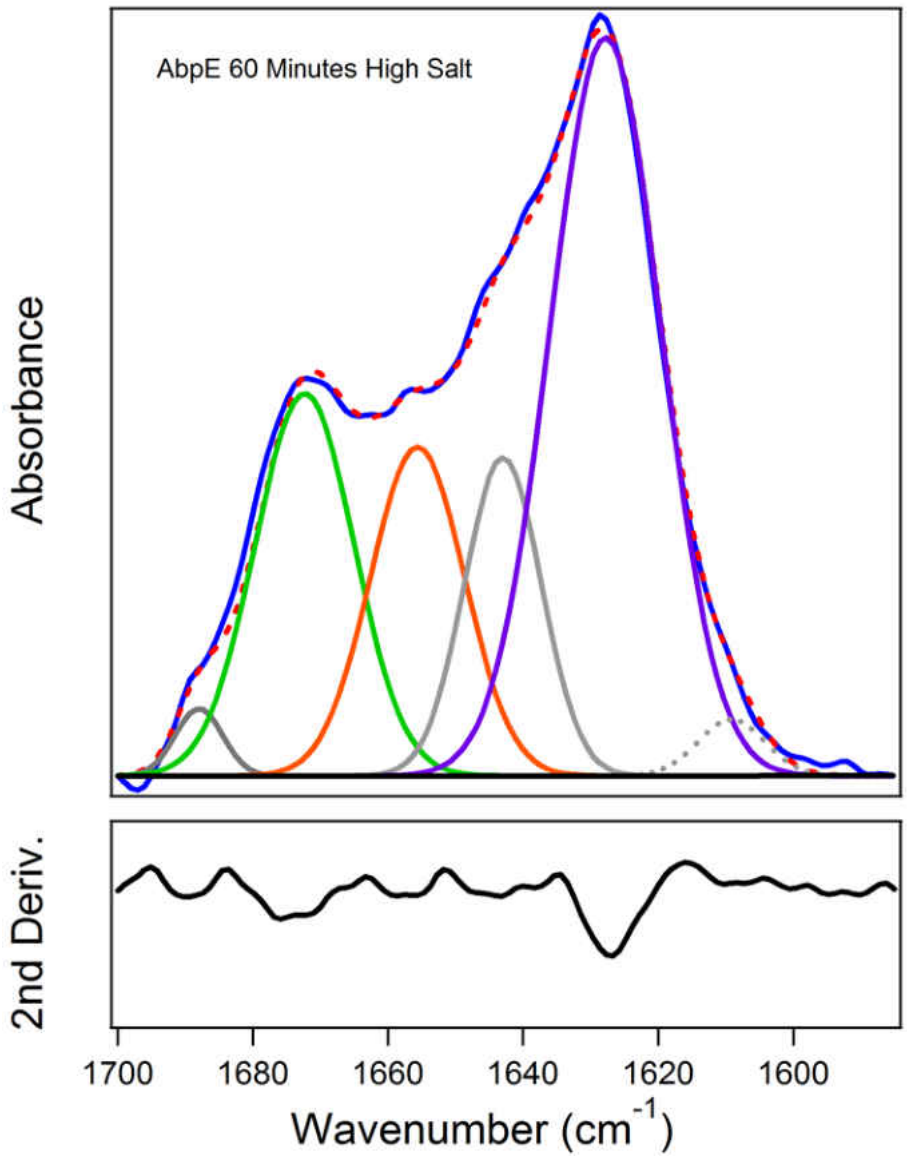
AbpE 60 Minutes High Salt
Absorbance
2nd Deriv.
1700
1680
1660
1640
1620
1600
Wavenumber (cm-1)

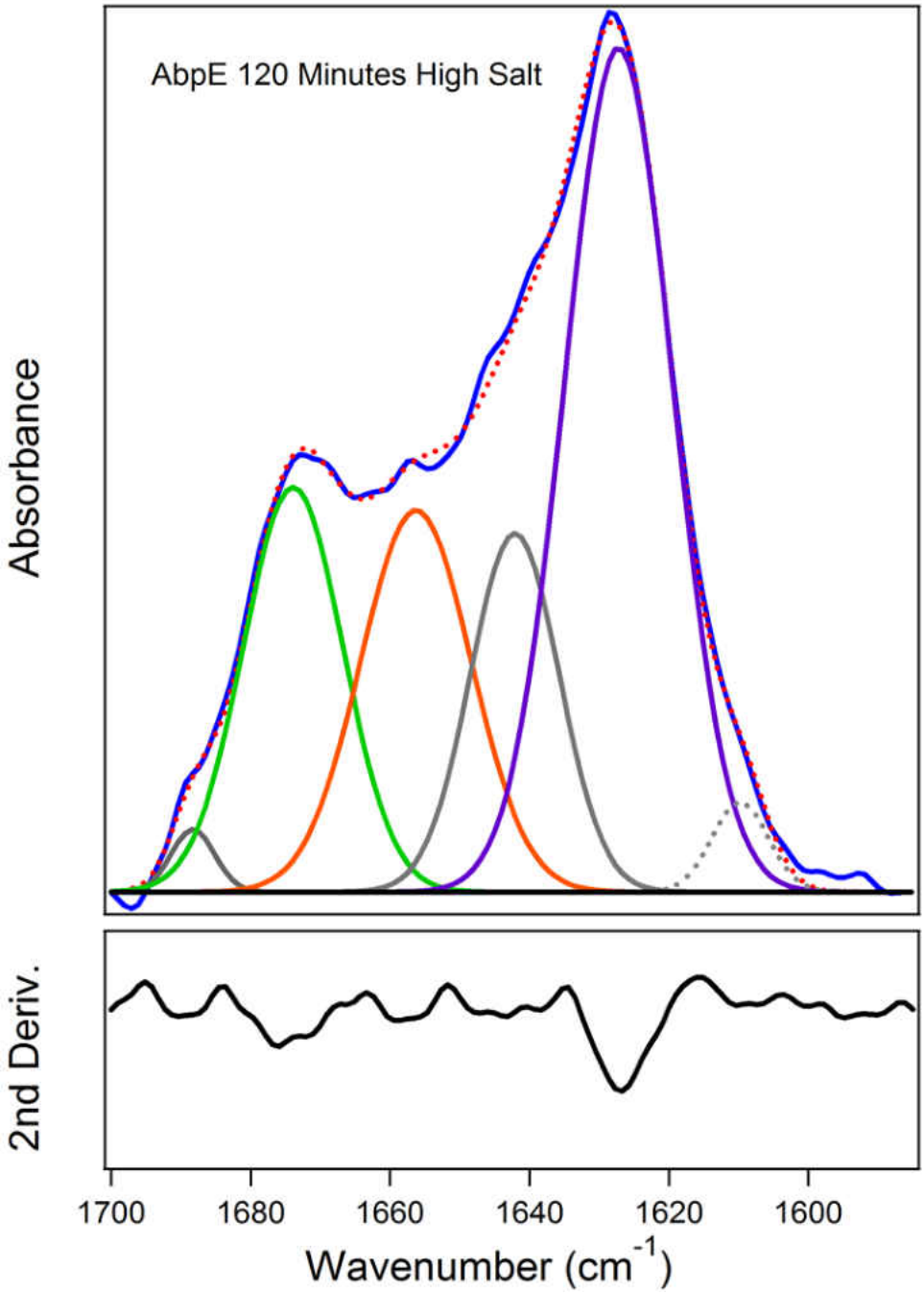
AbpE 120 Minutes High Salt
Absorbance
2nd Deriv.
1700
1680
1660
1640
1620
1600
Wavenumber (cm-1)

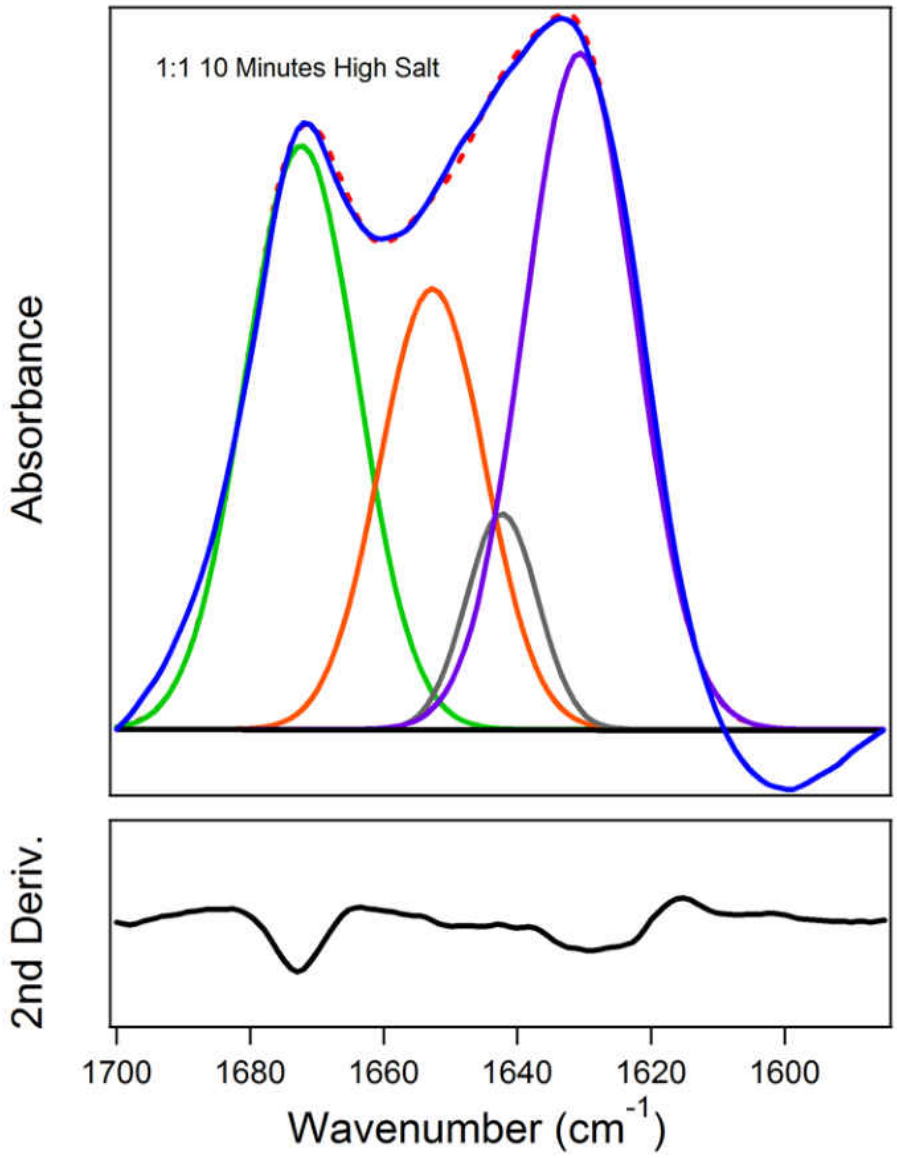
1:1 10 Minutes High Salt
Absorbance
2nd Deriv.
1700
1680
1660
1640
1620
1600
Wavenumber (cm-1)

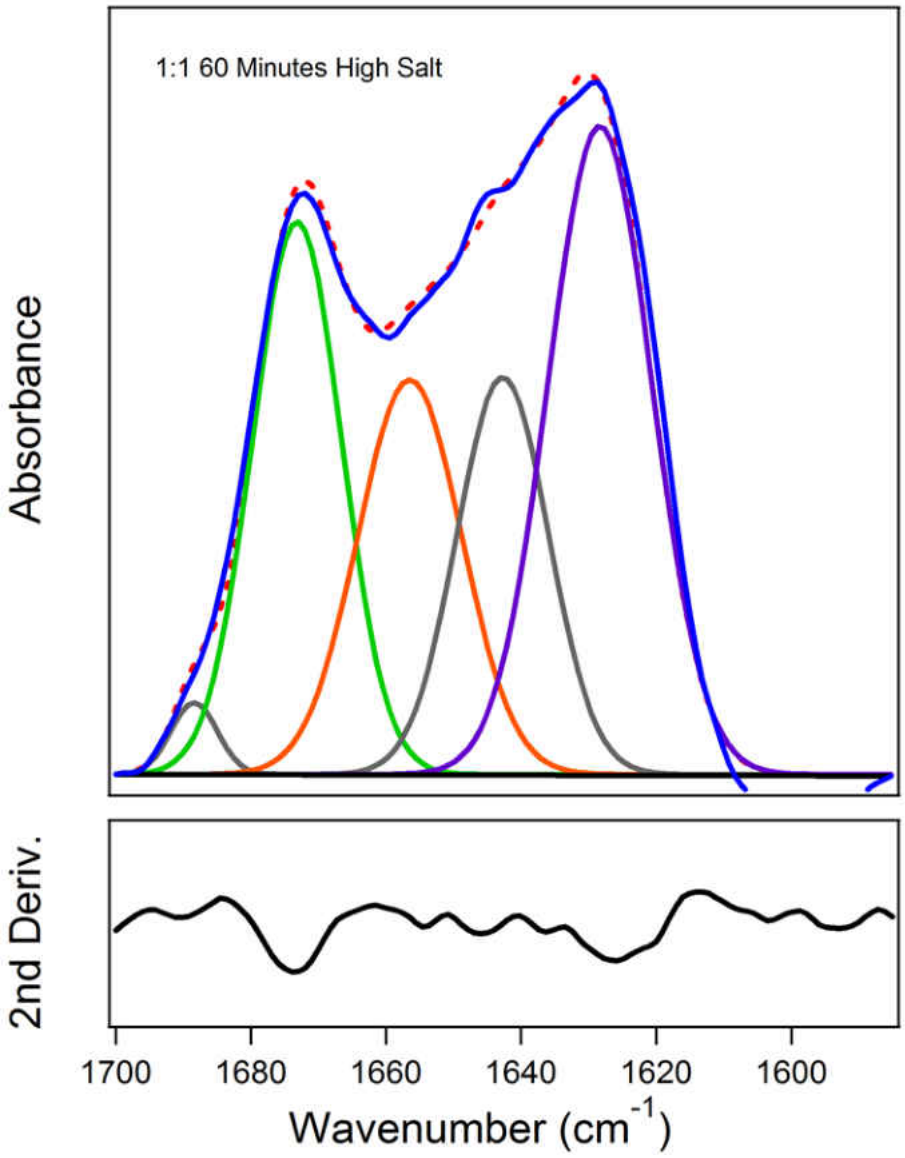
1:1 60 Minutes High Salt
Absorbance
2nd Deriv.
1700
1680
1660
1640
1620
1600
Wavenumber (cm-1)

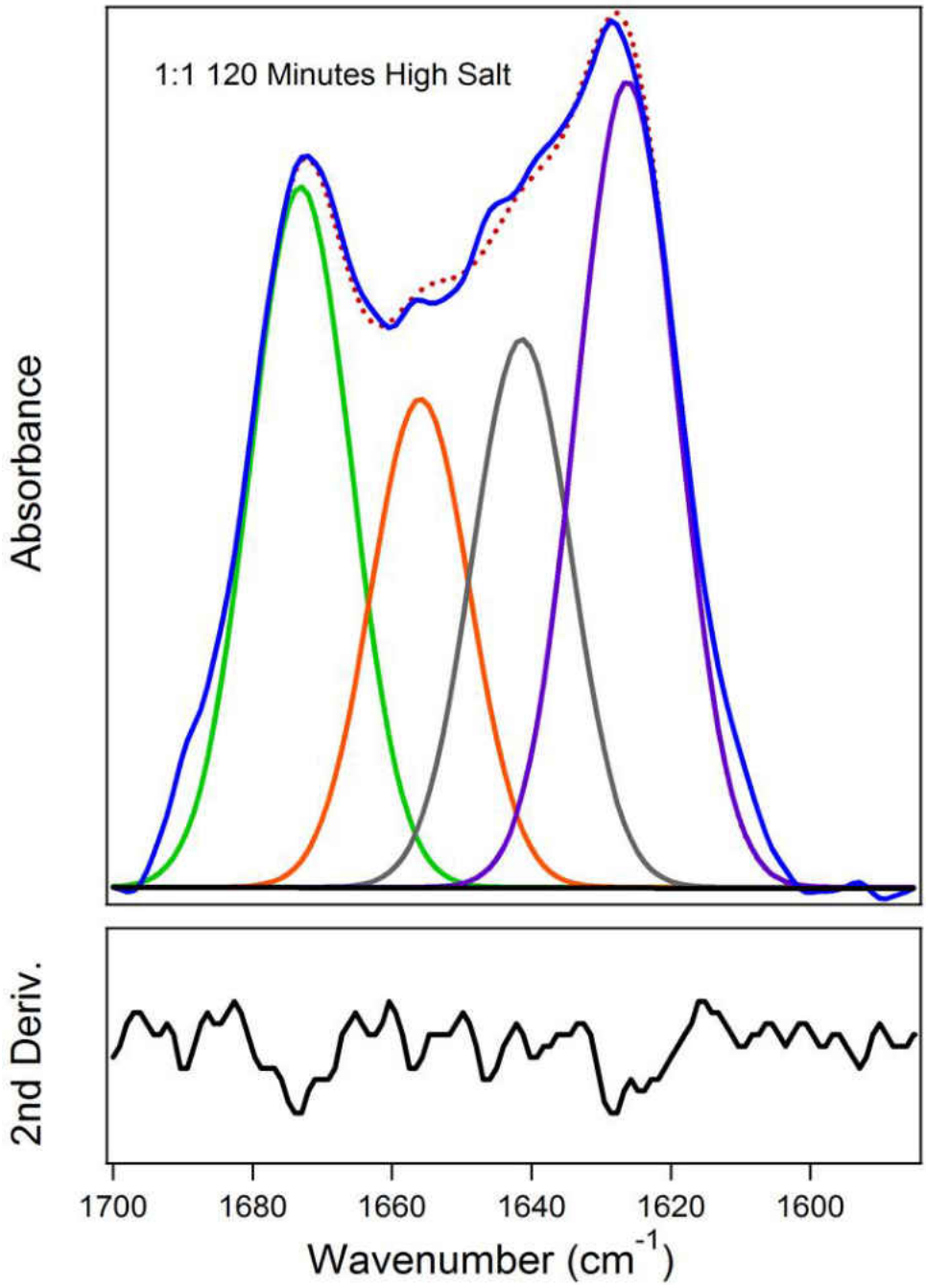
1:1 120 Minutes High Salt
Absorbance
2nd Deriv.
1700
1680
1660
1640
1620
1600
Wavenumber (cm-1)

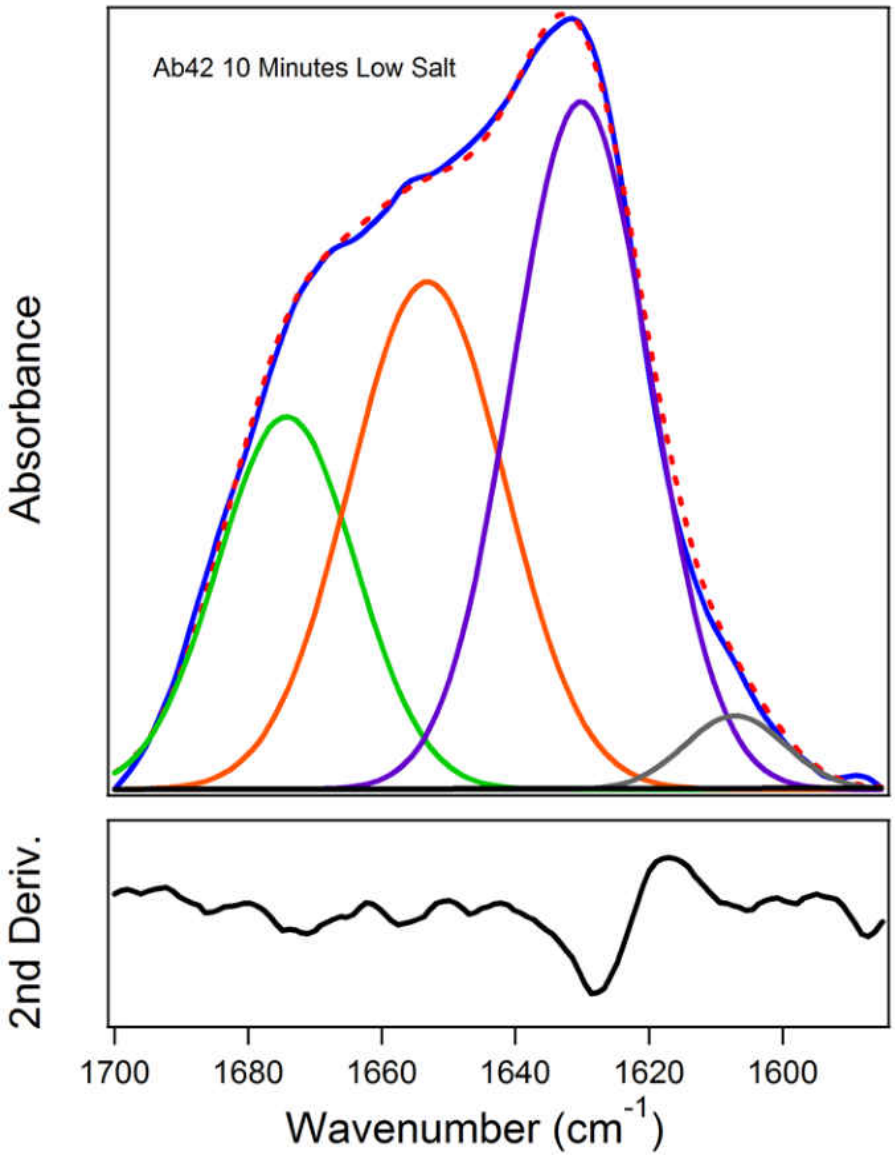
Ab42 10 Minutes Low Salt
Absorbance
2nd Deriv.
1700
1680
1660
1640
1620
1600
Wavenumber (cm-1)

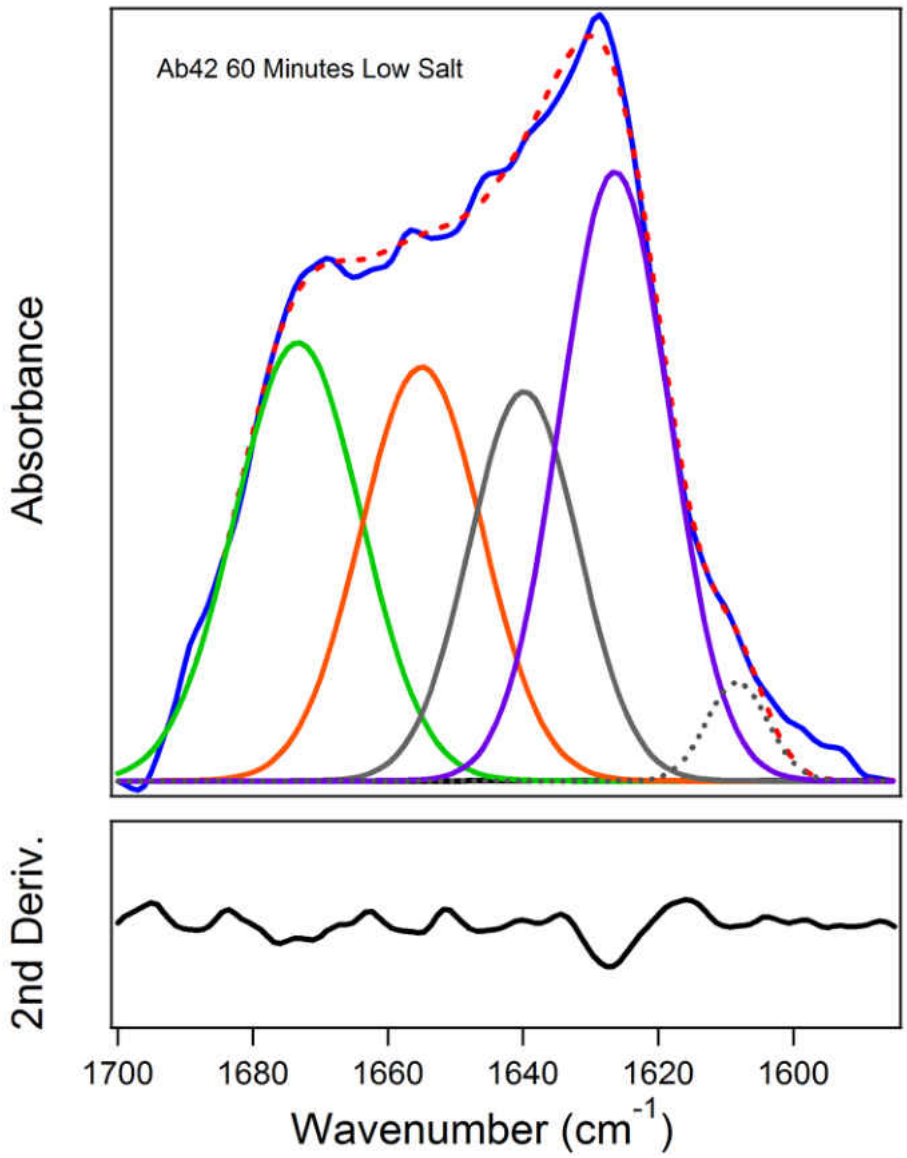
Ab42 60 Minutes Low Salt
Absorbance
2nd Deriv.
1700
1680
1660
1640
1620
1600
Wavenumber (cm-1)

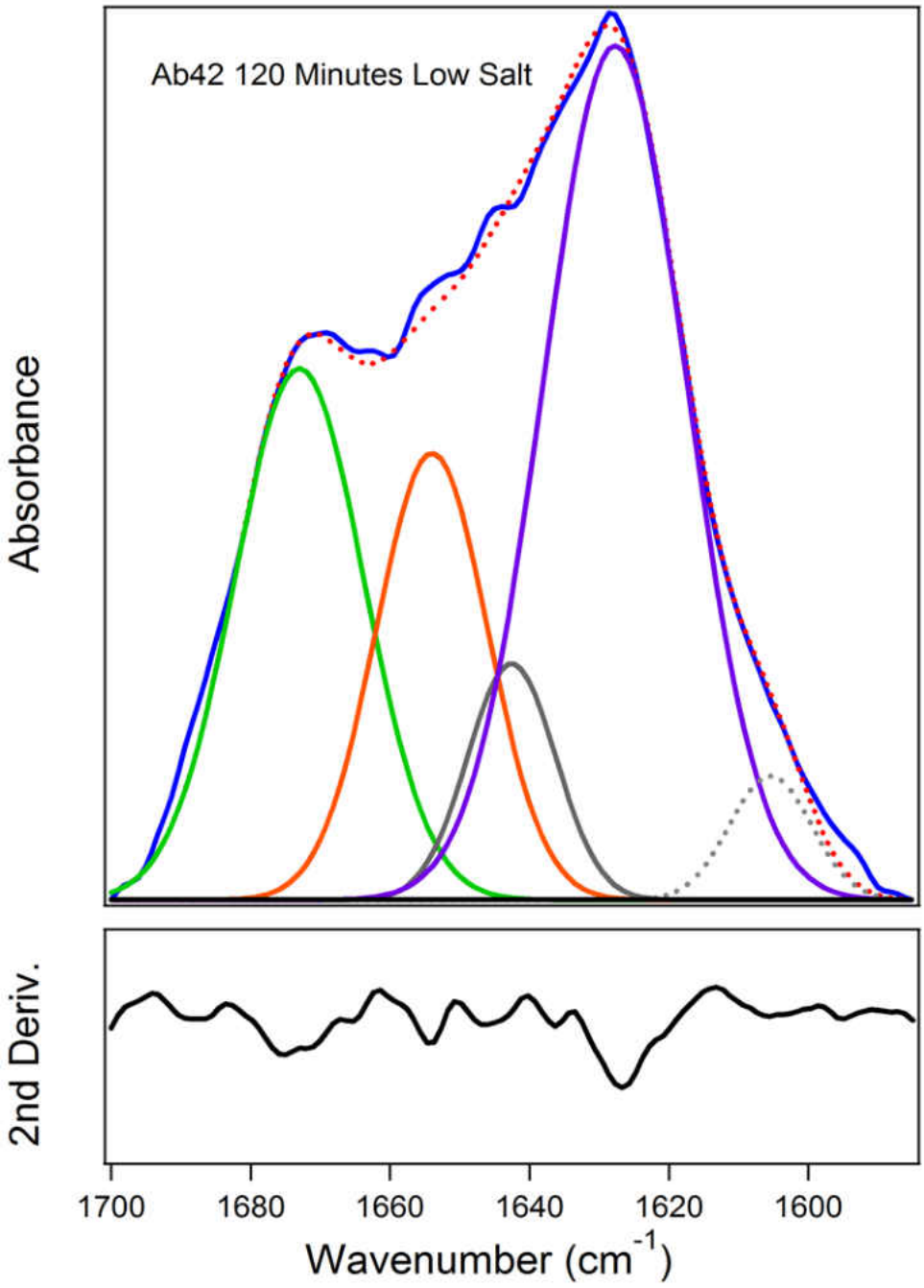
Ab42 120 Minutes Low Salt
Absorbance
2nd Deriv.
1700
1680
1660
1640
1620
1600
Wavenumber (cm-1)

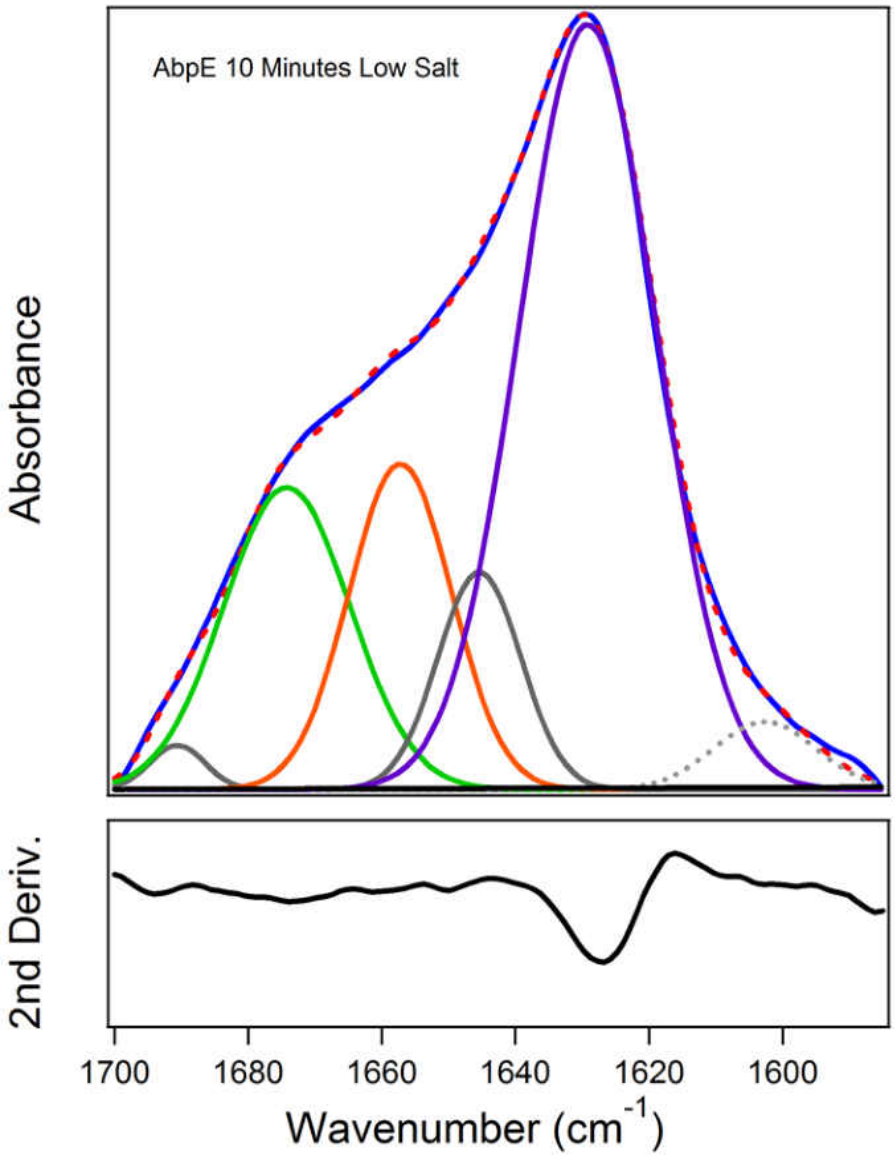
AbpE 10 Minutes Low Salt
Absorbance
2nd Deriv.
1700
1680
1660
1640
1620
1600
Wavenumber (cm-1)

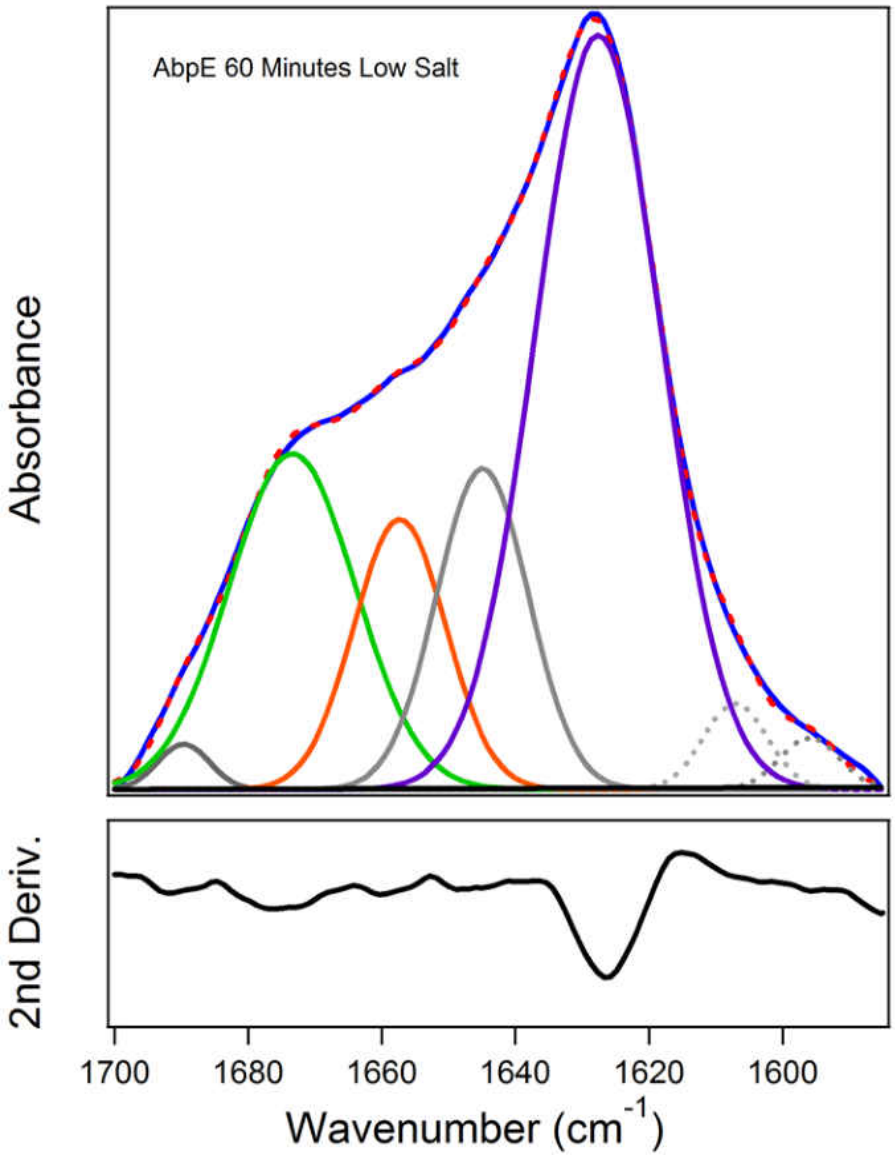
AbpE 60 Minutes Low Salt
Absorbance
2nd Deriv.
1700
1680
1660
1640
1620
1600
Wavenumber (cm-1)

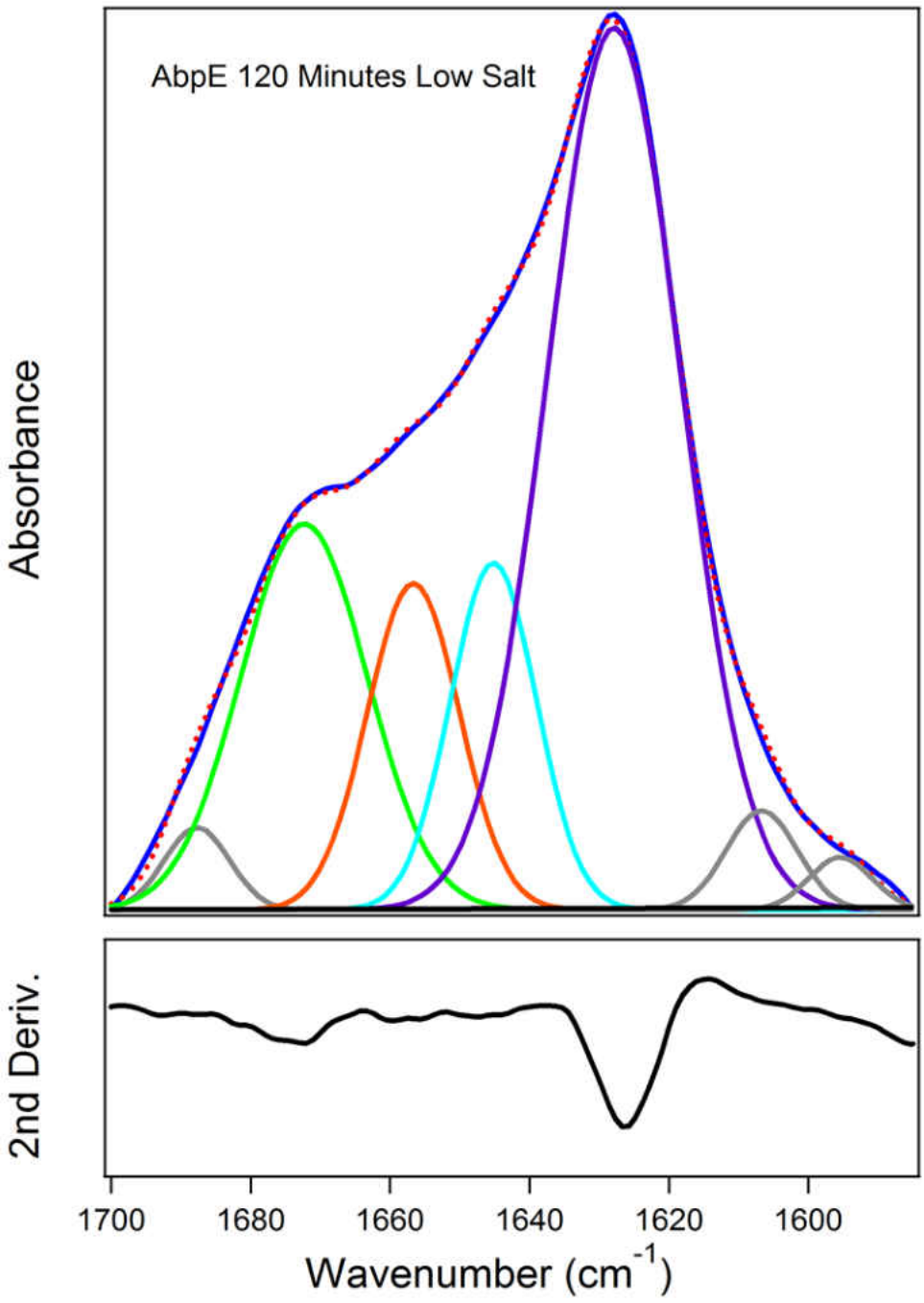
AbpE 120 Minutes Low Salt
Absorbance
2nd Deriv.
1700
1680
1660
1640
1620
1600
Wavenumber (cm-1)

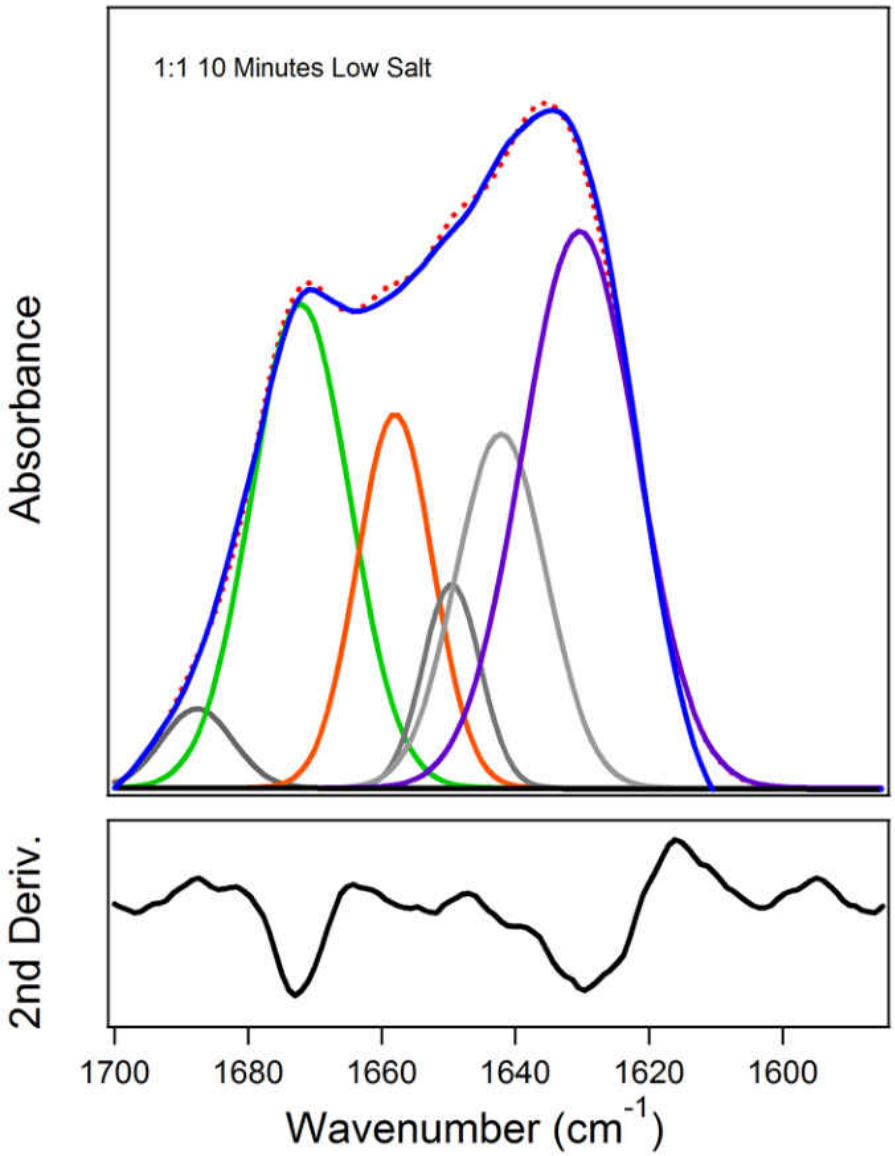
1:1 10 Minutes Low Salt
Absorbance
2nd Deriv.
1700
1680
1660
1640
1620
1600
Wavenumber (cm-1)

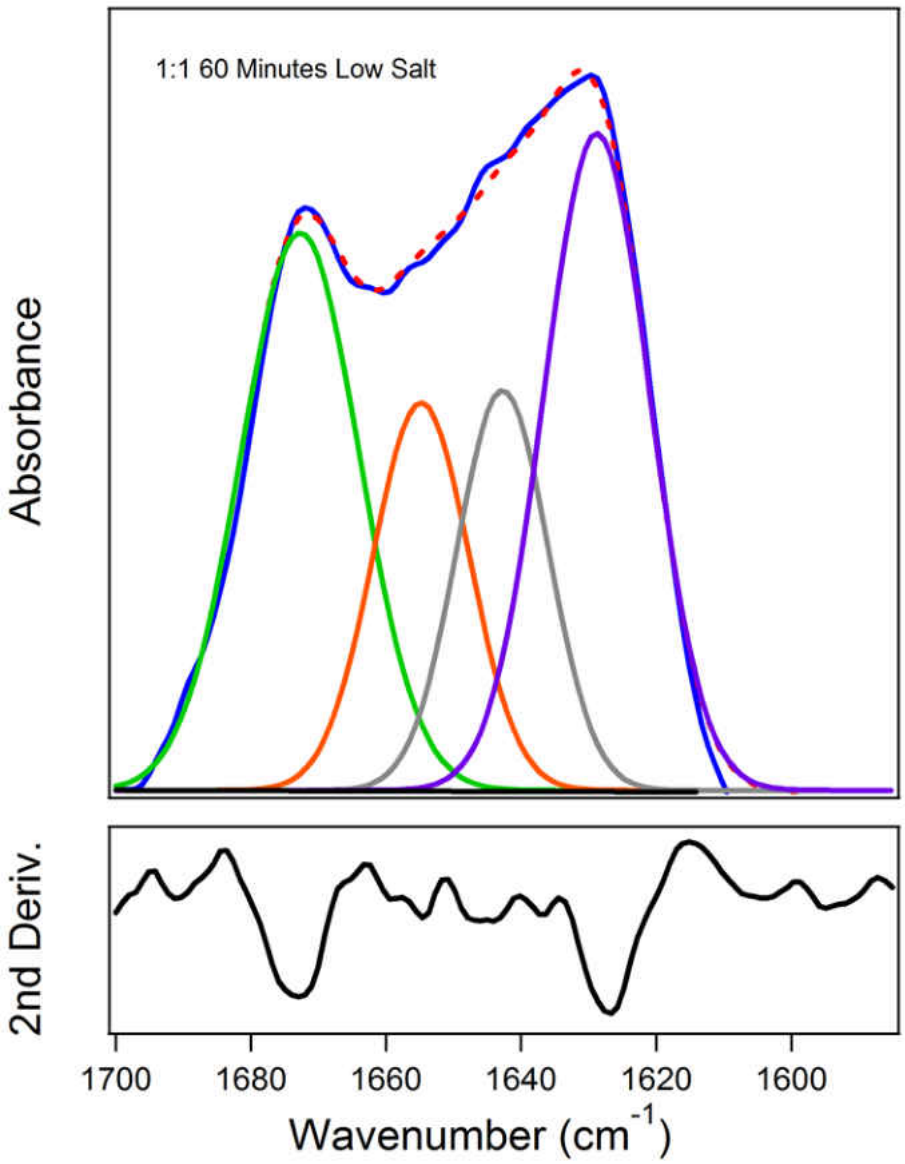
1:1 60 Minutes Low Salt
Absorbance
2nd Deriv.
1700
1680
1660
1640
1620
1600
Wavenumber (cm-1)

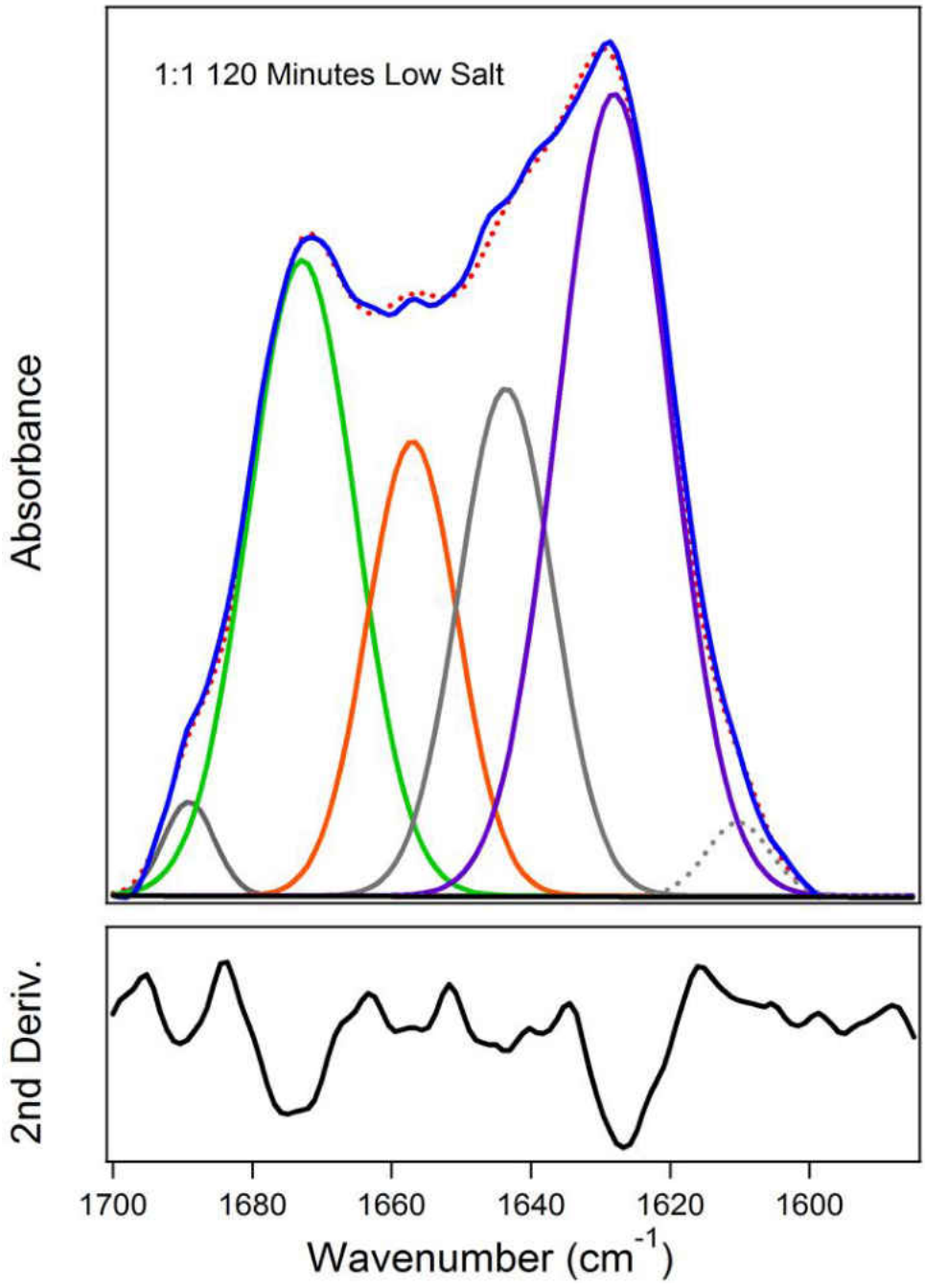
1:1 120 Minutes Low Salt
Absorbance
2nd Deriv.
1700
1680
1660
1640
1620
1600
Wavenumber (cm-1)

APPENDIX C: PEAK FITTING OF LABELED PEPTIDES

. Curve fit spectra of ^{13}C-labeled $A\beta_{1-42,}$ $A\beta_{pE3-42}$ and their equimolar combination in 10 mM phosphate pD 6.8 buffer (low salt conditions) as well as 50 mM phsosphate 50 mM NaCl pD 6.8 (physiological buffer) for 10, 60, and 120 minutes. Peptides were ^{13}C- and ^{15}N-labeled at either $K^{16}L^{17}V^{18}$ or $V^{36}G^{37}G^{38}V^{39}$.The experimental measurement is shown in Blue while the Red dotted line is the sum of all components, fit peaks correspond to turn (green), α-helix (orange), and β-sheet (purple) unattributed peaks are shown in grey and are primarily composed of unordered structure. Peaks corresponding to side chain interactions are shown in dotted grey and are not included in area calculations. The second derivative of the experimental spectra is shown in black underneath. Total peptide concentration is 50 μM.

Table 5. Distribution of secondary structures in 50 mM phosphate 50 mM NaCl pD 6.8 as calculated by curve fitting. Numbers are the averages at 10, 60, and 120 minutes in buffer, label combination refers to the fraction of the peak corresponding to the ^{13}C-label in KLV/VGG and VGGV/KLV spectra. Components counted as other, primarily unordered structure, are not included in the table.

High Salt	$A\beta_{1-42}$	$A\beta_{pE3-42}$	1:1
β-turn	19.5 ± 8.3	27.7±5.0	22.1±3.5
α-helix	24.4±10.7	18.1±10.6	26.9±7.2
β-sheet	41.1±5.0	45.4±5.6	36.2±10.8
^{13}C-Label KLV	7.4±1.0	8.0±1.5	5.8±0.7
^{13}C-Label VGGV	10.3±0.8	9.9±0.4	10.4±0.5
^{13}C-Label Combination	-	-	6.1±2.8

Physiological Buffer

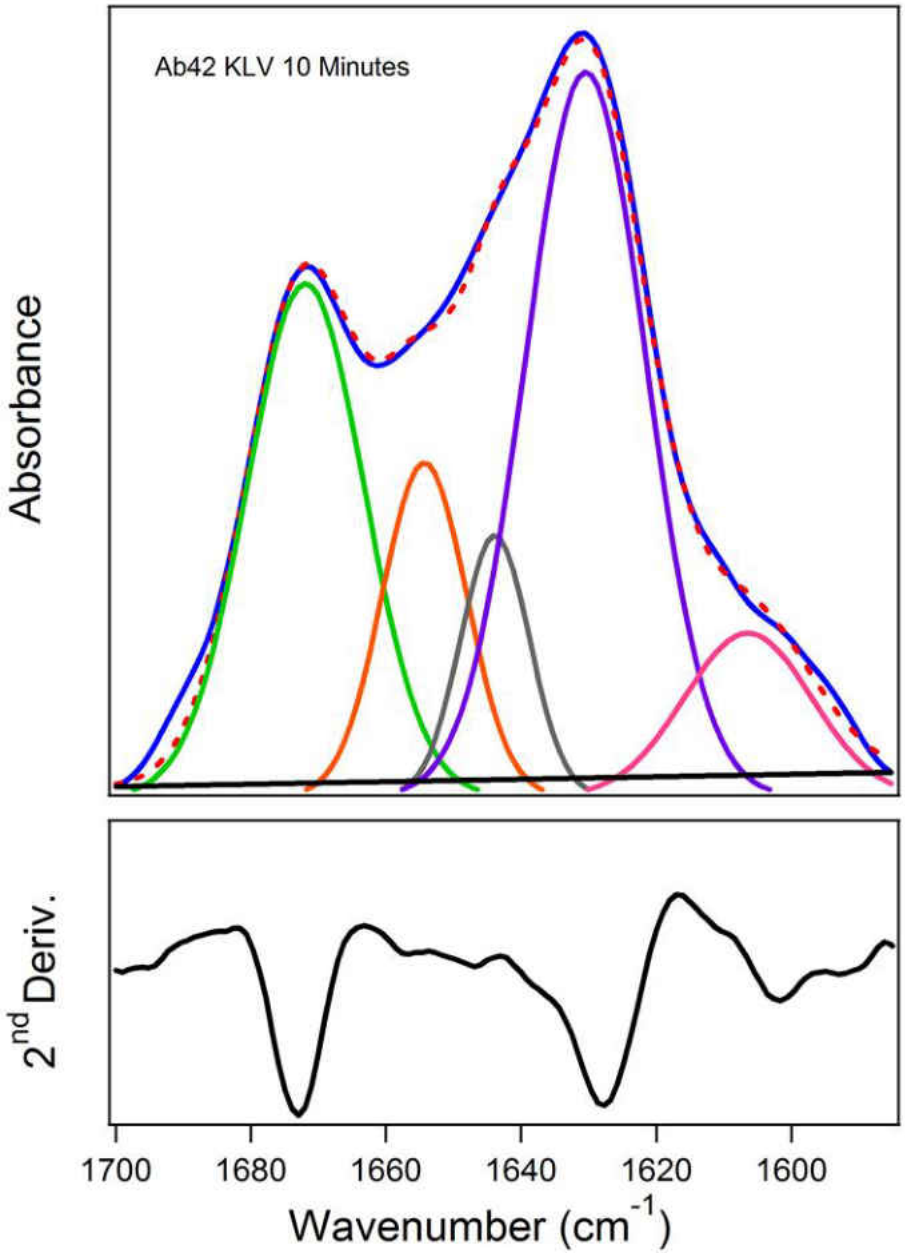

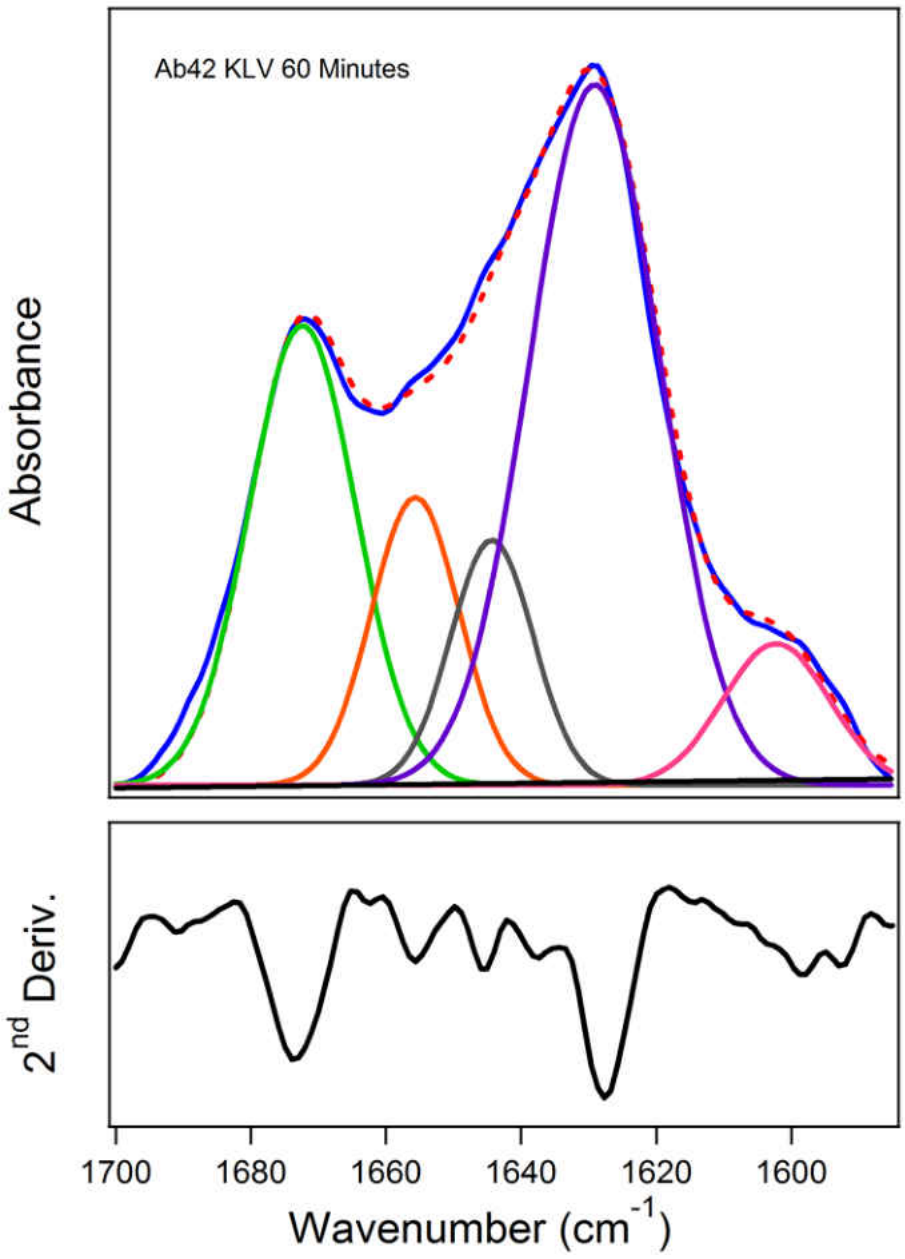
Ab42 KLV 60 Minutes
Absorbance
2nd Deriv.
1700
1680
1660
1640
1620
1600
Wavenumber (cm-1)

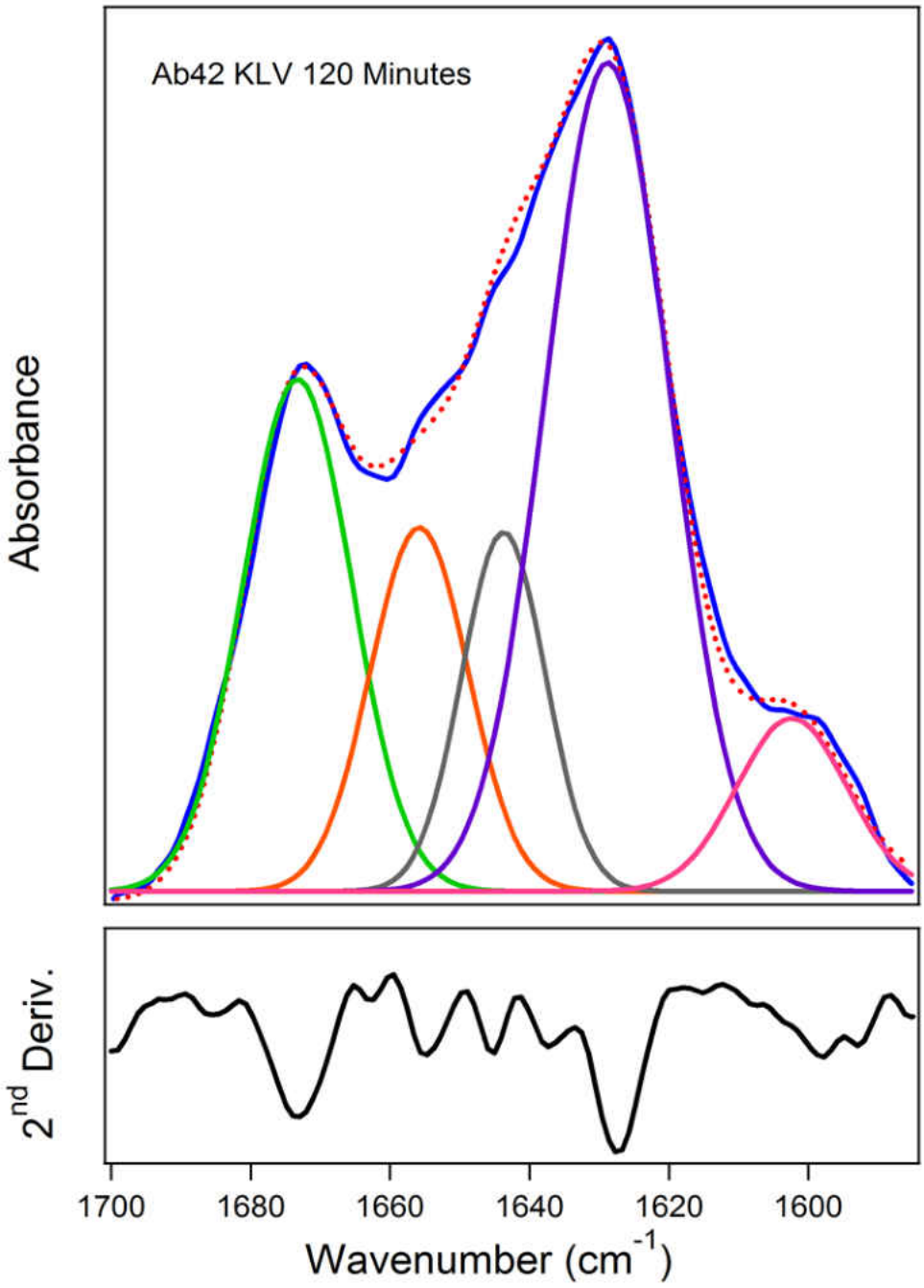
Ab42 KLV 120 Minutes
Absorbance
2nd Deriv.
1700
1680
1660
1640
1620
1600
Wavenumber (cm-1)

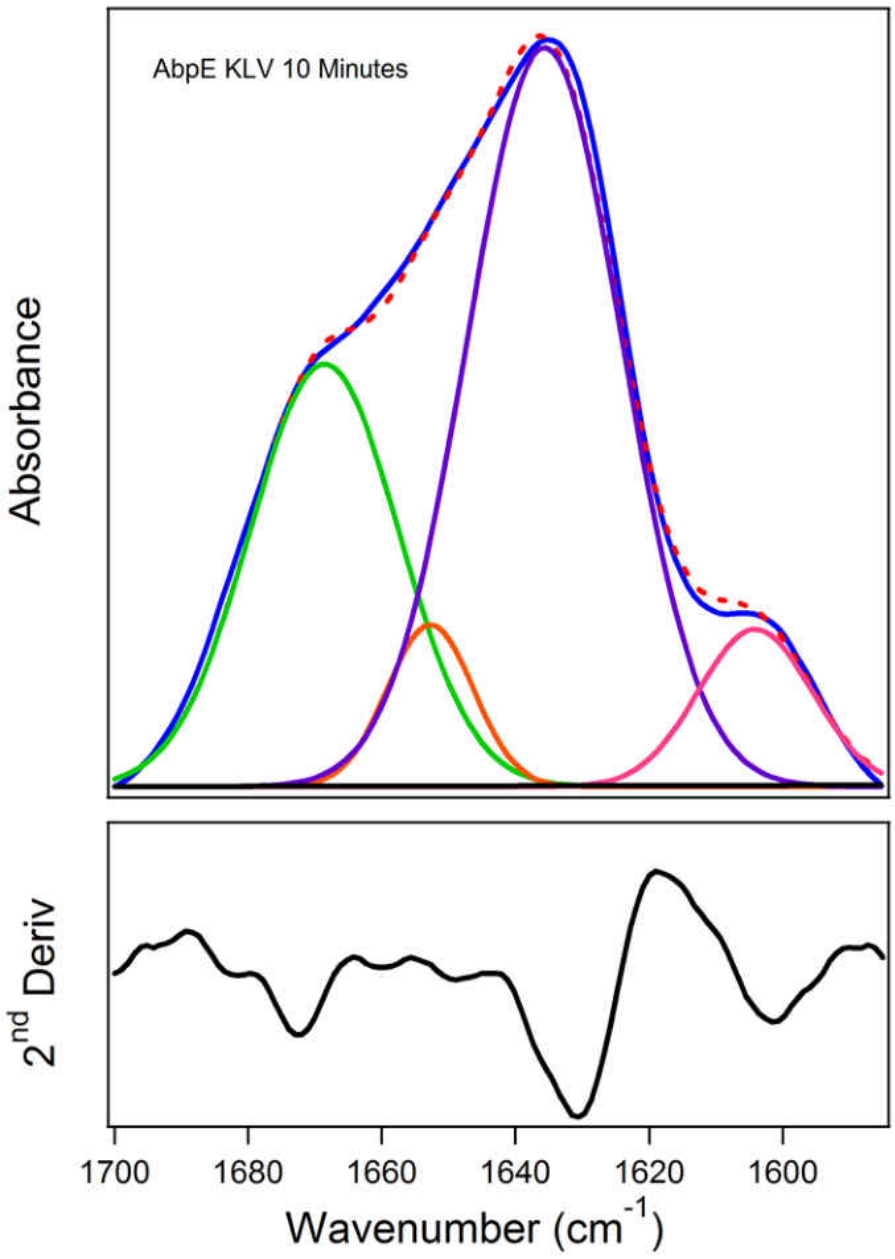
AbpE KLV 10 Minutes
Absorbance
2nd Deriv
1700
1680
1660
1640
1620
1600
Wavenumber (cm-1)

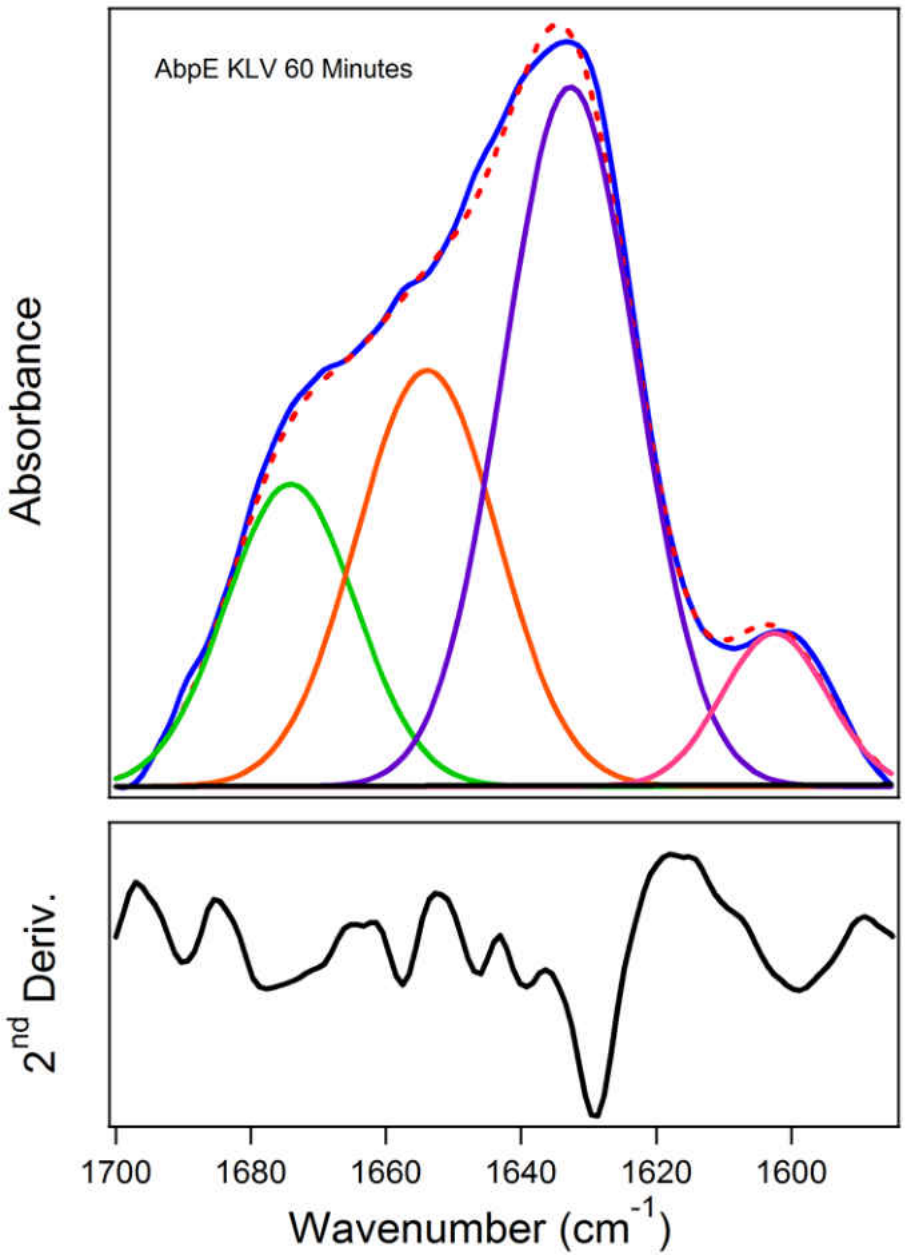
AbpE KLV 60 Minutes
Absorbance
2nd Deriv.
1700
1680
1660
1640
1620
1600
Wavenumber (cm-1)

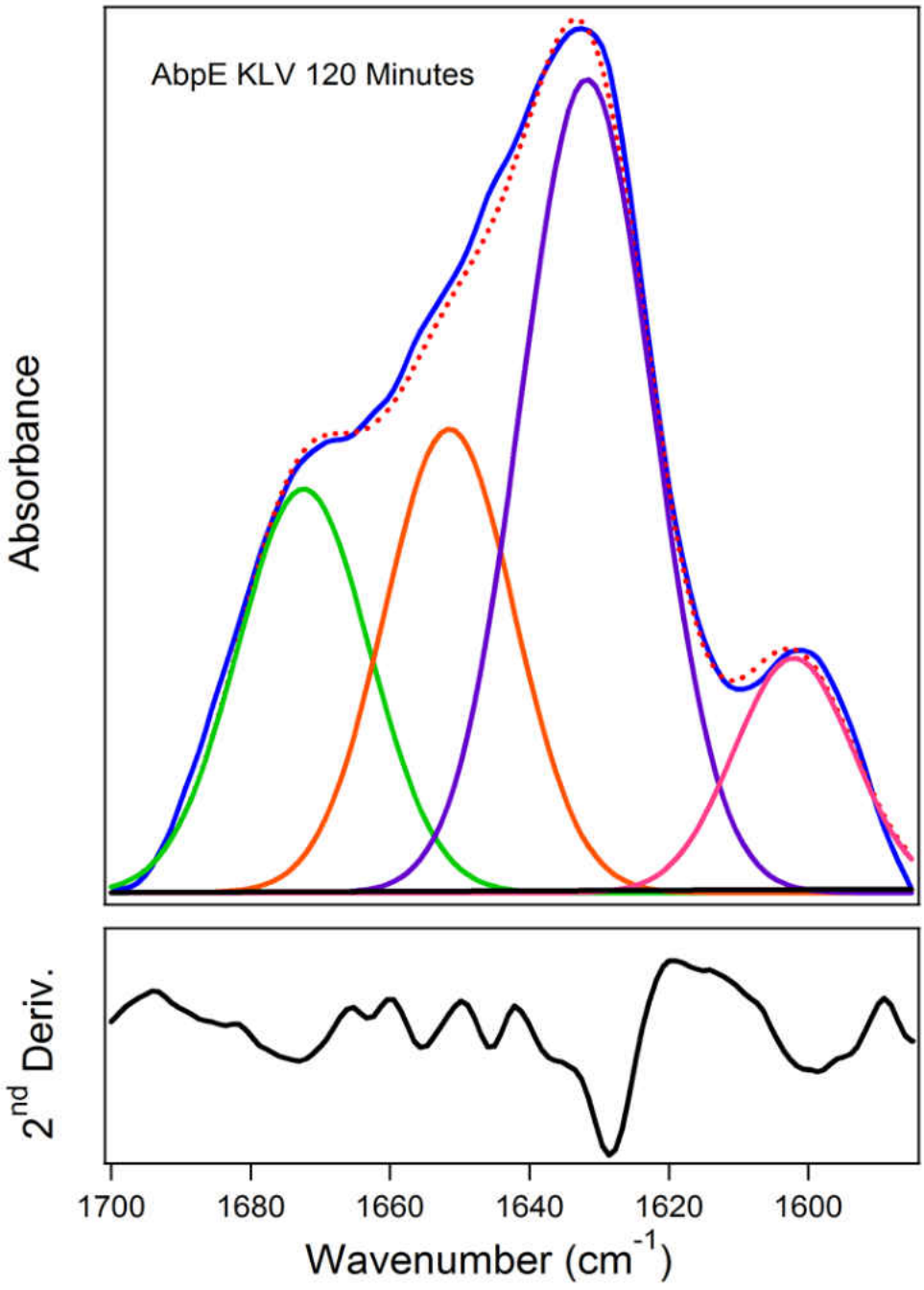
AbpE KLV 120 Minutes
Absorbance
2nd Deriv.
1700
1680
1660
1640
1620
1600
Wavenumber (cm-1)

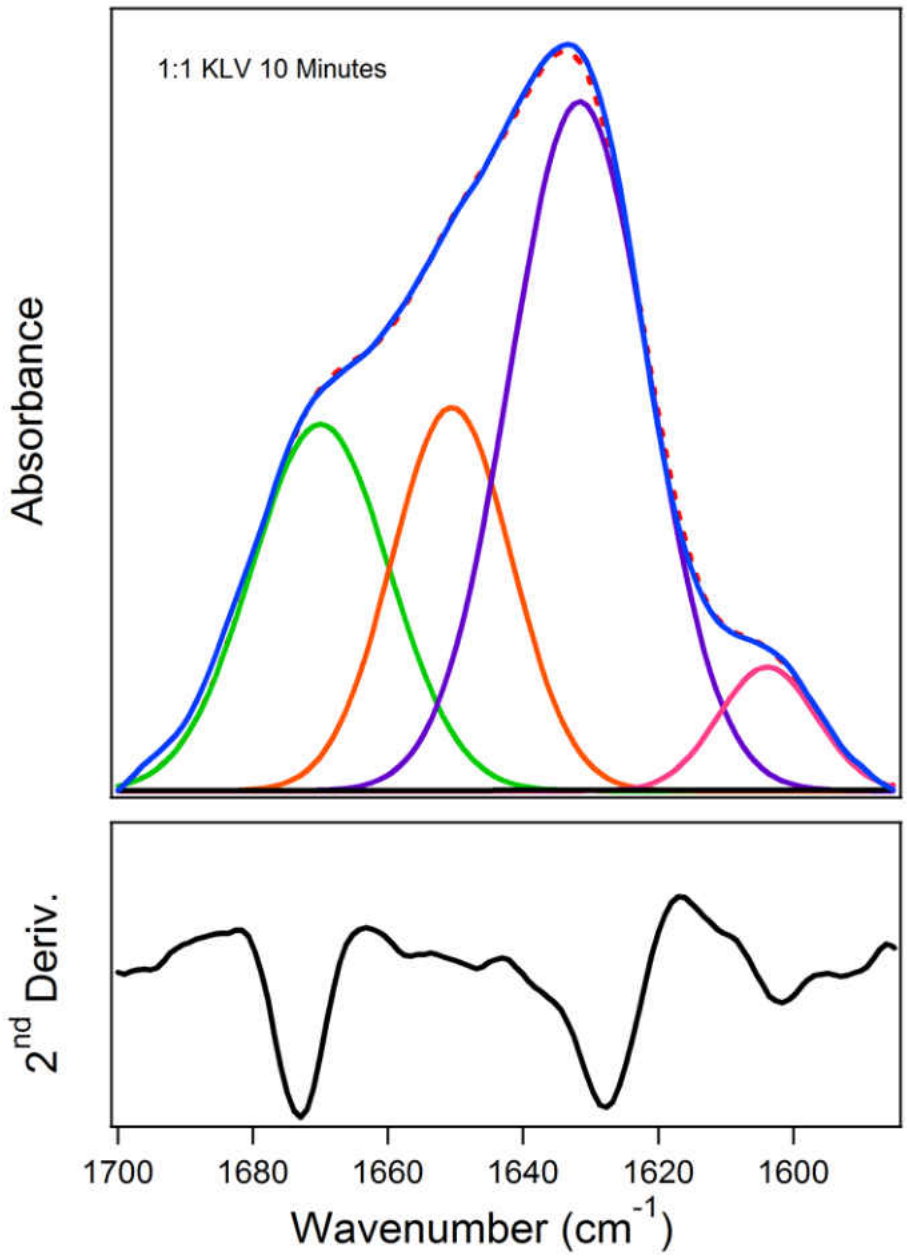
1:1 KLV 10 Minutes
Absorbance
2nd Deriv.
1700
1680
1660
1640
1620
1600
Wavenumber (cm-1)

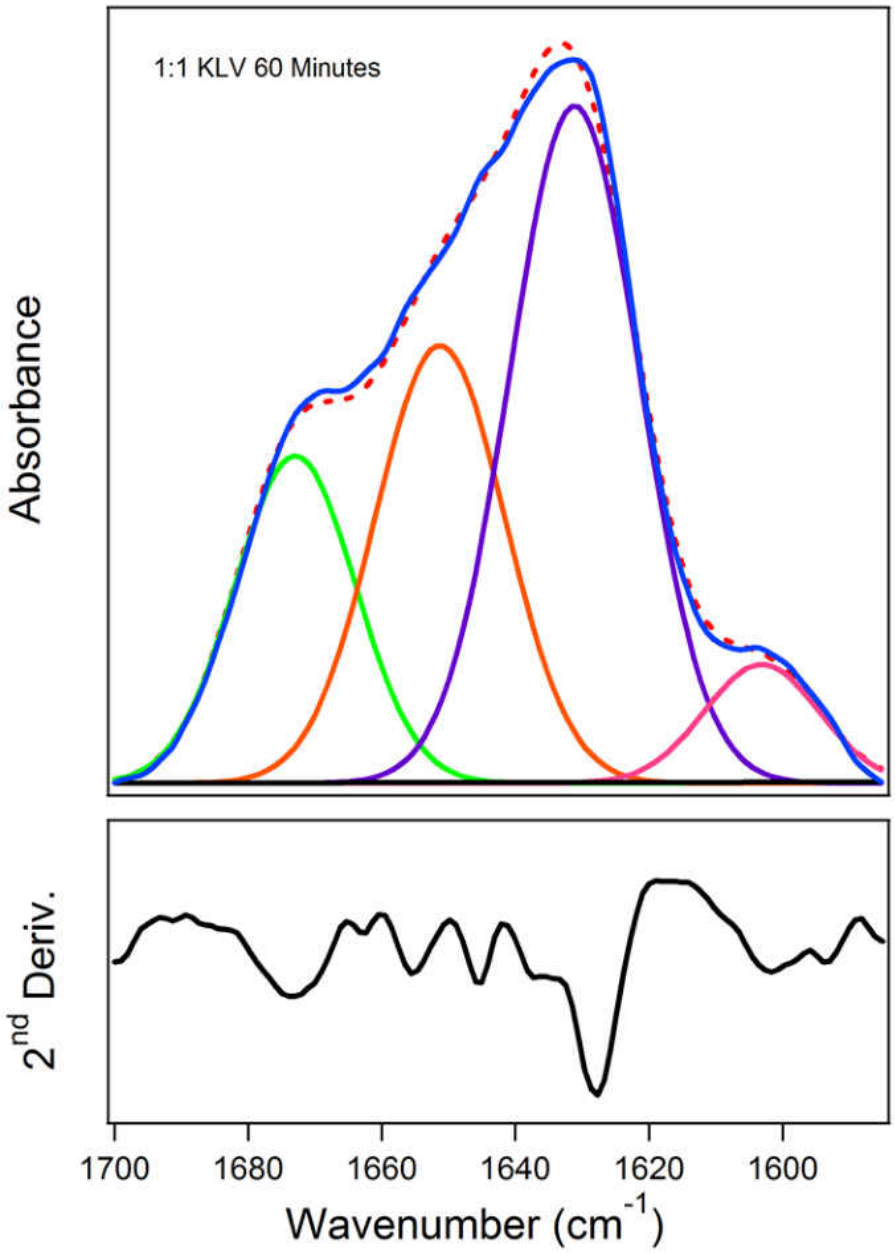
1:1 KLV 60 Minutes
Absorbance
2nd Deriv.
1700
1680
1660
1640
1620
1600
Wavenumber (cm-1)

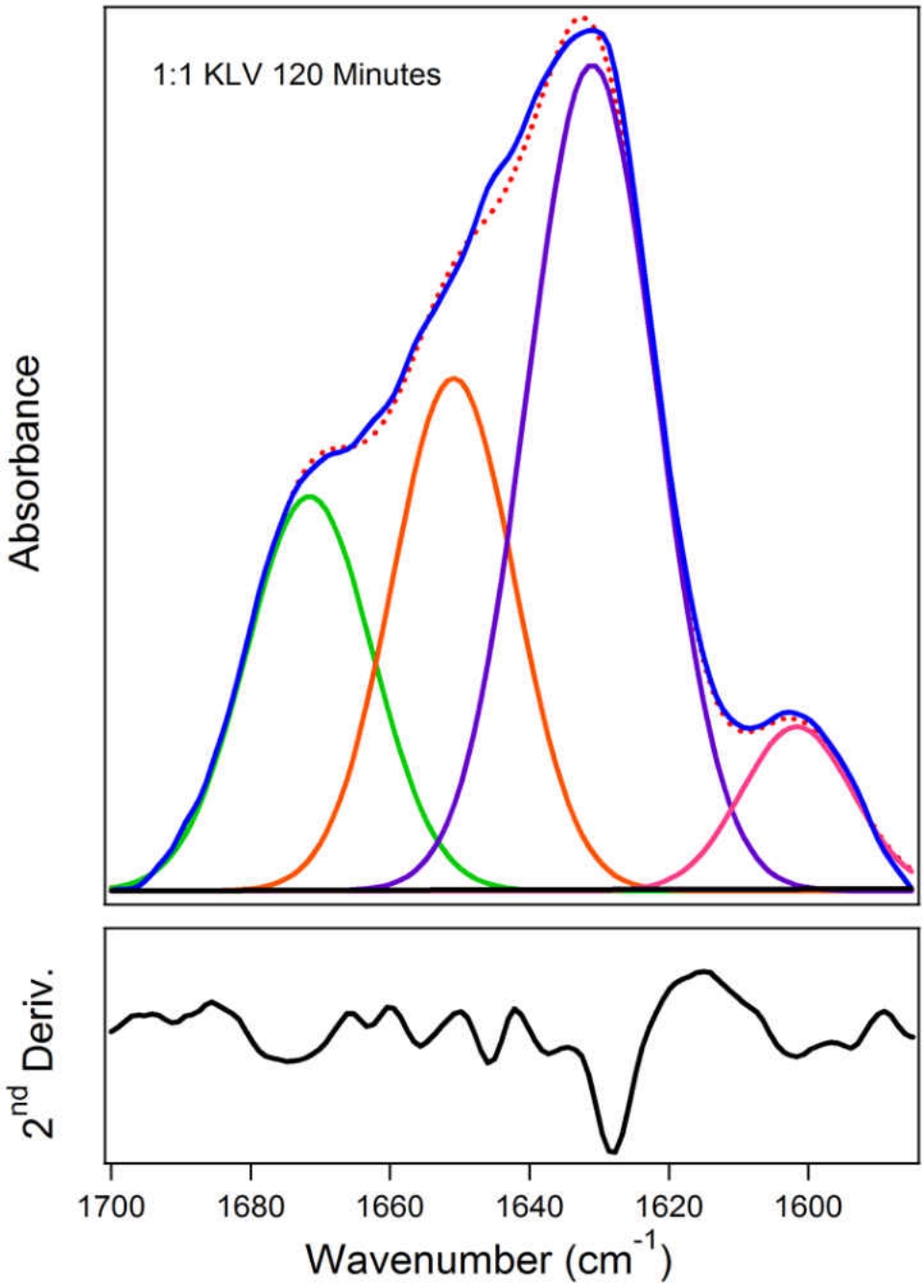
1:1 KLV 120 Minutes
Absorbance
2nd Deriv.
1700
1680
1660
1640
1620
1600
Wavenumber (cm-1)

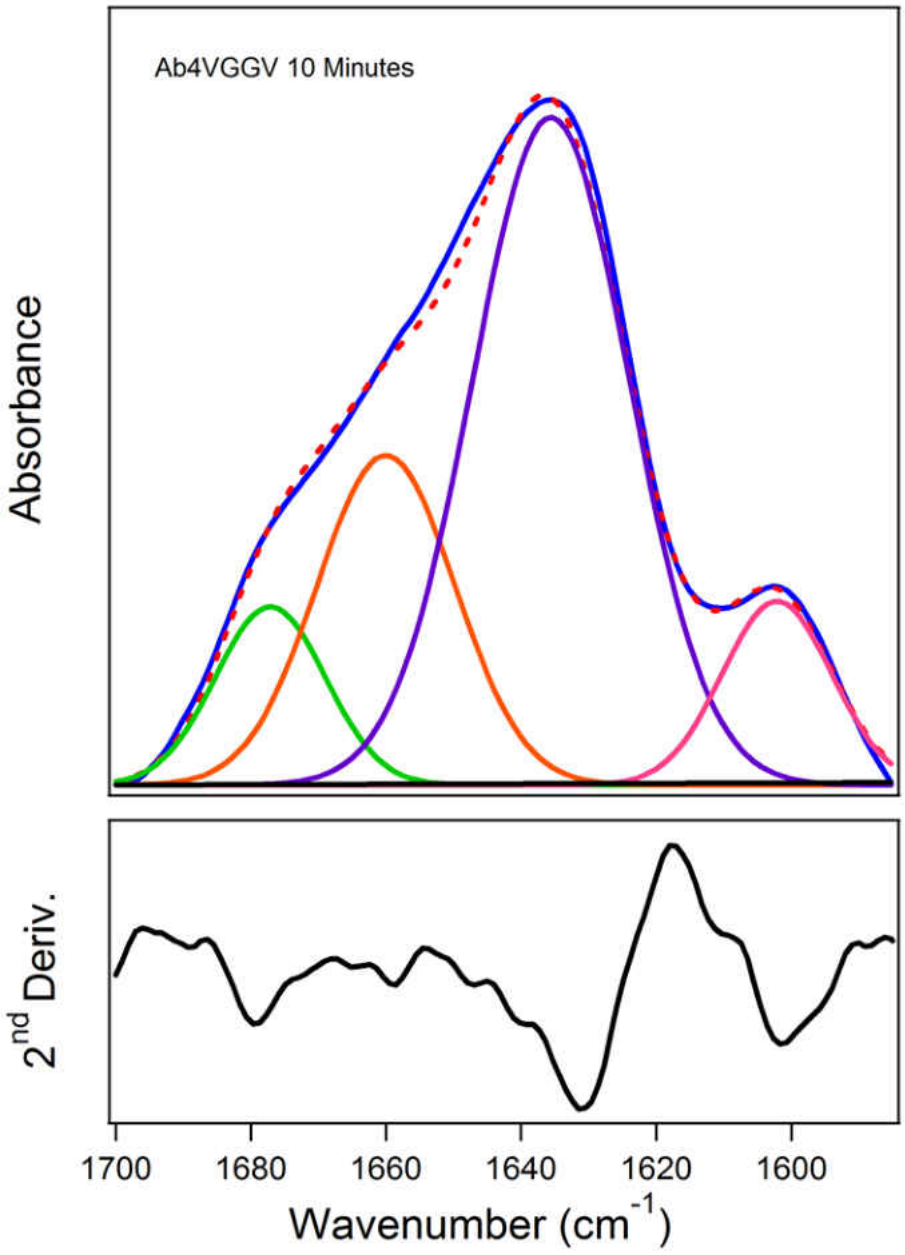
Ab4VGGV 10 Minutes
Absorbance
2nd Deriv.
1700
1680
1660
1640
1620
1600
Wavenumber (cm-1)

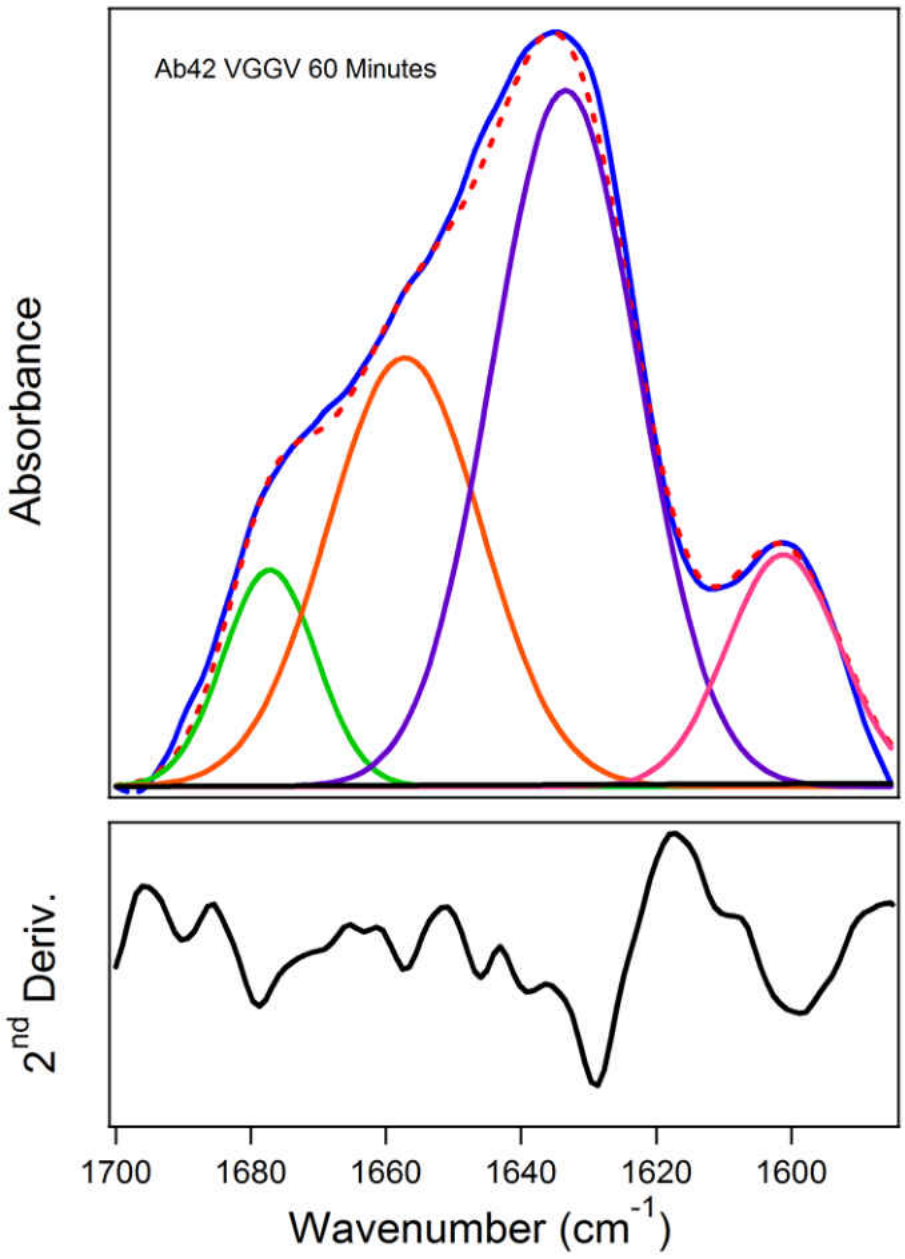
Ab42 VGGV 60 Minutes
Absorbance
2nd Deriv.
1700
1680
1660
1640
1620
1600
Wavenumber (cm-1)

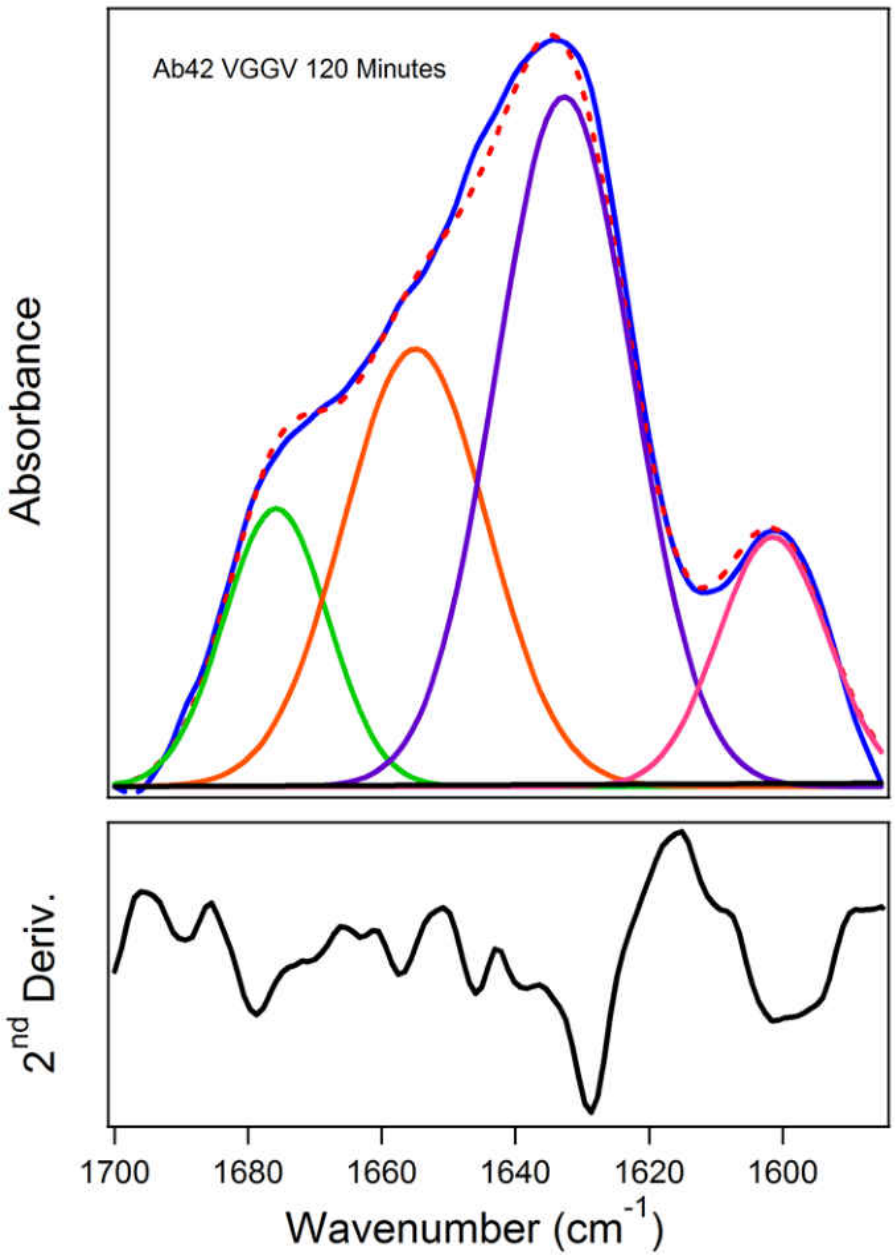
Ab42 VGGV 120 Minutes
Absorbance
2nd Deriv.
1700
1680
1660
1640
1620
1600
Wavenumber (cm-1)

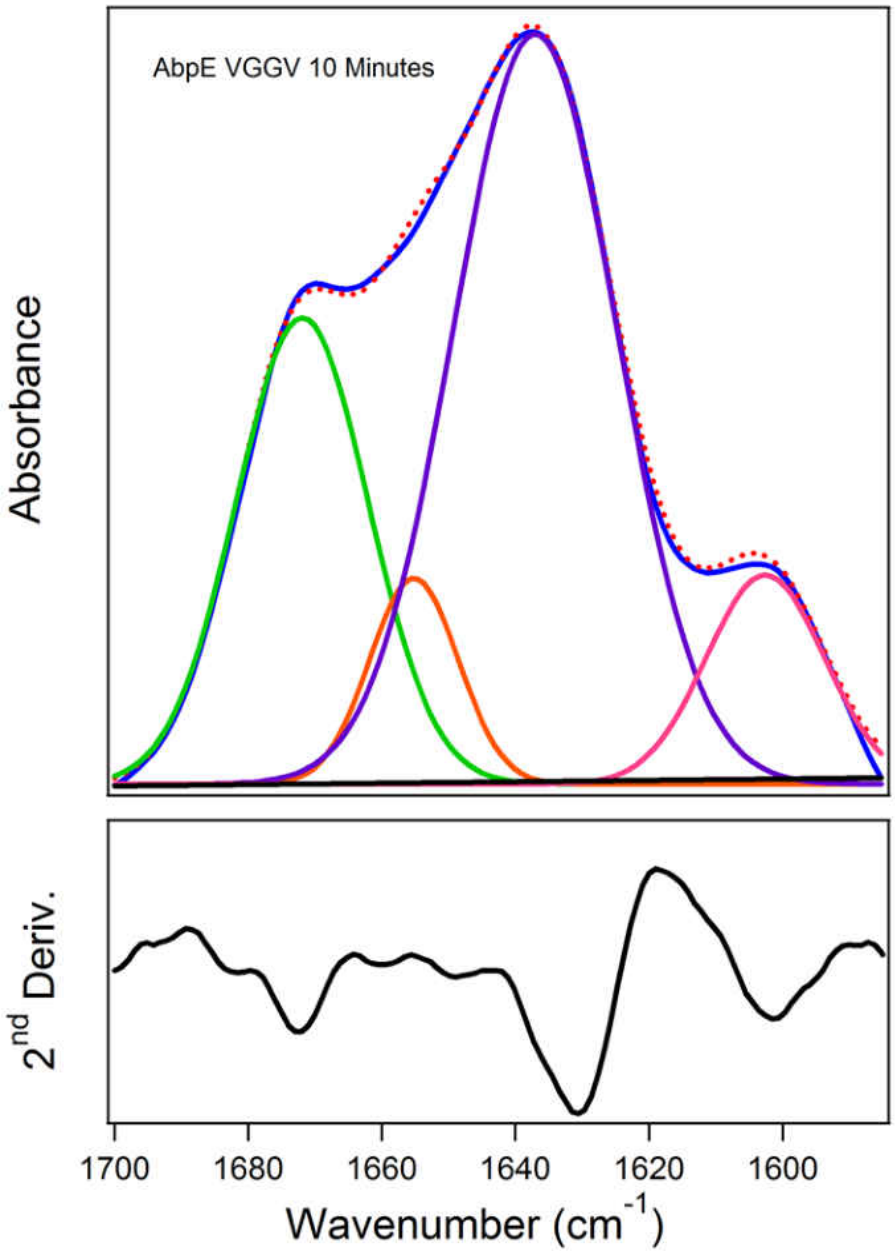
AbpE VGGV 10 Minutes
Absorbance
2nd Deriv.
1700
1680
1660
1640
1620
1600
Wavenumber (cm-1)

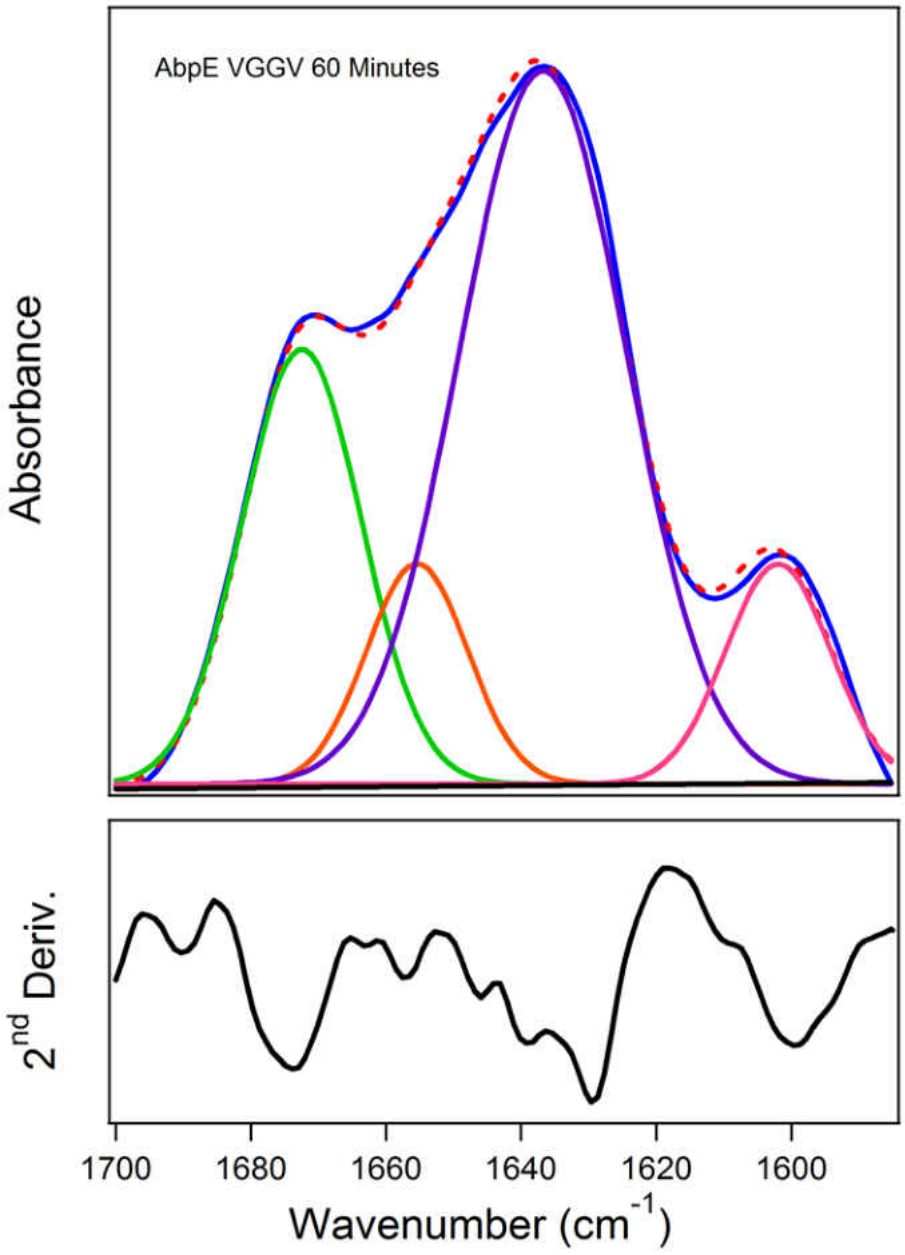
AbpE VGGV 60 Minutes
Absorbance
2nd Deriv.
1700
1680
1660
1640
1620
1600
Wavenumber (cm-1)

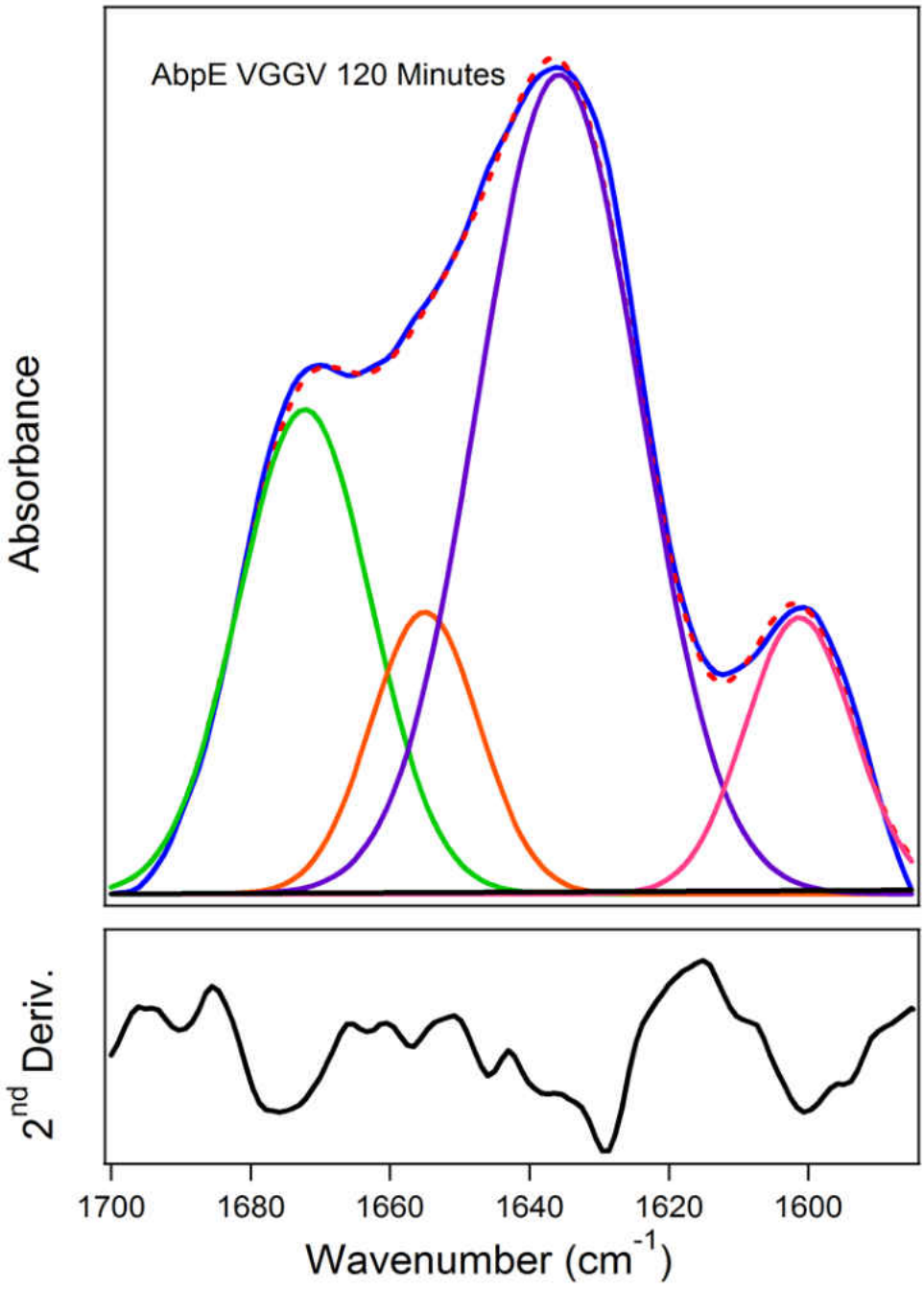
AbpE VGGV 120 Minutes
Absorbance
2nd Deriv.
1700
1680
1660
1640
1620
1600
Wavenumber (cm-1)

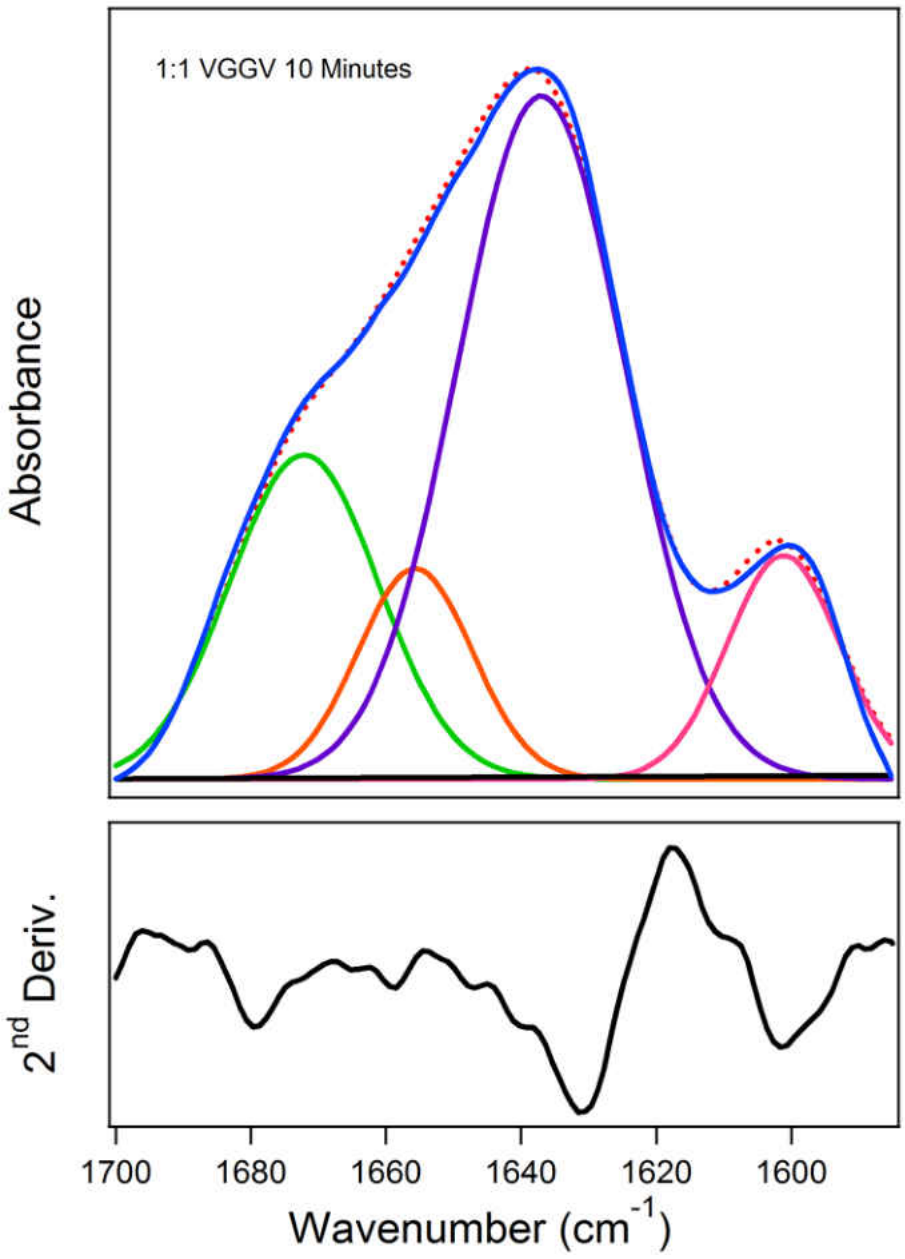
1:1 VGGV 10 Minutes
Absorbance
2nd Deriv.
1700
1680
1660
1640
1620
1600
Wavenumber (cm-1)

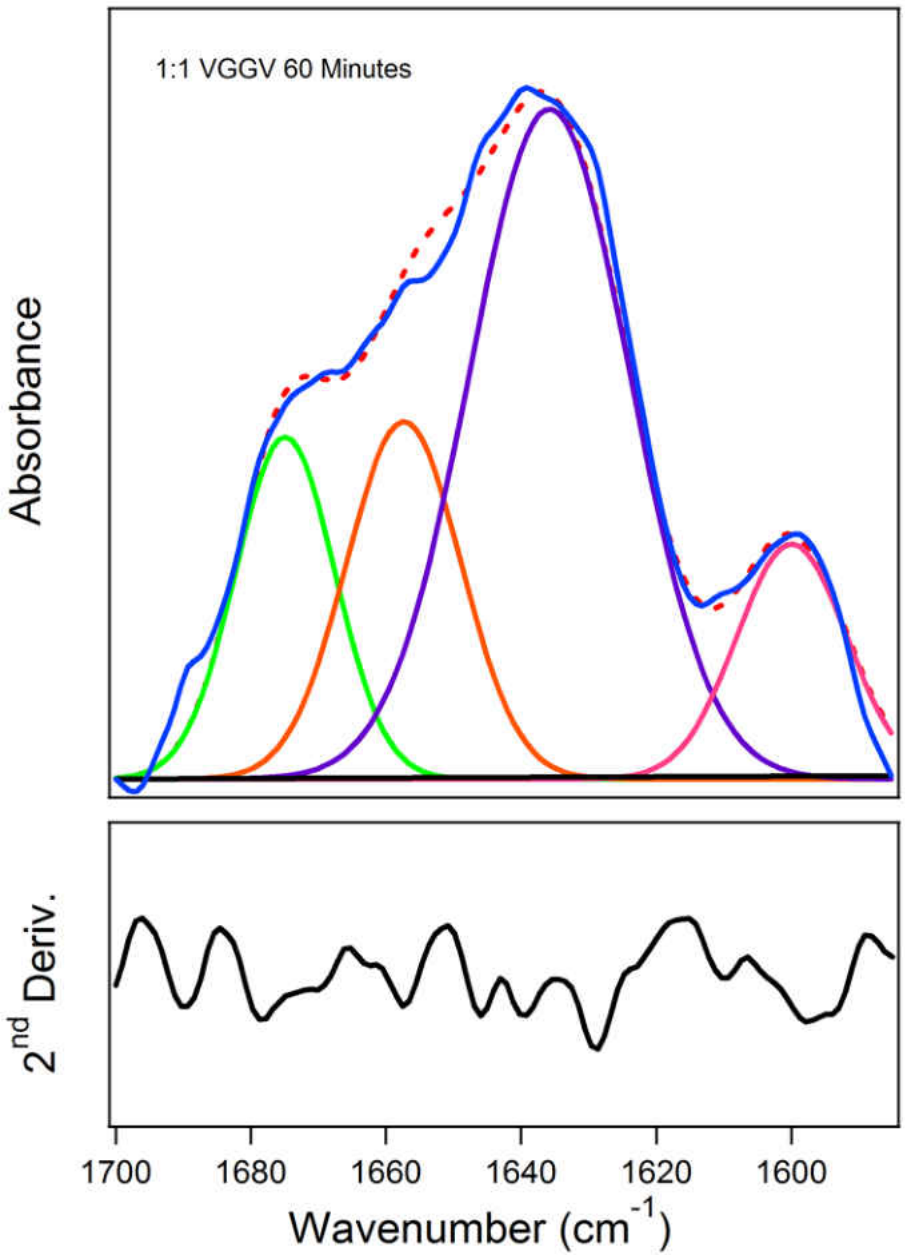
1:1 VGGV 60 Minutes
Absorbance
2nd Deriv.
1700
1680
1660
1640
1620
1600
Wavenumber (cm-1)

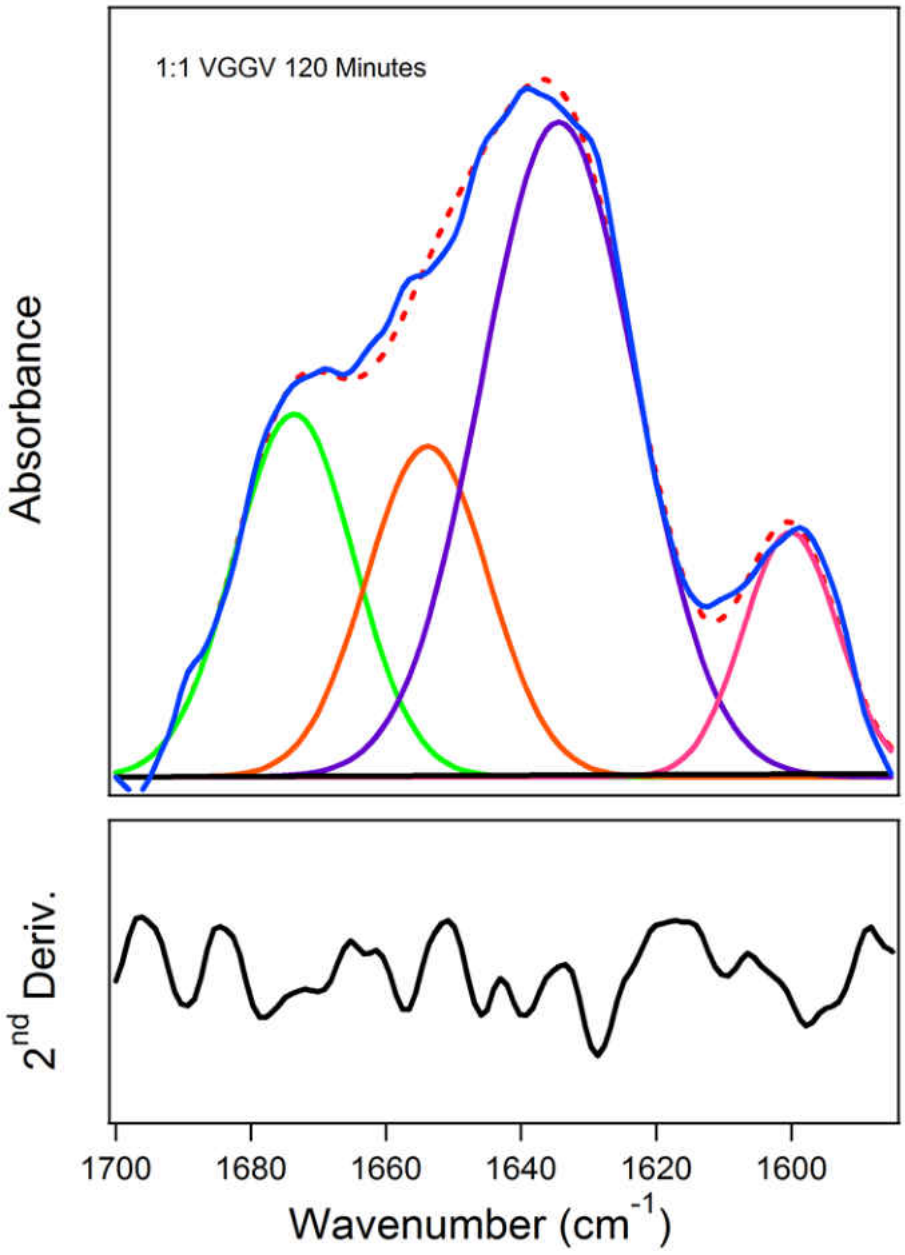
1:1 VGGV 120 Minutes
Absorbance
2nd Deriv.
1700
1680
1660
1640
1620
1600
Wavenumber (cm-1)

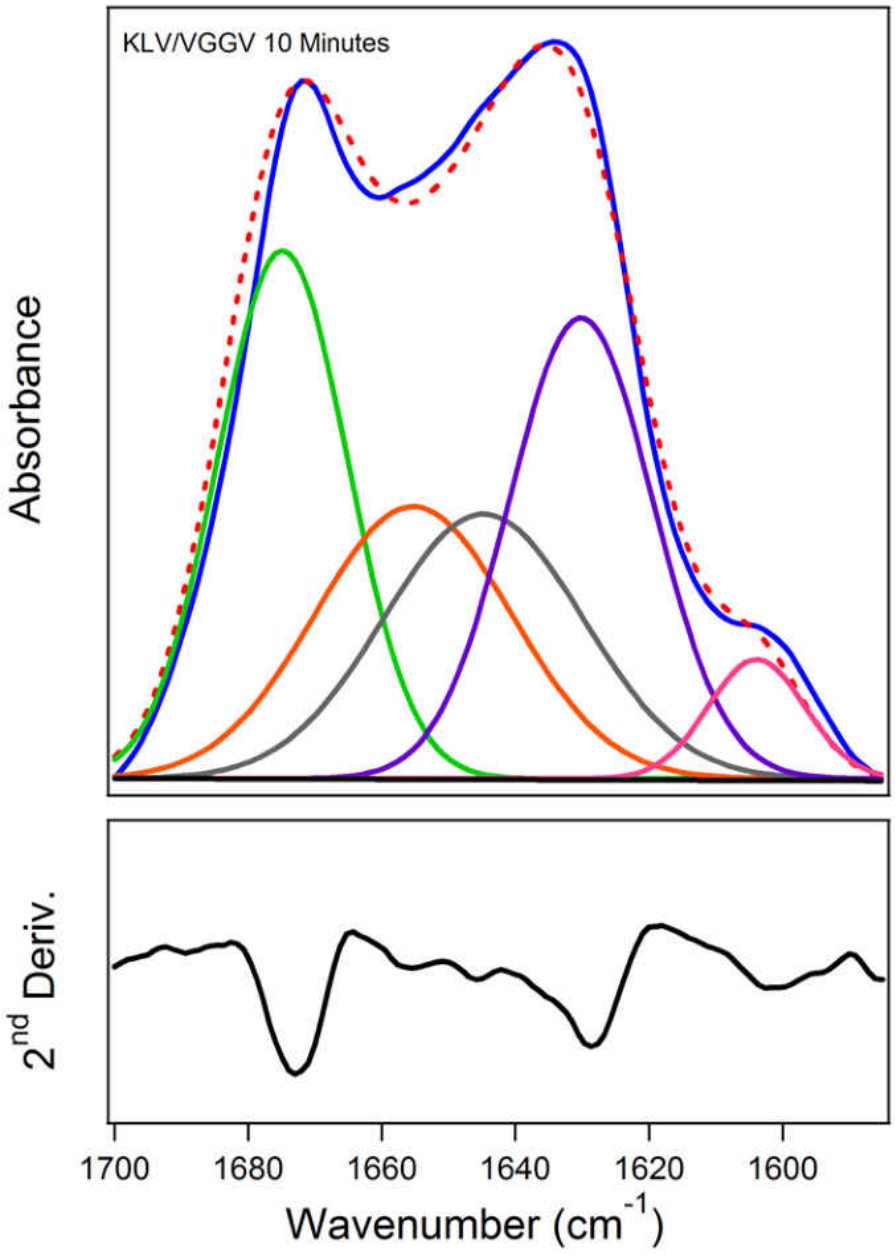
KLV/VGGV 10 Minutes
Absorbance
2nd Deriv.
1700
1680
1660
1640
1620
1600
Wavenumber (cm-1)

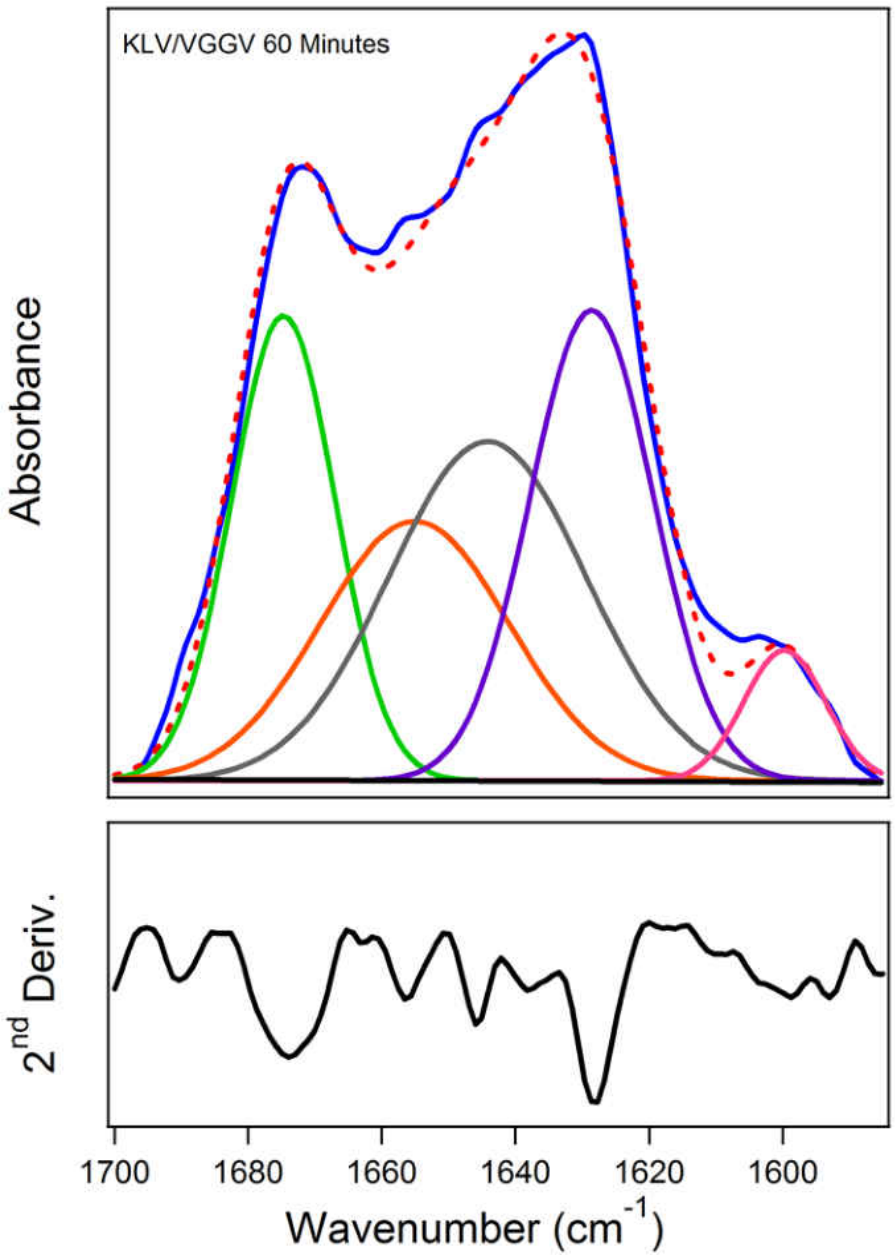
KLV/VGGV 60 Minutes
Absorbance
2nd Deriv.
1700
1680
1660
1640
1620
1600
Wavenumber (cm-1)

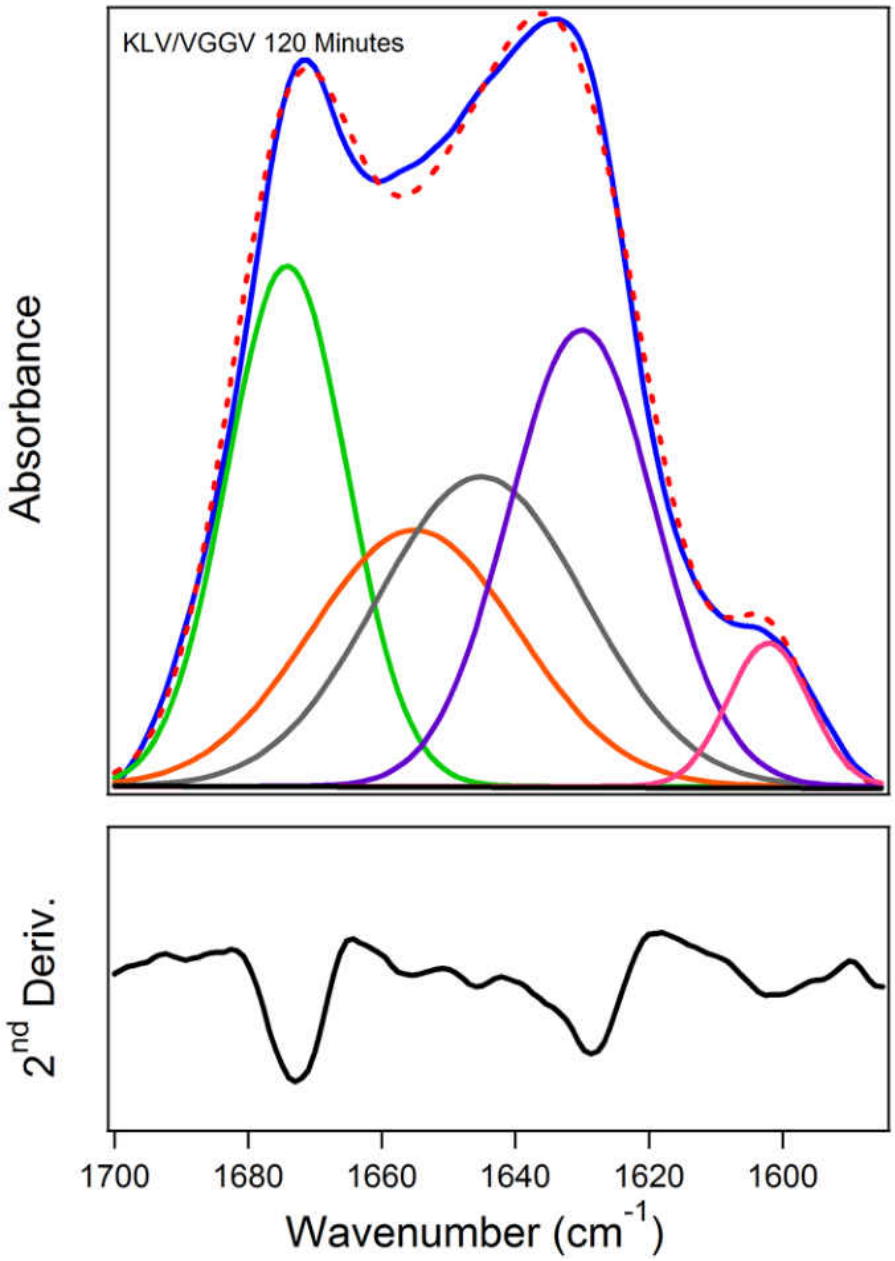
KLV/VGGV 120 Minutes
Absorbance
2nd Deriv.
1700
1680
1660
1640
1620
1600
Wavenumber (cm-1)

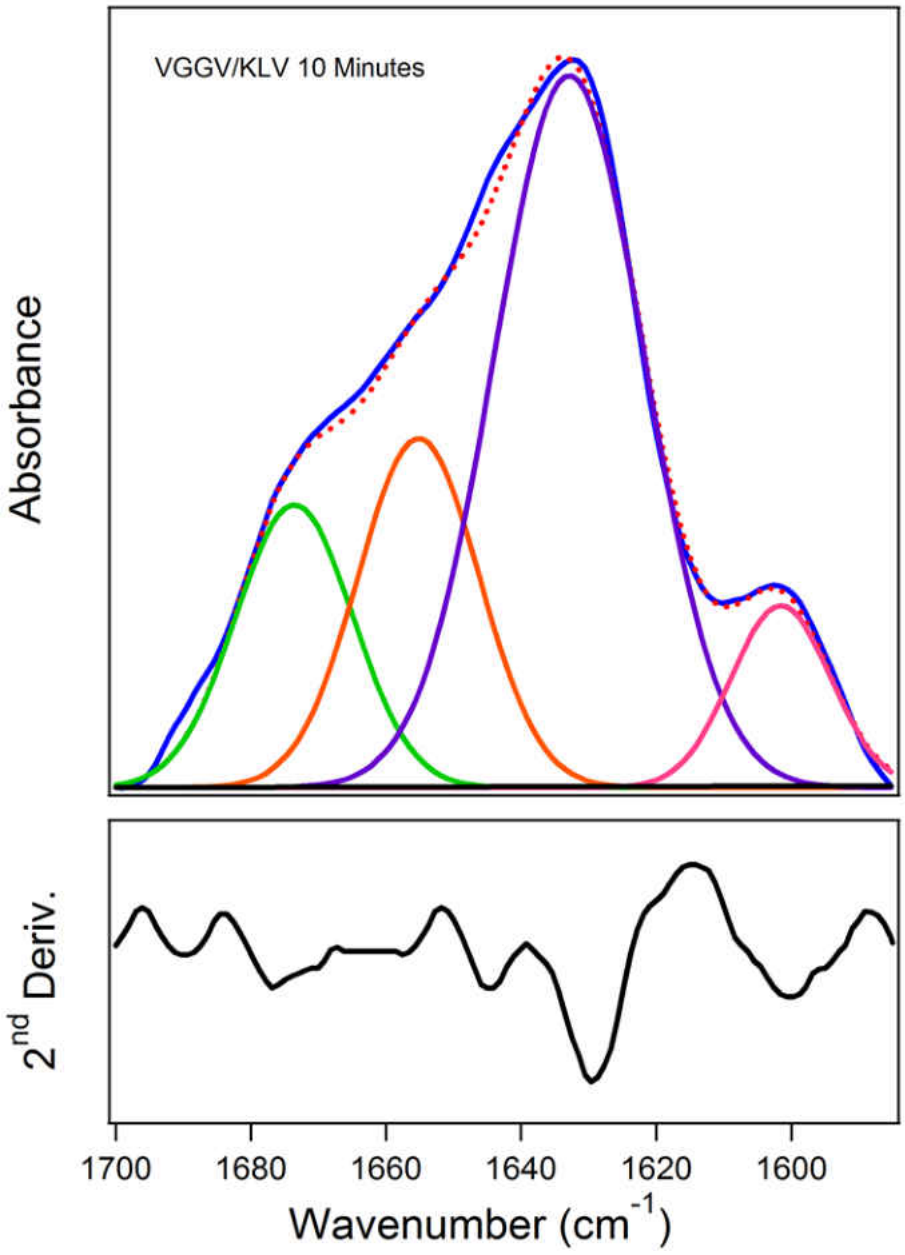
VGGV/KLV 10 Minutes
Absorbance
2nd Deriv.
1700
1680
1660
1640
1620
1600
Wavenumber (cm-1)

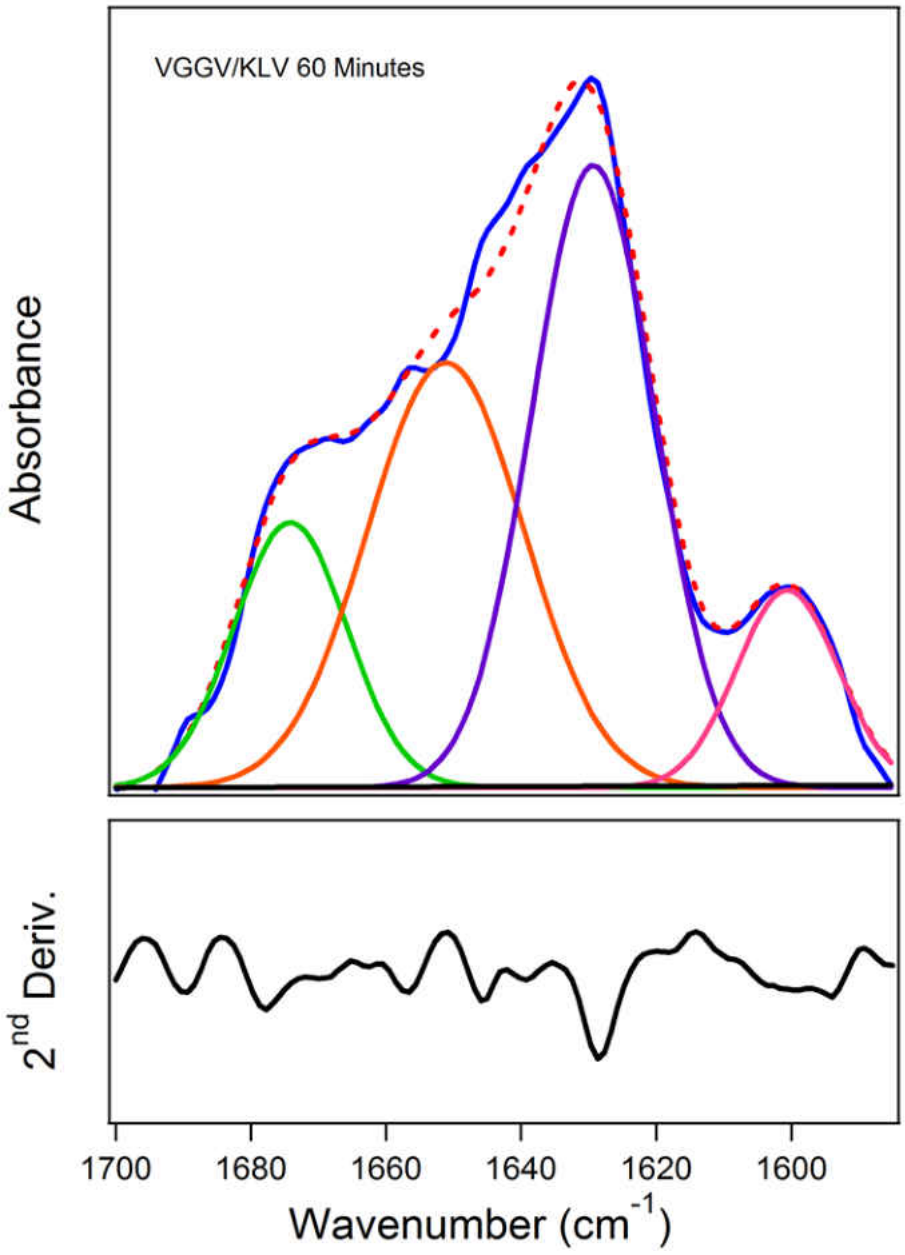
VGGV/KLV 60 Minutes
Absorbance
2nd Deriv.
1700
1680
1660
1640
1620
1600
Wavenumber (cm-1)

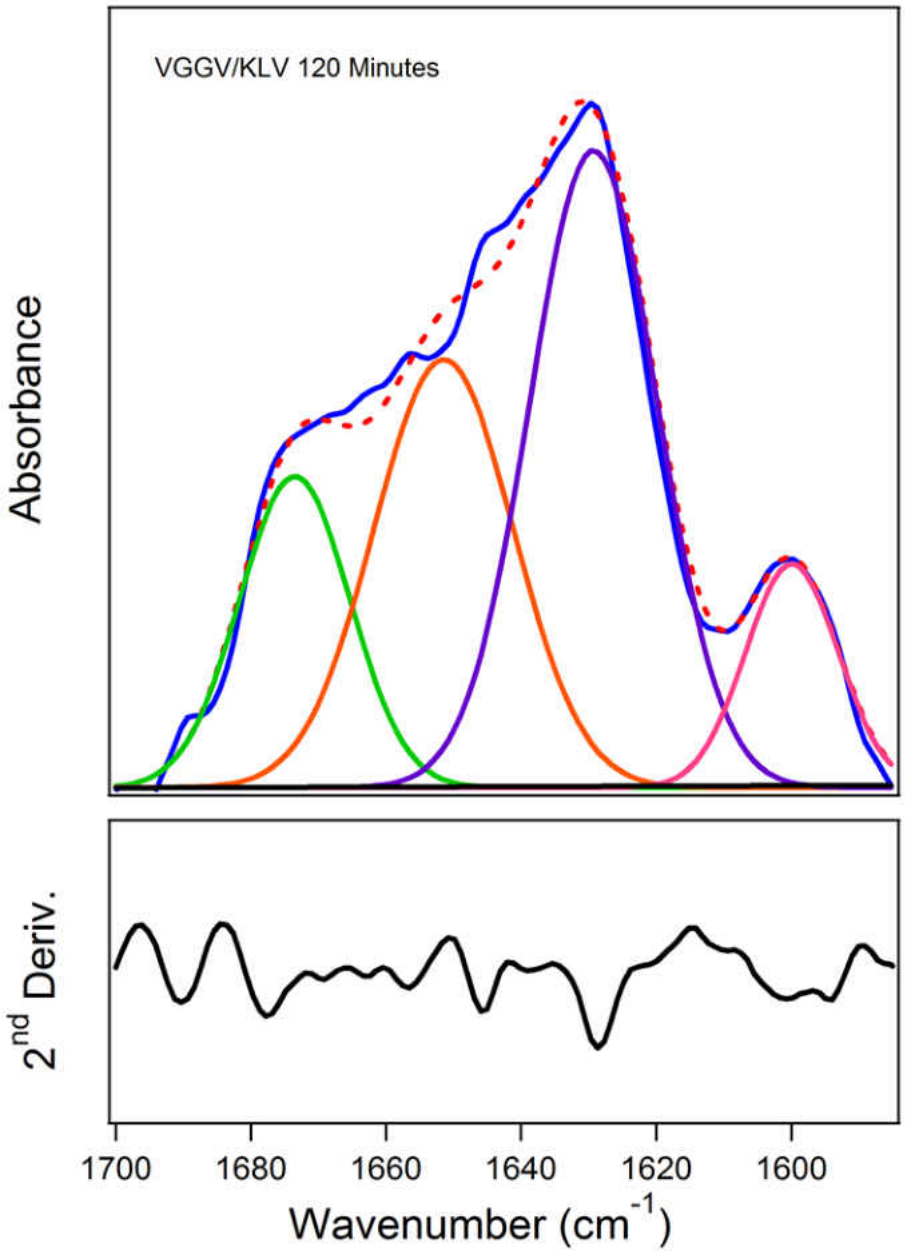
VGGV/KLV 120 Minutes
Absorbance
2nd Deriv.
1700
1680
1660
1640
1620
1600
Wavenumber (cm-1)

Low Salt Conditions

Table 6. Distribution of secondary structures in 10 mM phosphate pD 6.8 as calculated by curve fitting. Numbers are the averages at 10, 60, and 120 minutes in buffer, label combination refers to the fraction of the peak corresponding to the ^{13}C-label in KLV/VGG and VGGV/KLV spectra. Components counted as other, primarily unordered structure, are not included in the table.

Low Salt	$A\beta_{1-42}$	$A\beta^{pE3-42}$	1:1
β-turn	26.2±5.2	21.3±3.6	25.0±5.5
α-helix	21.8±7.9	21.5±8.1	15.3±6.0
β-sheet	34.2±9.5	35.2±10.2	36.5±8.5
^{13}C-Label KLV	4.9±0.6	6.7±0.5	6.3±0.6
^{13}C-Label VGGV	7.4±0.4	12.9±0.4	14.2±0.2
^{13}C-Label Combination	-	-	8.2±1.3

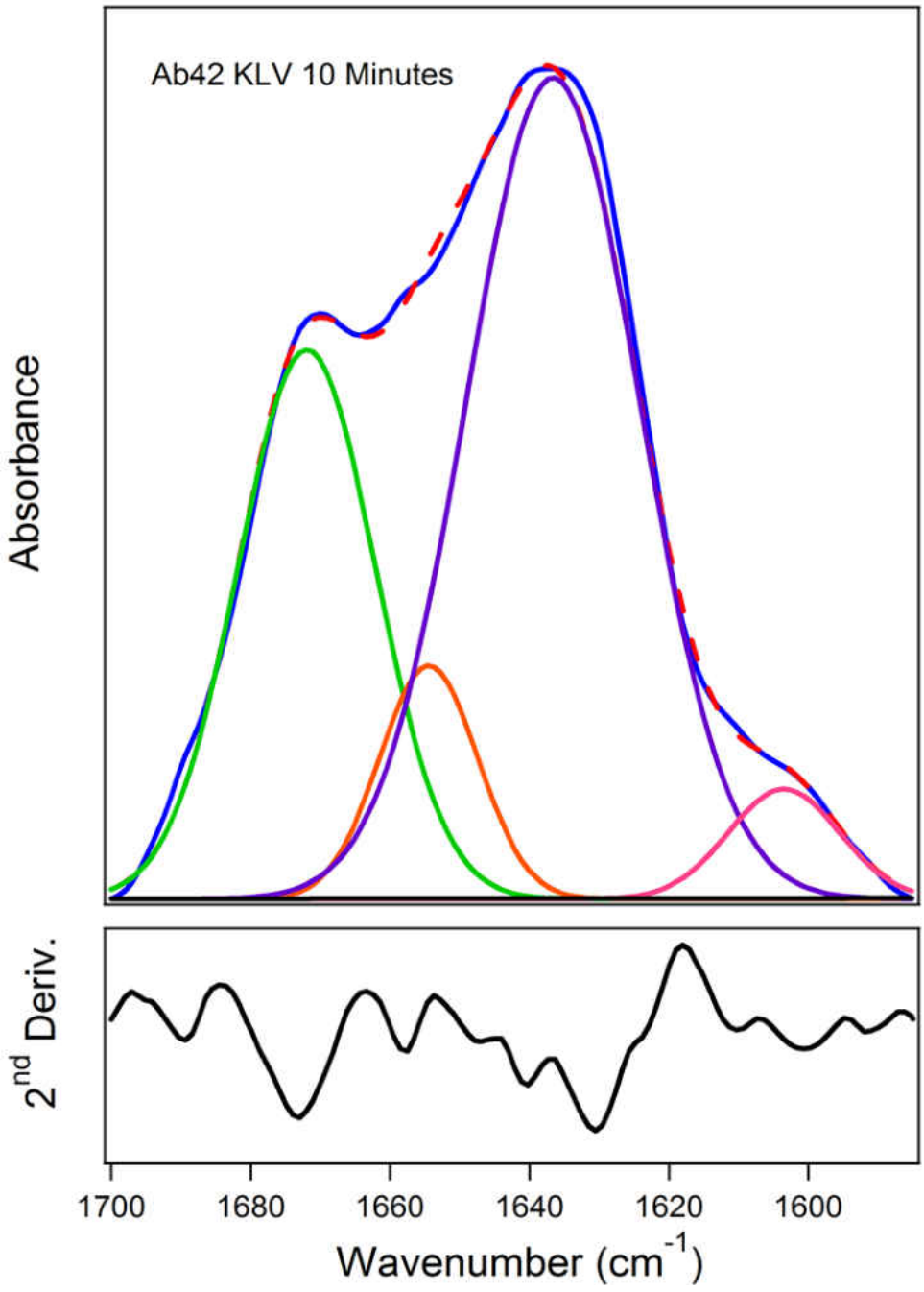
Ab42 KLV 10 Minutes
Absorbance
2nd Deriv.
1700
1680
1660
1640
1620
1600
Wavenumber (cm-1)

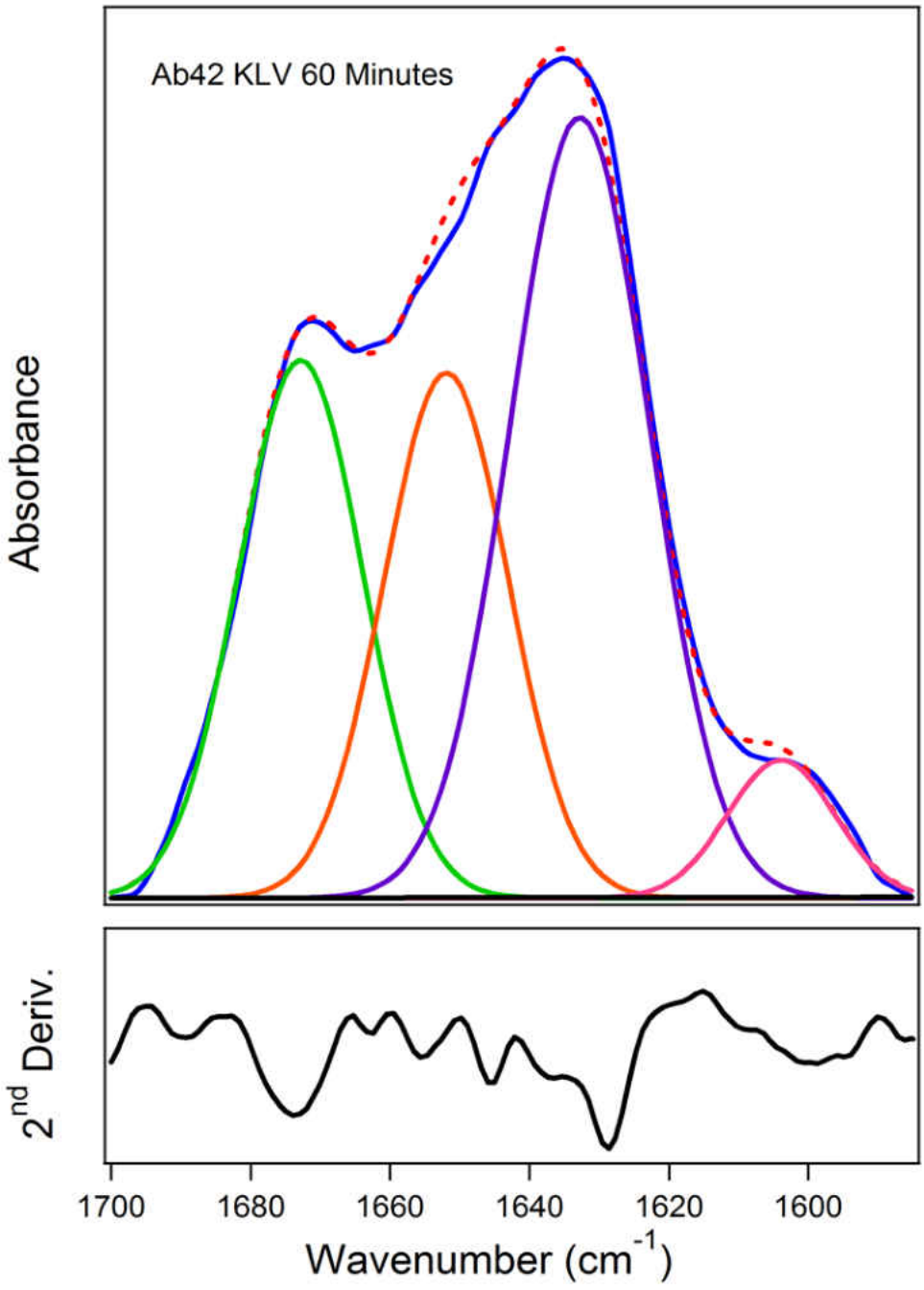
Ab42 KLV 60 Minutes
Absorbance
2nd Deriv.
1700
1680
1660
1640
1620
1600
Wavenumber (cm-1)

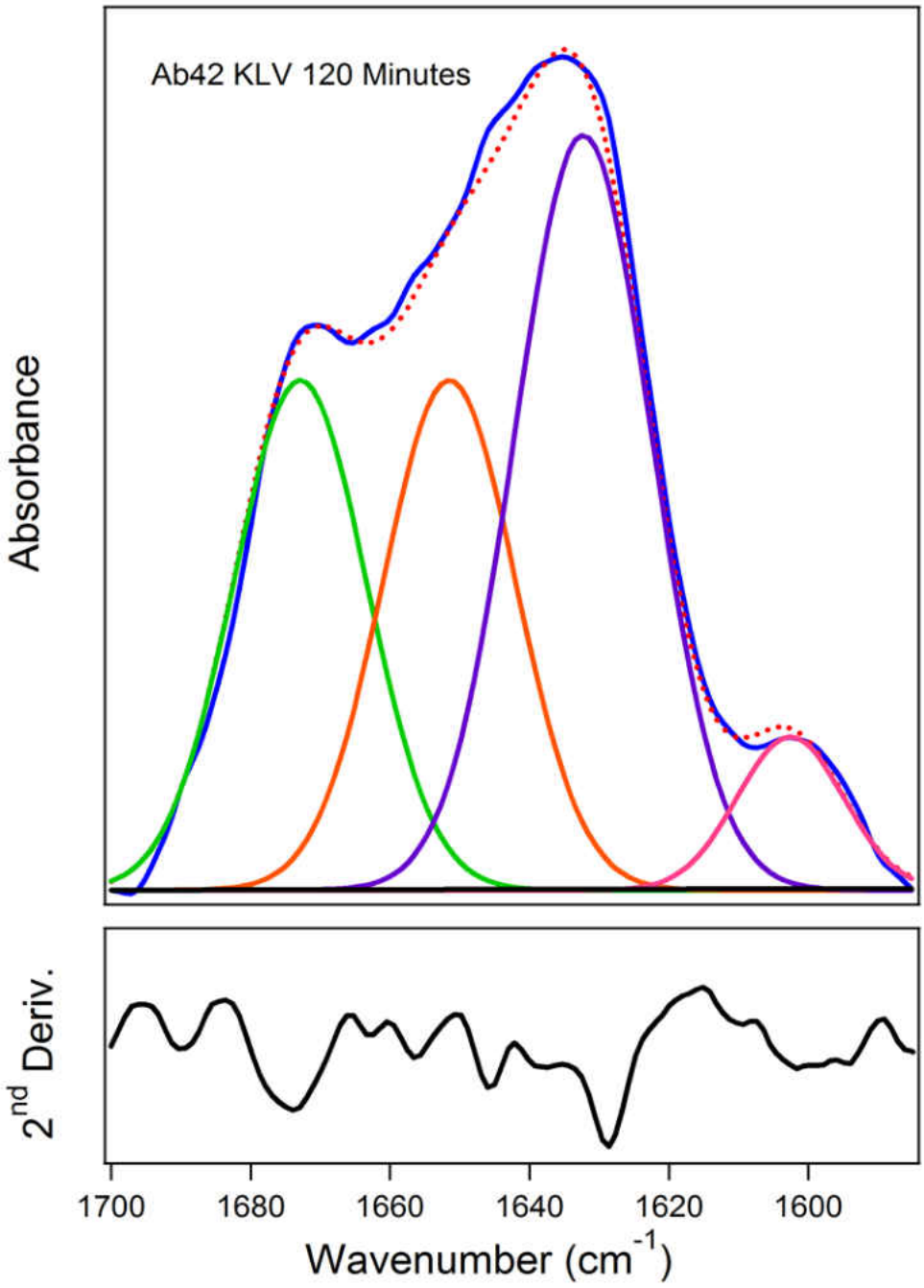
Ab42 KLV 120 Minutes
Absorbance
2nd Deriv.
1700
1680
1660
1640
1620
1600
Wavenumber (cm-1)

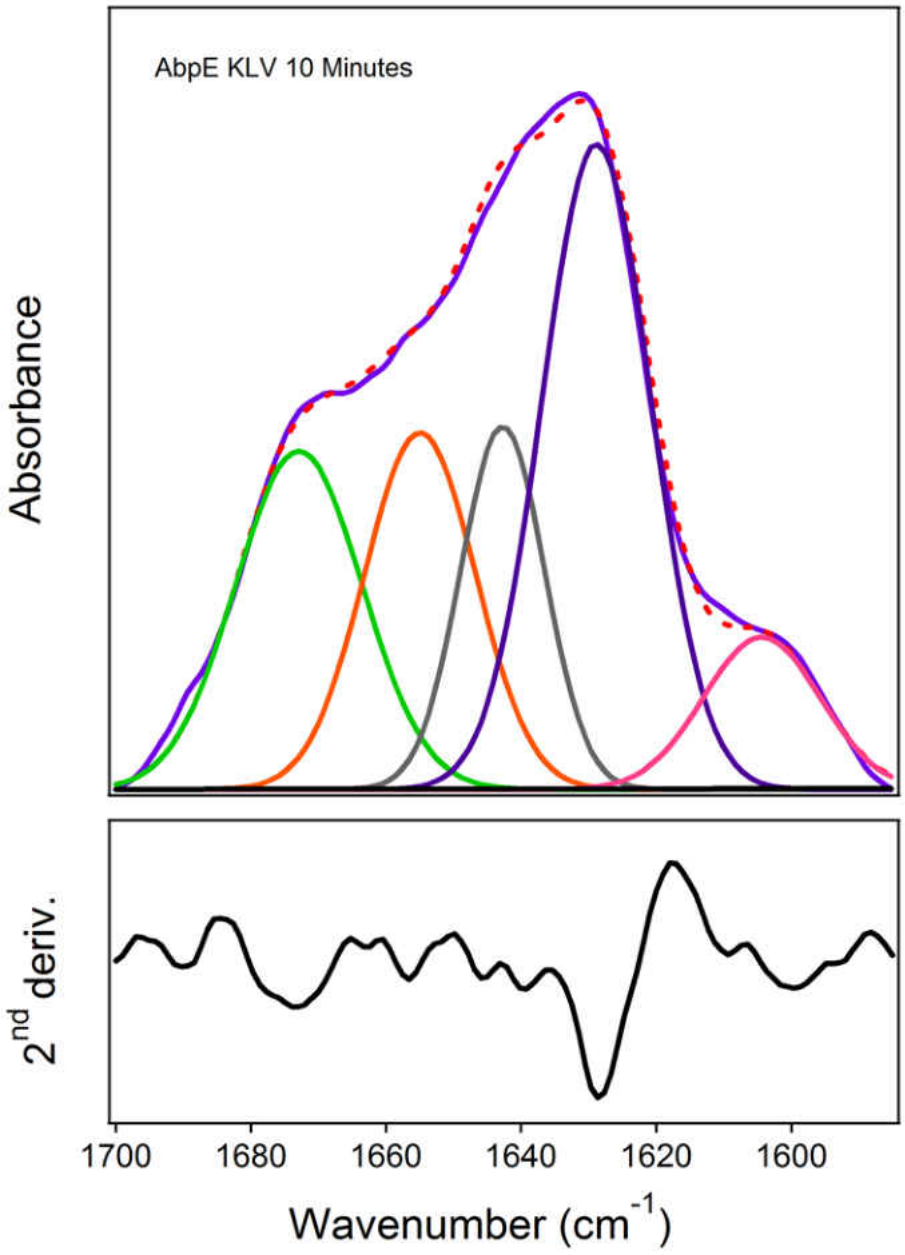
AbpE KLV 10 Minutes
Absorbance
2nd deriv.
1700
1680
1660
1640
1620
1600
Wavenumber (cm-1)

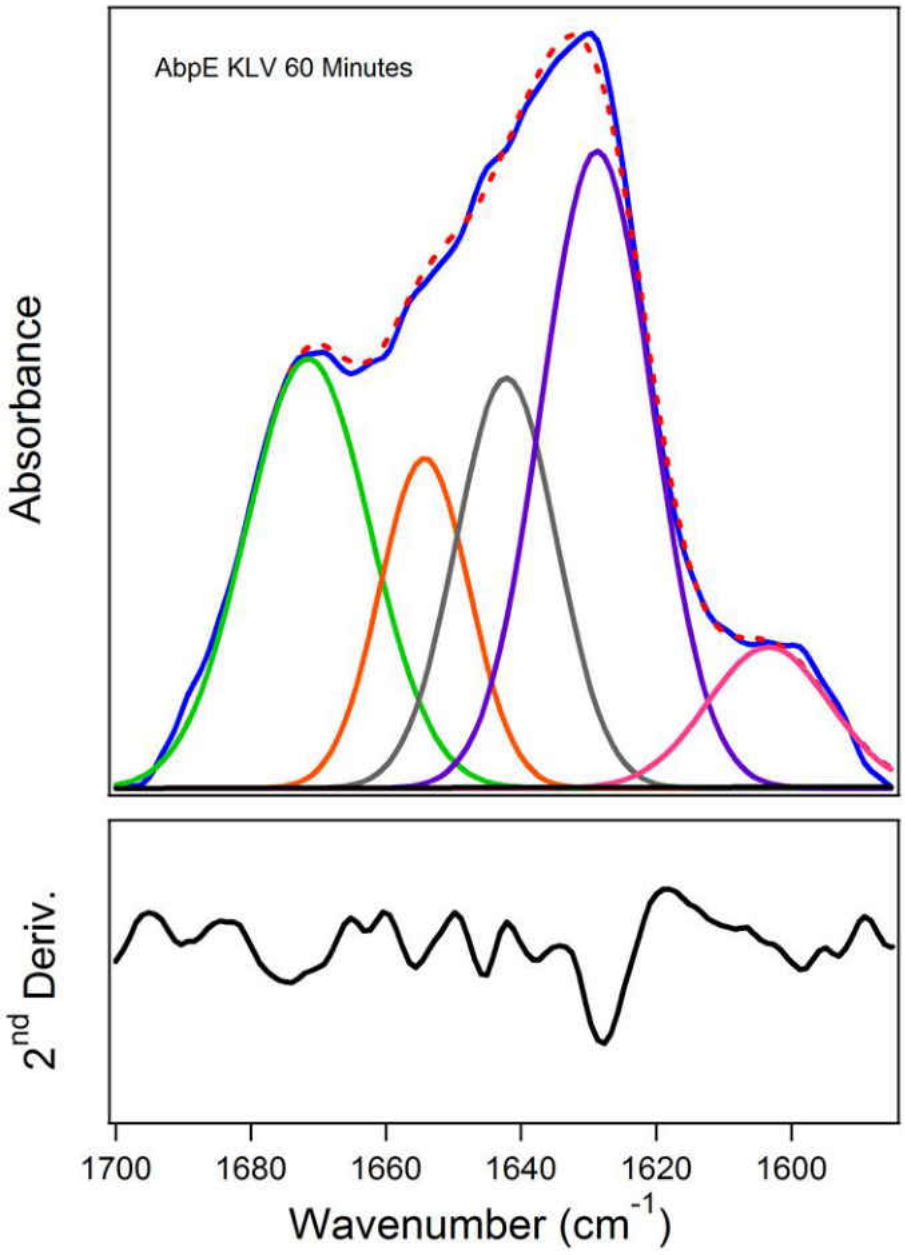
AbpE KLV 60 Minutes
Absorbance
2nd Deriv.
1700
1680
1660
1640
1620
1600
Wavenumber (cm-1)

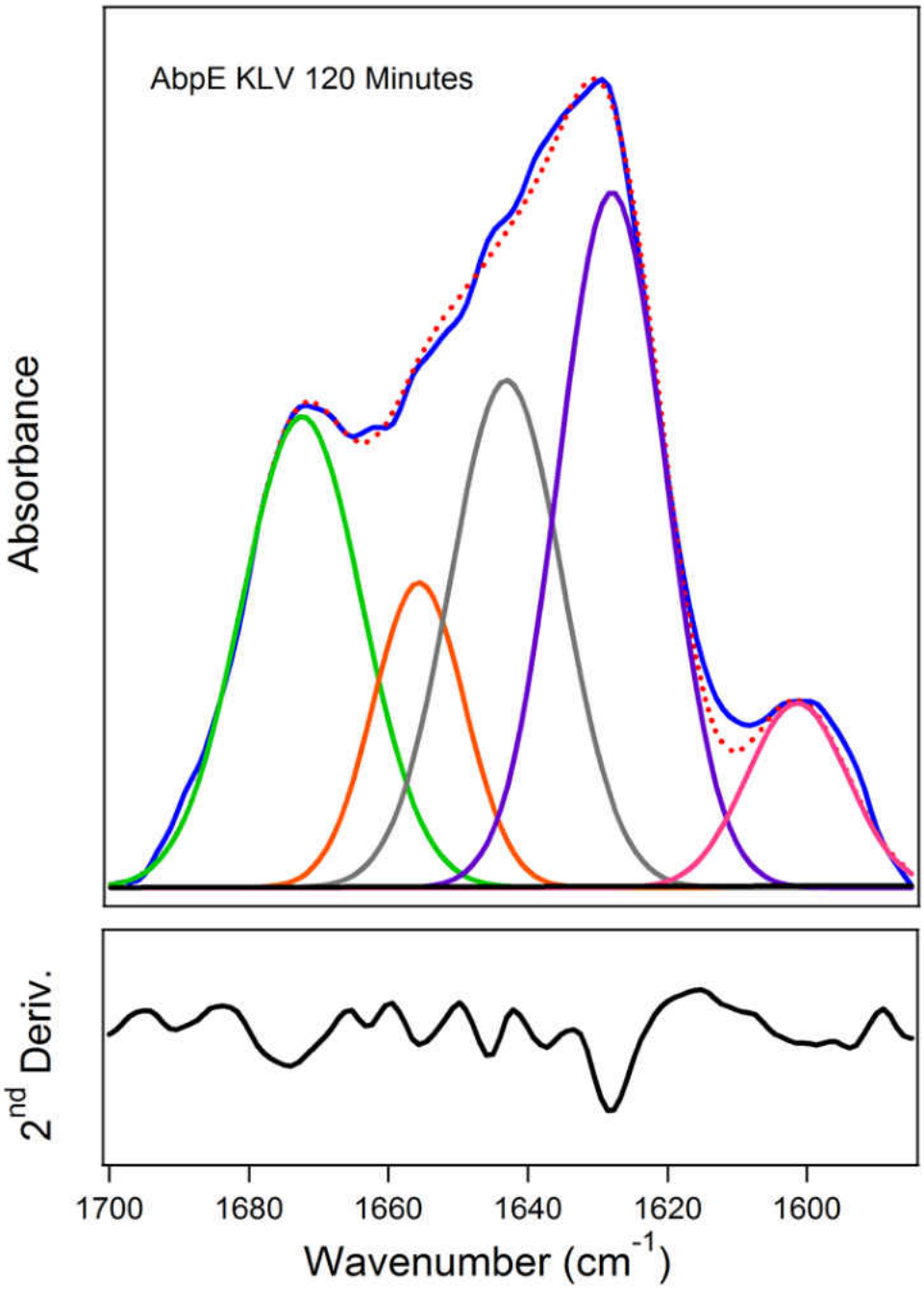
AbpE KLV 120 Minutes
Absorbance
2nd Deriv.
1700
1680
1660
1640
1620
1600
Wavenumber (cm-1)

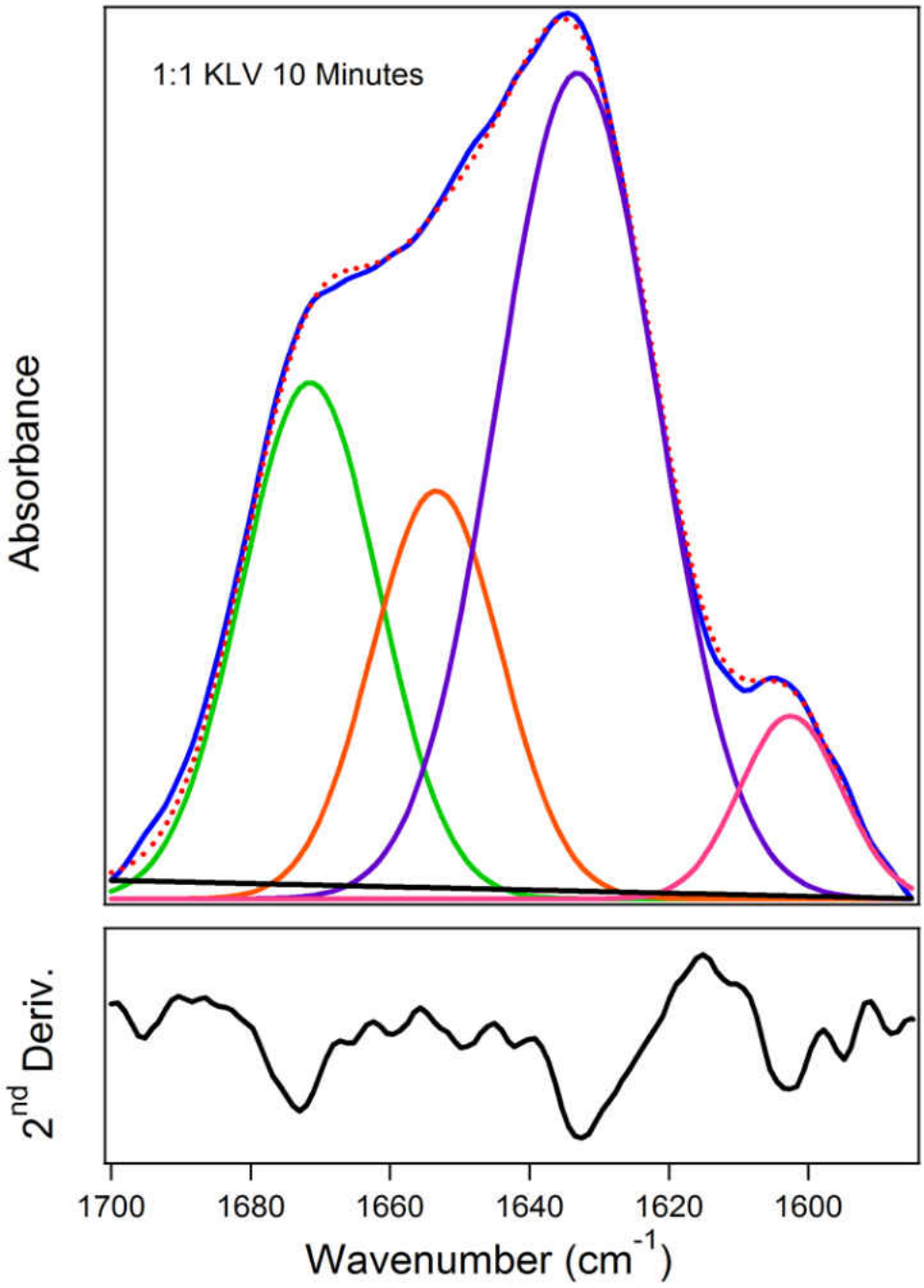
1:1 KLV 10 Minutes
Absorbance
2nd Deriv.
1700
1680
1660
1640
1620
1600
Wavenumber (cm-1)

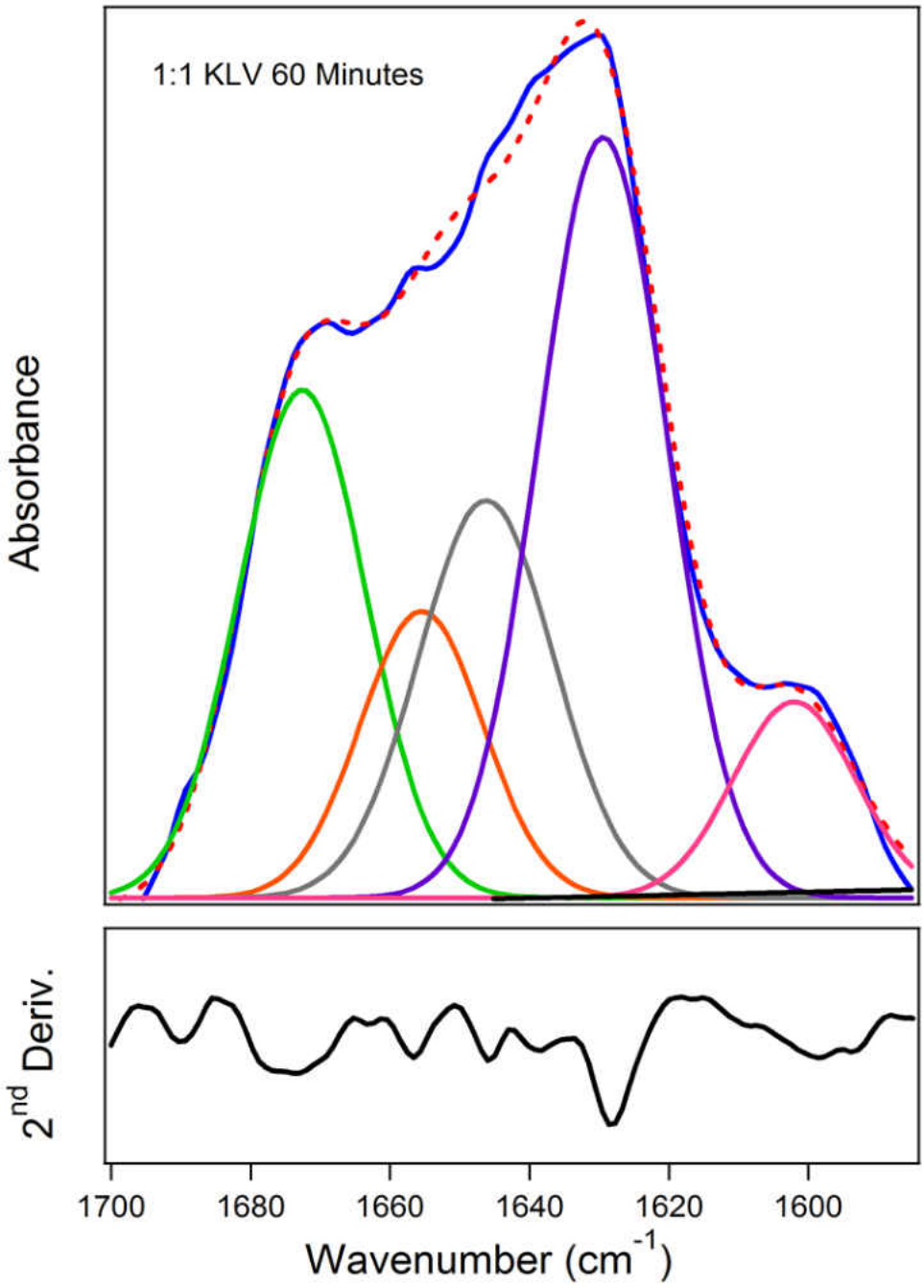
1:1 KLV 60 Minutes
Absorbance
2nd Deriv.
1700
1680
1660
1640
1620
1600
Wavenumber (cm-1)

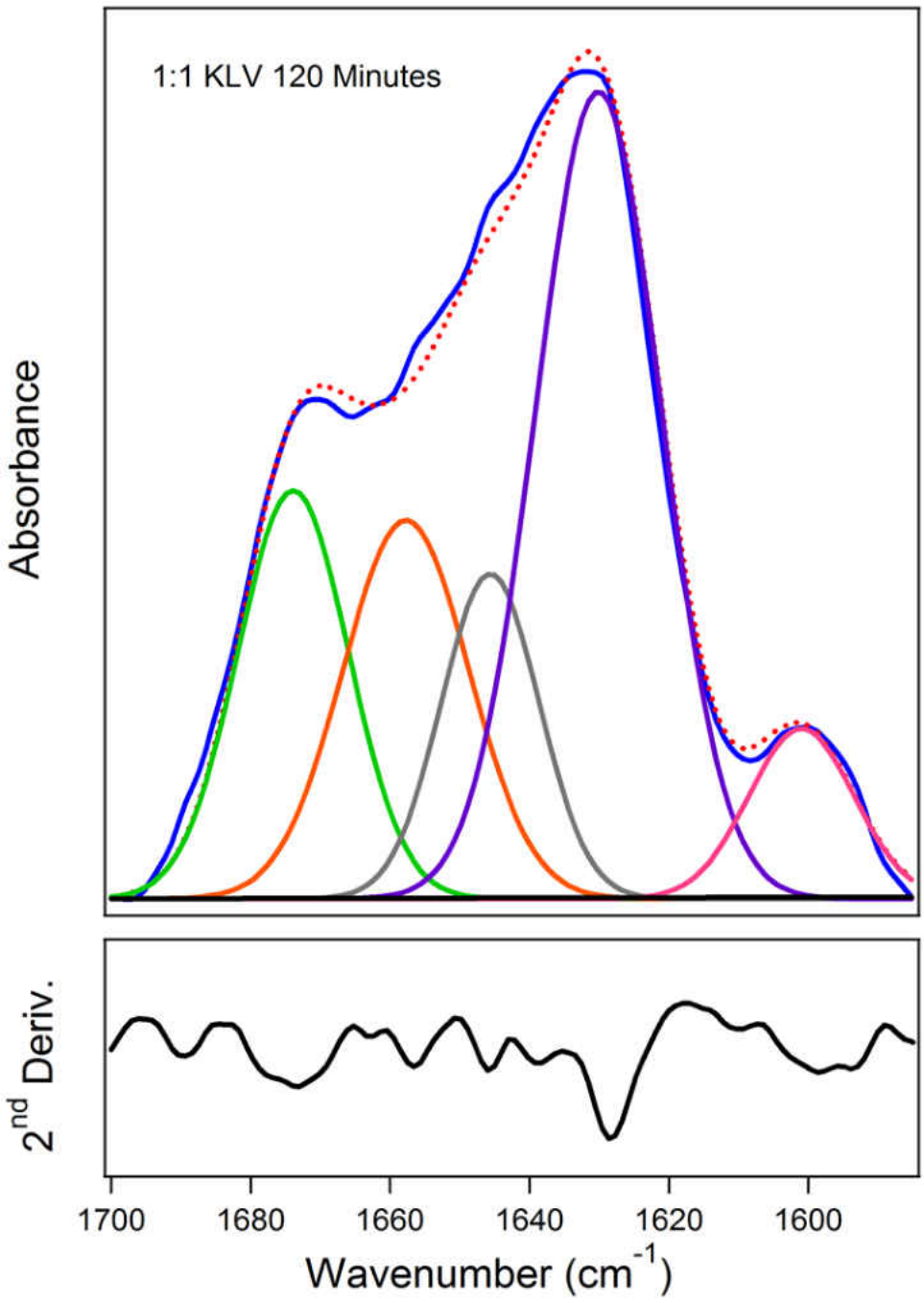
1:1 KLV 120 Minutes
Absorbance
2nd Deriv.
1700
1680
1660
1640
1620
1600
Wavenumber (cm-1)

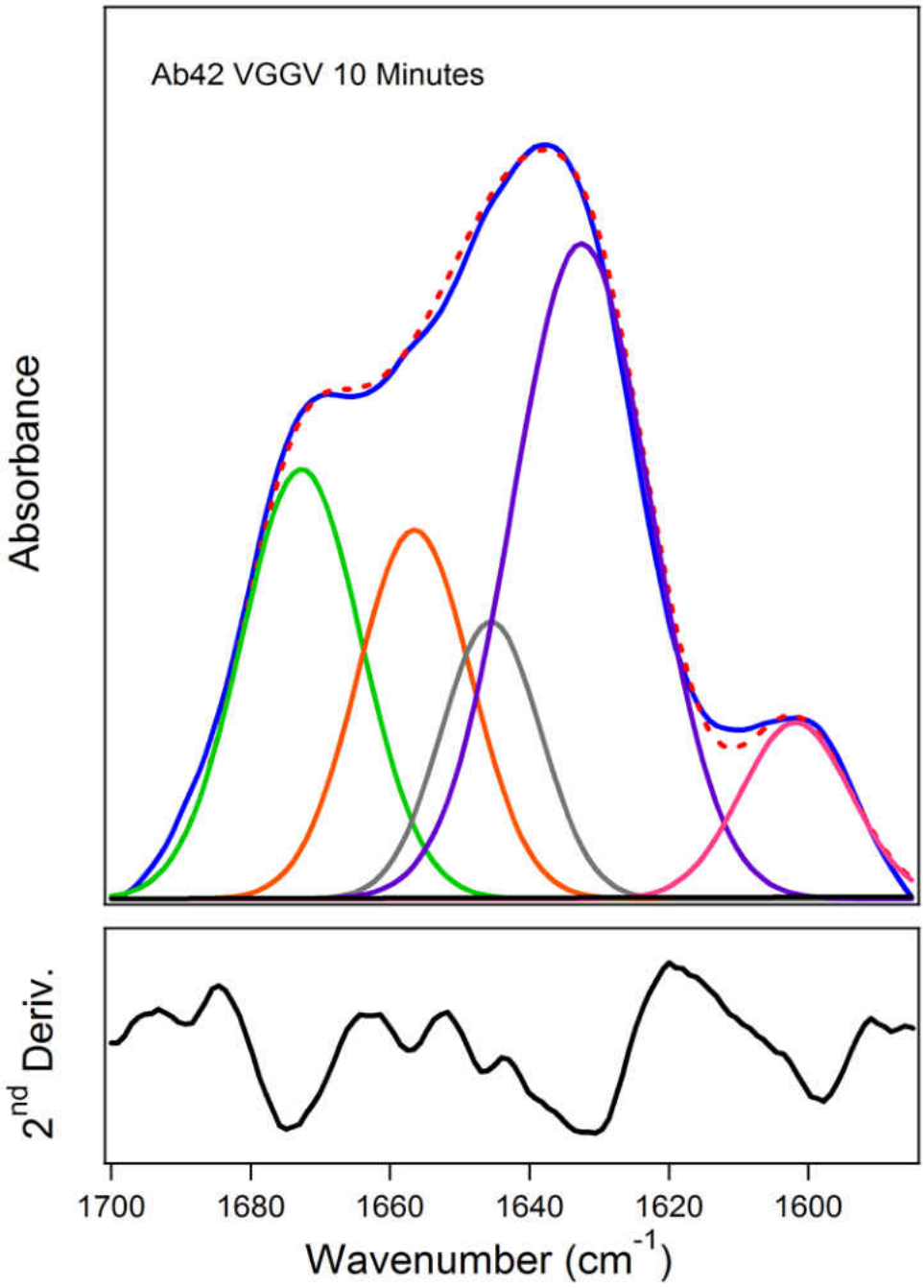
Ab42 VGGV 10 Minutes
Absorbance
2nd Deriv.
1700
1680
1660
1640
1620
1600
Wavenumber (cm-1)

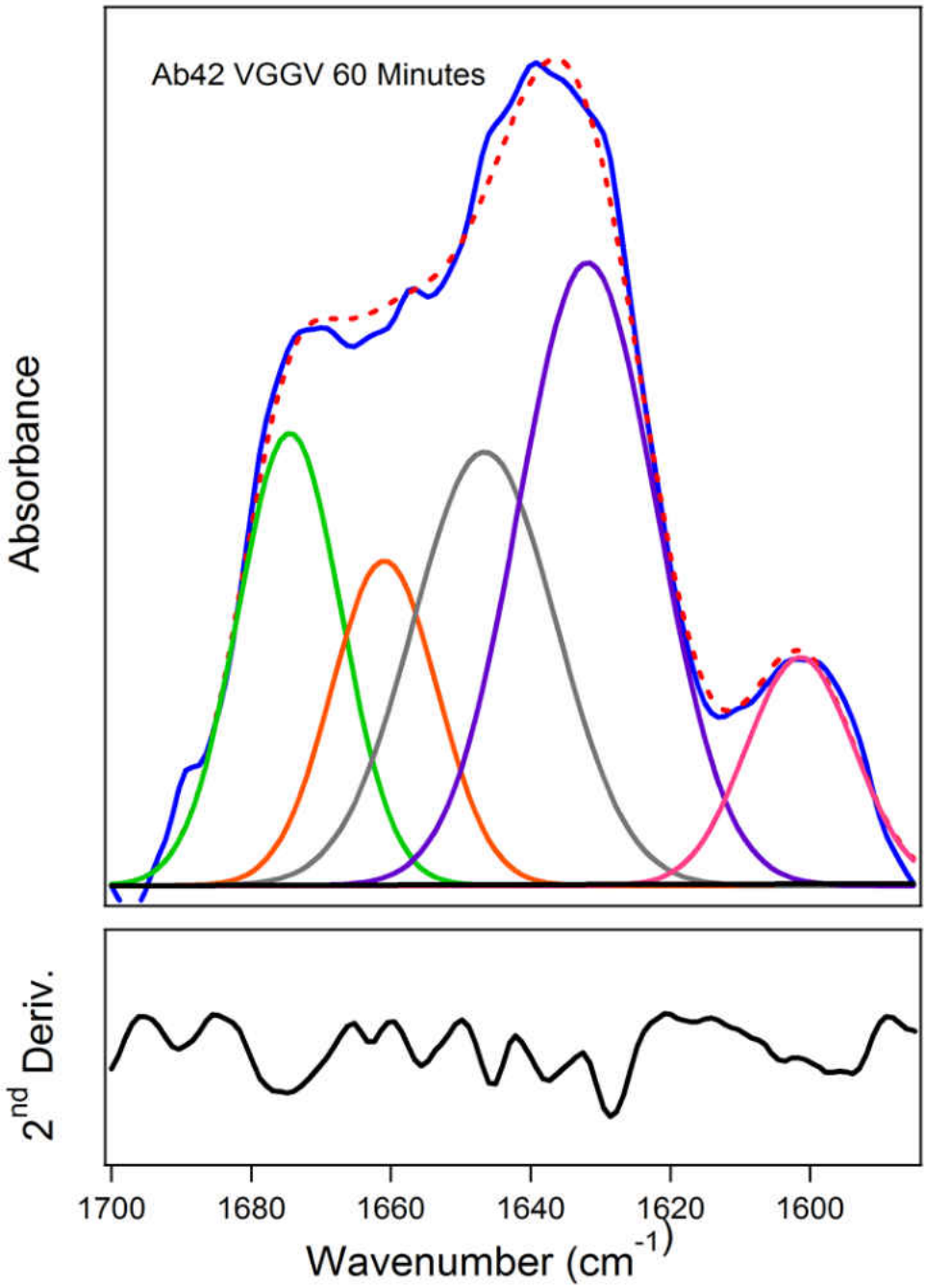
Ab42 VGGV 60 Minutes
Absorbance
2nd Deriv.
1700
1680
1660
1640
1620
1600
Wavenumber (cm-1)

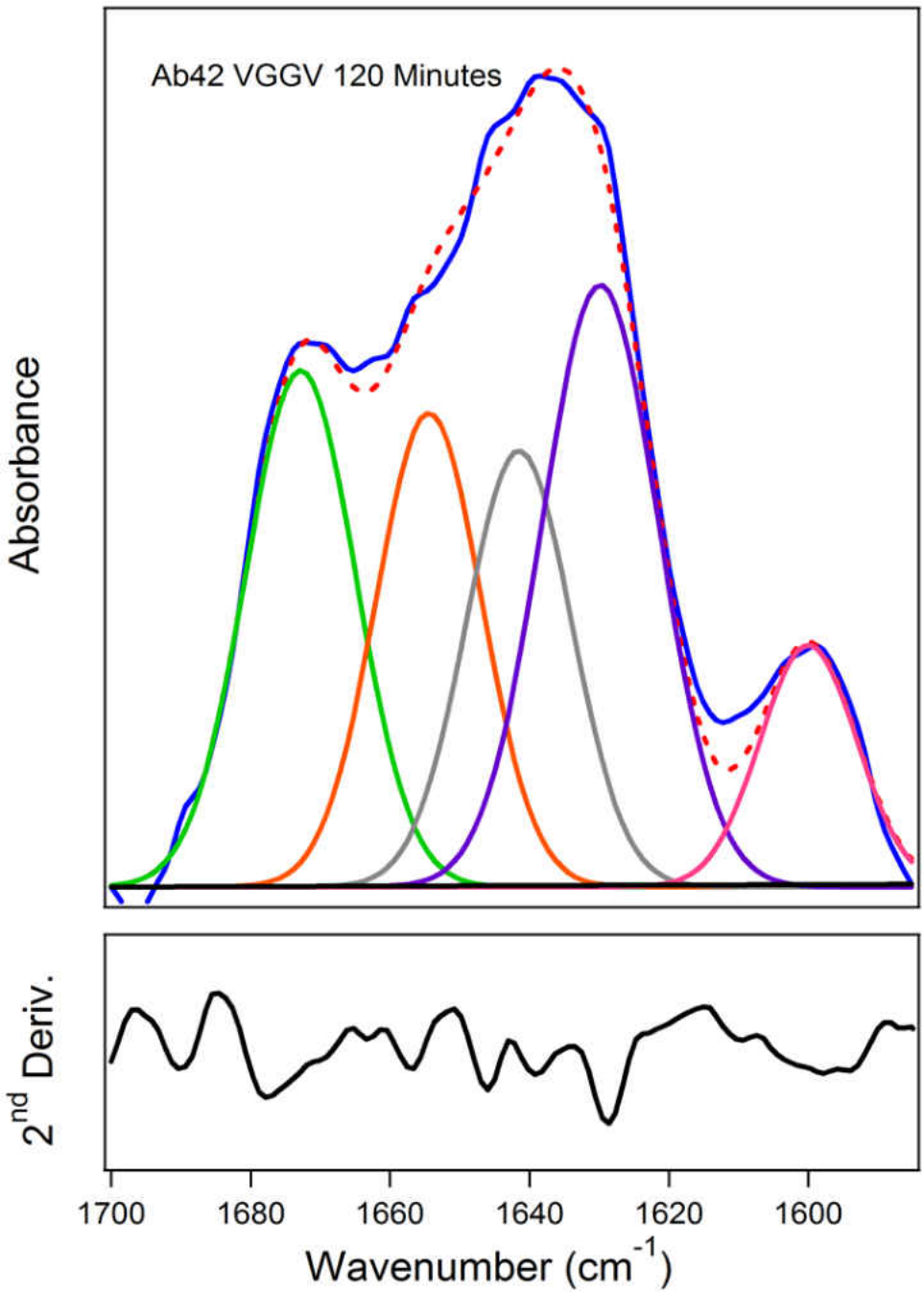
Ab42 VGGV 120 Minutes
Absorbance
2nd Deriv.
1700
1680
1660
1640
1620
1600
Wavenumber (cm-1)

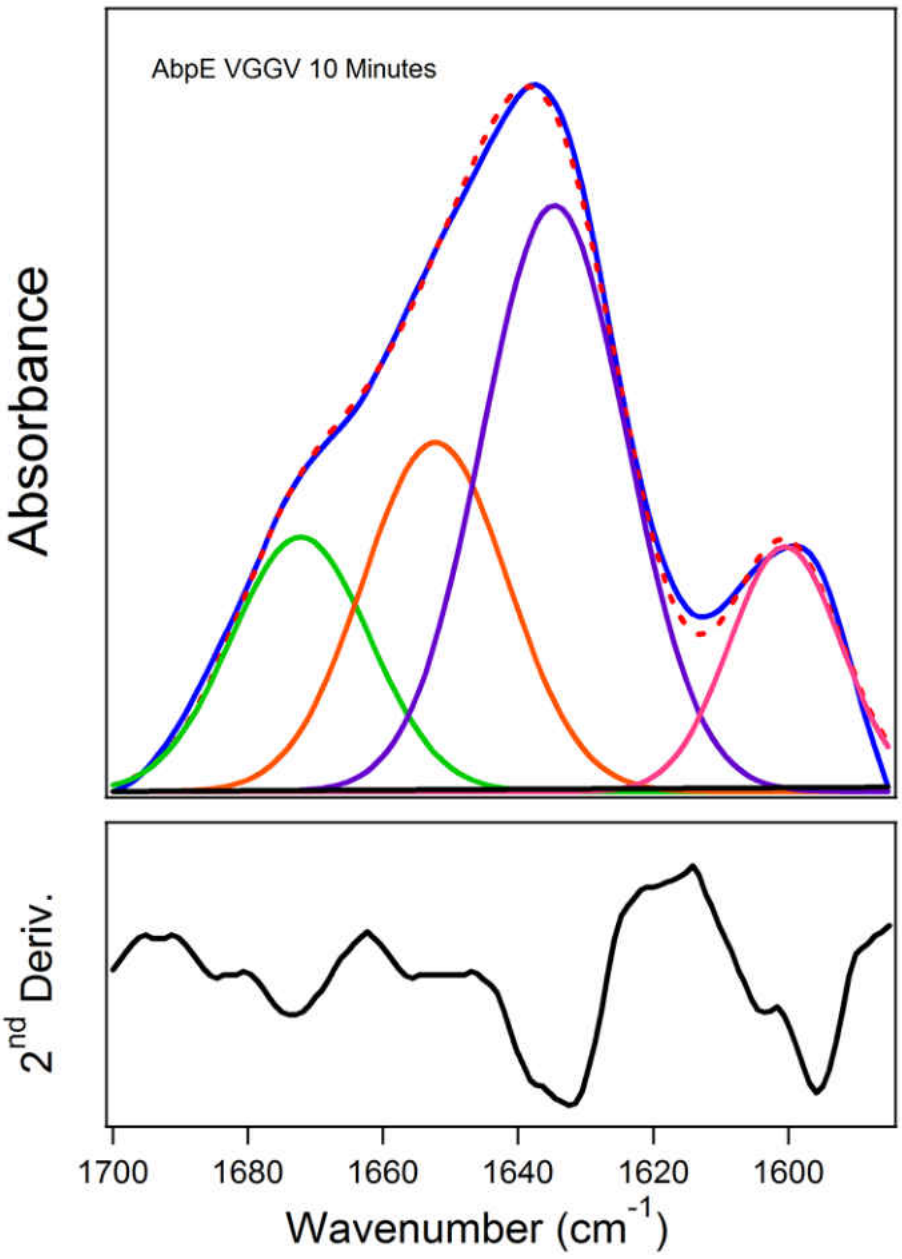
AbpE VGGV 10 Minutes
Absorbance
2nd Deriv.
1700
1680
1660
1640
1620
1600
Wavenumber (cm-1)

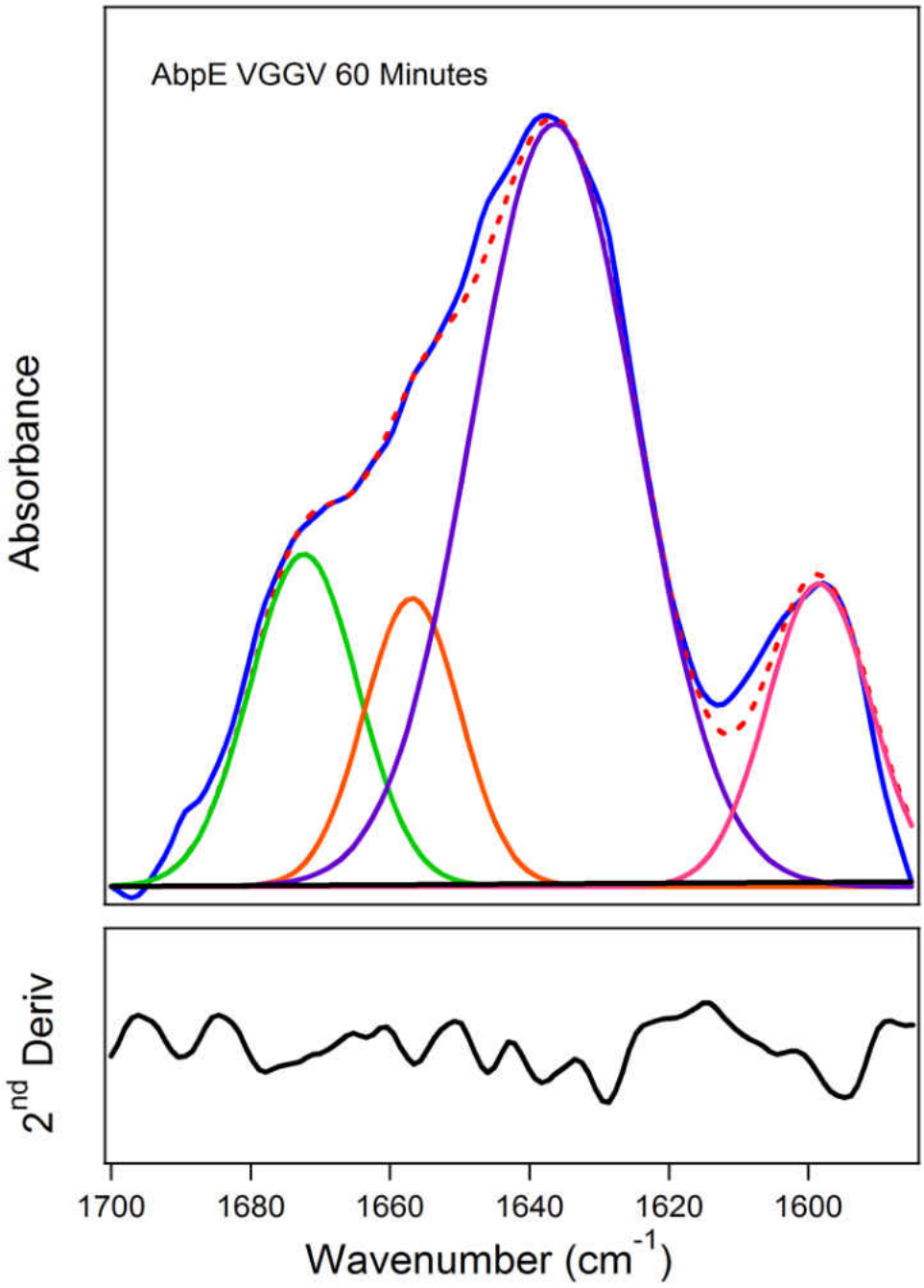
AbpE VGGV 60 Minutes
Absorbance
2nd Deriv
1700
1680
1660
1640
1620
1600
Wavenumber (cm-1)

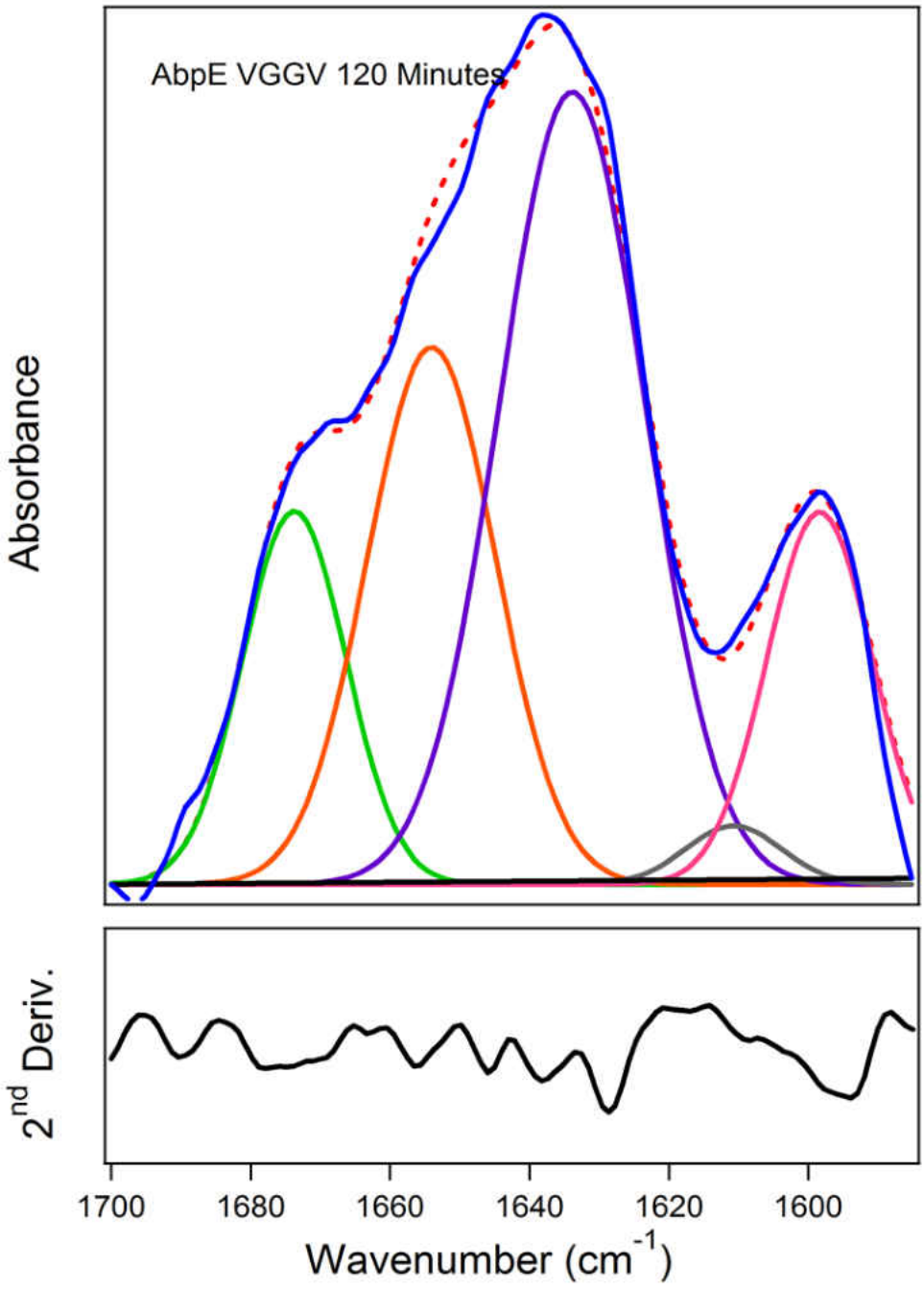
AbpE VGGV 120 Minutes
Absorbance
2nd Deriv.
1700
1680
1660
1640
1620
1600
Wavenumber (cm-1)

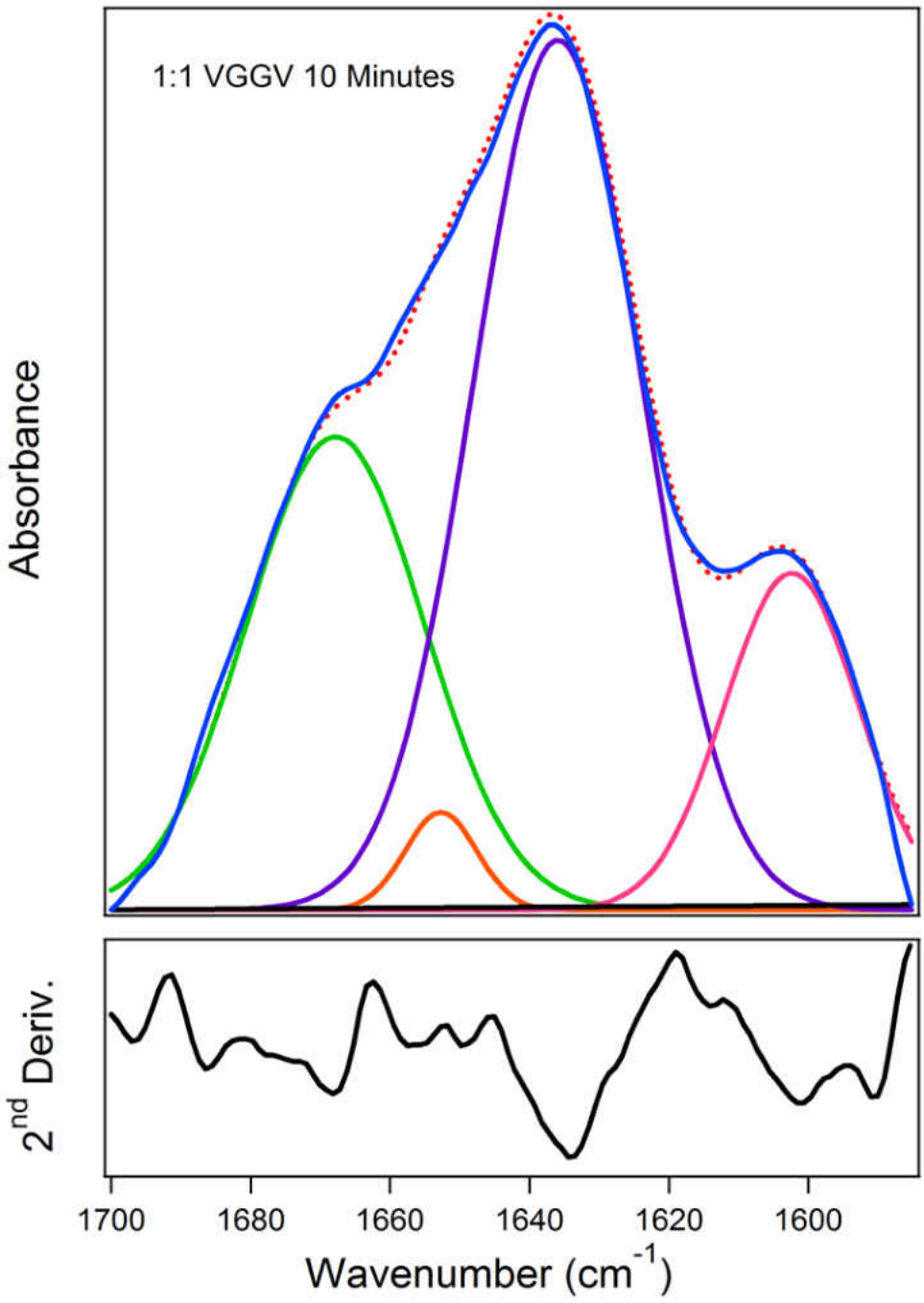
1:1 VGGV 10 Minutes
Absorbance
2nd Deriv.
1700
1680
1660
1640
1620
1600
Wavenumber (cm-1)

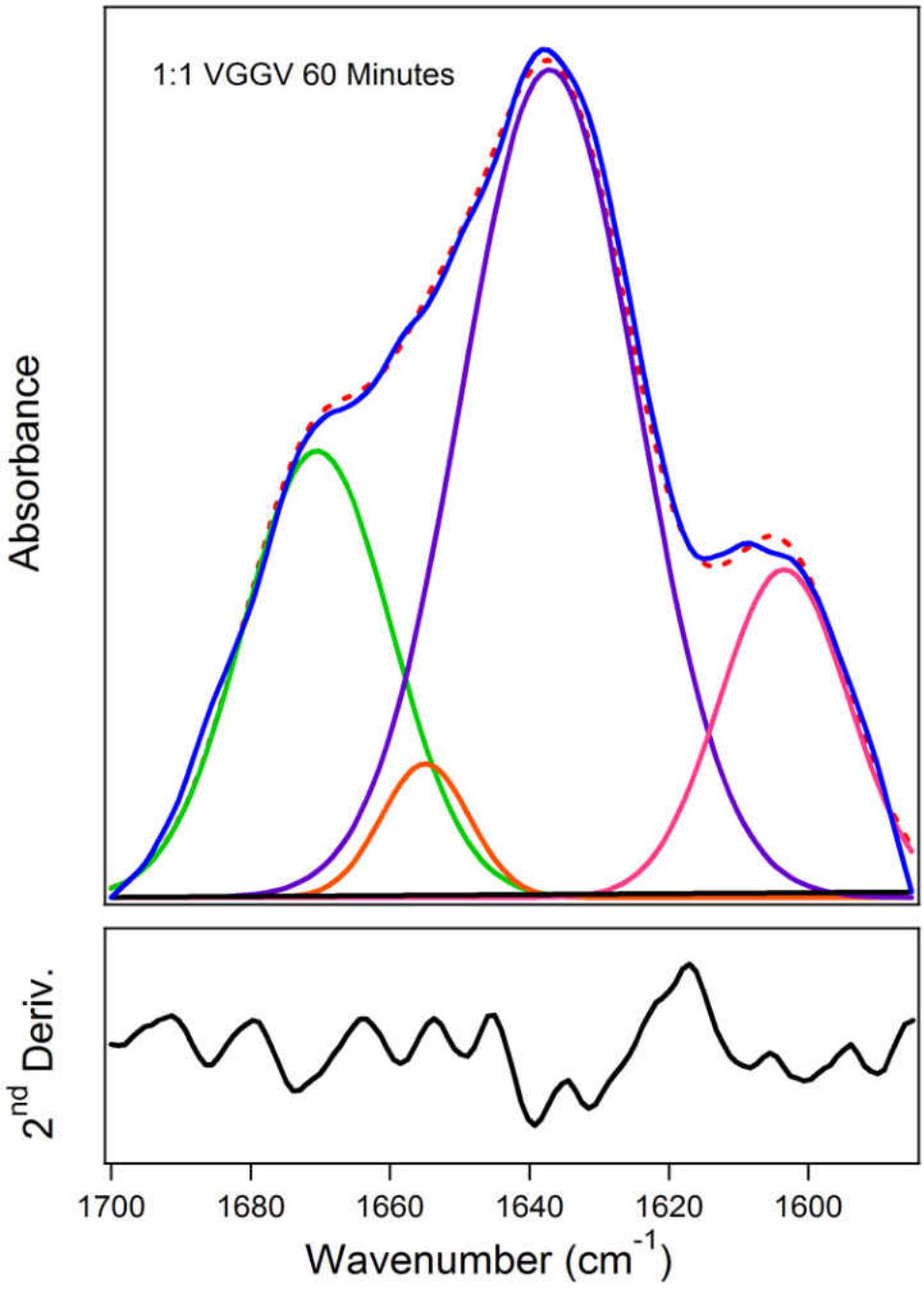
1:1 VGGV 60 Minutes
Absorbance
2nd Deriv.
1700
1680
1660
1640
1620
1600
Wavenumber (cm-1)

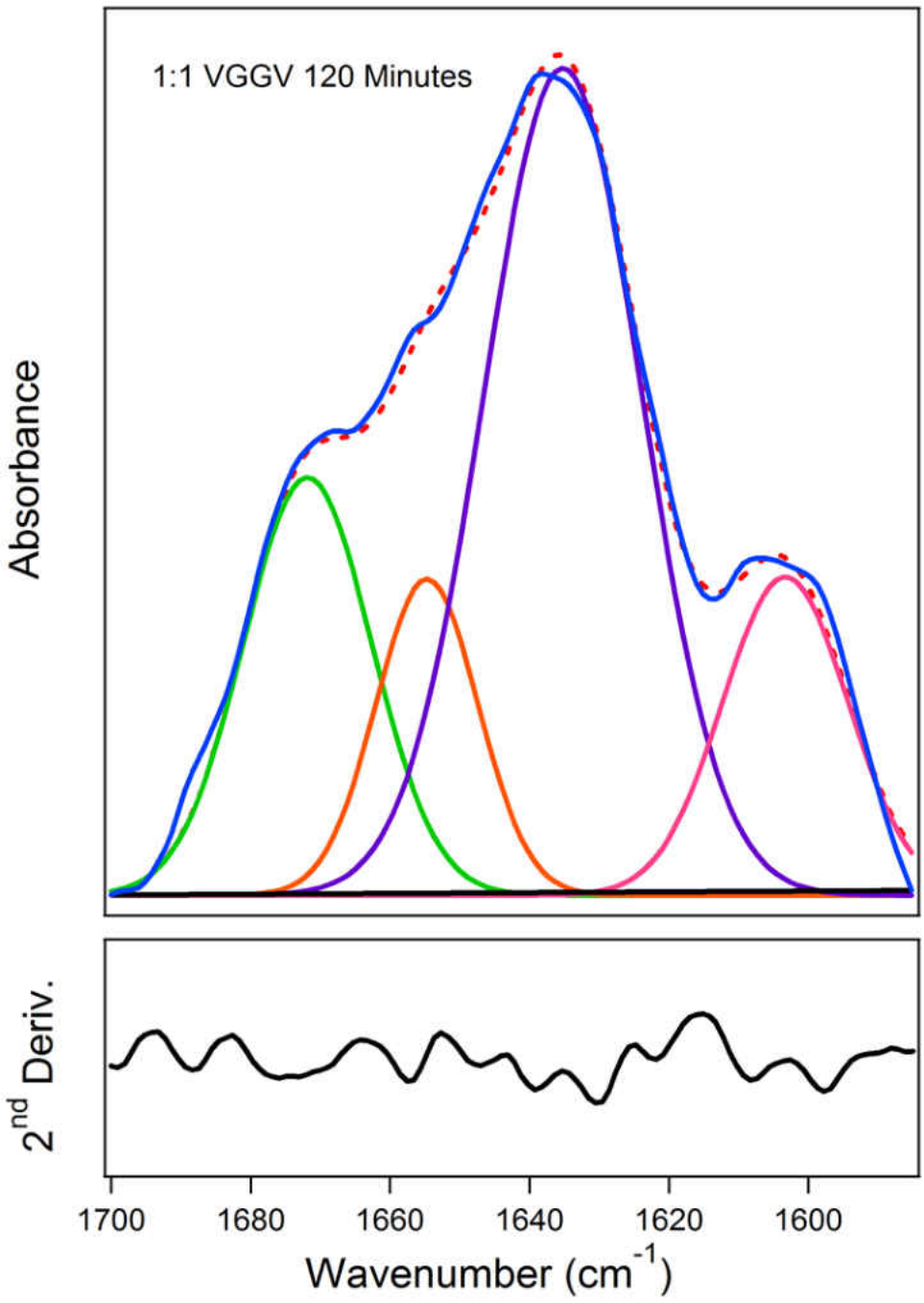
1:1 VGGV 120 Minutes
Absorbance
2nd Deriv.
1700
1680
1660
1640
1620
1600
Wavenumber (cm-1)

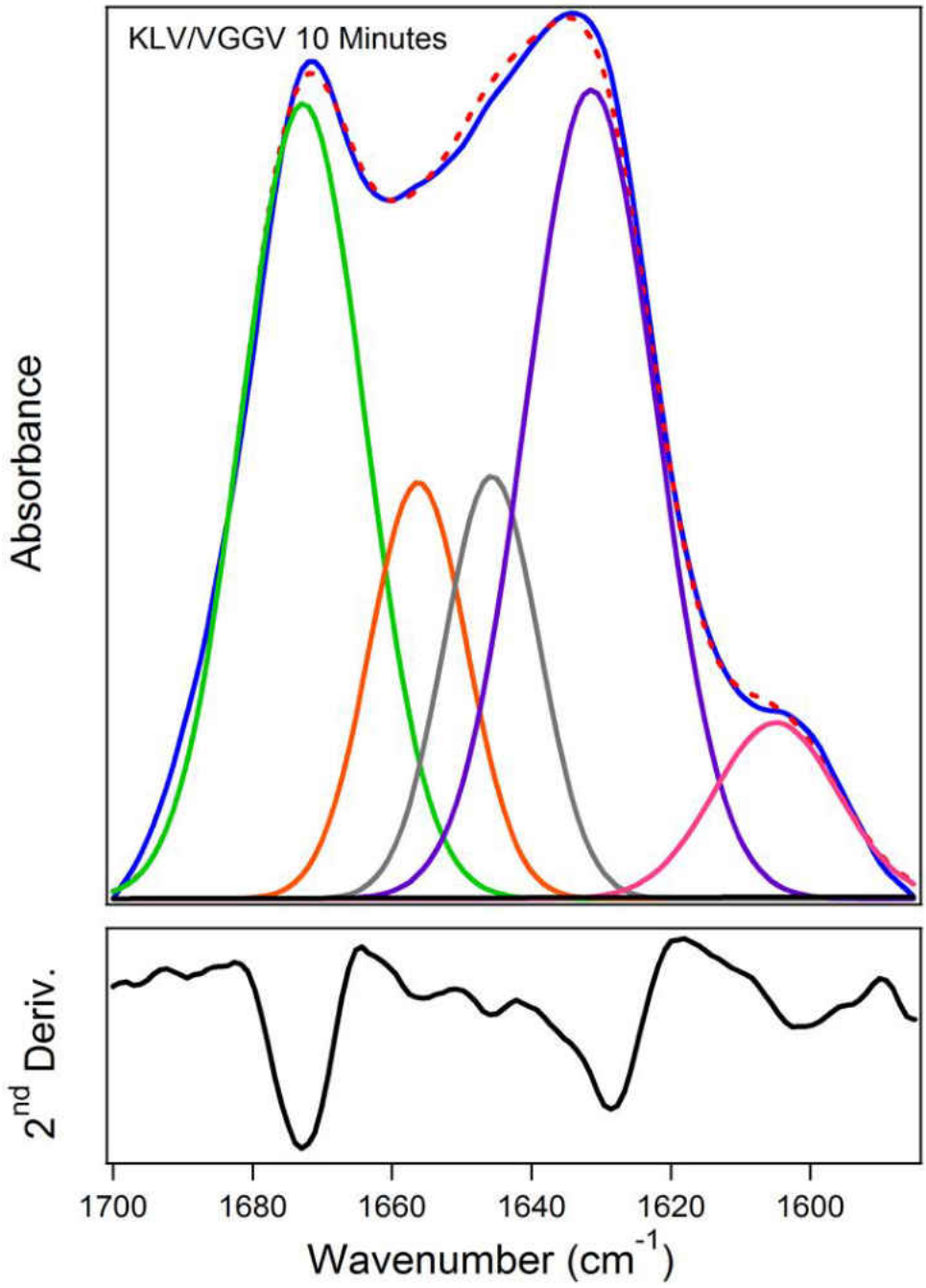
KLV/VGGV 10 Minutes
Absorbance
2nd Deriv.
1700
1680
1660
1640
1620
1600
Wavenumber (cm-1)

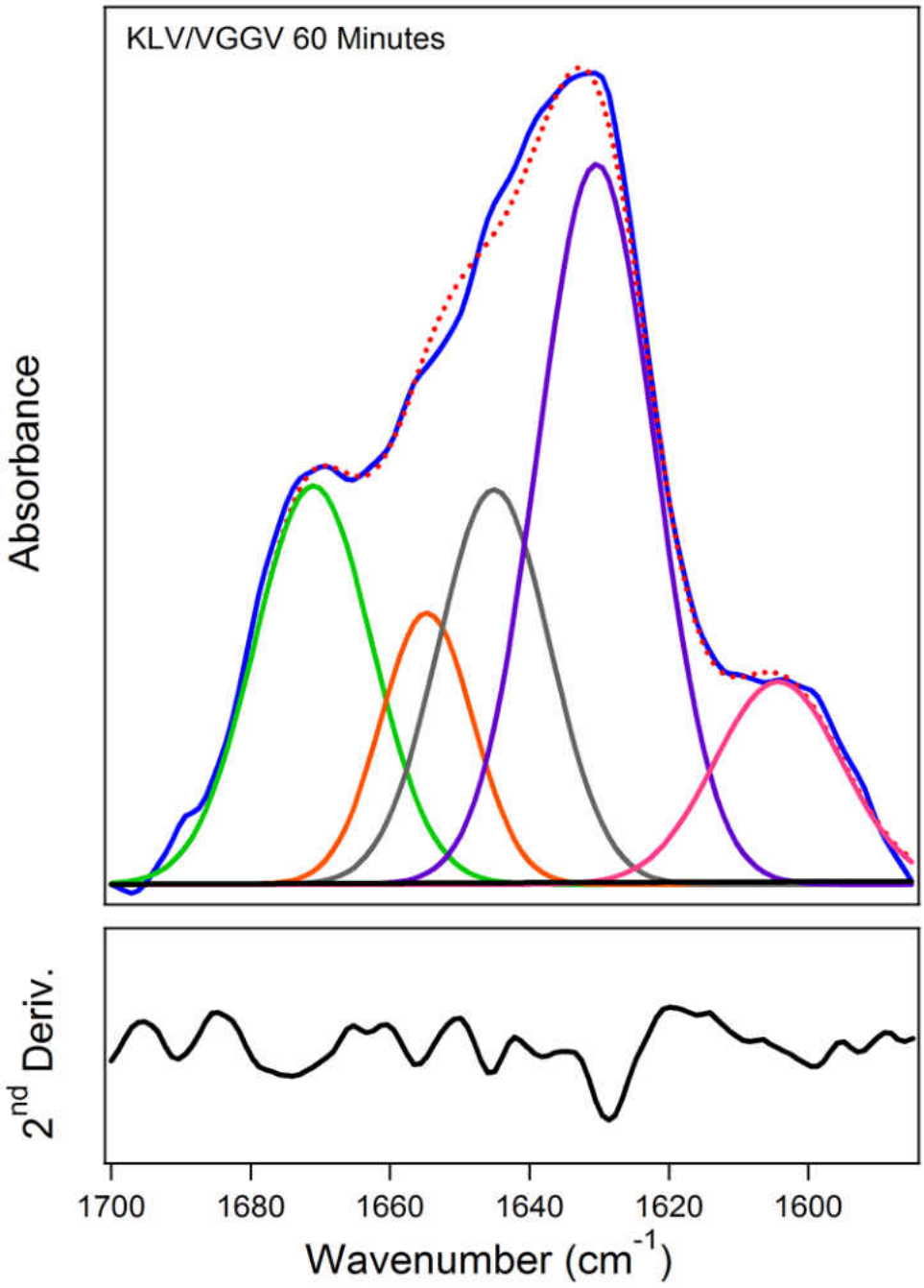
KLV/VGGV 60 Minutes
Absorbance
2nd Deriv.
1700
1680
1660
1640
1620
1600
Wavenumber (cm-1)

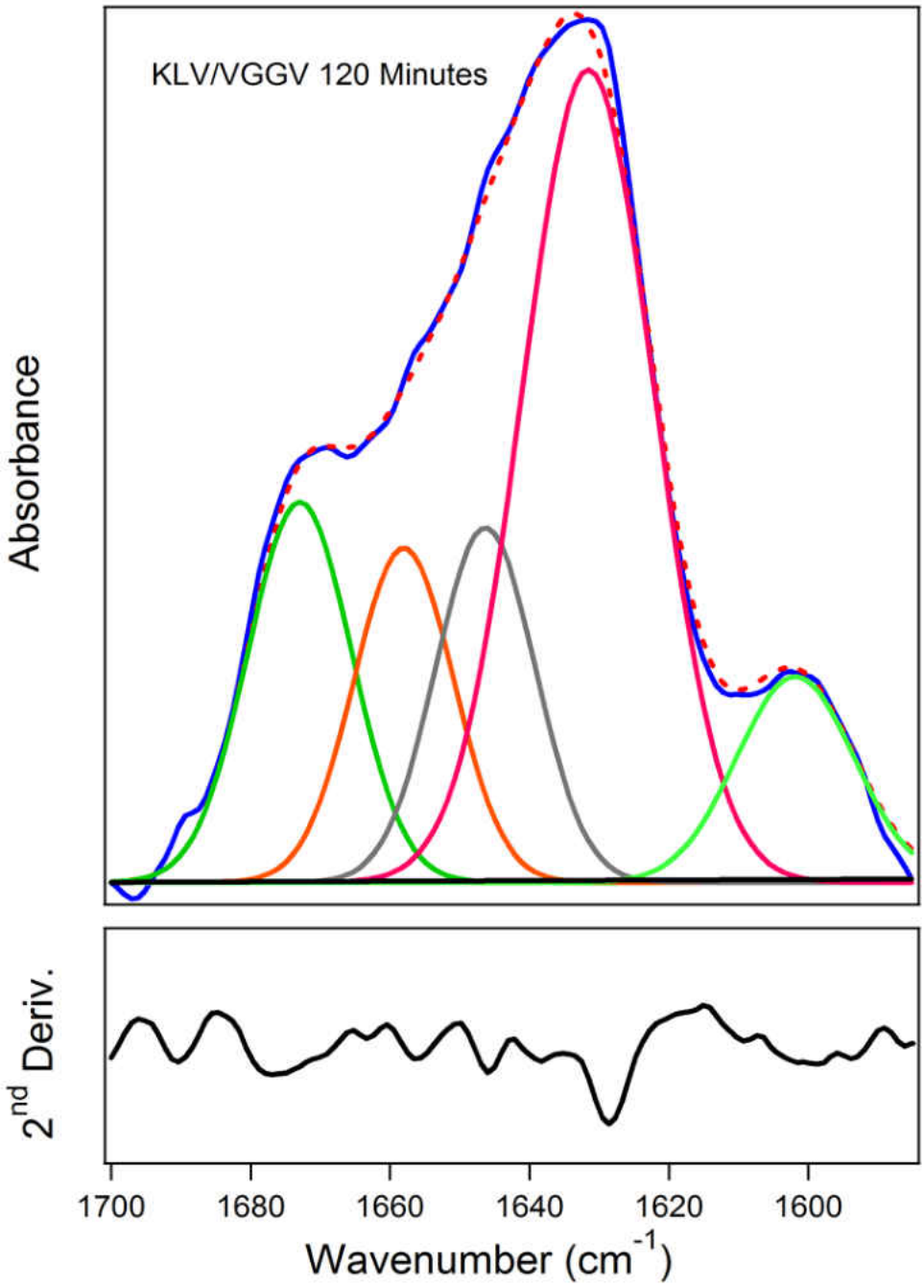
KLV/VGGV 120 Minutes
Absorbance
2nd Deriv.
1700
1680
1660
1640
1620
1600
Wavenumber (cm-1)

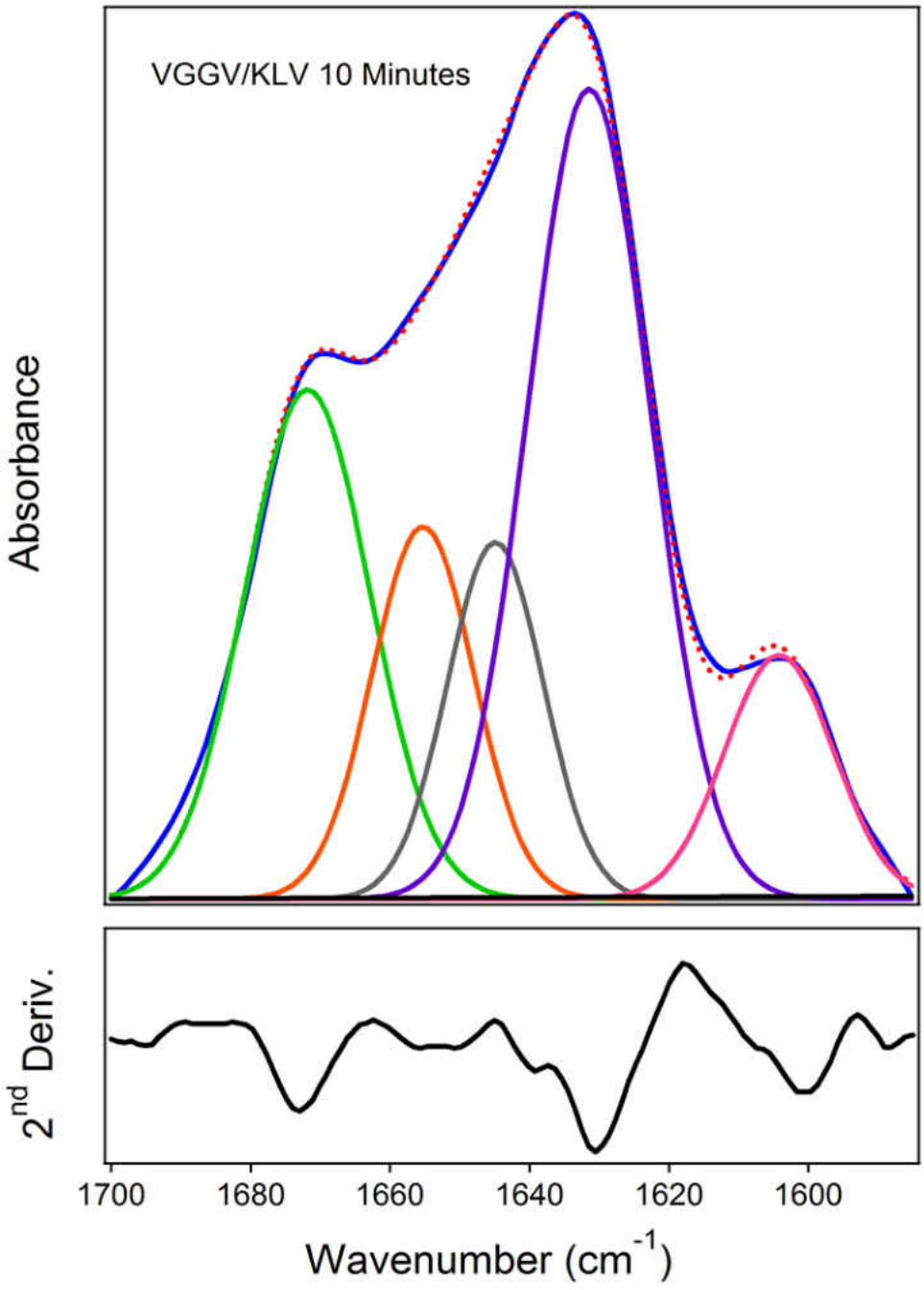
VGGV/KLV 10 Minutes
Absorbance
2nd Deriv.
1700
1680
1660
1640
1620
1600
Wavenumber (cm-1)

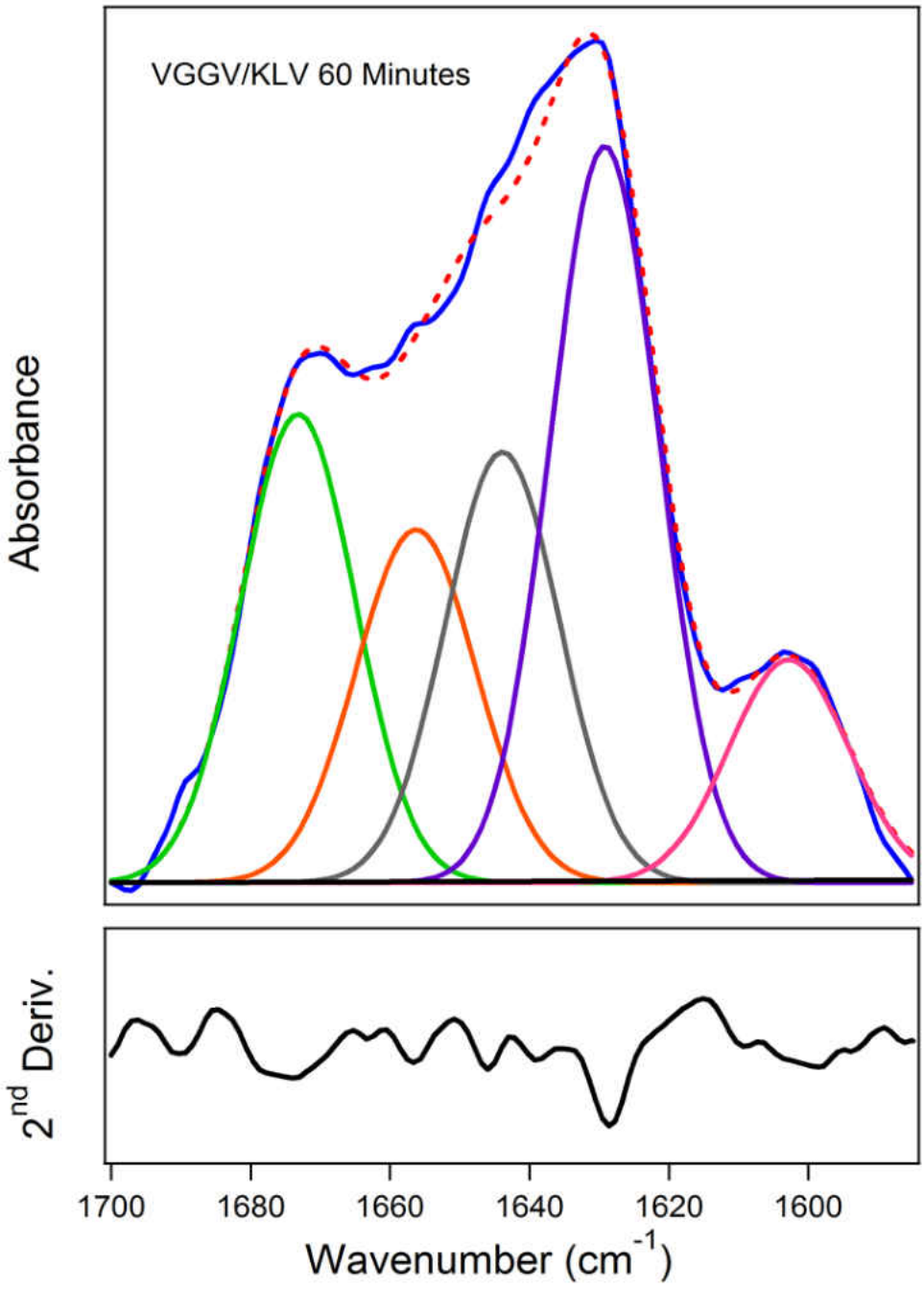
VGGV/KLV 60 Minutes
Absorbance
2nd Deriv.
1700
1680
1660
1640
1620
1600
Wavenumber (cm-1)

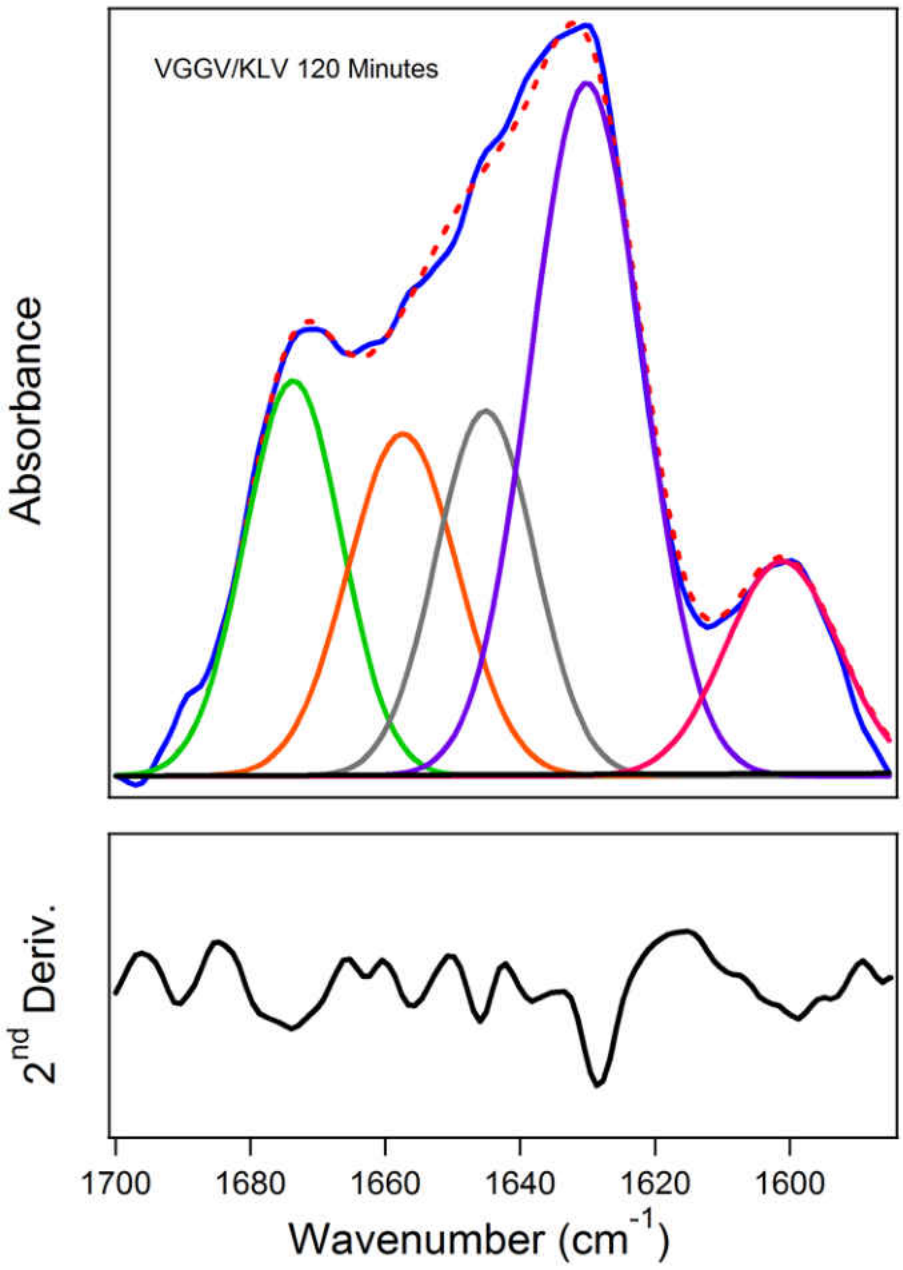
VGGV/KLV 120 Minutes
Absorbance
2nd Deriv.
1700
1680
1660
1640
1620
1600
Wavenumber (cm-1)

LIST OF REFERENCES

1. Querfurth, H. W., and F. M. LaFerla. 2010. MECHANISMS OF DISEASE Alzheimer's Disease. New England Journal of Medicine 362:329-344.
2. Hirtz, D., D. J. Thurman, K. Gwinn-Hardy, M. Mohamed, A. R. Chaudhuri, and R. Zalutsky. 2007. How common are the "common" neurologic disorders? Neurology 68:326-337.
3. Hebert, L. E., P. A. Scherr, J. L. Bienias, D. A. Bennett, and D. A. Evans. 2003. Alzheimer disease in the US population - Prevalence estimates using the 2000 census. Archives of Neurology 60:1119-1122.
4. Cummings, J. L., T. Morstorf, and K. Zhong. 2014. Alzheimer's disease drug-development pipeline: few candidates, frequent failures. Alzheimers Research & Therapy 6:7.
5. Coleman, P. D., and P. J. Yao. 2003. Synaptic slaughter in Alzheimer's disease. Neurobiology of Aging 24:1023-1027.
6. Tanzi, R. E., and L. Bertram. 2005. Twenty years of the Alzheimer's disease amyloid hypothesis: A genetic perspective. Cell 120:545-555.
7. Lue, L. F., Y. M. Kuo, A. E. Roher, L. Brachova, Y. Shen, L. Sue, T. Beach, J. H. Kurth, R. E. Rydel, and J. Rogers. 1999. Soluble amyloid beta peptide concentration as a predictor of synaptic change in Alzheimer's disease. American Journal of Pathology 155:853-862.
8. Haass, C., and D. J. Selkoe. 2007. Soluble protein oligomers in neurodegeneration: lessons from the Alzheimer's amyloid beta-peptide. Nature Reviews Molecular Cell Biology 8:101-112.
9. Dawkins, E., and D. H. Small. 2014. Insights into the physiological function of the beta-amyloid precursor protein: beyond Alzheimer's disease. Journal of Neurochemistry 129:756-769.
10. Haass, C. 2004. Take five - BACE and the gamma-secretase quartet conduct Alzheimer's amyloid beta-peptide generation. Embo Journal 23:483-488.
11. Haass, C., C. Kaether, G. Thinakaran, and S. Sisodia. 2012. Trafficking and Proteolytic Processing of APP. Cold Spring Harbor Perspectives in Medicine 2:25.
12. Gotz, J., and L. M. Ittner. 2008. Animal models of Alzheimer's disease and frontotemporal dementia. Nature Reviews Neuroscience 9:532-544.
13. Harigaya, Y., T. C. Saido, C. B. Eckman, C. M. Prada, M. Shoji, and S. G. Younkin. 2000. Amyloid beta protein starting pyroglutamate at position 3 is a major component of the amyloid deposits in the Alzheimer's disease brain. Biochemical and Biophysical Research Communications 276:422-427.
14. Weggen, S., J. L. Eriksen, P. Das, S. A. Sagi, R. Wang, C. U. Pietrzik, K. A. Findlay, T. E. Smith, M. P. Murphy, T. Butler, D. E. Kang, N. Marquez-Sterling, T. E. Golde, and E. H. Koo. 2001. A subset of NSAIDs lower amyloidogenic A beta 42 independently of cyclooxygenase activity. Nature 414:212-216.
15. Benilova, I., R. Gallardo, A. A. Ungureanu, V. C. Cano, A. Snellinx, M. Ramakers, C. Bartic, F. Rousseau, J. Schymkowitz, and B. De Strooper. 2014. The Alzheimer Disease Protective Mutation A2T Modulates Kinetic and Thermodynamic Properties of Amyloid-beta (A beta) Aggregation. Journal of Biological Chemistry 289:30977-30989.
16. Muratore, C. R., H. C. Rice, P. Srikanth, D. G. Callahan, T. Shin, L. N. P. Benjamin, D. M. Walsh, D. J. Selkoe, and T. L. Young-Pearse. 2014. The familial Alzheimer's disease APPV717I mutation

alters APP processing and Tau expression in iPSC-derived neurons. Human Molecular Genetics 23:3523-3536.

17. Weggen, S., and D. Beher. 2012. Molecular consequences of amyloid precursor protein and presenilin mutations causing autosomal-dominant Alzheimer's disease. Alzheimers Research & Therapy 4:14.

18. Achouri-Rassas, A., N. Ben Ali, S. Fray, S. H. Fredj, M. Kechaou, N. O. Zakraoui, A. Cherif, S. Chabbi, N. Anane, T. Messaoud, R. Gouider, and S. Belal. 2015. Novel presenilin 1 mutation (p.I83T) in Tunisian family with early-onset Alzheimer's disease. Neurobiology of Aging 36:3.

19. Borchelt, D. R., G. Thinakaran, C. B. Eckman, M. K. Lee, F. Davenport, T. Ratovitsky, C. M. Prada, G. Kim, S. Seekins, D. Yager, H. H. Slunt, R. Wang, M. Seeger, A. I. Levey, S. E. Gandy, N. G. Copeland, N. A. Jenkins, D. L. Price, and S. G. Younkin. 1996. Familial Alzheimer's disease-linked presenilin 1 variants elevate A beta 1-42/1-40 ratio in vitro and in vivo. Neuron 17:1005-1013.

20. Guntert, A., H. Dobeli, and B. Bohrmann. 2006. High sensitivity analysis of amyloid-beta peptide composition in amyloid deposits from human and PS2APP mouse brain. Neuroscience 143:461-475.

21. Scheuner, D., C. Eckman, M. Jensen, X. Song, M. Citron, N. Suzuki, T. D. Bird, J. Hardy, M. Hutton, W. Kukull, E. Larson, E. LevyLahad, M. Viitanen, E. Peskind, P. Poorkaj, G. Schellenberg, R. Tanzi, W. Wasco, L. Lannfelt, D. Selkoe, and S. Younkin. 1996. Secreted amyloid beta-protein similar to that in the senile plaques of Alzheimer's disease is increased in vivo by the presenilin 1 and 2 and APP mutations linked to familial Alzheimer's disease. Nature Medicine 2:864-870.

22. Russo, C., E. Violani, S. Salis, V. Venezia, V. Dolcini, G. Damonte, U. Benatti, C. D'Arrigo, E. Patrone, P. Carlo, and G. Schettini. 2002. Pyroglutamate-modified amyloid beta-peptides - A beta N3(pE)-strongly affect cultured neuron and astrocyte survival. Journal of Neurochemistry 82:1480-1489.

23. Walsh, D. M., I. Klyubin, J. V. Fadeeva, W. K. Cullen, R. Anwyl, M. S. Wolfe, M. J. Rowan, and D. J. Selkoe. 2002. Naturally secreted oligomers of amyloid beta protein potently inhibit hippocampal long-term potentiation in vivo. Nature 416:535-539.

24. Umeda, T., E. M. Ramser, M. Yamashita, K. Nakajima, H. Mori, M. A. Silverman, and T. Tomiyama. 2015. Intracellular amyloid beta oligomers impair organelle transport and induce dendritic spine loss in primary neurons. Acta Neuropathologica Communications 3:15.

25. Pensalfini, A., R. Albay, S. Rasool, J. W. Wu, A. Hatami, H. Arai, L. Margol, S. Milton, W. W. Poon, M. M. Corrada, C. H. Kawas, and C. G. Glabe. 2014. Intracellular amyloid and the neuronal origin of Alzheimer neuritic plaques. Neurobiology of Disease 71:53-61.

26. Chafekar, S. M., F. Baas, and W. Scheper. 2008. Oligomer-specific A beta toxicity in cell models is mediated by selective uptake. Biochimica Et Biophysica Acta-Molecular Basis of Disease 1782:523-531.

27. Hay, M., D. W. Thomas, J. L. Craighead, C. Economides, and J. Rosenthal. 2014. Clinical development success rates for investigational drugs. Nature Biotechnology 32:40-51.

28. Paul, S. M., D. S. Mytelka, C. T. Dunwiddie, C. C. Persinger, B. H. Munos, S. R. Lindborg, and A. L. Schacht. 2010. How to improve R&D productivity: the pharmaceutical industry's grand challenge. Nature Reviews Drug Discovery 9:203-214.

29. Venti, A., T. Giordano, P. Eder, A. I. Bush, D. K. Lahiri, N. H. Greig, and J. T. Rogers. 2004. The integrated role of desferrioxamine and phenserine targeted to an iron-responsive element in

the APP-mRNA 5 '-untranslated region. Protective Strategies for Neurodegenerative Diseases 1035:34-48.

30. Weggen, S., J. L. Eriksen, S. A. Sagi, C. U. Pietrzik, V. Ozols, A. Fauq, T. E. Golde, and E. H. Koo. 2003. Evidence that nonsteroidal anti-inflammatory drugs decrease amyloid beta 42 production by direct modulation of gamma-secretase activity. Journal of Biological Chemistry 278:31831-31837.

31. Eriksen, J. L., S. A. Sagi, T. E. Smith, S. Weggen, P. Das, D. C. McLendon, V. V. Ozols, K. W. Jessing, K. H. Zavitz, E. H. Koo, and T. E. Golde. 2003. NSAIDs and enantiomers of flurbiprofen target gamma-secretase and lower A beta 42 in vivo. Journal of Clinical Investigation 112:440-449.

32. Armstrong, R. A. 2014. A critical analysis of the 'amyloid cascade hypothesis'. Folia Neuropathologica 52:211-225.

33. Herrup, K. 2015. The case for rejecting the amyloid cascade hypothesis. Nature Neuroscience 18:794-799.

34. Sommer, B. 2002. Alzheimer's disease and the amyloid cascade hypothesis: Ten years on. Current Opinion in Pharmacology 2:87-92.

35. Pimplikar, S. W. 2009. Reassessing the amyloid cascade hypothesis of Alzheimer's disease. International Journal of Biochemistry & Cell Biology 41:1261-1268.

36. Klyubin, I., D. M. Walsh, C. A. Lemere, W. K. Cullen, G. M. Shankar, V. Betts, E. T. Spooner, L. Y. Jiang, R. Anwyl, D. J. Selkoe, and M. J. Rowan. 2005. Amyloid beta protein immunotherapy neutralizes A beta oligomers that disrupt synaptic plasticity in vivo. Nature Medicine 11:556-561.

37. Walsh, D. M., and D. J. Selkoe. 2004. Oligomers in the brain: The emerging role of soluble protein aggregates in neurodegeneration. Protein and Peptide Letters 11:213-228.

38. Townsend, M., G. M. Shankar, T. Mehta, D. M. Walsh, and D. J. Selkoe. 2006. Effects of secreted oligomers of amyloid beta-protein on hippocampal synaptic plasticity: a potent role for trimers. Journal of Physiology-London 572:477-492.

39. Cleary, J. P., D. M. Walsh, J. J. Hofmeister, G. M. Shankar, M. A. Kuskowski, D. J. Selkoe, and K. H. Ashe. 2005. Natural oligomers of the amyloid-protein specifically disrupt cognitive function. Nature Neuroscience 8:79-84.

40. Davis, D. G., F. A. Schmitt, D. R. Wekstein, and W. R. Markesbery. 1999. Alzheimer neuropathologic alterations in aged cognitively normal subjects. Journal of Neuropathology and Experimental Neurology 58:376-388.

41. Knopman, D. S., J. E. Parisi, A. Salviati, M. Floriach-Robert, B. F. Boeve, R. J. Ivnik, G. E. Smith, D. W. Dickson, K. A. Johnson, L. E. Petersen, W. C. McDonald, H. Braak, and R. C. Petersen. 2003. Neuropathology of cognitively normal elderly. Journal of Neuropathology and Experimental Neurology 62:1087-1095.

42. Nelson, P. T., I. Alafuzoff, E. H. Bigio, C. Bouras, H. Braak, N. J. Cairns, R. J. Castellani, B. J. Crain, P. Davies, K. Del Tredici, C. Duyckaerts, M. P. Frosch, V. Haroutunian, P. R. Hof, C. M. Hulette, B. T. Hyman, T. Iwatsubo, K. A. Jellinger, G. A. Jicha, E. Kovari, W. A. Kukull, J. B. Leverenz, S. Love, I. R. Mackenzie, D. M. Mann, E. Masliah, A. C. McKee, T. J. Montine, J. C. Morris, J. A. Schneider, J. A. Sonnen, D. R. Thal, J. Q. Trojanowski, J. C. Troncoso, T. Wisniewski, R. L. Woltjer, and T. G. Beach. 2012. Correlation of Alzheimer Disease Neuropathologic Changes With Cognitive Status: A Review of the Literature. Journal of Neuropathology and Experimental Neurology 71:362-381.

43. Roberson, E. D., K. Scearce-Levie, J. J. Palop, F. R. Yan, I. H. Cheng, T. Wu, H. Gerstein, G. Q. Yu, and L. Mucke. 2007. Reducing endogenous tau ameliorates amyloid beta-induced deficits in an Alzheimer's disease mouse model. Science 316:750-754.
44. Nussbaum, J. M., S. Schilling, H. Cynis, A. Silva, E. Swanson, T. Wangsanut, K. Tayler, B. Wiltgen, A. Hatami, R. Ronicke, K. Reymann, B. Hutter-Paier, A. Alexandru, W. Jagla, S. Graubner, C. G. Glabe, H. U. Demuth, and G. S. Bloom. 2012. Prion-like behaviour and tau-dependent cytotoxicity of pyroglutamylated amyloid-beta. Nature 485:651-655.
45. Ramser, E. M., K. J. Gan, H. Decker, E. Y. Fan, M. M. Suzuki, S. T. Ferreira, and M. A. Silverman. 2013. Amyloid-beta oligomers induce tau-independent disruption of BDNF axonal transport via calcineurin activation in cultured hippocampal neurons. Molecular Biology of the Cell 24:2494-2505.
46. Dahlgren, K. N., A. M. Manelli, W. B. Stine, L. K. Baker, G. A. Krafft, and M. J. LaDu. 2002. Oligomeric and fibrillar species of amyloid-beta peptides differentially affect neuronal viability. Journal of Biological Chemistry 277:32046-32053.
47. Klein, W. L., W. B. Stine, and D. B. Teplow. 2004. Small assemblies of unmodified amyloid beta-protein are the proximate neurotoxin in Alzheimer's disease. Neurobiology of Aging 25:569-580.
48. Necula, M., R. Kayed, S. Milton, and C. G. Glabe. 2007. Small molecule inhibitors of aggregation indicate that amyloid beta oligomerization and fibrillization pathways are independent and distinct. Journal of Biological Chemistry 282:10311-10324.
49. Tay, W. M., D. T. Huang, T. L. Rosenberry, and A. K. Paravastu. 2013. The Alzheimer's Amyloid-beta(1-42) Peptide Forms Off-Pathway Oligomers and Fibrils That Are Distinguished Structurally by Intermolecular Organization. Journal of Molecular Biology 425:2494-2508.
50. Stohr, J., J. C. Watts, Z. L. Mensinger, A. Oehler, S. K. Grillo, S. J. DeArmond, S. B. Prusiner, and K. Giles. 2012. Purified and synthetic Alzheimer's amyloid beta (A beta) prions. Proceedings of the National Academy of Sciences of the United States of America 109:11025-11030.
51. Aguzzi, A., and L. Rajendran. 2009. The Transcellular Spread of Cytosolic Amyloids, Prions, and Prionoids. Neuron 64:783-790.
52. Yan, Y. L., and C. Y. Wang. 2007. A beta 40 protects non-toxic A beta 42 monomer from aggregation. Journal of Molecular Biology 369:909-916.
53. Giuffrida, M. L., F. Caraci, B. Pignataro, S. Cataldo, P. De Bona, V. Bruno, G. Molinaro, G. Pappalardo, A. Messina, A. Palmigiano, D. Garozzo, F. Nicoletti, E. Rizzarelli, and A. Copani. 2009. beta-Amyloid Monomers Are Neuroprotective. Journal of Neuroscience 29:10582-10587.
54. Mori, H., K. Takio, M. Ogawara, and D. Selkoe. 1992. MASS-SPECTROMETRY OF PURIFIED AMYLOID-BETA PROTEIN IN ALZHEIMERS-DISEASE. Journal of Biological Chemistry 267:17082-17086.
55. Schilling, S., U. Zeitschel, T. Hoffmann, U. Heiser, M. Francke, A. Kehlen, M. Holzer, B. Hutter-Paier, M. Prokesch, M. Windisch, W. Jagla, D. Schlenzig, C. Lindner, T. Rudolph, G. Reuter, H. Cynis, D. Montag, H.-U. Demuth, and S. Rossner. 2008. Glutaminyl cyclase inhibition attenuates pyroglutamate A beta and Alzheimer's disease-like pathology. Nature Medicine 14:1106-1111.
56. Mandler, M., L. Walker, R. Santic, P. Hanson, A. R. Upadhaya, S. J. Colloby, C. M. Morris, D. R. Thal, A. J. Thomas, A. Schneeberger, and J. Attems. 2014. Pyroglutamylated amyloid-beta is associated with hyperphosphorylated tau and severity of Alzheimer's disease. Acta Neuropathologica 128:67-79.

57. Upadhaya, A. R., I. Kosterin, S. Kumar, C. A. F. von Arnim, H. Yamaguchi, M. Fandrich, J. Walter, and D. R. Thal. 2014. Biochemical stages of amyloid-beta peptide aggregation and accumulation in the human brain and their association with symptomatic and pathologically preclinical Alzheimer's disease. Brain 137:887-903.
58. Valenti, M. T., S. Bolognin, C. Zanatta, L. Donatelli, G. Innamorati, M. Pampanin, G. Zanusso, P. Zatta, and L. D. Carbonare. 2013. Increased Glutaminyl Cyclase Expression in Peripheral Blood of Alzheimer's Disease Patients. Journal of Alzheimers Disease 34:263-271.
59. Frost, J. L., K. X. Le, H. Cynis, E. Ekpo, M. Kleinschmidt, R. M. Palmour, F. R. Ervin, S. Snigdha, C. W. Cotman, T. C. Saido, R. J. Vassar, P. S. George-Hyslop, T. Ikezu, S. Schilling, H. U. Demuth, and C. A. Lemere. 2013. Pyroglutamate-3 Amyloid-beta Deposition in the Brains of Humans, Non-Human Primates, Canines, and Alzheimer Disease-Like Transgenic Mouse Models. American Journal of Pathology 183:369-381.
60. Bayer, T. A., and O. Wirths. 2014. Focusing the amyloid cascade hypothesis on N-truncated Abeta peptides as drug targets against Alzheimer's disease. Acta Neuropathologica 127:787-801.
61. Jawhar, S., O. Wirths, S. Schilling, S. Graubner, H. U. Demuth, and T. A. Bayer. 2011. Overexpression of Glutaminyl Cyclase, the Enzyme Responsible for Pyroglutamate A beta Formation, Induces Behavioral Deficits, and Glutaminyl Cyclase Knock-out Rescues the Behavioral Phenotype in 5XFAD Mice. Journal of Biological Chemistry 286:4454-4460.
62. De Kimpe, L., A. Bennis, R. Zwart, E. S. van Haastert, J. J. M. Hoozemans, and W. Scheper. 2012. Disturbed Ca2+ Homeostasis Increases Glutaminyl Cyclase Expression; Connecting Two Early Pathogenic Events in Alzheimer's Disease In Vitro. Plos One 7.
63. Wirths, O., C. Erck, H. Martens, A. Harmeier, C. Geumann, S. Jawhar, S. Kumar, G. Multhaup, J. Walter, M. Ingelsson, M. Degerman-Gunnarsson, H. Kalimo, I. Huitinga, L. Lannfelt, and T. A. Bayer. 2010. Identification of Low Molecular Weight Pyroglutamate A beta Oligomers in Alzheimer Disease A NOVEL TOOL FOR THERAPY AND DIAGNOSIS. Journal of Biological Chemistry 285:41517-41524.
64. Bouter, Y., K. Dietrich, J. L. Wittnam, N. Rezaei-Ghaleh, T. Pillot, S. Papot-Couturier, T. Lefebvre, F. Sprenger, O. Wirths, M. Zweckstetter, and T. A. Bayer. 2013. N-truncated amyloid beta (A beta) 4-42 forms stable aggregates and induces acute and long-lasting behavioral deficits. Acta Neuropathologica 126:189-205.
65. Chimon, S., M. A. Shaibat, C. R. Jones, D. C. Calero, B. Aizezi, and Y. Ishii. 2007. Evidence of fibril-like beta-sheet structures in a neurotoxic amyloid intermediate of Alzheimer's beta-amyloid. Nature Structural & Molecular Biology 14:1157-1164.
66. Rangachari, V., B. D. Moore, D. K. Reed, L. K. Sonoda, A. W. Bridges, E. Conboy, D. Hartigan, and T. L. Rosenberry. 2007. Amyloid-beta(1-42) rapidly forms protofibrils and oligomers by distinct pathways in low concentrations of sodium dodecylsulfatet. Biochemistry 46:12451-12462.
67. Mullan, M., F. Crawford, K. Axelman, H. Houlden, L. Lilius, B. Winblad, and L. Lannfelt. 1992. A PATHOGENIC MUTATION FOR PROBABLE ALZHEIMERS-DISEASE IN THE APP GENE AT THE N-TERMINUS OF BETA-AMYLOID. Nature Genetics 1:345-347.
68. Walker, E. S., M. Martinez, A. L. Brunkan, and A. Goate. 2005. Presenilin 2 familial Alzheimer's disease mutations result in partial loss of function and dramatic changes in A beta 42/40 ratios. Journal of Neurochemistry 92:294-301.

69. Hooli, B. V., G. Mohapatra, M. Mattheisen, A. R. Parrado, J. T. Roehr, Y. Shen, J. F. Gusella, R. Moir, A. J. Saunders, C. Lange, R. E. Tanzi, and L. Bertram. 2012. Role of common and rare APP DNA sequence variants in Alzheimer disease. Neurology 78:1250-1257.
70. Peng, X. L., L. Hou, S. H. Xu, Y. Hua, S. J. Zhou, Y. Zhang, Y. P. Zheng, Y. H. Fu, Q. Xu, L. S. Zhang, J. Wang, X. T. Guan, and J. S. He. 2014. Novel APP K724M mutation causes Chinese early-onset familial Alzheimer's disease and increases amyloid-beta 42 to amyloid-beta 40 ratio. Neurobiology of Aging 35:6.
71. Hashimoto, Y., and M. Matsuoka. 2014. A mutation protective against Alzheimer's disease renders amyloid beta precursor protein incapable of mediating neurotoxicity. Journal of Neurochemistry 130:291-300.
72. Muchnik, C., N. Olivar, M. C. Dalmasso, P. J. Azurmendi, C. Liberczuk, L. Morelli, and L. I. Brusco. 2015. Identification of PSEN2 mutation p.N141I in Argentine pedigrees with early-onset familial Alzheimer's disease. Neurobiology of Aging 36:2674-+.
73. Bentahir, M., O. Nyabi, J. Verhamme, A. Tolia, K. Horre, J. Wiltfang, H. Esselmann, and B. De Strooper. 2006. Presenilin clinical mutations can affect gamma-secretase activity by different mechanisms. Journal of Neurochemistry 96:732-742.
74. Holtzman, D. M., J. Herz, and G. J. Bu. 2012. Apolipoprotein E and Apolipoprotein E Receptors: Normal Biology and Roles in Alzheimer Disease. Cold Spring Harbor Perspectives in Medicine 2:23.
75. Deane, R., A. Sagare, K. Hamm, M. Parisi, S. Lane, M. B. Finn, D. M. Holtzman, and B. V. Zlokovic. 2008. apoE isoform-specific disruption of amyloid beta peptide clearance from mouse brain. Journal of Clinical Investigation 118:4002-4013.
76. Jiang, Q., C. Y. D. Lee, S. Mandrekar, B. Wilkinson, P. Cramer, N. Zelcer, K. Mann, B. Lamb, T. M. Willson, J. L. Collins, J. C. Richardson, J. D. Smith, T. A. Comery, D. Riddell, D. M. Holtzman, P. Tontonoz, and G. E. Landreth. 2008. ApoE promotes the proteolytic degradation of A beta. Neuron 58:681-693.
77. Koistinaho, M., S. Z. Lin, X. Wu, M. Esterman, D. Koger, J. Hanson, R. Higgs, F. Liu, S. Malkani, K. R. Bales, and S. M. Paul. 2004. Apolipoprotein E promotes astrocyte colocalization and degradation of deposited amyloid-beta peptides. Nature Medicine 10:719-726.
78. Wiseman, F. K., T. Al-Janabi, J. Hardy, A. Karmiloff-Smith, D. Nizetic, V. L. J. Tybulewicz, E. M. C. Fisher, and A. Strydom. 2015. A genetic cause of Alzheimer disease: mechanistic insights from Down syndrome. Nature Reviews Neuroscience 16:564-574.
79. Korbel, J. O., T. Tirosh-Wagner, A. E. Urban, X. N. Chen, M. Kasowski, L. Dai, F. Grubert, C. Erdman, M. C. Gao, K. Lange, E. M. Sobel, G. M. Barlow, A. S. Aylsworth, N. J. Carpenter, R. D. Clark, M. Y. Cohen, E. Doran, T. Falik-Zaccai, S. O. Lewin, I. T. Lott, B. C. McGillivray, J. B. Moeschler, M. J. Pettenati, S. M. Pueschel, K. W. Rao, L. G. Shaffer, M. Shohat, A. J. Van Riper, D. Warburton, S. Weissman, M. B. Gerstein, M. Snyder, and J. R. Korenberg. 2009. The genetic architecture of Down syndrome phenotypes revealed by high-resolution analysis of human segmental trisomies. Proceedings of the National Academy of Sciences of the United States of America 106:12031-12036.
80. Prasher, V. P., M. J. Farrer, A. M. Kessling, E. M. C. Fisher, R. J. West, P. C. Barber, and A. C. Butler. 1998. Molecular mapping of Alzheimer-type dementia in Down's syndrome. Annals of Neurology 43:380-383.

81. Thonberg, H., M. Fallstrom, J. Bjorkstrom, J. Schoumans, I. Nennesmo, and C. Graff. 2011. Mutation screening of patients with Alzheimer disease identifies APP locus duplication in a Swedish patient. BMC research notes 4:476.
82. Johansson, S., A. Jamsa, M. Vasange, B. Winblad, J. Luthman, and R. F. Cowburn. 2006. Increased tau phosphorylation at the Ser(396) epitope after amyloid beta-exposure in organotypic cultures. Neuroreport 17:907-911.
83. Feuillette, S., L. Miguel, T. Frebourg, D. Campion, and M. Lecourtois. 2010. Drosophila models of human tauopathies indicate that Tau protein toxicity in vivo is mediated by soluble cytosolic phosphorylated forms of the protein. Journal of Neurochemistry 113:895-903.
84. Fulga, T. A., I. Elson-Schwab, V. Khurana, M. L. Steinhilb, T. L. Spires, B. T. Hyman, and M. B. Feany. 2007. Abnormal bundling and accumulation of F-actin mediates tau-induced neuronal degeneration in vivo. Nature Cell Biology 9:139-U117.
85. Dillon, C., and Y. Goda. 2005. The actin cytoskeleton: Integrating form and function at the synapse. In Annual Review of Neuroscience. Annual Reviews, Palo Alto. 25-55.
86. Oddo, S., V. Vasilevko, A. Caccamo, M. Kitazawa, D. H. Cribbs, and F. M. LaFerla. 2006. Reduction of soluble A beta and Tau, but not soluble A beta alone, ameliorates cognitive decline in transgenic mice with plaques and tangles. Journal of Biological Chemistry 281:39413-39423.
87. Spires-Jones, T. L., K. J. Kopeikina, R. M. Koffie, A. de Calignon, and B. T. Hyman. 2011. Are Tangles as Toxic as They Look? Journal of Molecular Neuroscience 45:438-444.
88. Tackenberg, C., S. Grinschgl, A. Trutzel, A. C. Santuccione, M. C. Frey, U. Konietzko, J. Grimm, R. Brandt, and R. M. Nitsch. 2013. NMDA receptor subunit composition determines beta-amyloid-induced neurodegeneration and synaptic loss. Cell Death & Disease 4:10.
89. Mattson, M. P., B. Cheng, D. Davis, K. Bryant, I. Lieberburg, and R. E. Rydel. 1992. BETA-AMYLOID PEPTIDES DESTABILIZE CALCIUM HOMEOSTASIS AND RENDER HUMAN CORTICAL-NEURONS VULNERABLE TO EXCITOTOXICITY. Journal of Neuroscience 12:376-389.
90. Arundine, M., and M. Tymianski. 2003. Molecular mechanisms of calcium-dependent neurodegeneration in excitotoxicity. Cell Calcium 34:325-337.
91. Holth, J. K., V. C. Bomben, J. G. Reed, T. Inoue, L. Younkin, S. G. Younkin, R. G. Pautler, J. Botas, and J. L. Noebels. 2013. Tau Loss Attenuates Neuronal Network Hyperexcitability in Mouse and Drosophila Genetic Models of Epilepsy. Journal of Neuroscience 33:1651-1659.
92. Eckert, A., R. Nisbet, A. Grimm, and J. Gotz. 2014. March separate, strike together - Role of phosphorylated TAU in mitochondrial dysfunction in Alzheimer's disease. Biochimica Et Biophysica Acta-Molecular Basis of Disease 1842:1258-1266.
93. Lloret, A., M. C. Badia, E. Giraldo, G. Ermak, M. D. Alonso, F. V. Pallardo, K. J. A. Davies, and J. Vina. 2011. Amyloid-beta Toxicity and Tau Hyperphosphorylation are Linked Via RCAN1 in Alzheimer's Disease. Journal of Alzheimers Disease 27:701-709.
94. Naslund, J., V. Haroutunian, R. Mohs, K. L. Davis, P. Davies, P. Greengard, and J. D. Buxbaum. 2000. Correlation between elevated levels of amyloid beta-peptide in the brain and cognitive decline. Jama-Journal of the American Medical Association 283:1571-1577.
95. Noble, W., V. Olm, K. Takata, E. Casey, M. O, J. Meyerson, K. Gaynor, J. LaFrancois, L. L. Wang, T. Kondo, P. Davies, M. Burns, V. R. Nixon, D. Dickson, Y. Matsuoka, M. Ahlijanian, L. F. Lau, and K. Duff. 2003. Cdk5 is a key factor in tau aggregation and tangle formation in vivo. Neuron 38:555-565.

96. Forlenza, O. V., C. A. Torres, L. L. Talib, V. J. de Paula, H. P. G. Joaquim, B. S. Diniz, and W. F. Gattaz. 2011. Increased platelet GSK3B activity in patients with mild cognitive impairment and Alzheimer's disease. Journal of Psychiatric Research 45:220-224.

97. Jin, M., N. Shepardson, T. Yang, G. Chen, D. Walsh, and D. J. Selkoe. 2011. Soluble amyloid beta-protein dimers isolated from Alzheimer cortex directly induce Tau hyperphosphorylation and neuritic degeneration. Proceedings of the National Academy of Sciences of the United States of America 108:5819-5824.

98. Barrett, P. J., Y. L. Song, W. D. Van Horn, E. J. Hustedt, J. M. Schafer, A. Hadziselimovic, A. J. Beel, and C. R. Sanders. 2012. The Amyloid Precursor Protein Has a Flexible Transmembrane Domain and Binds Cholesterol. Science 336:1168-1171.

99. Nadezhdin, K. D., O. V. Bocharova, E. V. Bocharov, and A. S. Arseniev. 2011. Structural and Dynamic Study of the Transmembrane Domain of the Amyloid Precursor Protein. Acta Naturae 3:69-76.

100. Petkova, A. T., W. M. Yau, and R. Tycko. 2006. Experimental constraints on quaternary structure in Alzheimer's beta-amyloid fibrils. Biochemistry 45:498-512.

101. Sunde, M., L. C. Serpell, M. Bartlam, P. E. Fraser, M. B. Pepys, and C. C. F. Blake. 1997. Common core structure of amyloid fibrils by synchrotron X-ray diffraction. Journal of Molecular Biology 273:729-739.

102. Sawaya, M. R., S. Sambashivan, R. Nelson, M. I. Ivanova, S. A. Sievers, M. I. Apostol, M. J. Thompson, M. Balbirnie, J. J. W. Wiltzius, H. T. McFarlane, A. O. Madsen, C. Riekel, and D. Eisenberg. 2007. Atomic structures of amyloid cross-beta spines reveal varied steric zippers. Nature 447:453-457.

103. Nelson, R., M. R. Sawaya, M. Balbirnie, A. O. Madsen, C. Riekel, R. Grothe, and D. Eisenberg. 2005. Structure of the cross-beta spine of amyloid-like fibrils. Nature 435:773-778.

104. Sachse, C., C. Xu, K. Wieligmann, S. Diekmann, N. Grigorieff, and M. Fandrich. 2006. Quaternary structure of a mature amyloid fibril from Alzheimer's a beta(1-40) peptide. Journal of Molecular Biology 362:347-354.

105. Schmidt, M., C. Sachse, W. Richter, C. Xu, M. Fandrich, and N. Grigorieff. 2009. Comparison of Alzheimer A beta(1-40) and A beta(1-42) amyloid fibrils reveals similar protofilament structures. Proceedings of the National Academy of Sciences of the United States of America 106:19813-19818.

106. Zhang, R., X. Y. Hu, H. Khant, S. J. Ludtke, W. Chiu, M. F. Schmid, C. Frieden, and J. M. Lee. 2009. Interprotofilament interactions between Alzheimer's A beta(1-42) peptides in amyloid fibrils revealed by cryoEM. Proceedings of the National Academy of Sciences of the United States of America 106:4653-4658.

107. Paravastu, A. K., I. Qahwash, R. D. Leapman, S. C. Meredith, and R. Tycko. 2009. Seeded growth of beta-amyloid fibrils from Alzheimer's brain-derived fibrils produces a distinct fibril structure. Proceedings of the National Academy of Sciences of the United States of America 106:7443-7448.

108. Paravastu, A. K., R. D. Leapman, W. M. Yau, and R. Tycko. 2008. Molecular structural basis for polymorphism in Alzheimer's beta-amyloid fibrils. Proceedings of the National Academy of Sciences of the United States of America 105:18349-18354.

109. Luhrs, T., C. Ritter, M. Adrian, D. Riek-Loher, B. Bohrmann, H. Doeli, D. Schubert, and R. Riek. 2005. 3D structure of Alzheimer's amyloid-beta(1-42) fibrils. Proceedings of the National Academy of Sciences of the United States of America 102:17342-17347.
110. Qiang, W., W. M. Yau, Y. Q. Luo, M. P. Mattson, and R. Tycko. 2012. Antiparallel beta-sheet architecture in Iowa-mutant beta-amyloid fibrils. Proceedings of the National Academy of Sciences of the United States of America 109:4443-4448.
111. Lesne, S., M. T. Koh, L. Kotilinek, R. Kayed, C. G. Glabe, A. Yang, M. Gallagher, and K. H. Ashe. 2006. A specific amyloid-beta protein assembly in the brain impairs memory. Nature 440:352-357.
112. Shankar, G. M., S. M. Li, T. H. Mehta, A. Garcia-Munoz, N. E. Shepardson, I. Smith, F. M. Brett, M. A. Farrell, M. J. Rowan, C. A. Lemere, C. M. Regan, D. M. Walsh, B. L. Sabatini, and D. J. Selkoe. 2008. Amyloid-beta protein dimers isolated directly from Alzheimer's brains impair synaptic plasticity and memory. Nature Medicine 14:837-842.
113. Bernstein, S. L., N. F. Dupuis, N. D. Lazo, T. Wyttenbach, M. M. Condron, G. Bitan, D. B. Teplow, J. E. Shea, B. T. Ruotolo, C. V. Robinson, and M. T. Bowers. 2009. Amyloid-beta protein oligomerization and the importance of tetramers and dodecamers in the aetiology of Alzheimer's disease. Nature Chemistry 1:326-331.
114. Doran, T. M., E. A. Anderson, S. E. Latchney, L. A. Opanashuk, and B. L. Nilsson. 2012. Turn Nucleation Perturbs Amyloid beta Self-Assembly and Cytotoxicity. Journal of Molecular Biology 421:315-328.
115. Ono, K., M. M. Condron, and D. B. Teplow. 2009. Structure-neurotoxicity relationships of amyloid beta-protein oligomers. Proceedings of the National Academy of Sciences of the United States of America 106:14745-14750.
116. Ono, K., M. M. Condron, and D. B. Teplow. 2010. Effects of the English (H6R) and Tottori (D7N) Familial Alzheimer Disease Mutations on Amyloid beta-Protein Assembly and Toxicity. Journal of Biological Chemistry 285:23184-23195.
117. Cerf, E., R. Sarroukh, S. Tamamizu-Kato, L. Breydo, S. Derclaye, Y. F. Dufrene, V. Narayanaswami, E. Goormaghtigh, J. M. Ruysschaert, and V. Raussens. 2009. Antiparallel beta-sheet: a signature structure of the oligomeric amyloid beta-peptide. Biochemical Journal 421:415-423.
118. Huang, D. T., M. I. Zimmerman, P. K. Martin, A. J. Nix, T. L. Rosenberry, and A. K. Paravastu. 2015. Antiparallel beta-Sheet Structure within the C-Terminal Region of 42-Residue Alzheimer's Amyloid-beta Peptides When They Form 150-kDa Oligomers. Journal of Molecular Biology 427:2319-2328.
119. Bharadwaj, P., R. Head, R. Martins, V. Raussens, R. Sarroukh, H. Jegasothy, L. Waddington, and L. Bennett. 2013. Modulation of amyloid-beta 1-42 structure and toxicity by proline-rich whey peptides. Food & Function 4:92-103.
120. Kirkitadze, M. D., M. M. Condron, and D. B. Teplow. 2001. Identification and characterization of key kinetic intermediates in amyloid beta-protein fibrillogenesis. Journal of Molecular Biology 312:1103-1119.
121. Prangkio, P., E. C. Yusko, D. Sept, J. Yang, and M. Mayer. 2012. Multivariate Analyses of Amyloid-Beta Oligomer Populations Indicate a Connection between Pore Formation and Cytotoxicity. Plos One 7:10.

122. Vandersteen, A., M. F. Masman, G. De Baets, W. Jonckheere, K. van der Werf, S. J. Marrink, J. Rozenski, I. Benilova, B. De Strooper, V. Subramaniam, J. Schymkowitz, F. Rousseau, and K. Broersen. 2012. Molecular Plasticity Regulates Oligomerization and Cytotoxicity of the Multipeptide-length Amyloid-beta Peptide Pool. Journal of Biological Chemistry 287:36732-36743.
123. Nichols, M. R., M. A. Moss, D. K. Reed, S. Cratic-McDaniei, J. H. Hoh, and T. L. Rosenberry. 2005. Amyloid-beta protofibrils differ from Amyloid-beta aggregates induced in dilute hexafluoroisopropanol in stability and morphology. Journal of Biological Chemistry 280:2471-2480.
124. Lee, C. C., A. Nayak, A. Sethuraman, G. Belfort, and G. J. McRae. 2007. A three-stage kinetic model of amyloid fibrillation. Biophysical Journal 92:3448-3458.
125. D'Arrigo, C., M. Tabaton, and A. Perico. 2009. N-Terminal Truncated Pyroglutamyl beta Amyloid Peptide A beta py3-42 Shows a Faster Aggregation Kinetics than the Full-Length A beta 1-42. Biopolymers 91:861-873.
126. Jarrett, J. T., E. P. Berger, and P. T. Lansbury. 1993. THE CARBOXY TERMINUS OF THE BETA-AMYLOID PROTEIN IS CRITICAL FOR THE SEEDING OF AMYLOID FORMATION - IMPLICATIONS FOR THE PATHOGENESIS OF ALZHEIMERS-DISEASE. Biochemistry 32:4693-4697.
127. Ono, K., R. Takahashi, T. Ikeda, M. Mizuguchi, T. Hamaguchi, and M. Yamada. 2014. Exogenous amyloidogenic proteins function as seeds in amyloid beta-protein aggregation. Biochimica Et Biophysica Acta-Molecular Basis of Disease 1842:646-653.
128. Chiti, F., and C. M. Dobson. 2006. Protein misfolding, functional amyloid, and human disease. In Annual Review of Biochemistry. Annual Reviews, Palo Alto. 333-366.
129. Vandersteen, A., E. Hubin, R. Sarroukh, G. De Baets, J. Schymkowitz, F. Rousseau, V. Subramaniam, V. Raussens, H. Wenschuh, D. Wildemann, and K. Broersen. 2012. A comparative analysis of the aggregation behavior of amyloid-beta peptide variants. Febs Letters 586:4088-4093.
130. Garai, K., and C. Frieden. 2013. Quantitative analysis of the time course of A beta oligomerization and subsequent growth steps using tetramethylrhodamine-labeled A beta. Proceedings of the National Academy of Sciences of the United States of America 110:3321-3326.
131. Kusumoto, Y., A. Lomakin, D. B. Teplow, and G. B. Benedek. 1998. Temperature dependence of amyloid beta-protein fibrillization. Proceedings of the National Academy of Sciences of the United States of America 95:12277-12282.
132. Murakami, K., K. Irie, A. Morimoto, H. Ohigashi, M. Shindo, M. Nagao, T. Shimizu, and T. Shirasawa. 2002. Synthesis, aggregation, neurotoxicity, and secondary structure of various A beta 1-42 mutants of familial Alzheimer's disease at positions 21-23. Biochemical and Biophysical Research Communications 294:5-10.
133. Rezaei-Ghaleh, N., M. Amininasab, K. Giller, S. Kumar, A. Stundl, A. Schneider, S. Becker, J. Walter, and M. Zweckstetter. 2014. Turn Plasticity Distinguishes Different Modes of Amyloid-beta Aggregation. Journal of the American Chemical Society 136:4913-4919.
134. He, W. L., and C. J. Barrow. 1999. The A beta 3-pyroglutamyl and 11-pyroglutamyl peptides found in senile plaque have greater beta-sheet forming and aggregation propensities in vitro than full-length A beta. Biochemistry 38:10871-10877.

135. Sanders, H. M., R. Lust, and J. K. Teller. 2009. Amyloid-beta peptide A beta p3-42 affects early aggregation of full-length A beta 1-42. Peptides 30:849-854.
136. Archer, S. L. 2013. Mitochondrial Dynamics - Mitochondrial Fission and Fusion in Human Diseases. New England Journal of Medicine 369:2236-2251.
137. Muller, W. E., A. Eckert, C. Kurz, G. P. Eckert, and K. Leuner. 2010. Mitochondrial Dysfunction: Common Final Pathway in Brain Aging and Alzheimer's Disease-Therapeutic Aspects. Molecular Neurobiology 41:159-171.
138. Richter, C., J. W. Park, and B. N. Ames. 1988. NORMAL OXIDATIVE DAMAGE TO MITOCHONDRIAL AND NUCLEAR-DNA IS EXTENSIVE. Proceedings of the National Academy of Sciences of the United States of America 85:6465-6467.
139. Nunomura, A., G. Perry, G. Aliev, K. Hirai, A. Takeda, E. K. Balraj, P. K. Jones, H. Ghanbari, T. Wataya, S. Shimohama, S. Chiba, C. S. Atwood, R. B. Petersen, and M. A. Smith. 2001. Oxidative damage is the earliest event in Alzheimer disease. Journal of Neuropathology and Experimental Neurology 60:759-767.
140. Butterfield, D. A., and R. Sultana. 2007. Redox proteomics identification of oxidatively modified brain proteins in Alzheimer's disease and mild cognitive impairment: Insights into the progression of this dementing disorder. Journal of Alzheimers Disease 12:61-72.
141. Leuner, K., T. Schutt, C. Kurz, S. H. Eckert, C. Schiller, A. Occhipinti, S. Mai, M. Jendrach, G. P. Eckert, S. E. Kruse, R. D. Palmiter, U. Brandt, S. Drose, I. Wittig, M. Willem, C. Haass, A. S. Reichert, and W. E. Muller. 2012. Mitochondrion-Derived Reactive Oxygen Species Lead to Enhanced Amyloid Beta Formation. Antioxidants & Redox Signaling 16:1421-1433.
142. Greenlund, L. J. S., T. L. Deckwerth, and E. M. Johnson. 1995. SUPEROXIDE-DISMUTASE DELAYS NEURONAL APOPTOSIS - A ROLE FOR REACTIVE OXYGEN SPECIES IN PROGRAMMED NEURONAL DEATH. Neuron 14:303-315.
143. Chen, H. C., S. A. Detmer, A. J. Ewald, E. E. Griffin, S. E. Fraser, and D. C. Chan. 2003. Mitofusins Mfn1 and Mfn2 coordinately regulate mitochondrial fusion and are essential for embryonic development. Journal of Cell Biology 160:189-200.
144. Nakamura, T., P. Cieplak, D.-H. Cho, A. Godzik, and S. A. Lipton. 2010. S-Nitrosylation of Drp1 links excessive mitochondrial fission to neuronal injury in neurodegeneration. Mitochondrion 10:573-578.
145. Cho, D. H., T. Nakamura, J. G. Fang, P. Cieplak, A. Godzik, Z. Gu, and S. A. Lipton. 2009. S-Nitrosylation of Drp1 Mediates beta-Amyloid-Related Mitochondrial Fission and Neuronal Injury. Science 324:102-105.
146. Bossy, B., A. Petrilli, E. Klinglmayr, J. Chen, U. Lutz-Meindl, A. B. Knott, E. Masliah, R. Schwarzenbacher, and E. Bossy-Wetzel. 2010. S-Nitrosylation of DRP1 Does Not Affect Enzymatic Activity and is Not Specific to Alzheimer's Disease. Journal of Alzheimers Disease 20:S513-S526.
147. Yan, J., and Z. Y. Chen. 2013. BLOCKING GSK3 ss-MEDIATED DRP1 PHOSPHORYLATION PROVIDES NEUROPROTECTION AND RESCUES MEMORY DEFICITS IN APPSWE/PS1DE9 TRANSGENIC MICE. Clinical and Experimental Pharmacology and Physiology 40:3-3.
148. Mattson, M. P., and S. L. Chan. 2003. Calcium orchestrates apoptosis. Nature Cell Biology 5:1041-1043.

149. Demuro, A., M. Smith, and I. Parker. 2011. Single-channel Ca2+ imaging implicates A beta 1-42 amyloid pores in Alzheimer's disease pathology. Journal of Cell Biology 195:515-524.
150. Demuro, A., and I. Parker. 2013. Cytotoxicity of Intracellular A beta(42) Amyloid Oligomers Involves Ca2+ Release from the Endoplasmic Reticulum by Stimulated Production of Inositol Trisphosphate. Journal of Neuroscience 33:3824-3833.
151. Fonseca, A., P. I. Moreira, C. R. Oliveira, S. M. Cardoso, P. Pinton, and C. F. Pereira. 2015. Amyloid-Beta Disrupts Calcium and Redox Homeostasis in Brain Endothelial Cells. Molecular Neurobiology 51:610-622.
152. Kook, S. Y., H. Jeong, M. J. Kang, R. Park, H. J. Shin, S. H. Han, S. M. Son, H. Song, S. H. Baik, M. Moon, E. C. Yi, D. Hwang, and I. Mook-Jung. 2014. Crucial role of calbindin-D28k in the pathogenesis of Alzheimer's disease mouse model. Cell death and differentiation 21:1575-1587.
153. Del Prete, D., F. Checler, and M. Chami. 2014. Ryanodine receptors: physiological function and deregulation in Alzheimer disease. Molecular Neurodegeneration 9:15.
154. Supnet, C., J. Grant, H. Kong, D. Westaway, and M. Mayne. 2006. Amyloid-beta-(1-42) increases ryanodine receptor-3 expression and function in neurons of TgCRND8 mice. Journal of Biological Chemistry 281:38440-38447.
155. Stutzmann, G. E., I. Smith, A. Caccamo, S. Oddo, F. M. LaFerla, and I. Parker. 2006. Enhanced ryanodine receptor recruitment contributes to Ca2+ disruptions in young, adult, and aged Alzheimer's disease mice. Journal of Neuroscience 26:5180-5189.
156. Scimemi, A., J. S. Meabon, R. L. Woltjer, J. M. Sullivan, J. S. Diamond, and D. G. Cook. 2013. Amyloid-beta(1-42) Slows Clearance of Synaptically Released Glutamate by Mislocalizing Astrocytic GLT-1. Journal of Neuroscience 33:5312-5318.
157. Scott, H. A., F. M. Gebhardt, A. D. Mitrovic, R. J. Vandenberg, and P. R. Dodd. 2011. Glutamate transporter variants reduce glutamate uptake in Alzheimer's disease. Neurobiology of Aging 32:11.
158. Hynd, M. R., H. L. Scott, and P. R. Dodd. 2004. Glutamate-mediated excitotoxicity and neurodegeneration in Alzheimer's disease. Neurochemistry International 45:583-595.
159. Gu, Z., J. Cheng, P. Zhong, L. Qin, W. Liu, and Z. Yan. 2014. Abeta Selectively Impairs mGluR7 Modulation of NMDA Signaling in Basal Forebrain Cholinergic Neurons: Implication in Alzheimer's Disease. The Journal of neuroscience : the official journal of the Society for Neuroscience 34:13614-13628.
160. Um, J. W., A. C. Kaufman, M. Kostylev, J. K. Heiss, M. Stagi, H. Takahashi, M. E. Kerrisk, A. Vortmeyer, T. Wisniewski, A. J. Koleske, E. C. Gunther, H. B. Nygaard, and S. M. Strittmatter. 2013. Metabotropic Glutamate Receptor 5 Is a Coreceptor for Alzheimer A beta Oligomer Bound to Cellular Prion Protein. Neuron 79:887-902.
161. Cruz, J. C., H. C. Tseng, J. A. Goldman, H. Shih, and L. H. Tsai. 2003. Aberrant Cdk5 activation by p25 triggers pathological events leading to neurodegeneration and neurofibrillary tangles. Neuron 40:471-483.
162. Cruz, J. C., D. Kim, L. Y. Moy, M. M. Dobbin, X. Sun, R. T. Bronson, and L.-H. Tsai. 2006. P25/cyclin-dependent kinase 5 induces production and intraneuronal accumulation of amyloid beta in vivo. Journal of Neuroscience 26:10536-10541.
163. Lin, H., R. Bhatia, and R. Lal. 2002. Amyloid beta protein forms ion channels: implications for Alzheimer's disease pathophysiology (vol 15, pg 2433, 2001). Faseb Journal 16:1.

164. Inoue, S. 2008. In situ A beta pores in AD brain are cylindrical assembly of A beta protofilaments. Amyloid-Journal of Protein Folding Disorders 15:223-233.
165. Di Scala, C., H. Chahinian, N. Yahi, N. Garmy, and J. Fantini. 2014. Interaction of Alzheimer's beta-Amyloid Peptides with Cholesterol: Mechanistic Insights into Amyloid Pore Formation. Biochemistry 53:4489-4502.
166. Quist, A., L. Doudevski, H. Lin, R. Azimova, D. Ng, B. Frangione, B. Kagan, J. Ghiso, and R. Lal. 2005. Amyloid ion channels: A common structural link for protein-misfolding disease. Proceedings of the National Academy of Sciences of the United States of America 102:10427-10432.
167. Fantini, J., C. Di Scala, N. Yahi, J. D. Troadec, K. Sadelli, H. Chahinian, and N. Garmy. 2014. Bexarotene Blocks Calcium-Permeable Ion Channels Formed by Neurotoxic Alzheimer's beta-Amyloid Peptides. Acs Chemical Neuroscience 5:216-224.
168. Sepulveda, F. J., H. Fierro, E. Fernandez, C. Castillo, R. W. Peoples, C. Opazo, and L. G. Aguayo. 2014. Nature of the neurotoxic membrane actions of amyloid-beta on hippocampal neurons in Alzheimer's disease. Neurobiology of Aging 35:472-481.
169. Yoshiike, Y., R. Kayed, S. C. Milton, A. Takashima, and C. G. Glabe. 2007. Pore-forming proteins share structural and functional homology with amyloid oligomers. Neuromolecular Medicine 9:270-275.
170. Jang, H., F. T. Arce, S. Ramachandran, R. Capone, R. Lal, and R. Nussinov. 2010. beta-Barrel Topology of Alzheimer's beta-Amyloid Ion Channels. Journal of Molecular Biology 404:917-934.
171. Chang, Z. W., Y. Luo, Y. Zhang, and G. H. Wei. 2011. Interactions of A beta 25-35 beta-Barrel-like Oligomers with Anionic Lipid Bilayer and Resulting Membrane Leakage: An All-Atom Molecular Dynamics Study. Journal of Physical Chemistry B 115:1165-1174.
172. Di Scala, C., J. D. Troadec, C. Lelievre, N. Garmy, J. Fantini, and H. Chahinian. 2014. Mechanism of cholesterol-assisted oligomeric channel formation by a short Alzheimer beta-amyloid peptide. Journal of Neurochemistry 128:186-195.
173. Law, A., S. Gauthier, and R. Quirion. 2001. Say NO to Alzheimer's disease: the putative links between nitric oxide and dementia of the Alzheimer's type. Brain Research Reviews 35:73-96.
174. Lipton, S. A., Y. B. Choi, Z. H. Pan, S. Z. Z. Lei, H. S. V. Chen, N. J. Sucher, J. Loscalzo, D. J. Singel, and J. S. Stamler. 1993. A REDOX-BASED MECHANISM FOR THE NEUROPROTECTIVE AND NEURODESTRUCTIVE EFFECTS OF NITRIC-OXIDE AND RELATED NITROSO-COMPOUNDS. Nature 364:626-632.
175. Vodovotz, Y., M. S. Lucia, K. C. Flanders, L. Chesler, Q. W. Xie, T. W. Smith, J. Weidner, R. Mumford, R. Webber, C. Nathan, A. B. Roberts, C. F. Lippa, and M. B. Sporn. 1996. Inducible nitric oxide synthase in tangle-bearing neurons of patients with Alzheimer's disease. Journal of Experimental Medicine 184:1425-1433.
176. Nakamura, T., S. C. Tu, M. W. Akhtar, C. R. Sunico, S. I. Okamoto, and S. A. Lipton. 2013. Aberrant Protein S-Nitrosylation in Neurodegenerative Diseases. Neuron 78:596-614.
177. Abrams, A. J., A. Farooq, and G. F. Wang. 2011. S-Nitrosylation of ApoE in Alzheimer's Disease. Biochemistry 50:3405-3407.
178. Zahid, S., R. Khan, M. Oellerich, N. Ahmed, and A. R. Asif. 2014. DIFFERENTIAL S-NITROSYLATION OF PROTEINS IN ALZHEIMER'S DISEASE. Neuroscience 256:126-136.
179. Mannick, J. B. 2007. Regulation of apoptosis by protein S-nitrosylation. Amino Acids 32:523-526.

180. Qu, J., T. Nakamura, G. Cao, E. A. Holland, S. R. McKercher, and S. A. Lipton. 2011. S-Nitrosylation activates Cdk5 and contributes to synaptic spine loss induced by beta-amyloid peptide. Proceedings of the National Academy of Sciences of the United States of America 108:14330-14335.
181. Qu, J., T. Nakamura, E. A. Holland, S. R. McKercher, and S. A. Lipton. 2012. S-nitrosylation of Cdk5 Potential implications in amyloid-beta-related neurotoxicity in Alzheimer disease. Prion 6:364-370.
182. Tian, B., Q. A. Yang, and Z. X. Mao. 2009. Phosphorylation of ATM by Cdk5 mediates DNA damage signalling and regulates neuronal death. Nature Cell Biology 11:211-U221.
183. Kim, Y., J. Y. Sung, I. Ceglia, K.-W. Lee, J.-H. Ahn, J. M. Halford, A. M. Kim, S. P. Kwak, J. B. Park, S. H. Ryu, A. Schenck, B. Bardoni, J. D. Scott, A. C. Nairn, and P. Greengard. 2006. Phosphorylation of WAVE1 regulates actin polymerization and dendritic spine morphology. Nature 442:814-817.
184. Sen, N., M. R. Hara, M. D. Kornberg, M. B. Cascio, B.-I. Bae, N. Shahani, B. Thomas, T. M. Dawson, V. L. Dawson, S. H. Snyder, and A. Sawa. 2008. Nitric oxide-induced nuclear GAPDH activates p300/CBP and mediates apoptosis. Nature Cell Biology 10:866-873.
185. Hara, M. R., N. Agrawal, S. F. Kim, M. B. Cascio, M. Fujimuro, Y. Ozeki, M. Takahashi, J. H. Cheah, S. K. Tankou, L. D. Hester, C. D. Ferris, S. D. Hayward, S. H. Snyder, and A. Sawa. 2005. S-nitrosylated GAPDH initiates apoptotic cell death by nuclear translocation following Siah1 binding. Nature Cell Biology 7:665-U640.
186. Broersen, K., W. Jonckheere, J. Rozenski, A. Vandersteen, K. Pauwels, A. Pastore, F. Rousseau, and J. Schymkowitz. 2011. A standardized and biocompatible preparation of aggregate-free amyloid beta peptide for biophysical and biological studies of Alzheimers disease. Protein Engineering Design & Selection 24:743-750.
187. Stine, W. B., K. N. Dahlgren, G. A. Krafft, and M. J. LaDu. 2003. In vitro characterization of conditions for amyloid-beta peptide oligomerization and fibrillogenesis. Journal of Biological Chemistry 278:11612-11622.
188. Greenfield, N. J. 2006. Using circular dichroism spectra to estimate protein secondary structure. Nature Protocols 1:2876-2890.
189. Goormaghtigh, E., J. M. Ruysschaert, and V. Raussens. 2006. Evaluation of the information content in infrared spectra for protein secondary structure determination. Biophysical Journal 90:2946-2957.
190. Tatulian, S. A. 2013. Structural characterization of membrane proteins and peptides by FTIR and ATR-FTIR spectroscopy. Methods in molecular biology (Clifton, N.J.) 974:177-218.
191. Goormaghtigh, E., V. Cabiaux, and J. M. Ruysschaert. 1994. Determination of soluble and membrane protein structure by Fourier transform infrared spectroscopy. III. Secondary structures. Sub-cellular biochemistry 23:405-450.
192. Li, T. S. 2004. Investigation of protein-protein interactions by isotope-edited Fourier transformed infrared spectroscopy. Spectroscopy-an International Journal 18:397-406.
193. Taylor, M., T. Banerjee, S. Ray, S. A. Tatulian, and K. Teter. 2011. Protein-disulfide Isomerase Displaces the Cholera Toxin A1 Subunit from the Holotoxin without Unfolding the A1 Subunit. Journal of Biological Chemistry 286:22090-22100.

194. Saido, T. C., T. Iwatsubo, D. M. A. Mann, H. Shimada, Y. Ihara, and S. Kawashima. 1995. DOMINANT AND DIFFERENTIAL DEPOSITION OF DISTINCT BETA-AMYLOID PEPTIDE SPECIES, A-BETA(N3(PE)), IN SENILE PLAQUES. Neuron 14:457-466.

195. Tamm, L. K., and S. A. Tatulian. 1997. Infrared spectroscopy of proteins and peptides in lipid bilayers. Quarterly Reviews of Biophysics 30:365-429.

196. Sreerama, N., S. Y. Venyaminov, and R. W. Woody. 1999. Estimation of the number of alpha-helical and beta-strand segments in proteins using circular dichroism spectroscopy. Protein Science 8:370-380.

197. Goormaghtigh, E., V. Cabiaux, and J. M. Ruysschaert. 1994. Determination of soluble and membrane protein structure by Fourier transform infrared spectroscopy. II. Experimental aspects, side chain structure, and H/D exchange. Sub-cellular biochemistry 23:363-403.

198. Goldblatt, G., J. O. Matos, J. Gornto, and S. A. Tatulian. 2015. Isotope-edited FTIR reveals distinct aggregation and structural behaviors of unmodified and pyroglutamylated amyloid [small beta] peptides. Physical Chemistry Chemical Physics.

199. Shigemitsu, Y., N. Iwaya, N. Goda, M. Matsuzaki, T. Tenno, A. Narita, M. Hoshi, and H. Hiroaki. 2016. Nuclear magnetic resonance evidence for the dimer formation of beta amyloid peptide 1-42 in 1,1,1,3,3,3-hexafluoro-2-propanol. Analytical biochemistry 498:59-67.

200. Xu, Y. C., J. J. Shen, X. M. Luo, W. L. Zhu, K. X. Chen, J. P. Ma, and H. L. Jiang. 2005. Conformational transition of amyloid beta-peptide. Proceedings of the National Academy of Sciences of the United States of America 102:5403-5407.

201. Tycko, R. 2011. Solid-State NMR Studies of Amyloid Fibril Structure. In Annual Review of Physical Chemistry, Vol 62. S. R. Leone, P. S. Cremer, J. T. Groves, and M. A. Johnson, editors. Annual Reviews, Palo Alto. 279-299.